High- and Low-Density High Entropy Alloys for Hydrogen Storage

Von der Fakultät für Ingenieurwissenschaften,
Abteilung Maschinenbau und Verfahrenstechnik der
Universität Duisburg Essen

zur Erlangung des akademischen Grades
eines
Doktors der Ingenieurwissenschaften
Dr.-Ing.

genehmigte Dissertation

von

Frederik Winkelmann

aus

Gelsenkirchen

Gutachter: Prof. Dr. Hartmut Wiggers
Gutachter: Prof. Dr. Ferdi Schüth

Tag der mündlichen Prüfung: 24.05.2023

To my Family and Friends

"So treibt das Bedürfnis der Gesellschaft, aus der Leere und Monotonie des eigenen Inneren entsprungen, die Menschen zueinander, aber ihre vielen widerwärtigen Eigenschaften und unerträglichen Fehler stoßen sie wieder voneinander ab. Die mittlere Entfernung, die sei endlich herauszufinden und bei welcher ein Beisammensein bestehen kann, ist die Höflichkeit und feine Sitte."

Arthur Schopenhauer - 1851

Acknowledgment

First of all, I would like to thank Prof. Dr. Hartmut Wiggers for accepting me as a Ph.D. student, supporting me with questions and discussions, and helping me get different perspectives on the work. I want to thank Prof. Dr. Ferdi Schüth, who allowed me to work in his heterogeneous catalysis department and get to know an extremely friendly and helpful research group, which also gave me insight into many different scientific topics. I am very grateful, as this has greatly helped my development. A big thank you goes to Dr. Michael Felderhoff, who allowed me to work on my topic and stood by me with any questions, always giving me the confidence to complete the work. I am grateful to him for his calm and considerate way of solving problems and issues, which gave me the confidence to work on the challenging topic.

I am grateful to:

Dr. Rene Albert, who always stood by me privately as well as professionally and made my time at the institute very sweet. Thank you for our time with warm coffee, cold beer, or a little conversation. Any scientific and private discussion gave me great pleasure, and I definitely don't want to miss it.

I want to thank Wolfgang Kersten, Knut Gräfenstein, Dirk Ullner, Ralf Thomas, and all the employees of the precision mechanics department, who were always available with help and advice on technical problems. For example, the team repaired every leaking autoclave or broken ball mill with the utmost attention. Many thanks for this support, as well as the informative conversations about technology and application. In the same context, I would like to thank the team from the technical center, who always took care of the entire infrastructure so that the experiments could be carried out under safe conditions.

Furthermore, I would like to thank all the lab assistants and technicians, Florian Baum, Bastian Herrmann, Liam Josch, Marvin Dürr, Pascal Unkel, Marc Mayer, Andre Pommerin, and many others, who helped me in the lab during the execution of experiments and provided a very pleasant working atmosphere.

PD Dr. Claudia Weidenthaler, Hilke Petersen, and Jan Ternieden for all the XRD analyses and helpful discussions about the obtained results and the evaluations using the simulations. Silvia Palm, Norbert Pfänder as well as Hans-Josef Bongard for the investigations with the electron microscopes.

Schüth Group, in general, is full of intelligent and friendly people. Among many others: Alexander Bähr, Tugce Beyazay, Mingquan Yu, Jacopo de Bellis, Jessica Gonzalez, Alexander Hopf, Steffen Reichle, Abdurrahman Bilican, Niklas Stegmann, Marius Bilke, Edward Nürenberg, Amol Amrute, Cristina Ochoa, Pit Losch, Zhengwen Cao, Ezgi Onur Sahin, Özgül Agbaba, Joel Britschgi, Klara Kley, Rohini Khobragade, Linfeng Li, Jil Meyers, Sarah Trillers, Haritha Cheraparambil, Hilke Petersen, Simone Gallus, Isabella Kappel, Macro Bengsch and many many more. All of you have created a great atmosphere in the working group, and I have had extremely lovely parties and events with all of you.

I would also like to thank Annette Krappweis, who always stood up for me when something went wrong. Thank you for your support and your open ear in any crisis. I also thank Kirsten for the fun conversations and for allowing me to discover my pleasure in teaching.

A special thanks go to Alexander Bodach, who accompanied me almost the whole time in the Hydrogen Group and with whom I could spend an insane amount of enjoyable, instructive and humorous times.

Of course, I do not want to miss mentioning the coolest office in the world. Thanks to Christian, aka. Kiki, Wagner, Felipe Marques and Xiaoran Liu. Thanks to the three of you, I had a super good time in the basement during lunch break and after work.

The whole hydrogen group: Dr. Mateusz Balcerzak, Michael Felderhoff, Bastian Herrmann, Jolina Marie Keßler, Fabian Lange, Xiaoran Liu, Felipe Marques, Kateryna Peinecke, Jessica Ponsoni, Dr. Robert Urbanczyk, Kiki, Fei Wang, Dr. Jochen Ortmeyer, Dr. Drew Sheppard, Dr. Zhijie Cao, Marvin Dürr, Pascal Unkel, Rene Albert, Hao Zhong. Thank you all for your support in all the questions, helpfulness, and open ear. As well as for the beautiful breakfasts we were allowed to experience together.

Of course, my family, Gabriele and Georg Daume, Rainer Winkelmann, Saskia Winkelmann, and Janika Winkelmann. With unconditional support, I could experience and enjoy my studies and my time as a doctoral student in peace. For the support even in difficult times. To my friends, Julian Neises, Laura Kühnel, Kevin Blase, Moritz Busch, Johanna Meier, Verena Katte, Jan Miscke, and all the great people I met in Duisburg during my studies. For the outstanding time, I was allowed to spend with all of you to distract my head from work and to relax. My roommates, Konstantin Thronberens, Christian Schlenker and Katharina Kloppenborg. All the "Zottels" from Münsterland, Mario Piekatz, Matteo Späker, Tim Harke, Paul Freund, Justus

Sackarendt, Nils Miethe, Uli Quandt, Luca Hollenberg for the incredible youth we spent together.

Special thanks to Xiaoran Liu. You are a wonderful person; thank you for your uplifting words, patience, and courage to share your precious time with me. You were cheering me up when things went wrong and building me up when I was frustrated. Thank you.

Finally, I am grateful for the financial support from the International Max Planck Research School for Interface Controlled Materials for Energy Conversion (IMPRS-SurMat). A big thank you goes to Elke Gattermann for organizing the lectures and the special annual retreats, which allowed me to expand my scientific knowledge.

Abstract

Hydrogen is considered a secondary energy carrier and is expected to contribute to the transition from a fossil fuel to a renewable energy system. Under normal conditions, hydrogen is a colorless and odorless gas, and above 4 vol.% in the presence of oxygen results in an explosive atmosphere. These properties raise safety issues and complicate its storage concerning its low volumetric energy density as a gas. Therefore, the development of technologically viable storage possibilities is essential. A high potential exists in metal hydrides, which can be used for rechargeable batteries, hydrogen storage, hydrogen compression, and as thermal storage. The storage within the metal hydrides is based on chemical nature, in which the hydrogen is stored in the crystal lattice of the metal and can be released when required. However, a disadvantage of metal hydrides is that mostly heavy elements are used as storage materials, which reduces the gravimetric storage capacity or requires very high temperatures to recover the hydrogen. These properties are challenging for certain applications, such as in the transportation sector or for energy-efficient storage. To increase gravimetric storage capacity, lighter elements in the way of alloys can be used. One class of alloys that represent an interesting option is high entropy alloys. In contrast to bimetallic alloys, high entropy alloys consist of at least four to five elements in equiatomic or nearly equiatomic proportions. Mixing multiple elements in near-equiatomic ratios increases the configuration entropy to overcome the enthalpies of compound formation (intermetallic phase). Accordingly, the formation of a concentrated disordered solid solution consisting of the elements used would be favored and the presence of multiple phases could be suppressed. Considering that the hydrogen storage properties of metal hydrides strongly depend on the phase and the chemical composition, high entropy alloys with their high number of compositions open the way for chemical tunability of hydrogen storage properties. Consequently, this work focuses on the experimental synthesis of different high entropy alloys, specifically using light metals such as lithium, aluminum, and magnesium, to pursue increasing the gravimetric storage capacity. For this purpose, a detailed evaluation of the structural and hydrogen storage properties was carried out.

In the first part of the work, the new material composition AlLiMgTiZr-C_x was synthesized by mechanical alloying. The first experiments have shown that process control agents such as toluene, n-hexane, and ethanol are necessary for powder processing to suppress an enhanced cold welding effect. Based on time-dependent

experiments, it was found that the hydrocarbons decompose, resulting in the formation of a rocksalt-like crystal structure of a high entropy carbide, with zirconium hydride as the intermediate phase. Attempts to suppress the decomposition of the process control agents by reducing the grinding speed or using ZrH2 as the reactant were unsuccessful. The reduction of the milling speed from 1200 to 800/600 rpm showed only a change in the conversion rate, and further reduction to 400 rpm did not provide enough energy for the alloying process. The attempt to suppress the decomposition by using ZrH_2 as a reactant also ended in a rocksalt-like *fcc* structure, with an initial hydrogen content of 1.56 wt.% in the synthesized carbide detected via thermal gravimetry. Subsequent absorption experiments showed that the nanocrystalline (~3 nm) metal carbide can reversibly store up to 0.66 wt.% hydrogen at 150 °C and exhibits high phase stability during the first three cycles.

The work's second part focuses on the systematic investigation of $Ti_{0.325}V_{0.275}Nb_{0.275}Zr_{0.125}$ compounds, where aluminum and lithium have been incorporated explicitly into $MTi_{0.3}V_{0.25}Nb_{0.25}Zr_{0.1}$ alloys with M = $Li_{0.01}$, $Al_{0.01}$ or $Al_{0.05}Li_{0.05}$. It was found that lithium ($Li_{0.1}Ti_{0.3}V_{0.25}Nb_{0.25}Zr_{0.1}$) positively affects the gravimetric storage capacity (~ 2.6 wt.%), but the solid solution phase is destabilized, and disproportionation of the initial phase to the multiphase material occurs over several cycles of hydrogen storage. Aluminum in $Al_{0.1}Ti_{0.3}V_{0.25}Nb_{0.25}Zr_{0.1}$ was found to destabilize the metal hydride phase by reducing hydrogen capacity (~2.0 wt.%). The combination of aluminum and lithium in $Al_{0.05}Li_{0.05}Ti_{0.3}V_{0.25}Nb_{0.25}Zr_{0.1}$ led to the element's influence's compensation, so the properties appeared comparable to the quaternary compound studied. In addition, it was identified that reactive milling under a hydrogen atmosphere resulted in smaller particles than mechanical alloying due to the more brittle properties of the hydride phases and consequently reduced the dehydrogenation temperature (onset ~150 °C). Moreover, compared to the mechanically alloyed samples, the storage capacity was increased by reactive milling, which was observed with an increased phase transformation from *bcc* to *fcc* due to hydrogen uptake.

Kurzzusammenfassung

Wasserstoff wird als sekundärer Energieträger gehandelt und soll zu dem Wechsel von einem fossilen Brennstoff basierten Energiesystem zu einem auf erneuerbaren Energie basierten Energiesystem beitragen. Da Wasserstoff unter normal Bedingungen ein farbloses, geruchloses Gas ist und oberhalb von 4 Vol.% zu einer explosiven Atmosphäre führt, was in Anbetracht dieser Eigenschaften Sicherheits- und Speicherprobleme, im Sinne von niedriger volumetrischer Energiedichte, aufwirft, werden technologisch praktikable Speichermöglichkeiten unabdingbar. Eine hohes Potential diese Problematik anzugehen steckt in Metallhydriden, die für wiederaufladbare Batterien, Wasserstoffspeicherung, Wasserstoffkompression und als thermischer Speicher fungieren können. Die Speicherung innerhalb der Metalhydride basiert auf chemischer Natur, in dem der Wasserstoff in das Kristallgitter von dem Metall eingelagert wird und bei Bedarf wieder freigesetzt werden kann. Ein Nachteil der Metalhydride liegt aber darin, dass meist schwere Elemente in dem Speichermaterial verwendet werden, weshalb die gravimetrische Speicherkapazität reduziert ist oder sehr hohe Temperaturen benötigt werden um den Wasserstoff wieder nutzbar zu machen. Diese Eigenschaften sind problematisch für bestimmte Anwendungen wie zum Beispiel im Transportsektor oder für eine energieeffiziente Speicherung. Um die gravimetrische Speicherkapazität zu erhöhen können jedoch leichtere Elemente in Form von Legierungen eingesetzt werden. Eine Klasse von Legierungen, die eine interessante Option darstellen, sind hoch entropische Legierungen. Im Gegensatz zu bimetallischen Legierungen bestehen Hochentropie-Legierungen aus mindestens vier bis fünf Elementen in äquiatomischen oder nahezu äquiatomischen Verhältnissen. Durch das Mischen mehrerer Elemente in nahezu äquiatomischen Verhältnissen wird die Konfigurationsentropie ausreichend erhöht, um die Enthalpien der Verbindungsbildung (intermetallischer Phasen) zu überwinden. Dementsprechend wird die Bildung eines konzentrierten, ungeordneten Mischkristalls aus den verwendeten Elementen begünstigt und das Vorhandensein mehrerer Phasen unterdrückt werden. In Anbetracht der Tatsache, dass die Wasserstoff-speichereigenschaften von Metallhydriden stark von der Phase sowie von der chemischen Zusammensetzung abhängt, eröffnen hoch entropische Legierungen mit ihrer hohen Anzahl an Zusammensetzungen den Weg für eine chemische Abstimmbarkeit die Speichereigenschaften.

Im ersten Teil der Arbeit wurde die neue Werkstoffzusammensetzung AlLiMgTiZr-Cx durch mechanisches Legieren synthetisiert. Die ersten Experimente haben gezeigt, dass Prozesskontrollmittel wie Toluol, N-Hexan und Ethanol bei der Pulververarbeitung notwendig sind, um den Kaltschweißeffekt zu unterdrücken. Anhand von zeitabhängigen Experimenten wurde festgestellt, dass sich die Kohlenwasserstoffe zersetzen, was zur Bildung einer rocksalt-ähnlichen Kristallstruktur eines hoch entropischen Karbids führt, mit Zirkoniumhydrid als Zwischenphase. Die Versuche die Zersetzung der Prozesskontrollmittel zu unterdrücken über die Reduzierung der Mahlgeschwindigkeit oder den Einsatz von ZrH_2 als Edukt waren erfolglos. Die Verringerung der Mahlgeschwindigkeit von 1200 auf 800/600 Umdrehungen pro Minute zeigte nur eine Veränderung der Umwandlungsrate, und eine weitere Verringerung auf 400 Umdrehungen pro Minute lieferte nicht genügend Energie für den Legierungsprozess. Der Versuch, die Zersetzung durch die Verwendung von ZrH_2 als Reaktant zu unterdrücken, endete ebenfalls in einer rocksalt-ähnlcihen *fcc* Struktur mit einem anfänglichen Wasserstoffgehalt von 1,56 wt.-% im synthetisierten Karbid, der durch thermische Gravimetrie nachgewiesen wurde. Anschließende Absorptionsexperimente zeigten, dass das nanokristalline (~3 nm) Metallcarbid bis zu 0,66 wt.-% Wasserstoff bei 150 °C reversibel speichern kann und während der ersten drei Zyklen eine hohe Phasenstabilität aufweist.

Der zweite Teil der Arbeit befasste sich mit der systematischen Untersuchung von $Ti_{0.325}V_{0.275}Nb_{0.275}Zr_{0.125}$ Verbindungen, wobei Aluminium und Lithium gezielt in die $MTi_{0.3}V_{0.25}Nb_{0.25}Zr_{0.1}$ Legierungen mit M = $Li_{0.01}$, $Al_{0.01}$ or $Al_{0.05}Li_{0.05}$ eingearbeitet worden ist. Dabei wurde festgestellt, dass Lithium ($Li_{0.1}Ti_{0.3}V_{0.25}Nb_{0.25}Zr_{0.1}$) sich positiv auf die gravimetrische Speicherkapazität (~ 2.6 wt.%) auswirkt, aber die Phase der Festkörperlösung destabilisiert wird und über mehrere Zyklen der Wasserstoffspeicherung eine Disproportionierung der Ausgangsphase zum mehrphasigen Material stattfindet. In Metallhydridphase der $Al_{0.1}Ti_{0.3}V_{0.25}Nb_{0.25}Zr_{0.1}$-Legierung erwies sich Aluminium als destabilisierend, in dem eine verringerte Wasserstoffkapazität (~2.0 wt.%) festgestellt wurde. Die Kombination von Aluminium und Lithium in $Al_{0.05}Li_{0.05}Ti_{0.3}V_{0.25}Nb_{0.25}Zr_{0.1}$ führte dann zur Kompensation der Elemente, wodurch die Eigenschaften vergleichbar zu der untersuchten quaternären Verbindung festgestellt wurden. Darüber hinaus wurde festgestellt, dass das reaktive Mahlen unter Wasserstoffatmosphäre aufgrund der spröderen Eigenschaften der Hydridphasen zu kleineren Partikeln führte als das mechanische Legieren und folglich die Dehydrierungstemperatur (Onset ~150 °C) senkte. Außerdem wurde im Vergleich zu den mechanisch legierten Proben die Speicherkapazität durch reaktives Mahlen

erhöht, was mit einer verstärkten Phasenumwandlung von *bcc* zu *fcc* aufgrund der Wasserstoffaufnahme beobachtet wurde.

Contents

List of Abbreviations

- *bcc* Body-Centred Cubic
- *bct* Body-Centered Tetragonal
- BPR Ball-to-Powder Weight Ratio
- DSC Differential Scanning Calorimetry
- EA Elemental Analysis
- E_a Activation Energy
- EDX Energy-Dispersive X-Ray Spectroscopy
- *fcc* Face-Centred Cubic
- H/M Hydrogen to Metal Ratio
- *hcp* Hexagonal Close-Packed
- HEA High Entropy Alloys
- HR-TEM High-Resolution Transmission Electron Microscopy
- ICP-OES Inductively-Coupled Plasma – Optical Emission Spectrometry
- LOHC Liquid Organic Hydrogen Carrier
- MH_x Metal hydrides
- MS Mass Spectrometer
- ND Not Detectable
- PCA Process Control Agent
- PCI Pressure-Composition-Isotherm
- PTFE Polytetrafluoroethylene
- rpm Revolutions per Minute
- SEM Scanning Electron Microscopy
- TEM Transmission Electron Microscopy
- TGA Thermogravimetric Analysis
- T_m Melting Temperature
- VEC Valence Electron Concentration
- wt.% Percentage by Weight

- XRD X-Ray Diffraction
- δ Atomic Size Difference

List of Figures

List of Tables

Chapter 1

1. Introduction

Climate events such as storms, floods and bushfires are increasing worldwide due to anthropogenic climate change.[1] To reduce the associated problems such as starvation, loss of quality of life and biodiversity, the United Nations Framework Convention on Climate Change, 21st Conference of the Parties (COP 21), stipulated that the increase of global average temperature should remain below 2 °C above the pre-industrial level by 2050.[2] At this point, the focus needs to be shifted to so-called greenhouse gases, as these contribute to a large part of global warming and are produced in almost all processes such as energy conversion, the backbone of the industrial age.[1] However, to ensure warming below 2 °C, the net zero emissions scenario must be implemented by 2050. This scenario implies that no additional greenhouse gases, such as carbon dioxide, should be emitted, and current emissions must be reduced to zero.[3]

The net zero emission scenario poses a significant challenge to the world's population, so much of the scientific community is concerned with the question of how this can be achieved. One approach to this is the transition of the energy system based on fossil fuels to renewable energy sources. The challenge of renewable energy sources such as solar, wind, or hydropower is that they fluctuate frequently, and discrepancies in energy supply and consumption may arise. These discrepancies must be compensated, which is why the focus in the energy transition is not only on carbon-free energy transformation but also on distribution and energy storage.

The so-called hydrogen economy is a promising key technology to decouple the energy supply from the energy demand. In this hydrogen scenario, hydrogen is a secondary energy carrier. Molecular hydrogen can be obtained through electrolysis (water splitting), in which electrical energy from renewable sources is firstly converted into chemical energy (hydrogen). Subsequently, the hydrogen must be stored, transported, and, if required, converted back to electrical energy using fuel cell technology or into thermal energy by combustion of hydrogen with oxygen in combustion engines. The advantage of this scenario is the adaptability of this technology, as it covers a wide range of application sizes, such as in the automotive industry, forklifts, trains, trucks, and stationary energy conversion systems.[4-5] This sounds promising at first, but the bottleneck of this technology, the storage of hydrogen, must be addressed directly. A

safe and efficient storage technology must be developed so that the user is faced with safe handling even without prior knowledge or training. Accordingly, the following sections briefly overview the hydrogen molecule and its storage possibilities.

1.1. Hydrogen an „Energetic Molecule“

Hydrogen is the most common element in the universe, accounting for almost 90 % of all atoms. Compared to all other elements, hydrogen is the simplest atom, consisting of only one electron and one proton, and appears mainly in the molecular form of H_2 rather than in the atomic form H. In addition to this isotope, there are the less common isotopes deuterium (D/^{2}H) and tritium (T/^{3}H), which differ in their number of neutrons in the nuclei (D = 1, T = 2). Owing to its single valence electron, hydrogen is very reactive and usually exists bound in molecules, such as H_2. In nature, however, hydrogen is rarely found in its pure form; it is usually bound to many chemical compounds.[6-7] One of the best-known examples is the water molecule H_2O. This also shows that hydrogen must first be separated from its chemical compounds to store pure hydrogen. At the industrial level, steam reforming of methane with water vapor is usually carried out. The overall process can be described with the following reaction:

$$CH_4\,(g) + 2\,H_2O\,(g) \leftrightharpoons CO_2(g) + 4\,H_2\,(g) \qquad (1.1)$$

This reforming process poses an endothermic reaction enthalpy of 164.9 kJ mol^{-1} and usually requires high temperatures of 800 – 900 °C and pressures in the range of 20 – 30 bar.[8-9] Furthermore, carbon dioxide is released, which should be avoided in the zero-emission scenario. For this reason, there is also a high interest in water splitting utilizing electrolysis since only molecular hydrogen and oxygen are produced, and renewable energy sources can be used without greenhouse gas emissions. The energy stored in this way is then found in the chemical bond of the hydrogen molecule and can be recovered in two ways. Firstly, by generating electrical energy using fuel cell technology and secondly, by combustion with oxygen producing water. When hydrogen is burned with pure oxygen, water is produced as a reaction product, and an energy of 142 MJ kg^{-1} is released, taking into account the heat of condensation of the water.[7] The specific enthalpy of combustion of hydrogen is thus three times higher than that of hydrocarbons (~47 MJ kg^{-1}).[7, 10] This property makes hydrogen an ideal candidate to replace fossil fuels in the future and move closer to the goal of the zero-emission scenario. However, it must be considered that hydrogen is a highly flammable, colorless, and odorless gas under normal conditions, representing a safety risk. The properties of gases also mean that hydrogen has a low volumetric energy density

(~10.7 MJ m^{-3}) under normal conditions compared to liquid hydrocarbons (petrol 34200 MJ m^{-3}), making hydrogen storage a technical and economic challenge.[6, 11]

1.2. Hydrogen Storage

Hydrogen storage is a diverse interdisciplinary field, as chemical and physical techniques can be used to improve gravimetric and/or volumetric energy storage density to address the aforementioned problem that hydrogen is gaseous under normal conditions and therefore has a low volumetric energy density. The U.S. Department of Energy divides the hydrogen storage options into two subgroups, physical and material-based, as shown in Figure 1.

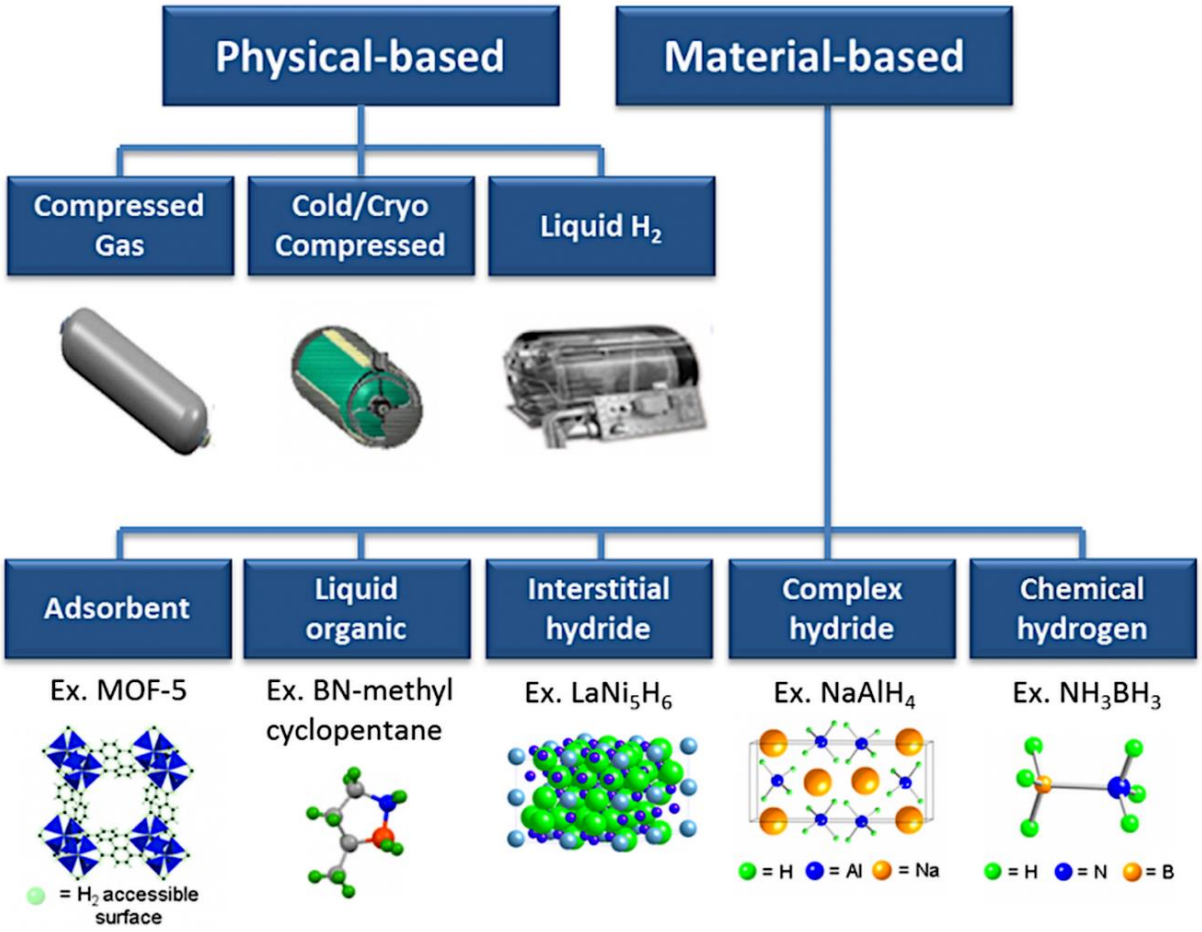

Figure 1: Overview of hydrogen storage technologies categorized by the U.S. Department of Energy. https://www.energy.gov/eere/fuelcells/hydrogen-storage, U.S. Department of Energy (accessed 13.05.21).

Physical storage technologies include gas compression, combined cryo-compression processes, and hydrogen liquefaction. For example, gas compression uses, among others, special composite pressure vessels in which hydrogen can be stored at pressures of 350 up to 700 bar, as it is found in commercially available fuel-cell driven cars.

However, 15 % of the energy content of hydrogen is also used for compression, and the volumetric energy density is still below that of fossil fuels. For comparison, liquid hydrogen has an energy density of 10.1 MJ l^{-1}, whereas gasoline has an energy density of 34.2 MJ l^{-1}.[11] In addition, hydrogen liquefaction consumes up to 20 to 30 % of the energy content in the liquefaction process.[6] This energy loss, in turn, reduces the efficiency of the liquefaction-storage methodology.[6] For a better overview, the gravimetric and volumetric energy densities of common energy carriers are listed in the following
Table 1.

Table 1: Volumetric and gravimetric energy densities of common fuels.[11]

Material	Energy per kilogram [MJ kg^{-1}]	Energy per liter [MJ l^{-1}]
Hydrogen (ambient pressure)	143	0.0107
Hydrogen (compressed, 700 bar)	143	5.6
Hydrogen (liquid)	143	10.1
Natural gas (compressed, 250 bar)	53.6	9
LPG propane (< 10 bar, liquid)	49.6	25.3
Gasoline (petrol, liquid)	46.4	34.2
Diesel (liquid)	45.4	34.6

The second subgroup comprises the material-based storage techniques, which differ in the physical and chemical properties of the materials and are briefly evaluated below. The storage technology with high-surface adsorbents (e.g., metal-organic frameworks, porous carbon materials) is based on physisorption and thus represents a mixture of the physical and material-based storage methods. The gaseous hydrogen adsorbs on

the material's surface or in the accessible pores and can then be recovered by heating or applying a mild vacuum. Nevertheless, because of the low adsorption enthalpy of hydrogen on these materials (in the order of 2 – 5 kJ mol^{-1}), the process must be carried out under cryogenic conditions at 77 K and is often realized with liquid nitrogen. This poses a technological and energetic challenge because, on the one hand, large quantities of liquid nitrogen are required, and, on the other hand, the liquefaction of the nitrogen requires a further conversion process and thus reduces the efficiency of the storage technology.[12]

A further classification concerns the materials to which hydrogen forms a chemical bond (covalent, ionic, and metallic) and are distinguished according to the following hydrogen carriers. These hydrogen carriers include small molecules (amine boranes, amides/imides), liquid organic hydrogen carriers (LOHCs) as cyclic hydrocarbons (benzene/cyclohexanes) or metal hydrides (MgH_2, $NaAlH_4$).[12-13]

Looking at the storage capacity of small molecules, for example, ammonia-borane exhibits a very high gravimetric hydrogen storage capacity (19.6 wt.%). However, the hydrogen release reactions are irreversible due to complex reaction mechanisms, which limits the reuse of such materials and is a significant technological disadvantage compared to reversible systems.[12]

Liquid organic hydrogen carriers (LOHCs) belong to the group of reversible systems, which will be explained using the example of the benzene/cyclohexane system. Cyclohexane represents the hydrogen carrier in the charged state, in which the hydrogen is covalently bonded to the molecule. If necessary, the bound hydrogen is released catalytically (Ni, Ru), and 7.2 wt.% can be utilized. The product is benzene, which can then be catalytically hydrogenated again if required. Technologically, LOHCs represent a very interesting storage option since the infrastructure for liquid fuels is already available, and development costs can be saved here. [13-14]

Volumetric storage capacity can be further increased by solid-state hydrogen storage materials, mainly metal hydrides. Since this thesis is mainly concerned with solid-state hydrogen storage, a separate **Chapter 2** is reserved for this class of materials. Figure 2 illustrates the different storage options in terms of their gravimetric and volumetric storage capacity and provides an overview of the different storage options in terms of capacity and operational conditions. As the graph shows, the metal hydrides are in the upper third in terms of volumetric storage capacity, but due to the mostly heavy metal atoms, metal hydrides have a reduced gravimetric storage capacity. The lighter the atoms become, as in the case of lithium-containing compounds, for example, the greater

the gravimetric storage density. However, these are usually not reversible. The compressed gas storage strongly depends on the storage media used, steel or composite material, and directly shows that real storage systems depend on the encapsulation material, which is not taken into account in this graph for the material-based storage media. For the application of material-based storage materials, this means that further weight has to be taken into account due to the encapsulation material and accordingly has a reducing influence on the gravimetric storage capacity.

Nevertheless, material-based storage materials such as metal hydrides can achieve higher volumetric storage capacities. Concerning the application, however, not only the storage capacity plays an important role, but also the cycling behavior, stability of the storage material, thermodynamic parameters such as hydrogenation (absorption) and dehydrogenation (desorption) temperatures, overall costs, environmental aspects, and kinetics with respect to hydrogenation/dehydrogenation speed are crucial to consider.[7, 12-13]

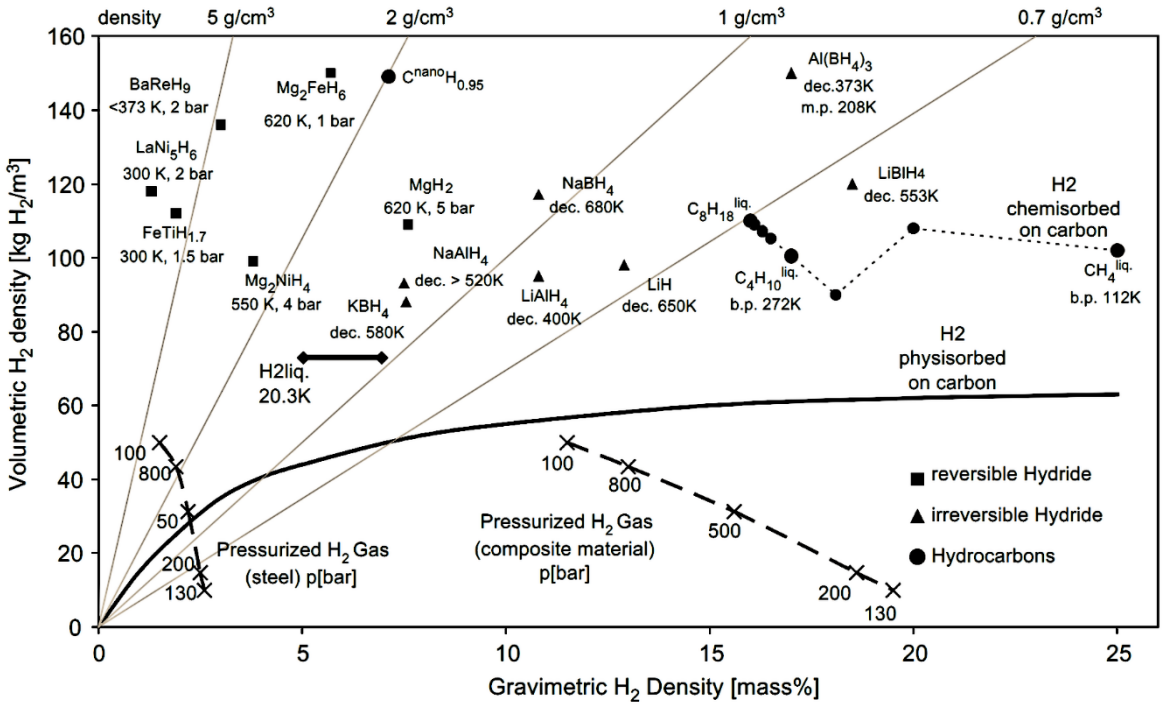

Figure 2: Overview of selected hydrogen storage materials/technologies, volumetric storage capacity versus gravimetric storage capacity.[6-7] (Copyright © 2010 Wiley-VCH Verlag GmbH & Co. KGaA, Copyright © 2001, Nature Publishing Group)

1.3. Objectives

The work presented here aims to describe the synthesis of new high-entropy alloys based on light and transition metals and, subsequently, to investigate their hydrogen storage behavior as interstitial storage materials. The selective use of light metals aimed to reduce the crystallographic density of the alloys/mean molar mass and thus increase the gravimetric storage capacity. The gravimetric capacity follows the correlation,

$$wt.\% = \frac{m_{H_2}}{m_{H_2} + m_{Host}} \cdot 100 = \frac{\left({}^{H}/_{M}\right) M_H}{M_{Host} + \left({}^{H}/_{M}\right) M_H} \cdot 100$$

where m_{H_2} is the mass of hydrogen, m_{Host} is the mass of the host material, H/M is the hydrogen-to-metal ratio, M_H is the molar mass of elemental hydrogen, and M_{Host} is the molar mass of the host material or metal. Following this relationship, the reduction of the host material leads to increased gravimetric storage capacity. Based on the findings in the literature that the synthesis methods, mechanical alloying and reactive milling, have proven to be helpful in terms of the formation of cubic solid solutions and their hydrogen storage properties, this synthesis approach is used exclusively in this work. The following list gives a brief overview of the contents of the respective chapters.

Chapter 2: The second chapter discusses the fundamentals of metal hydrides. For this purpose, the metal-hydrogen system is first addressed, and a brief literature review of previously investigated metal hydride systems is given.

Chapter 3: The third chapter deals with the definition and concept of high entropy alloys, followed by a literature review of the hydrogen storage properties of high entropy alloys, relating the significant material properties to the hydrogen storage properties.

Chapter 4: In this chapter, the fundamentals of mechanical alloying and reactive milling are first introduced, followed by a detailed description of the experimental data, and is concluded with a detailed description of the characterization methods used.

Chapter 5: A composition based on AlLiMgTiZr is presented in this chapter. This alloy was selected to investigate whether the empirically developed guide parameters (VEC, ΔH_{mix}, δ, and Ω; cf. Chapter 3.1) introduced by Zhang et al. and Guo et al. apply to an alloy mainly composed of light metals.[15-18] The guide parameters represent a concentration-weighted average for the respective quantity. VEC stands for valence

electron concentration; ΔH_{mix} takes into account the enthalpies of mixing of the individual elements. δ gives a percentage quantity for the atomic mismatch based on the mean atomic radius; and Ω is a dimensionless quantity that correlates the enthalpy of mixing with the entropy of mixing as well as the mean melting temperature. The alloy composition theoretically satisfies the selection criteria with a valence electron concentration of 2.8, a δ of 4.78 %, a ΔH_{mix} of 0.48 kJ $mol^{-1,}$ and an Ω of 35.58 (cf. Appendix 9.1). Subsequently, the objective was to examine practically whether the alloy forms a solid solution with a *bcc* structure since the VEC of 2.8 is below 6.87, the upper threshold for *bcc* formation (c.f. Chapter 3.1). Furthermore, the hydrogen storage behavior is investigated.

Chapter 6: The 6th chapter is based on the investigations of Montero et al., who identified the quaternary alloy $Ti_{0.325}V_{0.275}Nb_{0.275}Zr_{0.125}$ as a possible hydrogen storage material and then systematically investigated the influence of a fifth element (M = Mg, Al, Ta) in the material composition $M_{0.1}Ti_{0.3}V_{0.25}Nb_{0.25}Zr_{0.1}$.[19-22] From these results, this chapter presents the systematic investigation with another element, lithium, and the effects on the storage properties of the alloy by combining Al and Li to a respective proportion of 5 %. For the systematic study, the synthesis utilizing reactive milling of the same quaternary compound is first presented, which is then used as an internal reference for the later discussion.

Chapter 2

2. Fundamentals of Metal Hydrides

This chapter presents the fundamentals of the metal-hydrogen system. Conceptually, various metals, metal alloys, or intermetallic compounds can react with hydrogen to form a metal hydride. This reaction is usually an equilibrium reaction, and the equilibrium state is described by the equilibrium pressure curve and varies with material composition. After changing the ambient conditions (temperature/hydrogen gas pressure) and the equilibrium state, either the metal hydride is formed or leads to decomposition into the starting material and hydrogen gas. Due to the reversible reaction, these materials can be considered solid-state storage materials with high volumetric capacities.

In general, the following reaction equation 2.1 describes the reversible reaction between gaseous hydrogen (H_2) and the metal (M) to form metal hydrides (MH_x):

$$M\,(s) + \frac{x}{2}\,H_2\,(g) \leftrightharpoons MH_x\,(s) + \Delta H_R \qquad (\Delta H_R > 0) \qquad (2.1)$$

Under adequate reaction conditions depending on temperature and pressure, the hydrogen can react with the metal upon thermal energy release (exothermic hydrogenation reaction), and the metal hydride can be formed. To reverse the reaction, thermal energy needs to be added to the system (endothermic dehydrogenation), and the hydrogen can be utilized for other energy conversion processes. Besides the hydrogen storage possibilities, this reversible reaction can also be used in thermochemical energy storage systems, in which the reaction enthalpy of the conversion is used to store and release heat.

The reversible reaction case described above does not apply to all metals of the periodic system since not all metals form a reversible system with hydrogen at relevant technical conditions. In order to distinguish the metals, the hydride formation enthalpy must be taken into account, after which two groups can be identified in the periodic table (cf. Figure 3). On the one hand, metals with a high affinity for hydrogen have a negative enthalpy of formation and are called A-elements (red color code in Figure 3). On the other hand, the non-hydride-forming elements have a low affinity for hydrogen and are designated as B-elements (blue color code). This subdivision is shown in the following periodic table, taking into

account the enthalpies of formation of binary metal hydrides, and also serves as the basis for the combinatorial selection criterion for the synthesis of alloys that can form metal hydrides.

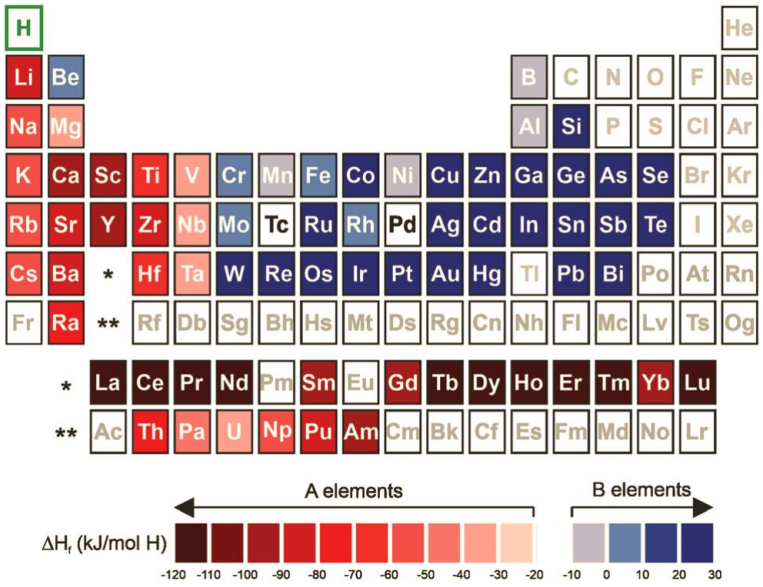

Figure 3: Periodic table with relative subdivision of A- and B-type elements, taking into account the enthalpies of formation of the binary metal hydrides.[23] (CC BY 3.0)

To synthesize hydrogen-absorbing alloys, A- and B-metals are mixed in different stoichiometric compositions to obtain a synergetic effect of alloying elements on hydride formation by influencing thermodynamic, kinetic and/or macroscopic properties such as storage capacity. Typical compositions are: AB (TiFe), AB_5 ($LaNi_5$), AB_2 ($ZrMn_2$) and A_2B (Mg_2Ni).[24]

One of the best-known examples is the TiFe-system, which briefly explains the A- and B-elements concept. In the alloy, titanium represents the A-element with a negative enthalpy of formation (-144.35 kJ mol^{-1} H_2), and accordingly, the hydrogen in the binary Ti/TiH_2 system is strongly bound, requiring high temperatures (> 400 °C) for the decomposition of the hydride phase.[25-26] Iron, on the other hand, has a positive enthalpy of formation (+7.9 kJ mol^{-1} H), so the formation of iron hydride is thermodynamically unfavorable.[27] The combination of both metals results in an alloy that, unlike the individual elements, can reversibly store up to 1.89 wt.% hydrogen at room temperature under 5 bar.[7, 28] The disadvantage, though, is that this alloy requires a complex activation process (high temperatures and pressures) actually to perform under the conditions mentioned.[29]

Since the hydrogenation process is more complicated, it will be dealt with in the following chapters, considering the thermodynamic characteristics. In addition,

different classes of metal hydrides are described depending on the types of bond (ionic, covalent, or metallic).

2.1. Metal-Hydrogen System

As mentioned above, metal hydrides can be synthesized via the reaction between gaseous hydrogen and the host material/metal. The formation of hydrides is somewhat more complicated than the simple absorption of hydrogen and can be divided into more steps.

For hydride formation, molecular hydrogen first adsorbs on the surface of the metal, where the hydrogen molecules dissociate at sufficient energy. The resulting hydrogen atoms diffuse on the surface and into the crystal lattice, losing their valence electron when crossing the boundary.[30] In the crystal lattice, the diffusion processes occur via the octahedral and tetrahedral interstitial sites, and the occupation of the interstitials is initially disordered. As a consequence, a solid solution is formed, the so-called α-phase. As the hydrogen concentration in the crystal lattice increases, the hydrogen-hydrogen interaction begins to play an increased role, and the occupation becomes more and more ordered. The ordered phase is called β-phase, starts to nucleate, and grows with increasing H_2 concentration in the crystal lattice.[7]

This process can also be explained using the pressure-composition isotherm (PCI). For a PCI curve, the equilibrium pressure is plotted against the mass concentration or the hydrogen-to-metal ratio, which must be measured under isothermal conditions. This is exemplified in Figure 4a) for an ideal binary metal hydride system. Several significant areas can be assigned to the process described above in the PCI curve. In the case of a low hydrogen concentration, the α-phase is formed first, and the equilibrium pressure increases. At a critical hydrogen loading, the α-phase and β-phase coexist, and a plateau forms at a certain equilibrium pressure. The plateau can also be understood as the hydrogen concentration increases, the growth of the β-phase reduces the proportion of the α-phase. In addition, the plateau gives information on the reversible storage capacity of the metal hydride. Furthermore, the plateau position of the equilibrium pressure gives a hint about the stability of the hydride, which can be seen from the fact that, e.g., unstable hydrides need lower temperatures to reach a certain equilibrium pressure. In the third region, the equilibrium pressure increases because the material is close to saturation, and additional hydrogen uptake causes higher internal stress and therefore requires increased pressures.

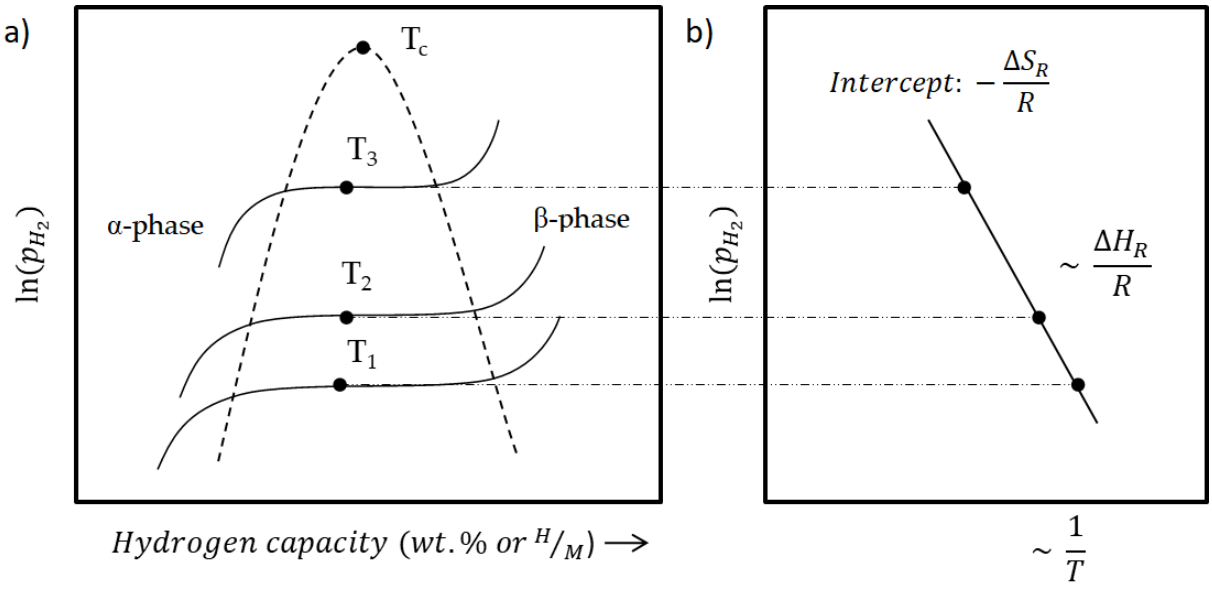

Figure 4: a) Schematic pressure-composition isotherm (PCI) at different temperatures of an ideal system b) corresponding van't Hoff plot.

Moreover, the PCI curves can be used to extract thermodynamic quantities such as the enthalpy change of formation, ΔH_R, and the entropy change, ΔS_R (cf. Figure 4b). For this, a sufficient number of isotherms must be measured at different temperatures and evaluated using the van't Hoff equation. To obtain the van't Hoff equation, the change in Gibbs free energy, ΔG, for the system can be expressed by Equations 2.2 and 2.3:

$$\Delta G = RT \ln p_{H_2} \tag{2.2}$$

$$\Delta G = \Delta H_R - T\Delta S_R \tag{2.3}$$

An endothermic process for the dehydrogenation reaction is assumed, which means that the hydride phase is more stable than the pure metal.[7, 24] By equating the above formulas, the van't Hoff Equation 2.4 is obtained.

$$\ln p_{H_2} = \frac{\Delta H_R}{RT} - \frac{\Delta S_R}{R} \tag{2.4}$$

With the universal gas constant, R, and given temperatures, T, the van't Hoff plot can be generated (cf. Figure 4b), and the thermodynamic variables can be determined. For the procedure, the pressure is plotted logarithmically against T^{-1} so that according to Equation 2.4, the y-axis intercept (T^{-1} = 0) describes the change in entropy and the slope the enthalpy of reaction divided by R, respectively. In general, the change in entropy from metal to its hydride phase is small (10 J K^{-1} mol^{-1}), so the change in entropy for hydride formation is mainly contributed by the entropy change of the hydrogen gas from the gas phase to the dissolved solid hydrogen

(130 J K^{-1} mol^{-1}). It can thus be assumed that the entropy change is constant regardless of the metal.[7, 24]

In contrast to the ideal-thermodynamic binary metal-hydrogen system, realistic non-ideal systems can have a slope, a hysteresis, or even several plateaus in the measured PCI curves. Inhomogeneities of the sample, impurities, or internal stresses can cause different parts of the material to absorb hydrogen at different equilibrium pressures, which then statistically add up to a slope of the plateau as the sum of many individual effects.[31-32] The hysteresis of a real PCI curve is characterized by an increased equilibrium pressure during hydrogen absorption than during desorption. Here, the hysteresis effect is assumed to be due to the plastic deformation of the metal hydride required during hydrogen absorption to compensate for the volume change of the crystal lattice.[32] The volume change is due to the uptake of hydrogen and results in a volume increase of the host crystal of ~2.9 $Å^3$ in the vast majority of interstitial metal hydrides.[33] The last feature, several plateaus, is due to intermediate stages of the reaction, as in the case of the pure metal vanadium, for example. The hydrogenation of vanadium follows the sequence V → V(H) → V_2H → VH_2, and accordingly shows a PCI with two plateaus.[34]

2.2. Classification

With an electronegativity of 2.2, hydrogen is located in the middle of the Pauling scale (0.7 – 4.0). In combination with the wide range of electronegativity of metals, the bonding properties of the formed metal hydride can be very different. Consequently, metal hydrides can be differentiated according to their ionic, covalent, or metallic bond types. However, it must also be considered that this division has mainly didactic uses and that the exact distinction between the classifications can become blurred. A more detailed discussion can be found in Grochala's work.[12, 35]

2.2.1. Ionic Metal Hydrides

Ionic metal hydrides are formed when hydrogen interacts with electropositive metals, such as alkali or alkaline earth metals. These often form stoichiometric hydrides such as LiH or MgH_2. The high difference in electronegativity means that the metal usually shifts its electron in the direction of hydrogen. Accordingly, the cations can be treated as M^{n+} and the anions as H^-. As a consequence of the ionic bond, relatively stable hydrides are formed. The increased stability of LiH, for example, is reflected in the decomposition temperature of 720 °C. However, the high decomposition temperature and the formation of aggressive lithium gas make using

this material technologically tricky, despite the high storage capacity of 12.6 wt.%.[35] Compared to LiH, MgH_2 plays a technologically more important role. Although the density of magnesium reduces the storage capacity to 7.6 wt.%, the hydrogen can be stored reversibly under working conditions (350 – 450 °C). These hydrogen storage properties make MgH_2 interesting for energy applications such as heat storage.[36]

2.2.2. Covalent Metal Hydrides

Metals from the p-block of the periodic table, specifically from groups 13 (Al, Ga, and In) and 14 (Si, Ge, Sn, Pb), form covalent metal hydrides. The covalent bond type in the hydrides often has the effect of forming unstable hydrides. The properties of the hydrides formed from the elements of group 14 (Si, Ge, Sn, and Pb) make them difficult to use technologically. The coordination environment of the central atoms is sufficiently saturated, which is why the hydrides of group 14 are often present in molecular form and generate highly flammable gases.[35] The hydrides formed from the elements of group 13, such as InH_3, tend to have polymeric structures, making the material's rehydrogenation impractical.[37] Aluminum hydride, for example, has a high storage capacity (10.1 wt.%), but for direct regeneration from aluminum and gaseous hydrogen, pressures above 700 MPa at ambient temperature are required.[38]

The so-called complex hydrides, $M_m^{\delta+}[MH_n]^{\delta-}$, play a unique role among the covalent metal hydrides with n hydrogen. These are formed by combining an electron-positive metal, often alkali or alkaline earth metal, with a metal-hydrogen complex $[MH_n]^{\delta-}$. The electropositive metals push their excess electrons to the complexes so that the resulting cation stabilizes the anionic character of the complex. $LiBH_4$, as one of these complex metal hydrides, has a very high storage density of 18.5 wt.%, but the reaction is not reversible. The complex hydrides are also very reactive to atmospheric moisture, making their technological application difficult.[39] A more promising system is $NaAlH_4$, although this has a reduced reversible storage capacity of 5.6 wt.%, the complete decomposition is divided into three steps. However, the reaction is reversible at moderate working temperatures with the addition of certain titanium catalysts.[12, 40] Therefore, this material could still be used for heat storage or hydrogen.

2.2.3. Metallic Metal Hydrides

When the metals from the d-block of the periodic table or lanthanide series form metal hydrides, the bond is often classified as metallic. This is because they retain their metallic appearance and electrical conductivity. However, as mentioned at the

beginning, this definition is difficult to support because a bond can also have mixed types.[35] Regardless of the exact bond type, this class has the distinction of having a wide range of non-stoichiometric compositions MH_x due to the occupation of the interstitial sites. Thus they are also called interstitial metal hydrides. For the transition metals, the hydrogen content (x) can vary from 0 to 2, and for the lanthanoids, from 0 to 3.[41-42] Normally, the crystal structures have a much higher number of available interstitial sites compared to the absorbed hydrogen atoms, so it could be assumed that even higher occupancies can be achieved. However, the occupation is limited, which can be explained by the Switendick criterion. This criterion states that due to H-H interactions, two hydrogen atoms cannot be closer than 2 Å.[43] Switendick's calculations have shown that introducing hydrogen into the host metal generates additional states and that the energetic position of these states depends on the hydrogen-hydrogen distance. If the distance is too short, the energetic states can be above the Fermi level and, therefore, not occupied. A meaningful occupation occurs only with an increased H-H distance, which according to his calculations is at 2 Å.[43] This minimum distance of H-H distance is also supported by the Westlake criterion, which takes geometric parameters into account.[44] As there is a wide range of crystal structures among the interstitial hydrides and chemically different compounds, examples will not be given here, as the focus is on hydrogen storage in high entropy alloys (HEA), described in more detail in **Chapter 3.2.** In principle, however, alloys in which different elements occupy the respective lattice sites can also be included in this class if no stoichiometric compounds are formed upon hydrogenation. If the type of alloying elements used is also considered, a reduced gravimetric storage capacity is often achieved due to their high density. In the literature, a rough limit of 2 wt.% is given, but this has already been exceeded by some work on Mg-, Ti- and V-based alloys, which then have the disadvantage of low cycle numbers due to degradation, complex activation processes or technically inapplicable working conditions.[12, 28, 34]

The following is a brief list of the most important properties of metal hydrides that need to be investigated so that hydrogen storage materials can be assigned to specific applications.

- The *gravimetric storage capacity* considers the mass of hydrogen relative to the weight of the storage material, including the hydrogen stored in the material, and is expressed in wt. %, kg kg^{-1} or mol kg^{-1}.[45] This is an essential parameter for the transportation sector, such as onboard applications, as the additional

weight of the host material should be low in order not to reduce the efficiency of such vehicles.

- The *volumetric storage capacity* takes into account the amount of hydrogen per unit volume of the storage material and is expressed accordingly in kg m^{-3} or mol m^{-3}. Both gravimetric and volumetric storage capacities are also often expressed in energy terms to represent the energy stored in the material, kWh kg^{-1} and kWh m^{-3}, respectively.[45] These are especially relevant for stationary applications, where as much energy as possible needs to be stored.
- *Long-term cycling stability* must be considered, as materials often lose capacity over many charge and discharge cycles. For example, the alloy $LaNi_{5.2}$ has been reported to lose up to 20% of reversible hydrogen storage capacity over 1500 cycles.[46] Therefore, long-term cycle stability is essential for all applications and must be investigated before the material is used. In the case of reduced durability, the storage materials would have to be replaced at great expense, which is an ecologically and economically relevant factor.
- *The storage material's sorption and desorption kinetic properties* are important because these determine the hydrogen adsorption and desorption rate. For the application, one must consider both thermodynamic and kinetic quantities. Because a material that can meet the expectation of the pressure and temperature ranges but could react very slowly to the changing working conditions (pressure or temperature), thus limiting the range of applications.
- *Thermodynamic quantities* determine the operating temperature and pressure ranges. The most interesting variables here are the enthalpy of formation and the enthalpy of decomposition, which are expressed in kJ mol^{-1}. These determine the amount of hydrogen stored at a certain pressure and temperature combination under equilibrium conditions.[45] Materials with high equilibrium pressures at mild operating temperatures, for example, can be interesting for hydrogen compression. Under reduced temperature, the materials could be loaded, and heating would result in an increased equilibrium pressure at which the hydrogen could be released.
- Another critical factor in terms of long-term stability is *resistance to gaseous impurities*. Impurities can arise depending on the hydrogen's synthesis method; for example, if hydrogen from steam reforming is used, carbon monoxide, hydrogen sulfide, or ammonia can be present in the gas. Traces of the molecules alone can poison the surface and thus significantly reduce the storage capacity over several cycles.[45]
- Metal hydrides often need to be subjected to an *activation process* that opens up diffusion paths or removes surface oxides so that the material can be

adequately used as a storage material. Activation involves repeated hydrogenation and dehydrogenation of the materials until full storage capacity is reached.

- From an economic point of view, the purchase price and, thus, the *storage medium's cost is relevant*. Depending on the application, different quantities are required, which can limit the use of expensive materials.
- The metal hydrides should be as *non-toxic* as possible to avoid negative environmental impacts and health hazards[35]

Chapter 3

3. Fundamentals of High Entropy Alloys

High entropy alloys (HEA) belong to a new class of metallic materials and were first described independently by Cantor et al. and Yeh et al. in 2004.[47-48] In contrast to conventional alloys, which typically consist of at least two elements, with at least one being a metal, the synthesis of HEAs involves mixing at least four to five elements in an equimolar or near-equimolar atomic ratio of 5 to 35 %. Cantor et al. termed this type of alloy a multicomponent alloy, but Yeh et al. independently introduced the concept of high entropy alloys.[47-48] This type of alloy has recently attracted much attention as some excellent mechanical properties at high temperatures, magnetism, corrosion resistance, energy storage, and conversion have been demonstrated.[49-53] Additionally intriguing is the property that these alloys can form disordered solid solutions with simple crystal structures such as body-centered cubic (*bcc*), face-centered cubic (*fcc*), or hexagonal close-packed (*hcp*).[23, 52-53] The property of forming single-phase systems over wide concentration ranges makes HEAs unique concerning hydrogen storage, as new insights into the influence of individual components can be obtained over this large number of unexplored areas (concentrations, phases/crystal structures). In the following, the concept of high entropy alloys and the material properties investigated so far with regard to hydrogen storage are discussed.

3.1. Concept of High Entropy Alloys

The concept of high entropy alloys is based upon increasing the configurational entropy of mixing elements so that a solid solution is preferred to forming intermetallic phases or multiple phases. The mixing entropy ΔS_{mix} of an equimolar solid solution consisting of n elements can be described by the Boltzmann Equation 3.1,

$$\Delta S_{mix} = -R \sum_{i=1}^{n} c_i \ln c_i = R \ln n \qquad (3.1)$$

where R is the gas constant, c_i is the molar fraction of the ith element, and n is the total number of constituent elements.[47, 50] Empirical and statistical investigations have shown that the entropy of mixing should have a value of at least 1.6 R so that the

formation of a solid solution takes place.[50] This is the case when n is five. However, considering entropy alone is insufficient to determine a solid solution's formation. For this, the Gibbs free energy of mixing ΔG_{mix} must be taken into account, as described by Equation 3.2.

$$\Delta G_{mix} = \Delta H_{mix} - T\Delta S_{mix} \quad (3.2)$$

With ΔH_{mix} the enthalpy of mixing, T the absolute temperature, and ΔS_{mix} the entropy of mixing, formula 3.2 can be used to explain the so-called high entropy effect. From a thermodynamic point of view, all possible phases compete with each other, and the phase with the lowest Gibbs free energy is usually formed. If it is considered that ΔH_{mix} is constant and element-dependent, it can be seen that ΔG_{mix} is minimized by maximizing ΔS_{mix}. In the case of five elements, this leads to a minimization of the Gibbs energy and, thus, to the stabilization of the disordered solid solution. However, this assumption is not generally valid for all materials, as other entropy contributions (magnetic, vibrational, and electronic) could play an important role.[53]

The ability of HEAs to form a single-phase solid solution is essential for the subsequent characterization of hydrogen properties, as the formation of multiple phases makes the characterization or unambiguous determination of a system complex. Considering the wide range of possible compositions, it quickly becomes apparent that additional parameters are needed. Therefore, it is even more important for the design of such alloys to have selection criteria that can be used and go beyond the explanation of the high entropy effect to predict the formation of such solid solutions. Various parameters influenced by the Hume-Rothery rules are proposed in the literature.[53] These empirically developed rules can help predict a particular phase's formation. According to these rules, forming the solid solution phase is favored when the alloying elements have similar atomic sizes, electronegativities, valences, and crystal structures. Consequently, the atomic size differences (δ), electronegativities, valence electron concentration (VEC), and thermodynamic parameters should be calculated based on the alloy composition.[17-18, 53-54] The thermodynamic parameters include the enthalpy of mixing (ΔH_{mix}) and the Ω parameter introduced by Zhang et al., which takes into account the enthalpy of mixing, entropy of mixing (ΔS_{mix}) and melting temperature (T_m).[54] All these parameters can be calculated with the following equations:

$$\delta = \sqrt{\sum_{i=1}^{n} c_i \left(1 - \frac{r_i}{\bar{r}}\right)^2} \times 100 \quad (3.3)$$

$$\delta_\chi = \sqrt{\sum_{i=1}^{n} c_i \left(1 - \frac{\chi_i}{\bar{\chi}}\right)^2} \times 100 \quad (3.4)$$

$$VEC = \sum_{i=1}^{n} c_i(VEC_i) \tag{3.5}$$

$$\Delta H_{mix} = \sum_{i=1, i\neq j}^{n} 4\Delta H_{ij}^{mix} c_i c_j \tag{3.6}$$

$$\Omega = \frac{T_m \Delta S_{mix}}{|\Delta H_{mix}|} \tag{3.7}$$

$$T_m = \sum_{i=1}^{n} c_i (T_m)_i \tag{3.8}$$

$$\bar{r} = \sum_{i=1}^{n} c_i r_i \tag{3.9}$$

$$\bar{\chi} = \sum_{i=1}^{n} c_i \chi_i \tag{3.10}$$

In the formulas, the subscript *i* refers to the *i*th element. Otherwise, r_i, χ_i, VEC_i stand for the respective element's atomic radius, electronegativity, and valence electron concentration. The formulae 3.9 and 3.10 correspond to the average atomic radius and the average electron negativity, respectively, c_i and c_j describe the atomic fractions, ΔH_{ij}^{mix} is the enthalpy of mixing of elements *i* and *j* at the equimolar concentration in regular binary solutions. T_m without index is used to describe the theoretical melting temperature of the alloy with respect to the individual components.

In order to obtain these empirical based formulas, much effort was put into evaluating many alloy compounds. Zhang et al. suggested that alloys with an atomic difference below 6.6 % and Ω > 1.1 tend to form stabilized solid solutions.[16, 54] It is also suggested that the enthalpy of mixing should be in a range from -15 kJ mol^{-1} to 5 kJ mol^{-1} for solid solution formation.[15-16, 50] Materials not meeting this condition tend to form intermetallic, precipitates, or amorphous phases. Guo et al. followed this empirical method by correlating the valence electron concentration with the expected crystal structure (*bcc*, *hcp*, or *fcc*).[17-18] It was found that alloys with VEC < 6.87 tend to form *bcc* alloys, and for VEC > 8, the formation of *fcc* phases is preferred.[17-18] These findings represent a powerful tool in terms of the development of single-phase metal alloys. Because for hydrogen storage, the crystalline structure is important with respect to the number of interstitial sites, considering that the *bcc* phase offers 12 tetrahedral interstitial sites that can potentially be occupied by hydrogen. In comparison, the *fcc* structures offer only 8 tetrahedral interstitial sites. However, it must be emphasized that the VEC selection rule was mainly applied to

alloys consisting of transition metals and that sufficient information on non-transition metals is lacking in the literature.[18] Nevertheless, these selection rules provide good guidelines for exploring the broad field of high entropy alloys.

3.2. Hydrogen Storage in High Entropy Alloys

Since the introduction of the HEAs concept in recent years, more and more effort has been put into the research of high entropy alloys. This includes not only the previously mentioned outstanding properties in terms of mechanical stability but also the interest in hydrogen storage materials has grown steadily. The broad scope for design concerning the concentrations of the alloying elements opens up a vast and still relatively unexplored field. At the present time, there are still few indications of exactly which parameters influence which storage properties. So far, three reviews have been published in the literature that carefully summarized these properties.[23, 55-56] The most important properties are briefly discussed below.

First, it should be emphasized that the alloys studied so far had different crystal structures (*bcc* or ordered intermetallic structures like C14 Laves phases). According to the number of publications, most of the effort has been put into the research of *bcc* alloys, and a minor part into C14 Laves phases.[23] In terms of hydrogen absorption/release, the C14 alloys maintain their structure, except that the lattice constant varies with the occupation or depletion of the interstitial sites.[55] The *bcc*-alloys, on the other hand, show a different mechanism. With increasing hydrogen concentration, the *bcc* phase expands until a symmetry change from *bct*, or *fcc* bi-hydrides occurs.[55] This mechanism is reversible upon hydrogen release, and the *bct*/*fcc* phase reverts to the previous *bcc* phase. This mechanism of expanding and symmetry change can be understood as the breathing of the material.[34]. Furthermore, the crucial parameters of the disordered solid solutions with simple cubic phases, which structurally differ from the Laves phases, will be discussed in the following since the main focus of this work is on the synthesis as well as the investigation on solid solutions with simple cubic phases.

The *bcc* HEAs studied so far from the literature have very different chemical compositions, complicating the correlation of the respective parameters with the hydrogen storage capacities. The compositions of these alloys vary from pure A-elements to materials composed only of B-elements. Most commonly, 3d and 4d transition metals have been used for synthesizing these alloys, with 80 % of the elements used being titanium, vanadium, and zirconium.[23] However, attempts have been made to increase the gravimetric storage capacity by adding lightweight

elements such as aluminum, magnesium, and scandium to the alloys, but this has not led to a general increase of the capacity, as the complex interactions of the individual alloying elements seem to play an essential role.[57-61]

The publication by Sahlberg et al. proved to be a propellant for the interest in high entropy alloys. The *bcc* alloy consisting of TiVHfNbZr showed an exceptionally high hydrogen uptake with a hydrogen-to-metal (H/M) ratio of 2.5 (corresponding gravimetric capacity of 2.7 wt.%) at 573 K and 5.3 MPa, which is usually expected to be 2 for *bcc* transition metal hydrides. To achieve such a high H/M ratio of 2.5, the tetrahedral and part of the octahedral interstices have to be filled since the complete occupation of the tetrahedrons and the octahedral interstices lead to a H/M ratio of 2 and 1, respectively. The occupation of both interstices is not the case, though, in *bcc* alloys or their individual elements, since the distance between the interstitial sites is less than 2 Å and thus violates the Switendick criterion.[41, 43, 62] The authors have suggested high lattice strain caused by the atomic mismatch (δ ~ 6.8 %) as the reason for the occupation of the tetrahedral and octahedral interstices for this unusual hydrogen uptake.[41] Further investigations using neutron scattering on the same alloy composition confirmed the assumption that the occupation of the tetrahedral and the octahedral interstices takes place. Karlsson et al. showed by neutron diffraction experiments that the occupation of the respective interstitials is approximately equal at high temperatures (53: 47). After cooling the samples, the occupation changed so that 92 % of the tetrahedral and 5.2 % of the octahedral gaps were filled, corresponding to H/M of 1.91 at 1 MPa.[63] The high H/M ratio of 2.5 was measured at a pressure of 5.3 MPa. Thus, the pressure difference of 1 to 5 MPa during the respective experiment could cause a difference in the H/M ratio. However, any alloy has not reproduced the high H/M ratio of 2.5 in subsequent investigations.[23]

Nygard et al. further pursued the hypothesis that the high H/M ratio is due to the high lattice mismatch by studying different alloys based on $TiVZr_xNbTa_{(1-x)}$ and $TiVZr_{(1+x)}Nb$.[64] Varying the zirconium or tantalum content resulted in alloys with *bcc* phases, where the atomic size mismatch δ was adjusted from 3.53 % to 6.34 %. None of the alloys studied could reproduce the high H/M ratio of 2.5. All alloys were in the corresponding dihydride phase (*fcc* or *bct*) after hydrogenation with a H/M ratio of about 1.9, indicating no trend between hydrogen capacity and atomic size mismatch. However, Nygard et al. found that the zirconium content in the alloys plays an essential role in phase stability—alloys with a Zr content higher than 12.5 at.% tended to phase segregate and thus lose their potential cycling properties—the materials below 12.5 at.% Zr content, on the other hand, showed increased stability to

high temperatures, in which the initial *bcc* phase was recovered after a hydrogenation cycle. In addition, the study revealed that an increasing zirconium content leads to a more stable hydride phase, as shown by the increasing dehydrogenation temperature.[64]

Another critical parameter is the valence electron concentration (VEC). The influence of this parameter has already been addressed in several papers in the literature.[65-67] The working group around Nygard et al. systematically investigated whether a correlation exists between the VEC and the hydrogen storage behavior.[65] They investigated different alloy compositions based on the ternary system TiVNb and added different elements (Zr, Hf, Ta, Cr, Mo, and mixtures) to scale the VEC. The study shows that the hydride phases are destabilized with increasing VEC, showing a two-step dehydrogenation process. However, the influence of VEC mainly affected the onset of the second dehydrogenation stage. The results concerning the hydrogen capacity indicate that alloys with a VEC above 5 showed a lower hydrogen absorption ($H/M \leq 1.5$), whereas the materials with a VEC below 5 showed a H/M ratio of about 2. In further theoretical work, Reverse Monte Carlo structure models were used to investigate the influence of the VEC on a local level. The findings show that the occupation probability of interstitial sites is increased when the local VEC is reduced.[66] When both papers are considered together, this strongly supports the assumption that VEC can be used to tune the hydrogen storage properties in terms of stability. However, it is unclear from this works whether the chemical nature of the alloying elements has the most significant influence. This question was then addressed by Silva et al. by studying three different alloys ($(TiVNb)_{85}Cr_{15}$; $(TiVNb)_{95.3}Co_{4.7}$; $(TiVNb)_{96.2}Ni_{3.8}$) with the same VEC of 4.87. The results did not show any significant differences in their hydrogenation properties (the equilibrium plateau pressure, the H/M ratio, and the structure of the hydride phase), although the chemical composition of the alloys varied greatly.[23, 67] This suggests that the valence electron concentration plays a significant role in the hydrogen storage properties of the alloys and might be used to tune their properties.

As mentioned at the beginning, the approach of increasing the gravimetric storage capacity of alloys and the corresponding hydrides has also been pursued by adding light metals such as aluminum or magnesium. Adding such low-density elements is intended to lower the average molar weight of the alloys and thus increase the storage capacity. However, the synthesis of such alloys initially turns out to be difficult, as the work of Sun et al. has shown.[68] In this study, the influence of light elements in various HEAs was investigated. The focus was on stability, taking into

account the synthesis methodology (conventional melting, rapid solidification processes, and mechanical alloying). The results indicate that adding magnesium to the alloys synthesized by melting processes led to the formation of intermetallic phases. Only the second process step, mechanical alloying, a non-equilibrium technique, led to the formation of solid solutions.[68] When synthesizing such alloys, the vapor pressure and/or the melting point of the alloying elements also play an essential role. For example, since titanium has a melting point of 1668 °C and lithium (T_m ~ 180 °C) is to be added to the alloy to lower the density, the melting point and vapor pressures differ immensely at the temperatures required for synthesis.[69-70] The high temperatures required for the melting process can lead to the evaporation of the elements with high vapor pressure and complicate the adjustment of the exact concentrations in the alloys. On the other hand, mechanical alloying with high-energy ball mills takes place at room temperature, which is advantageous since the equilibrium vapor of the respective element and equilibrium processes plays a minor role.

Apart from the difficulty of synthesizing low-density HEAs, it has also been shown that mechanical alloying has a positive effect on the hydrogen desorption properties obtained. In the work of Montero et al., the same alloy composition, $Ti_{0.325}V_{0.275}Nb_{0.275}Zr_{0.125}$, has been synthesized by three different methods, arc-melting, high energy ball milling, and reactive milling. The hydrogen desorption behavior of all three samples was different. The reactive milled alloy showed the lowest desorption temperature, followed by the arc-melted and mechanical alloyed samples. Several reasons for this order are given in the literature: the microstructure, surface passivation, and the history of the sample (exposed to air, cycled).[19] This behavior, that ball milling positively affects the hydrogen storage properties, was also demonstrated for the pure Mg/MgH_2 system. The effect of the mechanical forces during ball milling improved the adsorption kinetics of the processed Mg. The reason for this is an increased defect density (grain boundaries) and a reduced crystallite size. Besides the positive effect of mechanical processing on the adsorption kinetics of the metal hydrides, this effect is expected to be enhanced under a hydrogen atmosphere during reactive milling.[36] The brittle mechanical properties of the hydride phases can lead to increased nanostructuring during mechanical action and thus further improve the adsorption kinetics.[36] This is also reflected in the results where the desorption temperature of the reactively milled sample is the lowest compared to the arc-melted and mechanical alloyed sample.[19]

Reactive milling as a synthesis method was also first demonstrated in the work of Zepon et al. In the study, an alloy based on $MgZrTiFe_{0.5}Co_{0.5}Ni_{0.5}$ was synthesized, and its hydrogenation was investigated.[58] The sample synthesized under an inert atmosphere exhibited a *bcc* structure after alloying, showing a mixed *bcc* and *fcc* hydride phase after hydrogenation (H/M 0.7; 1.2 wt.%). Alternatively, the same composition was synthesized by reactive milling under a hydrogen atmosphere. As a result, the product obtained could be identified as a pure *fcc* hydride phase, but no hydrogen amount was given.[58] Taking these findings into account, reactive alloying promotes hydrogen uptake in such alloys.

Chapter 4

4. Methodology

This work aimed to investigate various high-entropy alloys that could be used as solid hydrogen storage materials. For this purpose, the initial focus was on synthesizing individual alloys, with particular attention paid to using light metals (Al, Li, and Mg) and substituting individual elements (c.f. Chapter 1.3). Since using light metals complicates the applicability of conventional melting processes due to the strongly varying vapor pressures, mechanical alloying was applied as the synthesis strategy. Mechanical alloying is explained in more detail below, along with the related process of reactive milling. Subsequently, the characterization methods are presented, divided into structural and chemical characterization and characterization of hydrogen storage properties.

4.1. Synthesis by Mechanical Alloying

Mechanical alloying fundamentally belongs to the field of mechanochemistry, where high-energy ball mills initiate a chemical reaction by applying mechanical energy. Specifically, in mechanical alloying, blended elemental solid powders are alloyed by means of repeated welding, fracturing, and re-welding of powder particles to produce desired material compositions. A special feature of the process is that it is a non-equilibrium process, which allows the synthesis of non-equilibrium phases, such as metastable crystalline and quasi-crystalline phases, nanostructured alloys, and supersaturated solid solutions.[71]

The energy required for the alloying process is provided in high-energy ball mills via the impacts and frictions of the accelerated milling balls. The impacts of the balls then lead to the transfer of mechanical energy in three different forms via high impact, shear, and torsional forces.[72] The energy transfer can trigger various phenomena in the mill feed, depending on the mechanical properties. Ductile metals have been shown to flatten and harden at the beginning of the process. The strong plastic deformation leads to the particles' solidification and fracture. Brittle metals, on the other hand, are directly crushed upon collision. Fracturing in both cases, however, leads to the formation of new surfaces, which are then reassembled via cold welding, which initially increases the particle size at the beginning of the

alloying process. From a certain degree of hardness of the material, further milling leads to a size reduction and homogenization of the particles. In the literature, different systems, whether ductile-ductile, ductile-brittle, or brittle-brittle, have been described with different alloying mechanisms.[71, 73-74]

In addition, the form of energy transfer has to be considered, which strongly depends on the mill used, and it is characterized by the motion of balls and mills. These types of mills are distinguished by the following nomenclature: planetary mills, shaking mills, attritor mills, and drum mills.[71] It should be mentioned that attritor mills and drum mills are mainly used for upscaling processes, while planetary and shaking mills are mainly used on a laboratory scale. Planetary and shaking mills differ regarding energy transfer from balls to processed powders. In the case of the shaking mills, it is assumed that the intensity of the impact forces is more pronounced in the relationship between shear and impact forces. Nevertheless, since planetary mills were mainly used for mechanical alloying in this work, they will be described in more detail in the following. Principally, planetary mills are named after their motion method, as the milling jars are moved in a planetary motion. The cylindrical grinding jars are mounted opposite each other on an axially rotating disk and are simultaneously rotated around their own axis. Based on the disc and grinding jar rotation, the two resulting centrifugal forces act on the grinding balls and powder. The combination of both centrifugal forces leads in superposition to an alternating force field from the inside to the outside so that the grinding balls initially run along the inner wall of the grinding jar (friction effect), and when the direction of the forces changes, lift-off occurs and the balls can then hit the opposite wall by impact (impact effect).[71]

If all the effects described above are taken into account, there are important process parameters that have an influence on the alloying process and which are explained briefly below:

- *Milling equipment*: The material of the grinding jars and the balls play an important role, and these are usually made of stainless steel, tungsten carbide, zirconia, or other hard materials (nitrides, carbides). The materials' density and mechanical properties directly influence the energy exchange between the ground stock and the balls. In addition, milling equipment's materials vary in their wear resistance, which has to be considered in terms of contaminations.
- *Milling speed*: The milling speed directly influences the balls' kinetic energy, which ultimately allows the energy input to be directly controlled. There are limitations with planetary mills, though, since, at too high rotational speeds,

the balls can be pinned to the inner wall, which minimizes the impact effect or even the whole conversion. Typical milling speeds are between 200 and 800 rpm, whereby the choice depends on the design of the ball mill used.

- *Milling time*: The milling time is essential to consider, as this can be used to decide whether the alloying process is complete. Depending on the elements used, this can vary greatly and is an important criterion to be checked. In addition, longer milling leads to higher contamination due to abrasion, so materials should only be milled for as long as necessary for synthesis. In the literature, synthesis times for different systems vary from one hour to 400 or even more hours.[71]
- *Ball-to-powder weight ratio (BPR)*: The BPR significantly influences the milling time required, as it can vary the number and intensity of impacts. The higher the BPR, the more impacts in relation to the ground material take place, and consequently, the required milling time is reduced. Care must be taken with the fill level, as the balls require a certain free volume to be accelerated to the appropriate velocities. Typical BPRs are 10:1 or 20:1, but these have also been reported from 1:1 up to 220:1.[71]
- *Milling atmosphere*: The milling atmosphere mainly concerns contamination since some metals, such as lithium, for example, can react with nitrogen and thus form undesired nitrides.[71] Therefore, alloying is often carried out under inert gas atmospheres such as argon or helium.
- *Process control agent (PCA)*: Since alloying can only occur if there is a balance between cold welding and fracturing, a PCA is often added to the powder mixture. The PCA can be understood as a surfactant that changes the surface energy of the particles and thus reduces the cold welding effect. It should also be considered that it can be incorporated as a contaminant into the alloy forming carbides.[71] Typical PCAs are ethanol, benzene, hexane, toluene, or stearic acid.[71]

In order to achieve a successful alloying process, it is necessary to maintain a balance between cold-welding and fracturing of the particles. If this balance is not achieved and the cold-welding effect is more pronounced, this can lead to the materials sticking to the mill equipment and thus significantly reducing the yield. One approach, as described above, is the addition of PCAs during mechanical alloying to influence the surface properties of the powders. Another approach involves the direct synthesis of the hydride phases under a hydrogen atmosphere, which is an adapted form of mechanical alloying and is called reactive milling. Milling under a

hydrogen atmosphere leads to direct hydrogenation of the metals and thus changes their mechanical properties, reducing the ductility of the metals and the cold-welding effect with the direct synthesis of metal hydrides. This is an excellent approach for synthesizing new metal hydrides because the materials are directly hydrogenated in this way. Furthermore, a more complex technological effort must be considered in terms of autoclave construction. The grinding jars must simultaneously withstand the conditions of mechanical stress and high pressure to provide a sufficient amount of hydrogen without damage. In addition, it is also necessary to verify whether the alloying process can occur when the metals are in hydrogenated form.

All samples presented in this work were prepared either by mechanical alloying or reactive milling, whereby three different types of mills (E_{max} from Retsch, Pulverisette 6, and 7 from Fritsch) were used. Pure metals were used for the syntheses, and details on purity and suppliers can be found in Table 2.

Table 2: Overview of chemicals used with manufacturer and specification.

Element	Form	Size	Purity	Distributor
Aluminum	Powder	-325 mesh	99.5%	Alfa Aesar
Hafnium	Powder	-325 mesh	99.6%	abcr GmbH
Iron	Powder	5-9 µm	99.5%	Sigma Aldrich
Lithium	Granular	4-10 mesh	99%	Sigma Aldrich
Magnesium	Powder	-325 mesh	99.8%	Alfa Aesar
Niobium	Powder	-45 µm	99.8%	abcr GmbH
Titanium	Powder	-60+100 mesh	99.5%	Alfa Aesar
Vanadium	Powder	-325 mesh	99.5%	abcr GmbH
Zirconium	Powder	-50 mesh	99.5%	abcr GmbH

All samples were prepared and manipulated exclusively under an inert gas atmosphere in a glove box to avoid oxygen contamination (argon, $O_2 < 0.1$ ppm, $H_2O < 0.1$ ppm). In the following, the respective types and process parameters are assigned to the respective chapter.

Chapter 5: Mechanical alloying of the AlLiMgTiZr compounds, the E_{max} model from Retsch was used. The elemental powders were weighed according to the molar ratios, 1:1:1:1:1 (in total ~2 g), and transferred to a 50 ml oval tungsten carbide grinding jar (Figure 5a). Tungsten carbide grinding balls (Ø 5 mm) were used as grinding media and the BPR was varied between 20:1, 40:1, and 60:1. The jars are sealed with a Viton® gasket to prevent atmospheric exchange during the milling process. The milling process was performed in cycles, and one cycle consisted of 10 minutes of active milling with a one-minute break. Since the process conversion was unclear, tracking experiments were carried out. The milling process was stopped in between, and small samples were taken for further investigation. As PCAs, different solvents (Ethanol, n-hexane, and toluene; 7 – 8 wt.%) were used. The solvents were dried by conventional methods to reduce the dissolved water content. The exact test details are assigned to the individual results and described in the evaluation.

Reactive milling was adapted from the publication of our collaboration partners (Zepon et al.).[23, 58] The elements were weighed in stoichiometric ratios (total ~3.6 g) and sealed in a high-pressure stainless steel jar (volume ~50 ml) with 18 stainless steel balls (Ø 10 mm). The BPR was fixed at 20:1, and the milling jar was pressurized up to 30 bars H_2. The milling was carried out on a Fritsch Pulverisette 6 planetary ball mill at a speed of 600 rpm and was performed in cycles. One milling cycle included 30 minutes of milling and a 5 minutes break in between, followed by a direction reversal. In total, the milling process lasted for 24 hours. After the process, the jar was depressurized, and the product was collected for further experiments. The grinding jars are equipped with a unique filter lid (Figure 5b), so no powder can escape when the pressure is released. One experiment deviated from the prescribed procedure by using 10 stainless steel grinding balls (Ø 10 mm) so that 2 g of powder with a BPR of 20:1 were weighed in. The grinding jar was pressurized with 180 bar hydrogen, and the grinding process was carried out at 450 rpm. One cycle consisted of 10 min of grinding and one minute of pause followed by a direction reversal.

Chapter 6: Mechanical alloying of the high entropy alloys based on TiVNbZr was carried out on Pulverisette 7 from Fritsch. According to the stoichiometry in Table 3, the elemental powders were weighed (in total ~3.25 g) and transferred to a 45 ml stainless steel grinding jar (Figure 5c). The BPR was fixed to 26:1, and 20 stainless steel balls (Ø 10 mm) were used. The grinding jars were sealed with polytetrafluoroethylene (PTFE) gaskets and encapsulated with duct tape to establish a second barrier against an atmospheric exchange. One grinding cycle included 15 minutes of grinding at 700 rpm, and after each step of ball milling, the powder

was scraped from the inner walls of the grinding jar by hand, and a small sample was taken. The total grinding times differ taking into account the alloying progress.

Table 3: Targeted chemical composition.

$Ti_{0.325}V_{0.275}Nb_{0.275}Zr_{0.125}$	$Li_{0.1}Ti_{0.3}V_{0.25}Nb_{0.25}Zr_{0.1}$	$Al_{0.05}Li_{0.05}Ti_{0.3}V_{0.25}Nb_{0.25}Zr_{0.1}$	$Al_{0.1}Ti_{0.3}V_{0.25}Nb_{0.25}Zr_{0.1}$

Reactive milling of the alloys was carried out on Pulverisette 6 from Fritsch. According to the stoichiometry in Table 3, the elemental powders were weighed (in total ~3.6 g) and transferred to a 50 ml stainless steel grinding jar. The BPR was fixed to 20:1, and 18 stainless steel balls (Ø 10 mm) were used. After sealing, the pressure was increased to 30 bars of hydrogen. A grinding cycle consisted of 30 minutes of grinding at 600 rpm followed by 10 minutes of pauses and a subsequent reversal of direction. The grinding was interrupted to monitor the alloying progress by taking small samples. Subsequently, the grinding jar was closed and pressurized again with 30 bar H_2, and the grinding process continued.

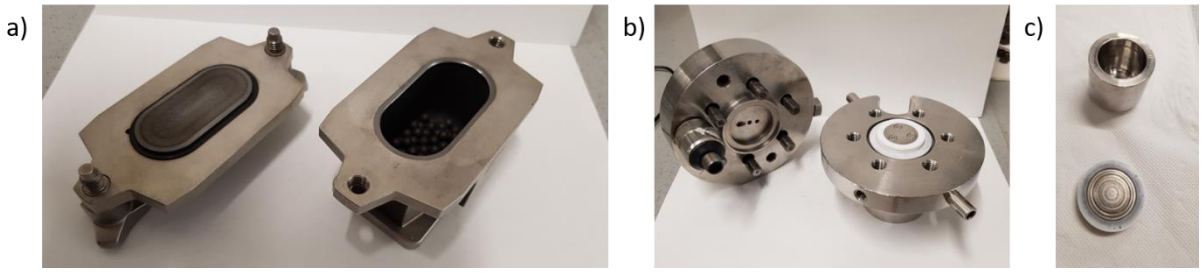

Figure 5: Photographs of the grinding jars: a) tungsten carbide grinding jar for E_{max}; b) stainless steel high-pressure grinding jar with filter system for Pulverisette 6; c) stainless steel grinding jar for Pulverisette 7.

4.2. Characterization

This work mainly comprises experimental results on synthesizing novel alloys and their hydrogen storage properties. In order to obtain a comprehensive picture of the samples and, from this, a chemical correlation with their hydrogen storage properties, various analytical techniques were employed. Primarily, structure-resolving techniques such as X-ray scattering, but also imaging techniques of electron microscopy were used. These techniques are briefly presented below, and the main parameters are recorded. Finally, the techniques used to determine hydrogen storage properties are presented.

4.2.1. Structural and Chemical Characterization

Different analytical techniques have to be combined to analyze novel alloys. X-ray diffraction (XRD) experiments can be applied to study alloys' crystalline and structural properties. Imaging techniques such as energy dispersive X-ray spectroscopy (EDX) can be used to obtain information on the chemical composition, e.g., elemental distribution within the alloy. Since some samples contain lithium and quantification of lithium by EDX was initially not possible, elemental analyses by classical dissolution method were also performed to validate the respective methods against each other. Information on morphology can be obtained by scanning electron microscopy (SEM), an imaging technique. With the help of the high-resolution transmission electron microscopy method, information about the crystallite size can be obtained, and high-resolution elemental distributions can be obtained utilizing EDX.

X-Ray diffraction (XRD)

Powder X-ray patterns were recorded in Debye-Scherrer geometry on a STOE Stadi P diffractometer using Mo radiation (0.7093 Å), equipped with a primary Ge(111) monochromator (Mo $K_{\alpha 1}$) and a position-sensitive Mythen1K detector. A 50 kV and 40 mA generator setting was applied to generate X-rays. Data were collected between 5° and 50° with a step width of 0.015°. The measuring time per step was 40 s. For each sample, several scans were collected and summed after data collection. Sample preparation was performed in the glove box under an argon atmosphere. The powder samples were carefully ground with a pestle and mortar and placed in boron glass capillaries with a diameter of either 0.3 or 0.5 mm. The capillaries were sealed in the glovebox with vacuum grease and permanently sealed outside using a flame torch. The measured patterns were evaluated qualitatively by comparison with entries from the ICCD PDF-2 powder patterns database and simulated data (crystal structure data were taken from the ICSD database, FIZ Karlsruhe). Assuming that the samples were in simple cubic and hexagonal phases crystal structures (space group: $Fm\bar{3}m$, $Im\bar{3}m$, P63/mmc), the lattice parameters were refined using the Pawley method.[75] For this purpose, the TOPAS6 software was used.[76] The instrumental broadening was determined by an external silicon standard, considering the simple axial model and the Thompson-Cox-Hastings pseudo-Voigt peak shape function. In addition, the macro for the whole powder pattern modeling was applied to determine the volume-weighted average crystallite size.[77-81]

Scanning electron microscopy (SEM)

Morphological information about the samples was collected using scanning electron microscopy (SEM). The analysis were performed on a Hitachi TM3030 PLUS table-top scanning electron microscope equipped with an Xplore Compact 30 detector from Oxford Instruments and operated at an acceleration voltage of 15 kV. Since the samples were all pyrophoric or highly flammable after synthesis, small sample volumes were transferred to a snap vial and passivated overnight in the air by inserting a syringe into the lid. The passivated samples were then fixed on carbon tape and analyzed in the instrument. Chemical compositions were determined using scanning mode to obtain an elemental distribution map. Since the samples were passivated with oxygen as previously described, the elements were quantified relative to each other, not considering the oxygen content.

Transmission electron microscopy (TEM)

High-resolution transmission electron micrographs (HR-TEM) were collected with a C_S probe-corrected Hitachi HD-2700 microscope at an acceleration voltage of 200 kV equipped with a cold field emission gun and two EDAX Octane T Ultra W EDX detectors. For this instrument, a sample holder was used that allows transfer under an inert atmosphere (Ar) to exclude possible oxidation of the samples. All samples for the HR-TEM measurements were sprinkled dry on lacey carbon-coated copper grids.

Elemental Analysis (EA)

Additional elemental analyses (EA) were performed to verify the elemental distribution maps. For this purpose, inductively coupled plasma and optical emission spectrometry (ICP-OES) measurements were performed with a SPECTROGREEN DSOI instrument equipped with UVPlus optics (165 – 770 nm and optimized Rowland Circle Alignment) and carried out in crossflow. The samples were dissolved in a solution of nitric acid (67 %; 2.5 ml) and hydrochloric acid (37 %; 7.5 ml) under an argon atmosphere using an Anton Paar Multiwave 5000. The samples were heated to 90 °C and then to 180 °C. After cooling to room temperature, the solution was transferred to tared 50 ml centrifuge tubes and made up to 50 ml with deionized water. Some samples were diluted a second time to obtain a uniform concentration level. As standard solutions, various volumes of commercial standards (1 g L^{-1}) of Berndkraft were mixed and filled up to 50 ml. From this solution, a dilution series was prepared to obtain a calibration curve for the respective elements.

Each value is an average of a 3-fold determination of signal intensity in counts at a given wavelength (cf. Appendix 9.2).

One elemental analysis was carried out by Mikroanalytisches Laboratiorium Kolbe (Mülheim, Germany) via atomic absorption spectroscopy.

Raman spectroscopy

The Raman data were collected with an InVia spectrometer (Renishaw Ltd., Wotton-under-Edge, U.K.) with an excitation wavelength of 532 nm at a laser power of 5 mW. A spectral resolution of 1 cm^{-1} was obtained through an 1800 mm^{-1} grating. The laser was focused on the sample with a 50× objective. Three spectra were measured at three locations on the sample with 10 seconds per step, repeated three times, and summed up.

4.2.2. Characterization of Hydrogen Storage Properties

For the development of hydrogen storage materials, the investigation of their hydrogen storage properties is essential to evaluate their usability for specific applications. As described in **Chapter 2.1**, these properties include the maximum and reversible hydrogen capacity, the kinetics (absorption, desorption time as well as activation energies), and the thermodynamic parameters of the reaction (equilibrium pressure, reaction enthalpy as well as absorption- and desorption temperatures).

With regard to the storage capacity, it has become common practice that the capacity is given in H/M or wt.%. The H/M ratio at this point allows comparison between different alloys since an accurate ratio is given at the elemental level of hydrogen to metal, and the density of the host material is neglected. This allows different alloys to be better compared to their molecular storage capacity. The following equation is used to convert the H/M ratio from the weight percent,

$$wt.\% = \frac{\left({}^{H}/_{M}\right) M_H}{M_{Host} + \left({}^{H}/_{M}\right) M_H} \cdot 100 \qquad (4.1)$$

where H/M is the hydrogen-to-metal or material host atom ratio, M_H is the molar mass of elemental hydrogen, and M_{Host} is the molar mass of the host material or metal.[45] The weight percent, on the other hand, can be described by Equation 4.2,

$$wt.\% = \frac{m_{H_2}}{m_{H_2} + m_{Host}} \cdot 100 \qquad (4.2)$$

where m_{H_2} is the mass of hydrogen and m_{Host} is the mass of the host material.[45] The weight percent is also common because it incorporates the weight of the metal and is thus an important parameter depending on the application. The weight percent is also initially the parameter that can be determined experimentally and is accessible via various methods (manometric or gravimetric).

Sievert's Method

The most common manometric technique is the so-called Sievert method. The principle is based on the stepwise measurement of hydrogen uptake and is related to recording the pressure change in a precisely calibrated volume during the absorption/desorption of hydrogen. The relationship between the mole number and the pressure described by the ideal gas law can be used to convert the pressure change (under isochoric and isothermal conditions) into a molar number change to obtain hydrogen uptake. Since real gases often deviate from the ideal behavior, which is, for example, taken into account in the compression coefficient Z, the real gas equation (pV/nRT=Z) is used for the methodology (cf. Eq. 4.3).[82] An experimental setup is illustrated in Figure 6, on which the measurement principle is briefly explained.

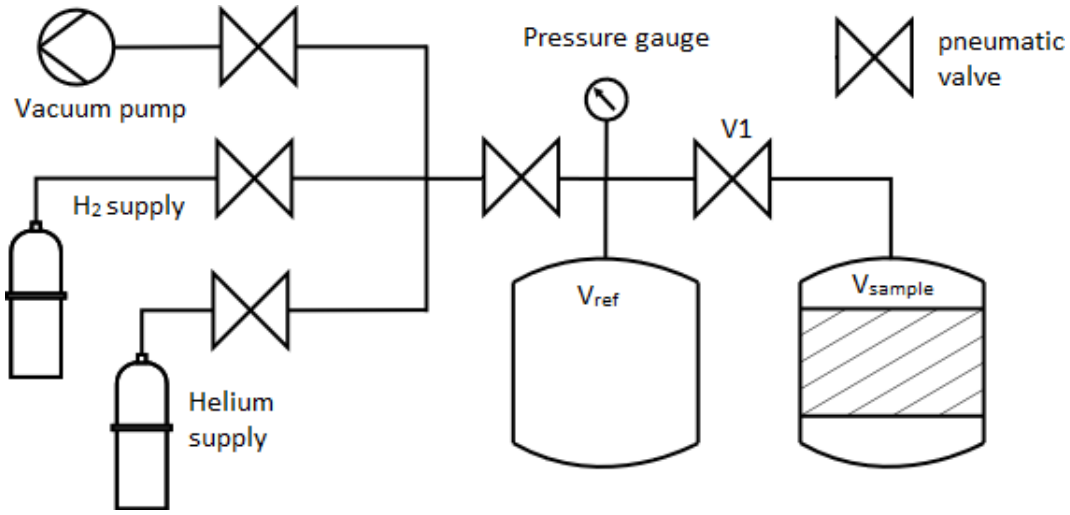

Figure 6: Schematic illustration of the Sieverts apparatus.

For the measurement methodology, a calibrated reference volume (V_{ref}) is filled with hydrogen at a specific pressure (p_{ref}) at temperature T_{ref}. Then, by opening valve V1, the gas is expanded into the volume of the sample chamber (V_{sample}) at temperature T_{sample}, and a system pressure p_{sys} throughout both volumes (V_{ref} + V_{sample}) is established. Since V_{ref} and V_{sample} are calibrated, the pressure drop caused by the expansion can be estimated using Boyle's law. Each further pressure change corresponds to the hydrogen uptake/release of the sample. Typically, several small

pressure doses are applied to the material so that the hydrogen uptake can be monitored in smaller steps, and Equation 4.3 can describe the number of mole of hydrogen uptake/release for the *k*th-step:

$$\Delta n_H^k = 2\left\{\left[\frac{p_{ref}^k}{Z(p_{ref}^k, T_{ref}^k)RT_{ref}^k} - \frac{p_{sys}^k}{Z(p_{sys}^k, T_{ref}^k)RT_{ref}^k}\right]V_{ref} - \left[\frac{p_{sys}^k}{Z(p_{sys}^k, T_{sample}^k)RT_{cell}^k} - \frac{p_{sys}^{k-1}}{Z(p_{sys}^{k-1}, T_{sample}^{k-1})RT_{sample}^{k-1}}\right]\left[V_{sample} - \frac{m_x(n_H^k)}{\rho_x(n_H^k)}\right]\right\} \quad (4.3)$$

Equation 4.3 also considers the correction by the sample volume $V_x=m_x/\varrho_x$, which in turn depends on the hydrogen content of the material.[82] The total change in hydrogen content of the sample can then be obtained by the sum of the individual steps. At each step, a waiting time is applied until the pressure change approaches zero so that the system can be assumed to be at equilibrium. Finally, the determined hydrogen uptake at the corresponding equilibrium pressure is plotted in the pressure-composition isotherms (cf. Figure 4). In general, Sievert's method or Sievert's apparatus can be used to study various properties: kinetics of absorption/desorption, pressure-composition isotherms (thermodynamic quantities), and life-cycle performances.

The manometric measurements from this work were performed with a commercially automated SETARAM PCT-PRO system. For the measurements, between 0.5 - 1.5 g of sample material was weighed into a stainless steel cell (T_{max} 500 °C, p_{max} 100 bar) and sealed with metal gaskets. The measuring cell was then connected to the measuring instrument. Before measurements, all samples were activated for 2 hours at 340 °C and under a vacuum (10-3 bar). A reference volume of 17.23 ml was used for all measurements. The kinetics measurements were performed with an initial pressure of 40 or 55 bar of hydrogen. Other experimental conditions are marked in the respective measurement data.

Thermal analysis

Thermal analyses were used to investigate the hydrogen desorption properties. These methods provide information on the release of hydrogen as a function of temperature, such as the onset of desorption temperature, reaction enthalpy, or activation energy (E_a). Using the thermal gravimetric analysis (TGA), the weight loss of the sample can be recorded, allowing direct measurement of the gravimetric storage capacity. Differential scanning calorimetry (DSC) allows the energy flux (whether the reaction is endo- or exothermic) to be identified as a function of temperature. For this work, three measurement techniques were used

simultaneously in combination. The TGA and DSC measurements were performed simultaneously with a Mettler Toledo TGA/DSC 1 thermal analyzer equipped with a GC 200 gas controller (argon flow: 50 ml min^{-1}). Since the TGA detects only the weight loss, a mass spectrometer was also connected to the gas outlet of the thermal analyzer. The qualitative analysis of the exhaust gas stream was performed with a mobile mass spectrometer (MS) Thermostar GSD 300 T2 from Pfeiffer Vacuum. The samples were prepared exclusively under an argon atmosphere. Before the measurements, 40 µl aluminum crucibles were weighed with a Mettler Toledo microbalance, and the exact weight was determined by differential weighing so that 10 – 20 mg of sample was contained in the crucible.

The activation energy of dehydrogenation can be determined by the Kissinger method.[83] According to this method, the activation energy of the reaction can be determined using a series of DSC curves obtained at different heating rates. The temperature shift of the endothermic signal as a function of the heating rate is then used to determine the activation energy using the Kissinger equation 4.4:

$$ln\left(\frac{H}{T_p^2}\right) = -\frac{E_a}{R\,T_p} + ln(k_0) \qquad (4.4)$$

where H is the heating rate, T_P is the corresponding peak temperature, E_a is the activation energy, R is the general gas constant, and k_0 is a constant. According to Equation 4.4, a plot of $ln\left(\frac{H}{T_p^2}\right)$ versus $-\frac{1}{R\,T_p}$ gives a linear behavior. Accordingly, a linear regression function can be used to obtain the activation energy based on the slope.

Chapter 5

5. Light Weight HEA: AlLiMgTiZr - C_x

This chapter discusses the synthesis approaches for the alloy composition AlLiMgTiZr. The aim was to clarify whether the empirically developed selection criteria for the formation of a stable solid solution ($\delta < 6.6$ %, $\Omega > 1.1$ and -15 kJ mol^{-1} $< \Delta H_{mix} < 5$ kJ mol^{-1} , cf. Chapter 3.1) can also be applied to an alloy consisting mainly of the main group elements (Al, Li, and Mg). The first selection criteria are initially theoretically fulfilled with a δ of 4.78 %, a ΔH_{mix} of 0.48 kJ mol^{-1}, and an Ω of 35.58 (cf. Appendix 9.1). Therefore, it was assumed that a solid solution could be formed. Furthermore, according to Guo et al, a *bcc* phase is expected for alloys with a VEC below 6.87 (cf. Chapter 3.1).[17, 18] Consequently, it should be also examined whether the formation of a solid solution with a *bcc* phase can be expected with a VEC of 2.87. The investigations were carried out with various parameters such as different process control agents (PCAs), milling speed, and influence of different reactants. To better understand the alloying process, XRD analyses were performed at different stages of the alloying process. Furthermore, the materials were characterized by TEM, EDX, Raman spectroscopy, and elemental analysis. Their hydrogen desorption behavior was investigated by thermal analysis. In addition, reactive milling was applied to study the formation of metal hydrides based on a high-entropy alloy. Finally, the previously established hypothesis is evaluated to determine whether the empirically developed selection criteria apply to the presented alloy composition and could serve as guiding parameters in the search for a single-phase alloy on the given composition.

5.1. Processability of the Elemental Powders

At the beginning of this work, the processability of the AlLiMgTiZr alloy was first examined without the addition of process control agents to keep contamination to a minimum. This involved investigating whether a balanced process between fragmentation and rewelding is enabled during mechanical alloying. The preliminary tests were carried out with different mills (E_{max}, Pulverisette, and a cryogenic shaker mill from Retsch). First, the pure elemental powders in equimolar ratios were weighed into the grinding jars, and the grinding process was visually inspected. Based on this assessment, the condition of the ground material was to be

determined initially, whether the material was still present as a powder or stuck together and thus not processable. For this purpose, the respective experiments were stopped after different time intervals. The first experiment, shown here as an example of the preliminary tests without PCA, illustrates the necessity of this examination. Figure 7 shows two photographs of the grinding jars with the processed material in a) without PCA and b) with PCA (ethanol). Mechanical alloying without a PCA leads to increased cold welding of the particles so that the materials stick to the grinding walls and can be classified as non-processable (Figure 7a). On the other hand, processing with a PCA results in the material remaining in powder form and therefore being considered processable (Figure 7b).

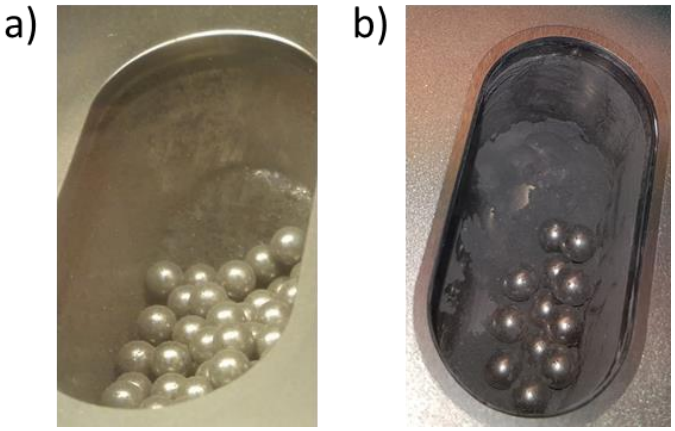

Figure 7: Photographs of elemental powders: a) processed without PCA; b) processed with ethanol as PCA.

Cryogenic milling has also been used as an alternative to PCAs. Cryogenic grinding is described in the literature as beneficial in reducing the ductility of the materials and thus increasing fragmentation and corresponding processability.[72, 84] For these experiments, a cryogenic shaker mill from Retsch was used, in which a double-walled container allows liquid nitrogen (-196 °C) to flow around it. The grinding jar and the balls are made of stainless steel. For the process, the ball-to-powder ratio of 12:1 was maintained using three grinding balls with a diameter of 10 mm (total ~ 12 g). Prior to the grinding, a pre-cooling time of 10 min at a frequency of 5 Hz was given. The grinding process was carried out in cycles, consisting of one hour of grinding at 25 Hz followed by a cooling period of 10 min at 5 Hz. Interestingly, after 4 hours of milling, the material was found as a powder. The connected XRD analyses did not show any alloying progress, and the pure elements could still be identified (cf. Appendix 9.3). These findings prompted to continue the process, as cryogenic grinding seemed promising at first. After 12 hours of processing, however, it was also found that the materials were clumped together in the corners of the grinding jar, and the process can be classified as unsuccessful. In summary, regardless of the

mill and process parameters used, all trials without a PCA proved unsuccessful. The materials in combination appear to be too ductile and thus favoring cold welding. Cold welding reduces the processability of the powders and prevents the desired alloying process. For the processing of the material combination, it can therefore be concluded that a PCA is necessary to ensure sufficient powder processing.

5.1.1. Influence of Process Control Agent

The preliminary results indicate that a PCA is required for AlLiMgTiZr alloy processing. To that, it is reported that different PCAs can interact with the powder and form compounds included in the powder particles during milling in the form of inclusions and/or as dispersoids.[71] Different PCAs can affect final phase formation, solid solubility, and the degree of contamination by PCA decomposition.[71] For example, the decomposition of carbonaceous PCAs can lead to the formation of by-products such as carbides.[71, 85-86] Considering the different influences on the synthesis, different PCAs (toluene C_7H_8, ethanol C_2H_5OH, as well as n-hexane C_6H_{14}) were used during mechanical alloying. The PCAs differ in the shape of the molecules (linear or cyclic) and in the number of carbon, hydrogen, and oxygen atoms, which can result in different resistance to the decomposition of the PCAs. The aim was to check whether the PCAs had a different effect on the alloying process and the final product. XRD experiments monitored the synthesis progress to investigate the influence of the different PCAs. Subsequently, the stability of the materials was investigated by thermal analysis followed by XRD analysis to determine structural differences.

5.1.1.1. Ethanol as PCA

For the synthesis using ethanol (7 – 8 wt.%) as PCA, the elemental powders of Al, Li, Mg, Ti, and Zr (total 2 g) were weighed into the tungsten carbide grinding jar at a ball-to-powder ratio of 20:1. The milling was carried out at 1200 rpm for 10 minutes with a minute pause, followed by a change of direction. The grinding process was repeatedly stopped, and samples were taken to study the alloying process. The samples were analyzed by XRD, and the measured data were normalized to the highest intensity and plotted against 2 Theta in Figure 8. The respective diffraction pattern is labeled with corresponding milling times.

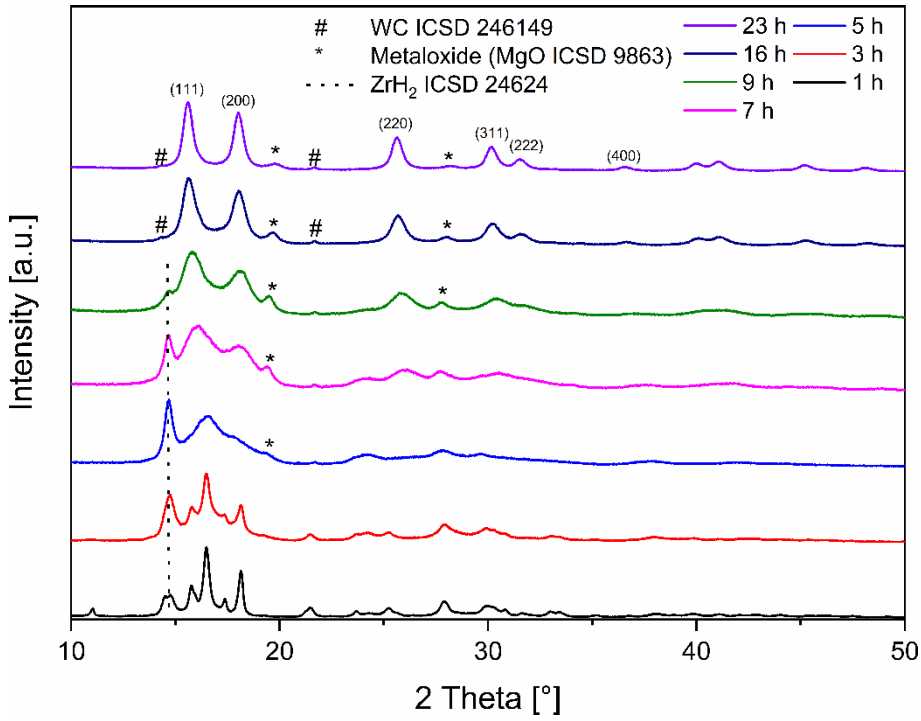

Figure 8: Powder XRD patterns of equiatomic AlLiMgTiZr after varying milling time and processed with ethanol as PCA.

The entire alloying process was followed over 23 hours of milling time. In detail, several features can be identified from the XRD analyses. After one hour, the elements can be identified mainly in their elemental forms. In addition, zirconium slowly formed a hydride phase (ZrH_2), with the most intense reflection of the (101)-plane at 14.80° indicated by the dashed line in Figure 8. Zirconium hydride serves as a reference to assess the alloying progress since it has the highest intensity due to the higher scattering cross-section of zirconium and is, therefore, easier to track.[87] However, based on the X-ray diffraction result, it cannot be ruled out that the other elements may also have formed hydride phases because the reflections are usually superimposed and, therefore, difficult to differentiate. The formation of the zirconium hydride phases can be explained by the interaction of ethanol with the individual metals since there is no other hydrogen source. Ethanol and metals are partially activated under mechanical influence and can thus form metal carbides, oxides, or hydrides, although the exact mechanism cannot be elucidated from the XRD experiments. A similar mechanism was observed in the literature for milling zirconium with hydrocarbons. During milling, zirconium carbide was formed with zirconium hydride as an intermediate phase, which is explained by the decomposition of the hydrocarbons.[85] With further grinding, additional ethanol molecules can be activated, and accordingly, the intensity of the zirconium hydride phase increases after three hours. After 5 hours of milling, the measured data shows a maximum of the zirconium hydride phase. The reflections of the previously

recognizable crystalline phases of the other elements decreased, and a broadening of the reflections can be seen. Amorphization may have led to the broadening of the reflections, in which the long-range order of the crystalline phases has been lost. Nevertheless, it is also possible that the alloying process has started, whereby the reflections of several phases overlap and are reflected in a strongly broadened measurement characteristic. The exact cause cannot be determined at this point. At an advanced process of 7 hours, the formed zirconium hydride phase decreases in intensity, and simultaneously a new phase is slowly formed, recognized by the reflections around 15 and 18°. This crystalline phase continues to form as the milling process progresses up to 23 hours, recognizable by the increasing intensity of the reflections. This phase can be described with an *fcc* crystal structure and is indexed with the corresponding lattice planes. In addition to the formation of the *fcc* structure, a new reflex can be seen at about 20°, which is marked with (*) and remains constant during the grinding process. At the end of the grinding process after 23 h, this reflex can be described by a magnesium oxide crystal structure, but the exact identification is difficult due to the different metals used. However, it is assumed that it is qualitatively a metal oxide phase obtained from the reaction of the oxygen contained in the ethanol and reactants. Nevertheless, an exact statement needs further investigation where the chemical compositions are revealed. The formation of the oxide phase also suggests that the used ethanol could decompose, leading to the oxidation of the reactants. Moreover, with advanced milling, the contamination due to the abrasion becomes apparent. In addition to the *fcc* and oxide phase, the tungsten carbide phase becomes evident from 16 hours and is marked by (#). However, this abrasion cannot be avoided due to the processing with ball mills.

The data obtained by XRD after 23 hours of milling was then analyzed by the Pawley method to obtain the lattice parameters of the structure. An *fcc* phase ($Fm\bar{3}m$) was assumed to describe the crystal structure, and the MgO phase and WC phase were also included in the simulations. The MgO phase was added to describe the metal oxide phase, which cannot be assumed to be pure MgO but serves to describe the same *fcc* crystal symmetry. The analysis from the Pawley method is shown in Figure 9. Based on the analysis, the lattice parameter of the *fcc* structure is determined to be 4.5145(6) Å and lies between the lattice constants of a pure zirconium carbide phase (46764(3) Å; ICSD 14822) and a titanium carbide phase (4.328(2) Å; ICSD 1546), sharing the same *fcc* symmetry (known as rocksalt structure). Considering the mechanism of zirconium carbide formation described in the literature and the comparable lattice parameters, which differ due to the other alloying elements, it is first assumed that a carbide has formed opposite to the expected *bcc* structure.

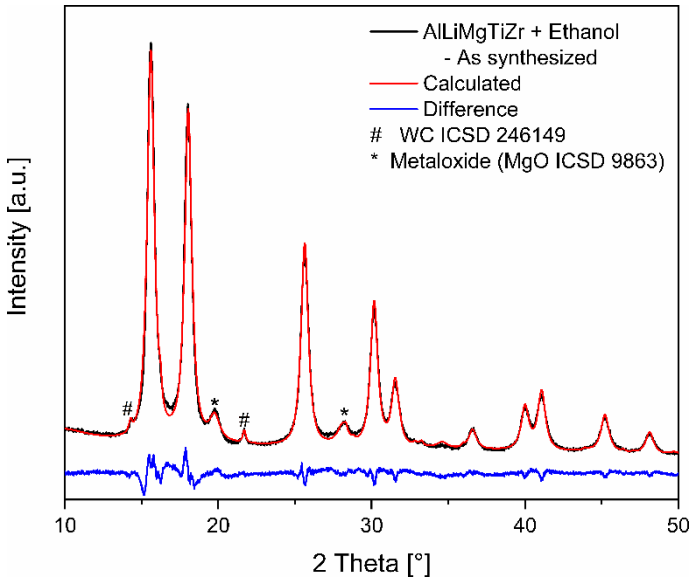

Figure 9: Powder XRD pattern of ball milled AlLiMgTiZr compound (black), related Pawley simulation (red) and corresponding difference curve (blue).

Since XRD experiments mainly provide information about the crystal structure rather than the chemical composition, they are insufficient to describe the material thoroughly. In order to obtain information about the chemical composition, a chemical analysis by energy dispersive X-ray spectroscopy (EDX) was performed using a scanning transmission electron microscope. A brightfield micrograph and the corresponding elemental mapping are shown in Figure 10. The images represent the TEM analysis and give an insight into the chemical composition of the material. In the bright field image, the lighter outline of the particle is noticeable, which is due to a material with a lower density or scattering cross-section. When looking at the individual mappings, especially the fluorine and carbon mappings, it is revealed that the lighter surrounding consists of fluorine and carbon. However, since no fluorine was used in the synthesis, abrasion from the seal ring could be the cause. The seal ring is made of a fluorinated hydrocarbon material (Viton®) and did not appear to withstand the harsh conditions of ball milling. However, the fluoroelastomer appears to have been deposited mainly like a surfactant on the surface, as can be seen from the more pronounced fluorine contrast at the edges of the particle. The carbon, on the other hand, shows a more homogeneous distribution over the entire particles and indicates that not only the elastomer is responsible for the carbon content within the material. In this case, the carbon and oxygen distributions across the particles are striking, indicating that the particles are not composed exclusively of the metals used. Some of the particles appear to be surface oxidized, evidenced by the increased oxygen concentration at the edges of the imaged particles. If the XRD and EDX analyses are now considered together, it can be concluded that ethanol is decomposed during the grinding process, and the materials react to form the metal

oxide and metal carbide. Regardless of the carbide formation, the quantification from the EDX analyses (cf. Table 4) shows relatively good agreement with the nominal ratios of the metals, indicating that the carbide formation did not prevent the alloying process. It is more likely that a multicomponent carbide has formed, with the lattice sites randomly occupied by the respective metals, since the microstructure of the particles appears largely homogeneous (Figure 10). Slight deviations can be attributed to the randomly driven milling process, as seen in the magnesium mapping case, where smaller inhomogeneous regions can be identified.

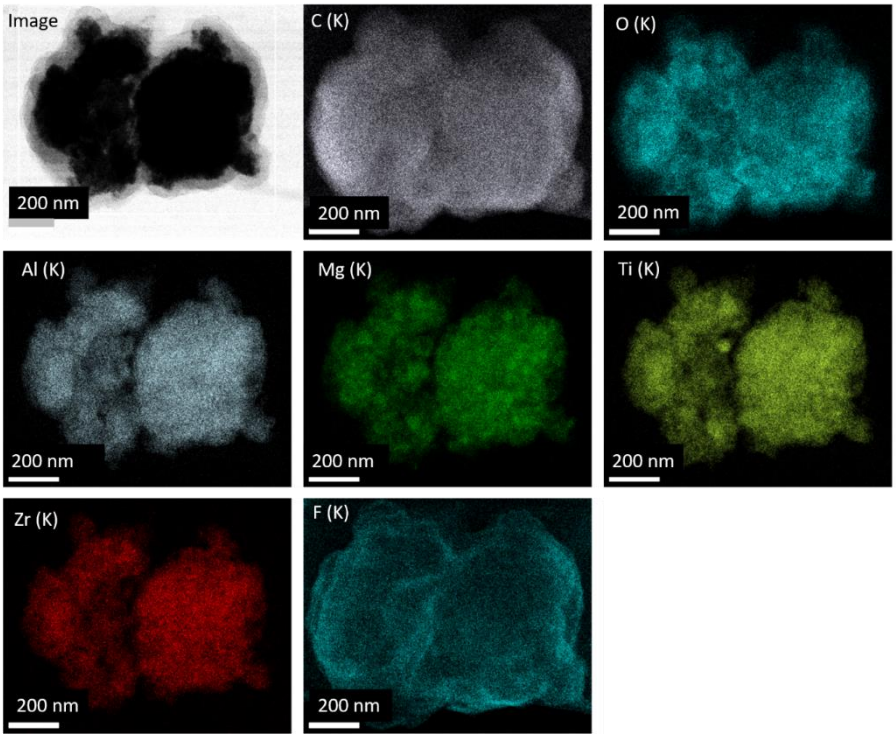

Figure 10: TEM micrograph of ball milled AlLiMgTiZr compound in bright field mode and EDX elemental maps captured over bright field image.

However, as far as the quantification (cf. Table 4) is concerned, these should not be considered fully accurate since the quantification via EDX on particles can be influenced by multiple scattering effects, absorption within the particles, and geometrical factors such as surface properties.[88] Accordingly, the concentrations of the metals should be considered mainly relative since, in addition also, the lithium could not be analyzed with the detector used. Nevertheless, the TEM-EDX results indicate that a highly entropic carbide based on the used elements AlLiMgTiZr-C_x has been synthesized with minor impurities of small portions of fluoroelastomer, tungsten carbide, as well as the oxide phase.

Table 4: Quantitative EDX analysis of AlLiMgTiZr sample synthesized with ethanol as PCA.

Element	C (K)	O (K)	F (K)	Li (K)	Al (K)	Mg(K)	Ti (K)	Zr (K)
Measured (at.%)	38.98 (0.24)	16.95 (0.58)	20.62 (0.64)	ND	5.08 (0.52)	6.80 (0.35)	5.84 (0.28)	5.72 (0.44)
Relative ratio (%)	-	-	-	-	21.67	29.01	24.91	24.40
Nominal (at.%)	-	-	-	-	25	25	25	25

In order to determine whether the samples could already absorb hydrogen during synthesis and release it again upon heat supply, the samples were subjected to thermal analysis. It is assumed that the hydrogen is supplied by ethanol. The TGA analyses combined with MS were carried out in a measuring range of 25 to 625 °C with a heating rate of 5 K min^{-1}, and the obtained measurement data are shown in Figure 11.

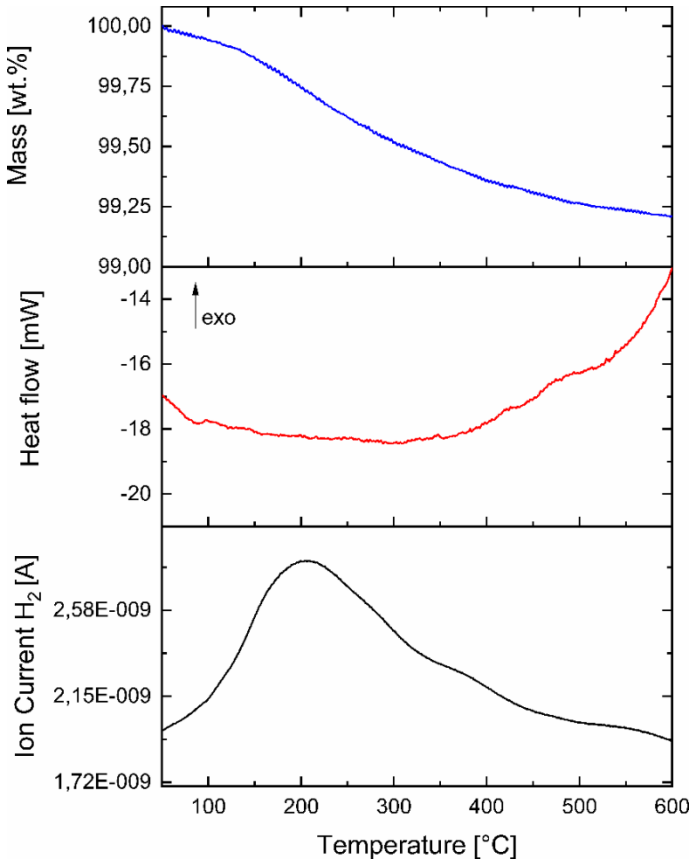

Figure 11: Thermal analysis of as-synthesized material: TGA weight loss profile (top), DSC heat flow (middle), and MS ion current of H_2 (bottom).

It is noticeable from the measurement that the material continuously releases mainly hydrogen from a temperature of 50 °C. In addition to hydrogen, the gases H_2O, O_2, and CO_2 were also measured. No noticeable changes were identified for H_2O and O_2. The CO_2 signal was three orders of magnitude below that of hydrogen and thus at the resolution limit of the mass spectrometer used, so the amount of CO_2 is assumed to be negligibly small and the origin is unclear. The continuous release of H_2 is characterized by a broad endothermic signal from 100 to 400 °C, and a multistage decomposition process can be assumed based on the hydrogen signal. The multistage process starts with an increasing hydrogen signal at about 150°C, with the first peak at about 200 °C. The second peak, which resembles a shoulder due to the overlap, is in the range of 320 – 400 °C. This type of multistep desorption behavior has also been found for various high entropy alloys, but a clear interpretation of this phenomenon has not yet been proposed.[23] A possible reason was suggested by Ek et al., who studied deuterated HEAs and proposed that deuterium jumps from tetrahedral sites with high local VEC to octahedral sites with low local VEC during the desorption process.[42] Supported by Reverse Monte Carlo simulations, the different occupancy possibilities with varying local VEC indicates that the hydrogen atoms are bound to different extents. Therefore the activation energies can differ locally, which might be reflected in a multistep dehydrogenation mechanism.[66] At this point, however, the interpretation should be made with caution since contamination by oxides, surface fluorine, or a broad particle size distribution may also be responsible for the multiple desorption stages.[89-95] Furthermore, the material shown is not an alloy but rather a carbide with a rocksalt-like crystal structure, which means that the interstitial sites of the compound are additionally occupied by carbon atoms and can thus have a different influence on desorption.[96]

At the end of the measurement at about 550 °C, the weight loss stagnates, so an overall weight loss of 0.8 wt.% can be noted. In order to understand structural changes, the thermal treatment was followed by XRD analysis. For this purpose, the sample was taken out of the instrument under argon and transferred to a capillary. The obtained diffractogram is shown with the corresponding Pawley simulation in Figure 12. Based on the XRD data, the lattice parameter of the *fcc* structure ($Fm\bar{3}m$) after heat treatment could be determined to be 4.5089(6) Å and accordingly deviates slightly from the initial structure after synthesis. Furthermore, no phase transformation as described for high entropy alloys from *fcc* (hydrogenated phase) to *bcc* phase (dehydrogenated phase) is identified after heat treatment, which may be caused by the interstitial carbon stabilizing the *fcc* structure.[23]

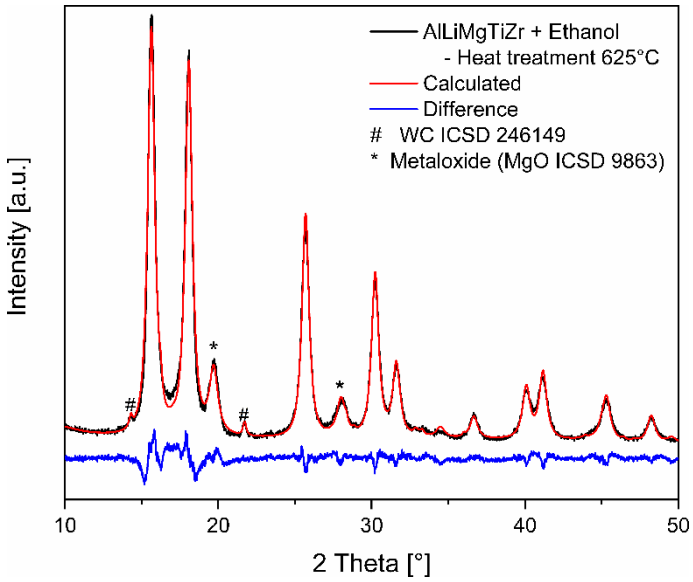

Figure 12: Powder XRD pattern of heat-treated AlLiMgTiZr compound (black), related Pawley simulation (red) and corresponding difference curve (blue).

In addition, the reflections of the oxide phase, indicated by the (*), are relatively enlarged, which may have been caused by the handling of the sample since oxygen contamination cannot be entirely excluded by taking the sample from the TGA instrument. In principle, however, it can be stated that the new *fcc* structure is predominantly phase stable to thermal treatment up to 625 °C and capable of releasing hydrogen, which might cause the lattice to decrease upon heat treatment.

An alloy carbide based on the metals (Al, Li, Mg, Ti, and Zr) can be synthesized using ethanol as PCA. However, the use of ethanol seems to lead to oxidation of the material, which may prevent its use as a hydrogen storage material. Oxides are often reported contaminating metal hydrides by inhibiting storage capacity and overall hydrogen uptake and release. Accordingly, metal hydrides are often subjected to an activation process to open passivation layers (oxides) and make the storage materials accessible.[45]

5.1.1.2. Toluene as PCA

The synthesis using toluene as PCA was performed with the same synthesis parameters previously described (1200 rpm, BPR: 20, 10 minutes milling, followed by 1 minute pause). Instead of ethanol, 7 – 8 wt.% toluene was used as PCA. This experiment aimed to verify if toluene as PCA is more suitable and could withstand the high energetic impacts of ball milling. In addition, the material's oxidation should be prevented this way since toluene is an oxygen-free molecule. The recorded XRD data are shown in Figure 13 below to monitor the evolution of the alloying process.

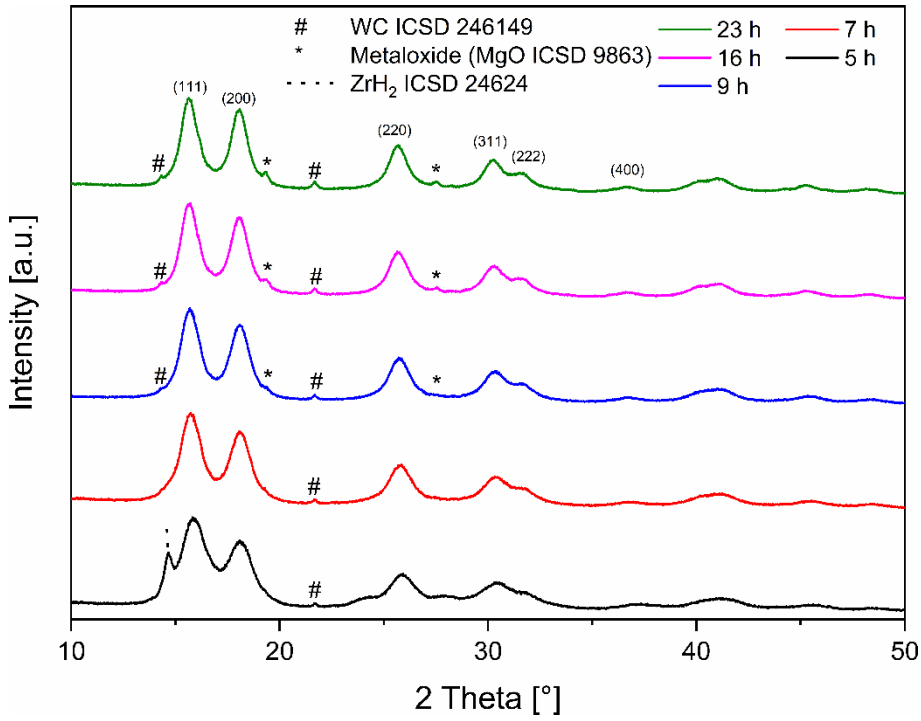

Figure 13: Powder XRD patterns of equiatomic AlLiMgTiZr after varying milling time and processed with toluene as PCA.

In contrast to the sample synthesized using ethanol, samples for XRD analysis could only be taken after 5 hours of milling. Inspection of the materials after one and three hours each showed a solidified material, so further drops of toluene were added to the synthesis (increasing toluene content to 9 wt.%). After 5 hours, the materials were in powder form, and the alloying process could be examined using XRD samples. Interestingly, compared to the previously described results, the formation of an *fcc* phase is already significantly more advanced after 5 hours of milling. In addition, next to the primary phase, a zirconium hydride (ZrH_2) phase is recognizable, disappearing as the process continues. Similar to the synthesis with ethanol, this indicates a mechanically activated interaction between toluene and the metals, which led to the hydrogenation of zirconium resulting in the zirconium hydride phase and the formation of metal carbides. Contrary to expectations that oxidation of the materials can be avoided, the measured data show a small amount of metal oxide after 9 hours of process time indicated by (*), which can be described with the same symmetry as the MgO phase. An atmospheric exchange during milling could cause the identified metal oxide phase since the reactants were handled in argon. However, slightly oxidized aluminum and magnesium cannot be completely ruled out since these are highly sensitive to oxygen. When opening the grinding jars, a slightly increased pressure was detected, which was recognizable because small amounts of powder escaped when the screws were loosened. During the grinding process, the pressure may already have increased to such an extent that the sealing rings could

not withstand, and an exchange with the atmosphere occurred. After opening the grinding jar, the oxygen sensor in the glovebox also indicated a briefly increased oxygen value, which can be caused by released hydrogen or oxygen. Accordingly, the oxidation might be explained by the failure of the seals so that oxygen entered and caused the oxidation. Finally, the minor contamination due to the abrasion of tungsten carbide is also identified and marked by (#). The major *fcc*, WC, and metal oxide phases can be identified at the end of the synthesis.

After 23 hours of synthesis, the final product was analyzed by the Pawley method (cf. Figure 14), assuming an *fcc* phase for simulation. The lattice parameter of the *fcc* phase is obtained as 4.5189(4) Å and is comparable to the ethanol synthesized sample.

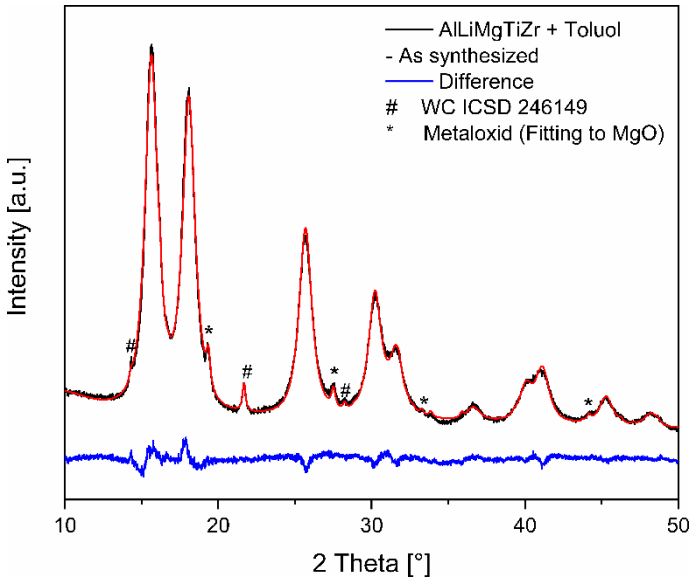

Figure 14 Powder XRD pattern of ball milled AlLiMgTiZr compound (black), related Pawley simulation (red) and corresponding difference curve (blue).

The chemical analyses using EDX elemental mappings are shown in Figure 15. The respective elemental distributions are shown in different colors and added to the respective graphs. Basically, it can be seen that the elements used are widely homogeneously distributed, excluding magnesium. The magnesium is not homogeneously distributed in the particles shown as an example, which can be due to the ball milling process. Ball milling is a random process that depends on the impact of the balls. The random component of the impacts can also cause the particles to experience different numbers of impacts, resulting in a different alloying process and, thus, not all particles having the same alloying progression. In addition, the EDX images show only a small elemental overlap of Mg with oxygen, which could indicate the formation of a pure magnesium oxide phase. Therefore, it is

assumed that the oxide phase identified in de XRD experiments is a mixture of several metals, mainly Mg. Otherwise, as with the ethanol sample, it is noticeable that the particle surfaces appear oxidized based on the increased color contrast at the edges, which supports the previously mentioned explanation regarding atmospheric exchange. Besides, no fluorine impurities were detected during the investigation. The mapping of the carbon shows a homogeneous distribution over the particle, as with the other detectable elements. Accordingly, considering the lattice parameter, which is in the order of monocarbides and the homogeneous carbon distribution, it can be assumed that the toluene is also decomposed during the milling process, and an alloy carbide is formed. As described in the literature and identified during the tracking experiments, a zirconium hydride phase is formed as an intermediate phase and transforms into a carbide phase with a structure similar to *fcc* rocksalt as the milling process continues.

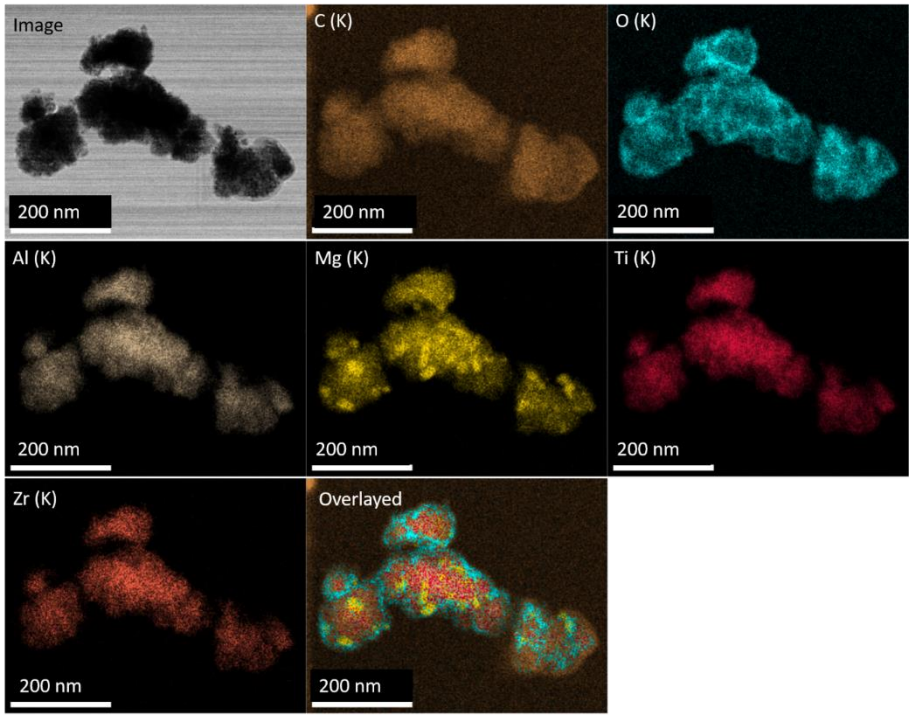

Figure 15: TEM micrograph of ball milled AlLiMgTiZr compound in bright field mode and EDX elemental maps captured over bright field image.

Table 5 contains the quantitative EDX results. However, the results shown are used as qualitative evidence. Due to the particle's oxidation, the metals' ratios are considered exclusively at this point. In addition, only a minimal section of the sample is shown, whereby lithium is not detectable, and thus, no quantitative statement about the material composition is possible. Moreover, as mentioned before, quantitative EDX analysis on nanoparticles is complicated due to the multiple interactions between elements and X-rays.[88] Furthermore, carbon cannot be

quantified at this point because the sample holders used to have a carbon film, so the X-rays from the sample and sample holder may be superimposed. However, the results indicate an excellent approximation of the nominal equimolar ratio of the metals, comparing the four detectable elements to each other. As seen from the mapping for the magnesium, areas of increased intensity can be identified, resulting in an increased proportion of magnesium of 28.97 %. Further, the mappings reveal an almost homogenously elemental distribution over the shown particles indicating, together with the XRD results, that a disordered solid solution with carbon has formed and suggests the formation of a high entropy carbide.

Table 5: Quantitative EDX analysis of AlLiMgTiZr sample synthesized with toluene as PCA.

Element	C (K)	O (K)	Li	Al (K)	Mg (K)	Ti(K)	Zr (K)
Measured (at.%)	64.56 (0.26)	16.88 (0.88)	ND	4.08 (0.75)	5.38 (0.59)	4.43 (0.63)	4.68 (1.07)
Relative ratio (%)	-	-	-	21.97	28.97	23.86	25.20
Nominal (at.%)	-	-	-	25	25	25	25

Thermal analysis reveals a different desorption behavior, and the corresponding measurement curves are plotted in Figure 16. The mass loss is determined to be 0.6 wt.% and lower than the ethanol sample. One reason for the differently measured hydrogen release is the increased hydrogen content of the PCA used; toluene generally has more carbon atoms in the molecule (C_7H_8), so the hydrogen content is determined to be 8.75 wt.%. Ethanol (C_2H_5OH), on the other hand, has an H_2 mass fraction of 13.12 wt.%. If it is now assumed that the whole amount of PCA used (8 wt.% of 2 g) is decomposed during the process and that the total amount of hydrogen in the PCA is absorbed by the material, the mass of absorbed hydrogen can be estimated. For ethanol and toluene, respectively, this would mean a theoretical amount of 1.05 wt.% and 0.7 wt.% (cf. Appendix 9.4). In reality, however, the pressure in the grinding jars was increased after synthesis, indicating that not all of the hydrogen could have been absorbed since hydrogen could be present in the gas phase. Accordingly, the mass losses of 0.8 wt.% for ethanol and 0.6 wt.% for toluene differ from the theoretical results but represent a good approximation of the hydrogen capacity. Furthermore, a multistage desorption process can be seen, with

the maximum desorption at about 400 °C. This process could also be due to the local valence electron concentration differences. Nevertheless, experimental evidence for this hypothesis is lacking.[23] The other characteristics mentioned above, such as particle size distribution, oxide layer thickness, or contamination, which can act as catalysts, may also have led to the changed desorption behavior.[93-96]

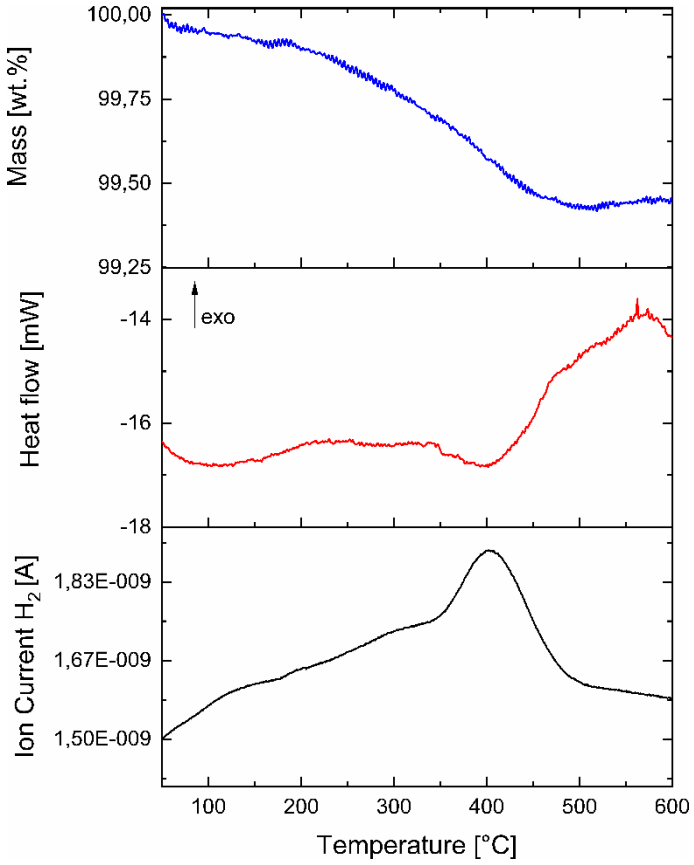

Figure 16: Thermal analysis of as-synthesized material: TGA weight loss profile (top), DSC heat flow (middle) and MS ion current of H_2 (bottom).

Overall, from a temperature of about 50 °C, a small amount of hydrogen is continuously released. The endothermic peak at 400 °C is striking, which subsequently changes to an exothermic signal from 500 °C, possibly due to a phase change or segregation. Accordingly, the heat-treated sample was also subjected to an XRD experiment. The obtained XRD pattern is shown in Figure 17.

As can be seen from the measurement data, the material did not undergo any phase change. The lattice parameter determination of the *fcc* phase was also in a comparable order of magnitude with a value of 4.5103(4) Å. The relatively increased intensity of the oxide phase indicates an enlarged portion of the oxide phase, which the material handling could have caused after the TGA measurement. Although the reactor is permanently flushed with argon after the measurement, the sample can still be exposed to air when the crucible is removed from the measuring chamber.

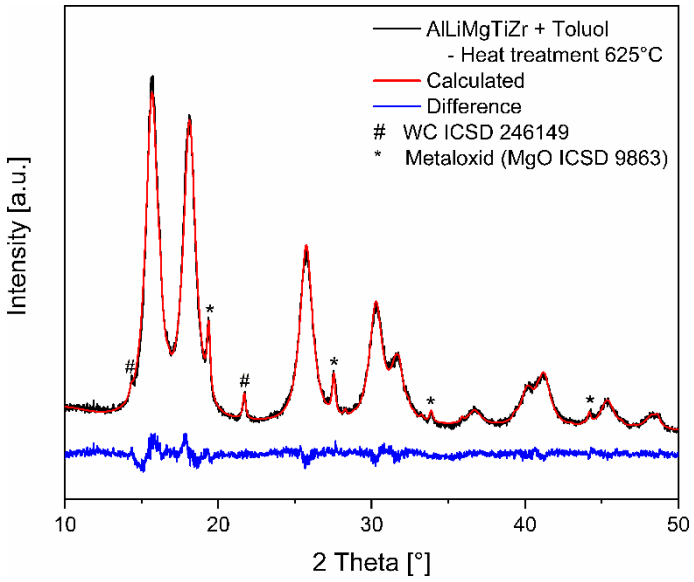

Figure 17: Powder XRD pattern of heat-treated AlLiMgTiZr compound (black), related Pawley simulation (red) and corresponding difference curve (blue).

In general, however, it can be stated that, as with the ethanol sample, no significant change in the structure can be detected concerning the XRD analysis. The lattice parameters after thermal analysis are of a similar order of magnitude as at the beginning directly after synthesis. Moreover, both syntheses are assumed to lead to an analogous final product. The differences in desorption behavior, ethanol with the main maxima at 200 °C and toluene at 400 °C, could be due to differences in the degree of oxidation. For magnesium and other metal hydrides, it has already been suggested that the oxide layer has a balancing effect on the activation energy of metal hydrides. In this context, it was assumed that the oxide layer inhibits the diffusion of hydrogen, which is reflected in an increased activation energy and a correspondingly higher desorption temperature.[97]

5.1.1.3. N-Hexane as PCA and Reduced Milling Speed

Based on the findings from the previous chapters 5.1.1.1. and 5.1.1.2. three parameters, PCA, milling speed, and BPR, were changed for the synthesis with n-hexane (7 – 8 wt.%). First, it should be checked whether n-hexane is also activated as PCA and leads to the formation of an alloy carbide. Second, the milling speed was reduced to 800 rpm to apply less energy during the milling process and reduce the decomposition of PCA; while doing so, the BPR was increased to 60:1 to enhance the number of impacts. Since this experiment was only used to find a good PCA,

tracking experiments were mainly performed using XRD. The obtained data are shown in Figure 18.

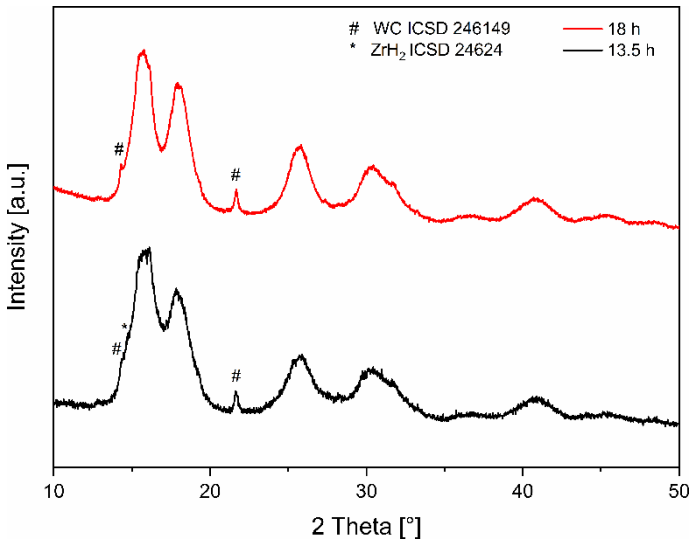

Figure 18: Powder XRD patterns of equiatomic AlLiMgTiZr after varying milling time and processed with n-hexane as PCA.

The graph shows the XRD data obtained after 13.5 and 18 hours of mechanical alloying. After 13.5 hours, the XRD data reveal a comparable structure to the previous experiments with ethanol and toluene. The shoulder at 14.80° again implies a small amount of remaining zirconium hydride, which disappears after further grinding. Accordingly, it can be assumed that the reduction of the velocity and the exchange to n-hexane did not influence the decomposition of the PCA. The similarity of the measurement data suggests that n-hexane also interacted with the metals and led to the formation of metal carbide. No further analysis was used since the goal was to synthesize a high entropy alloy. However, it should be noted that with the material composition and the PCAs used, a high entropy carbide can be synthesized directly, which could be of interest for other applications but is not part of this work.

5.1.2. Influence of Milling Speed

Since the PCAs tend to decompose at too high rotational speeds, this chapter aimed to verify whether the targeted high entropy alloy AlLiMgTiZr can be synthesized at reduced milling speeds. Toluene was used as PCA for these experiments, and three different milling speeds (400, 600, and 800 rpm) were applied. The experiments were each performed with a ball-to-powder ratio of 40:1. As in the previous experiments, samples were taken from the grinding jars after specific times indicated in the corresponding graphs and then analyzed by XRD experiments. The obtained measured data are shown in the respective figures in a 2 Theta range from 10° to 30°

and indexed with the corresponding grinding speed and grinding time, starting with the sample synthesized at 800 rpm (cf. Figure 19).

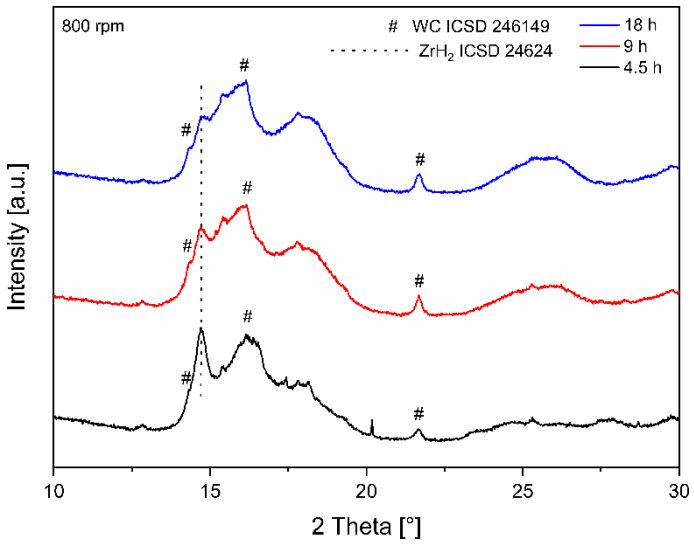

Figure 19: Powder XRD patterns of equiatomic AlLiMgTiZr after varying milling time and processed with toluene as PCA and 800 rpm.

The experiment shows that zirconium hydride is formed as an intermediate, which indicates the decomposition of toluene. After 4.5 hours, some metals are still present in their crystalline form, recognized by the sharp reflections sticking out of the enveloping measurement curve, whereby the differentiation due to the overlapping of the reflections is again not considered beneficial. After 9 and 18 hours, the intensity of the reflections of the zirconium hydride phase is reduced, and the previously described *fcc* phase becomes visible. The broadening of the reflections at this point may be caused by a small size of the coherently scattering crystallite domains or by the random occupation of the lattice site leading to increased lattice strain. However, no further indication can be given at this point. Therefore, it can be stated that 800 rpm did not lead to a reduced decomposition of toluene.

The other experiment carried out at a further reduced speed of 600 rpm (cf. Figure 20) shows that after 9 hours the reflections of the crystalline phases of zirconium and titanium can be identified. Only a small fraction has transformed into zirconium hydride. It can be concluded that no dominant alloying process has yet taken place and that the decomposition of toluene could be reduced by lowering the grinding speed. However, the continuation until 13.5 hours leads to the hydrogenation of the zirconium phase, which can be considered an indication of the decomposition of the PCA.

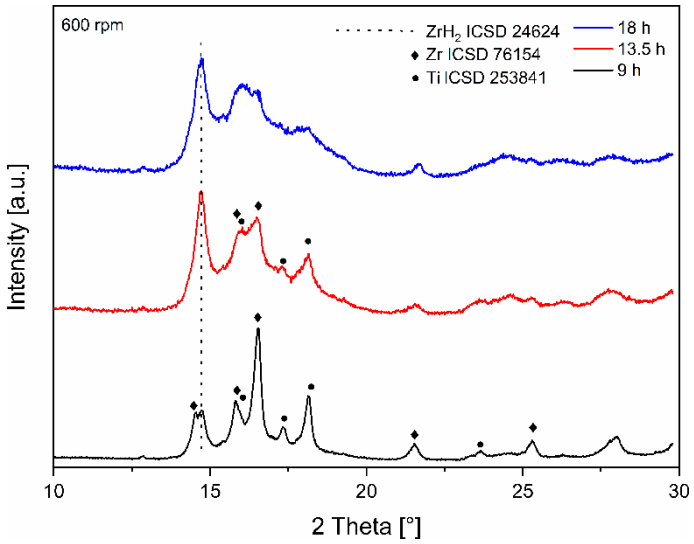

Figure 20: Powder XRD patterns of equiatomic AlLiMgTiZr after varying milling time and processed with toluene as PCA and 600 rpm.

In addition, it is seen from the XRD data recorded after 18 hours that the reflections of the crystalline titanium and zirconium phases have strongly decreased, and broad reflections at about 16°and 18° suggest the formation of the crystalline *fcc* phase described in chapter 5.1.1. Accordingly, it can be assumed that, as described in the literature, the transition from the metals via the zirconium hydride phase to the metal carbide also occurs at 600 rpm. The reduction of the rpm only led to a slower conversion rate. If the process is continued, it can be assumed that the conversion to the *fcc* phase also occurs here. An even more precise time profile for the conversion can be seen from the experiment with 400 rpm (cf. Figure 21).

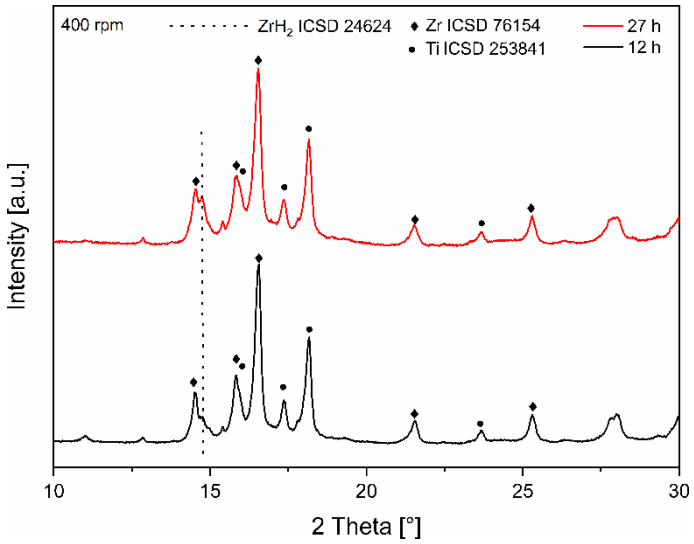

Figure 21: Powder XRD patterns of equiatomic AlLiMgTiZr after varying milling time and processed with toluene as PCA and 400 rpm.

In this experiment, the pure elements zirconium and titanium are still visible even after 27 hours of process time. Only a small portion of the PCA appears to decompose, as indicated by the low intensity of the (101)-plane of the zirconium hydride phase. However, it can also be seen that zirconium, for example, does not change the process. Except for the hydrogenation of parts of the zirconium, no direct alloying process can be seen. This suggests that a specific energy threshold is required for the alloying process, but this threshold is above the decomposition of toluene. This, in turn, leads to the assumption that the reduction of rpm does not lead to the desired effect of producing the desired alloy by ball milling without consuming the PCA as an educt and consequently synthesizing the high entropy carbide.

5.2. Hydrogen Supported Synthesis

The results in section 5.1 indicate that mainly metal carbides are synthesized with the support of a PCA. The mechanism seems to be via the decomposition of the PCAs with the intermediate zirconium hydride phase to the later metal carbide, as reported for the synthesis of pure zirconium carbide.[85] To investigate the synthesis of a light metal alloy without the interstitial carbon, synthesis via reactive milling was pursued. In addition, an attempt was made to start with zirconium hydride as the starting material, which could act as an inhibitor for the decomposition of the PCA.

5.2.1. Reactive Milling

The syntheses under a reactive hydrogen atmosphere were carried out in a custom-made stainless steel grinding jar. Two experiments were carried out to verify whether the material can be processed as a powder with the formation of a metal hydride and without liquid hydrocarbons as PCA. In the first experiment, a BPR of 20:1 was used, with 2 g of material weighed in, and 10 stainless steel balls (Ø 10 mm) were used. The grinding jar was then pressurized with 180 bar hydrogen, and one cycle consisted of 10 min at 450 rpm and one minute pause. In this experiment, the phase change during the grinding process was monitored by taking samples at different times. The second experiment was also carried out with a BPR of 20:1, using 18 balls (Ø 10 mm) and 3.6 g of starting material. The hydrogen pressure was 30 bar, and one milling cycle consisted of 30 min milling at 600 rpm followed by a 5 min pause. No tracking experiments were performed in this experiment. At the end of the test, the materials were present as fine black powders so that the XRD experiments

could be conducted. The measurement data obtained are shown in the following Figure 22.

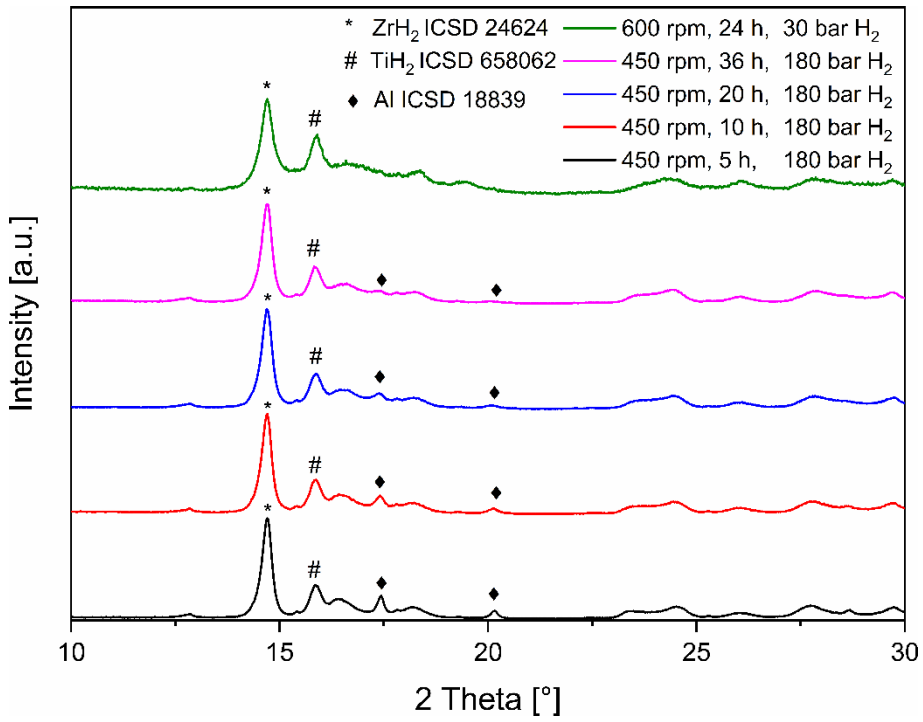

Figure 22: Powder XRD patterns of equiatomic AlLiMgTiZr after varying milling time and processed with different milling speeds and hydrogen pressures.

After 5 hours of process time, zirconium hydride (ZrH_2) and titanium hydride (TiH_2) are detectable. Even at an advanced process time of 36 hours, no change in the hydride phases can be observed. The only directly visible change can be seen in the (111)-reflections at 17.44° of the crystalline aluminum phase (#). This reflex overlaps with the (002)-reflection of crystalline titanium (ICSD 253841), but to a similar extent, the (200)-reflection at 20.17° of the aluminum phase decreases and can accordingly be assigned to aluminum. The decrease of the intensity caused by aluminum and the increase of the broadened background indicate amorphization. The loss of crystalline phases accompanies amorphization at this point and, thus, the loss of the coherent contribution of the long-range order, reflected in the increase of the broad background. However, since no transformation process into a crystalline phase can be seen, it is assumed that the process only leads to the amorphization of the materials. A similar observation is confirmed by the process at a higher speed (600 rpm). The XRD profile is very close to the profile after 36 h with 450 rpm, with the amorphous background being even more pronounced from 15° to about 18°. Only the crystalline phases of the identified metal hydrides are recognizable. Finally, these experiments show that synthesizing a single-phase metal alloy based on the proposed composition in a hydrogen atmosphere is challenging as mainly

amorphization and hydrogenation of the individual elements (Zr, Ti) take place. The time profile of the milling process at 450 rpm gives indications of the amorphization of the elements used, which is supported by the results at higher rpm. Since no direct change in the d-elements can be detected, it is assumed that the system requires more energy to perform the alloying process in the final crystalline phase.

5.2.2. Synthesis Starting from ZrH_2

All of the experiments shown above indicate that the synthesis of a single-phase alloy composed of AlLiMgTiZr is hampered. The experiments with various PCAs consistently show that the PCAs decompose, successfully synthesizing a high entropy carbide but not the desired *bcc* alloy. Zirconium hydride was repeatedly identified as an intermediate, leading to the assumption that elemental zirconium is responsible for activating the PCAs. To overcome this effect, using zirconium hydride as a starting material should be investigated to see if the decomposition of the PCAs can be suppressed and the formation of a carbide phase bypassed. In addition, the hydride phase serves as an additional hydrogen source to achieve an increased hydrogen content of the material. For the experiment, the powders were weighed into the tungsten carbide grinding jars at a molar ratio of the nominal concentration. A BPR of 20:1 was kept, and one grinding cycle included 10 min of grinding at 1200 rpm followed by a 1 min pause and a change of direction. As a model system, toluene (7 – 8 wt.%) was added to the synthesis as PCA. The experiments were stopped after labeled time intervals, and the powders were first examined with XRD experiments. Figure 23 shows the results of the tracking experiments.

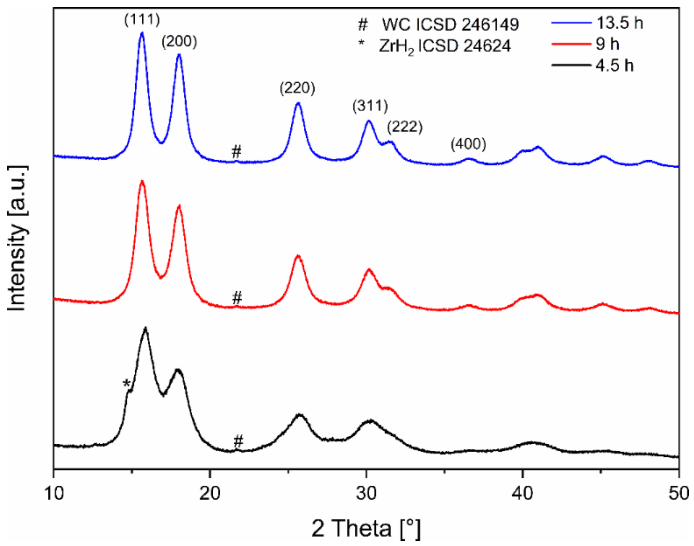

Figure 23: Powder XRD patterns of equiatomic AlLiMgTi-ZrH_2 after varying milling time and processed with toluene as PCA.

Similar to the experiment without zirconium hydride from chapter 5.1.1.2. the crystalline *fcc* phase seems to form already after 4.5 hours, and the zirconium hydride phase, star marked (101)-plane at 14.80°, is still present. After 9 hours, the zirconium hydride phase is no longer detectable, and the previously described *fcc* phase becomes dominant. Further processing up to 13.5 hours changes the result of the XRD experiments only slightly concerning the shape of the reflections. These become narrower and sharper with continued processing, which may be due to larger coherent scattering domains and a higher degree of crystallinity of the sample caused by better homogenization.[81] However, this cannot be further elucidated at this point. In addition to the crystalline phase, tungsten carbide contamination, unavoidable during the ball milling process, should be emphasized. Finally, the process was stopped after 13.5 hours, and the final measurement was also investigated by Pawley simulation. An *fcc* crystalline structure ($Fm\bar{3}m$) and tungsten carbide was included in the simulation, and the data obtained are shown in Figure 24.

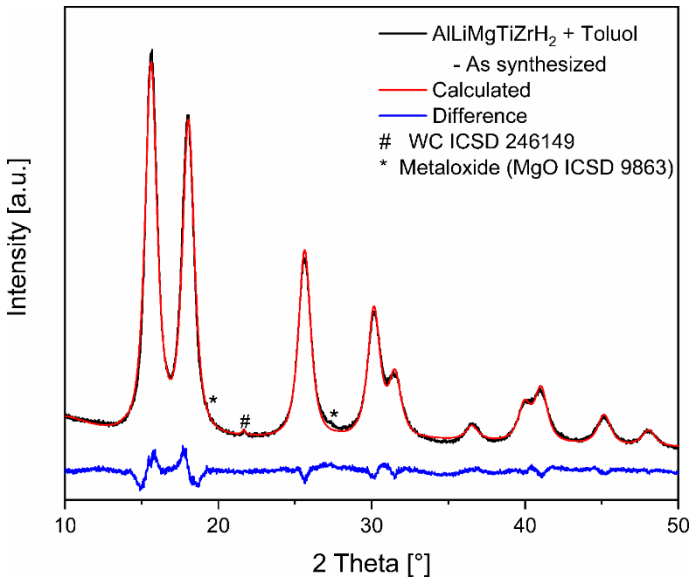

Figure 24: Powder XRD pattern of ball milled AlLiMgTi-ZrH_2 compound (black), related Pawley simulation (red) and corresponding difference curve (blue).

Using the Pawley simulation, the lattice parameter of the *fcc* phase could be determined to be 4.5281(6) Å and is accordingly in a comparable order of magnitude to the previously simulated *fcc* phase synthesized with ethanol and toluene. These findings suggest that a very similar product was formed. Otherwise, the regions at 19.3° and 27.6° are conspicuous and could again be caused by a metal oxide phase. However, the oxide phase was not included in the simulation because the superposition of reflections complicated discrimination at 19.3°. In addition, the volume-weighted mean crystallite size of 3.3 ± 0.8 nm was determined using the

WPPM macro.[81] The subsequent TEM images support the result of the XRD analysis, and two high-resolution micrographs are shown in Figure 25.

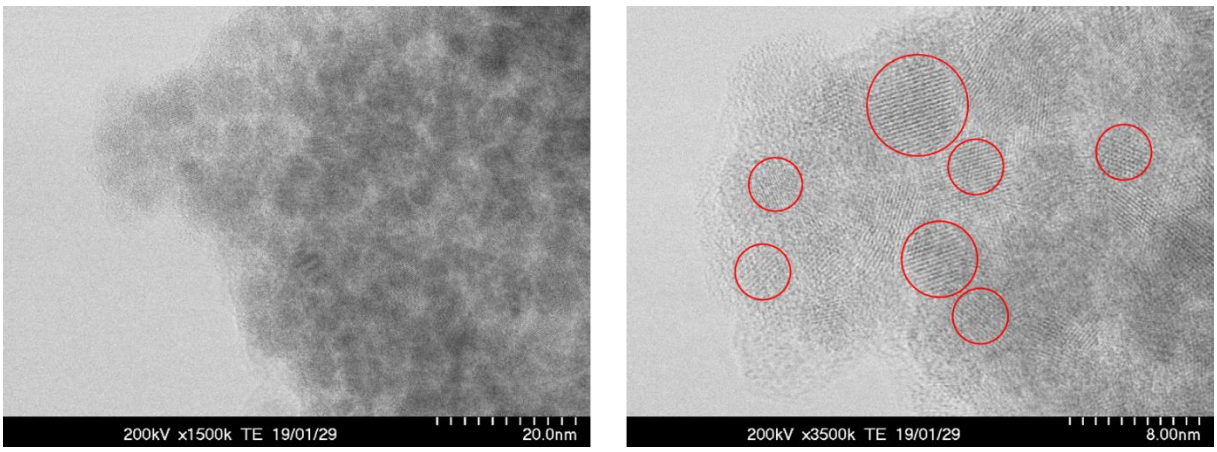

Figure 25: HR-TEM micrographs of ball milled AlLiMgTi-ZrH_2 compound: a) 1500k magnification and b) 3500k magnification and crystal domains highlighted with red circles.

The HRTEM image at 1500k magnification (Figure 25a) shows an agglomerated particle cluster, which on closer inspection, reveals the crystalline domains of the particles (cf. Figure 25b at 3500k magnification). These can be differentiated by the lattice fringes and are exemplified by red circles. The size of the analyzed domains in the range of 3 to 6 nm agrees in good approximation with the results from the XRD analysis (3.3 ± 0.8 nm). However, the agglomerated particles hindered recording several separated domains so that no size distribution could be recorded through TEM analysis. Moreover, the particles were analyzed for their chemical composition by EDX mapping at different magnifications, exemplified in Figures 26 and 27.

The mapping reveals a predominantly homogeneous microstructure. However, the element distribution of titanium and magnesium shows small areas of a higher concentration, which can be attributed to an incomplete alloying process due to ball milling and is considered an exception. The homogeneous distribution of the carbon content is also striking in the images, which suggests that a high entropy metal carbide has been synthesized. In addition, the chemical analysis again detects some oxygen and is consistent with the earlier assumption that a metal oxide causes additional reflections in the XRD data. However, the overlay of the elements suggests that the oxygen appears mainly superficial, which could have been caused by the sample preparation or by the previously described atmospheric exchange during the milling process. The micrograph (cf. Figure 27) with increased resolution also indicates a chemically homogeneous microstructure. Only titanium and aluminum show small areas of a higher concentration, which is negligible considering the XRD analyses, which showed no secondary phases of the individual elements.

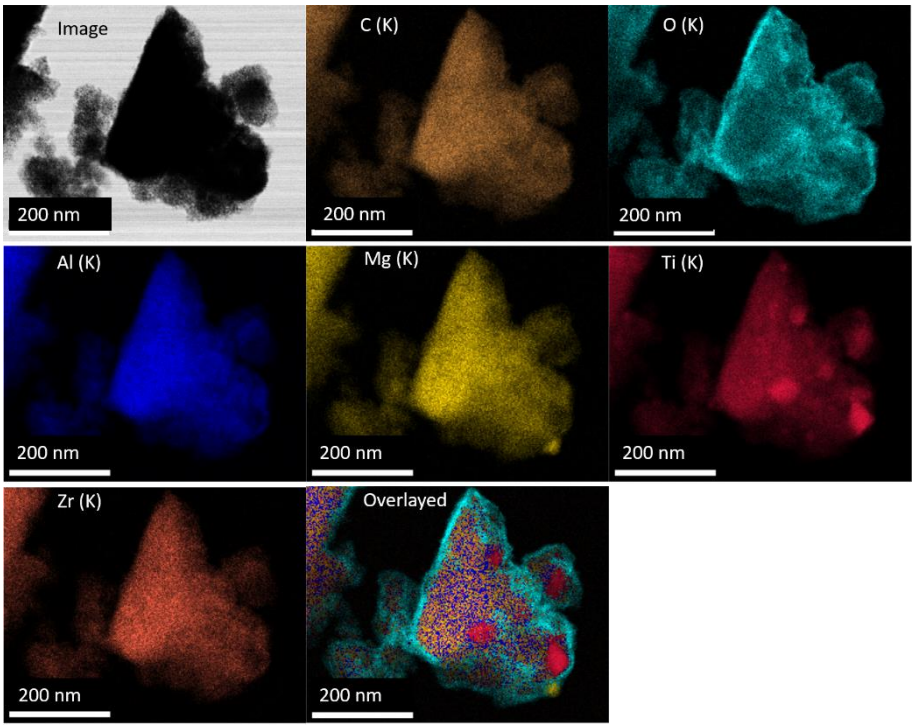

Figure 26: TEM micrograph of ball milled AlLiMgTi-ZrH_2 compound in bright field mode and EDX elemental maps captured over bright field image.

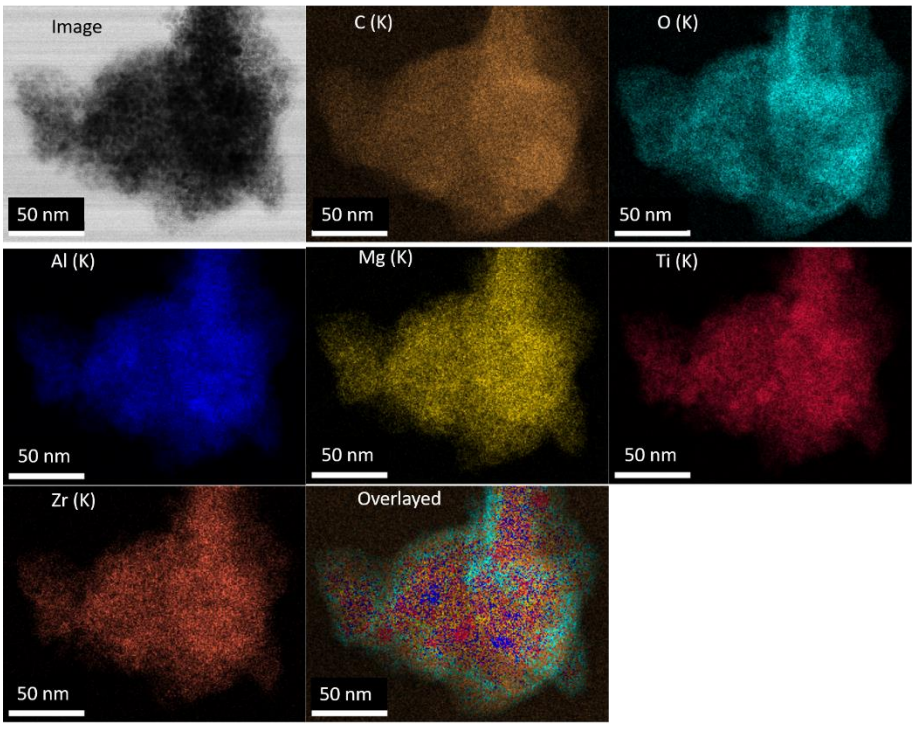

Figure 27: TEM micrograph of ball milled AlLiMgTi-ZrH_2 compound in bright field mode and EDX elemental maps captured over bright field image.

The quantitative EDX results are shown in the following table, whereby lithium was not detectable with the instrument used, and the results are compared qualitatively. In addition, it must be pointed out at this point that the shape of the investigated particles can influence the X-ray intensities. For the EDX analysis by TEM and SEM,

it is known that the shape of the analyzed specimen and, thus, the origin of the generated X-rays photons cannot be adequately quantified since different path lengths of the photons can lead to further interaction products with the sample and thus falsify the results.[88] Accordingly, the atomic percentages shown in Table 6 must be viewed with caution. Nevertheless, they give a good first approximation of the elemental distribution.

Table 6: Quantitative EDX analysis of AlLiMgTi-ZrH_2 sample synthesized with toluene as PCA and captured from Figure 26 and Figure 27.

Element	C (K)	O (K)	Li	Al (K)	Mg (K)	Ti (K)	Zr (K)
Figure 26 Measured (at.%)	30.61 (0.33)	18.16 (0.46)	ND	12.11 (0.32)	10.77 (0.35)	14.06 (0.26)	14.29 (0.53)
Relative ratio (%)	-	-	-	23.64	21.02	27.44	27.89
Figure 27 Measured (at.%)	52.08 (0.29)	21.33 (0.62)	ND	6.51 (0.56)	5.93 (0.55)	6.74 (0.52)	7.36 (0.90)
Relative ratio (%)	-	-	-	24.53	22.34	25.40	27.73
Nominal (at.%)	-	-	-	25	25	25	25

In order to strengthen the results of the EDX analyses and to obtain information on the lithium content, this sample was sent to the Kolbe Microanalytical Laboratory for a macroscopic elemental analysis carried out by decomposition. The results obtained are listed in Table 7. If the elements used are compared explicitly, the relative compositions agree very well with the nominal concentration of the respective elements. In addition, the results indicate that the abrasion by tungsten carbide is relatively low compared to the materials used. Regardless of the low contamination, the analyses provide evidence of the lithium content, although local verification that lithium is also homogeneously distributed over the microstructure would be desirable. Unfortunately, this is not possible within the scope of this work since all available analytical methods require preparation in air, and the synthesized materials are pyrophoric.

Table 7: Elemental analysis conducted at Microanalytical Laboratory Kolbe.

Element	C	Li	Al	Mg	Ti	Zr	W
EA Kolbe (at.%)	31.70	13.94	13.30	13.86	13.65	13.34	0.185
Relative ratio (%)	-	20.47	19.53	20.35	20.04	19.59	-
Nominal (at.%)	-	20	20	20	20	20	-

Furthermore, thermal analysis was used to check whether the use of zirconium hydride led to an increased hydrogen content in the sample and whether the material was thermally stable. The measurement data obtained are shown in Figure 28.

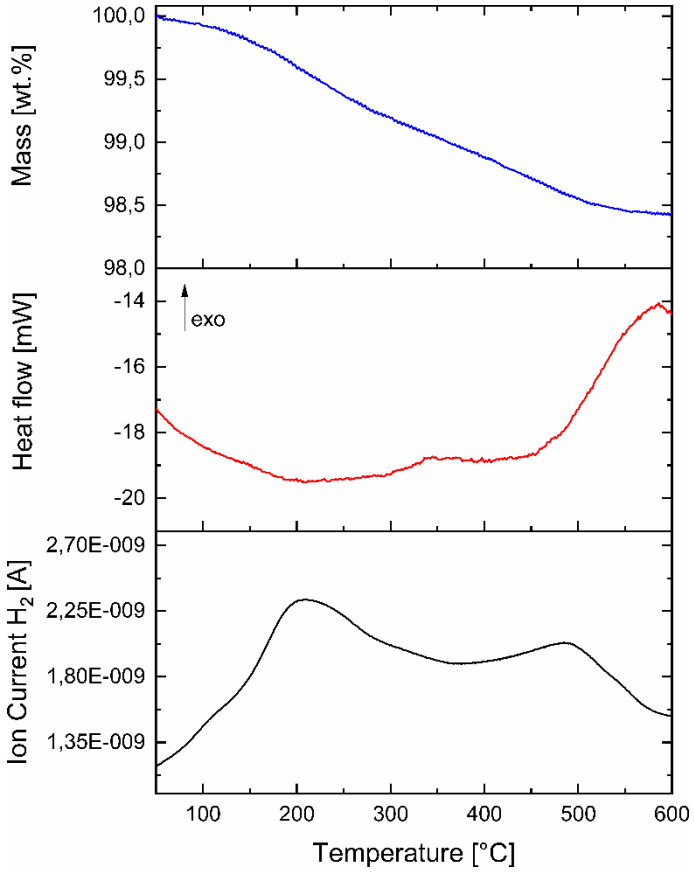

Figure 28: Thermal analysis of as-synthesized material: TGA weight loss profile (top), DSC heat flow (middle) and MS ion current of H_2 (bottom).

According to the TGA, the total weight loss that can be correlated to hydrogen desorption is about 1.56 wt.%. The desorption profile again proceeds via a more

complex mechanism, indicated by two separated endothermic desorption events. The hydrogen release has an initial onset temperature at about 50 °C. At about 120 °C, a shoulder can be seen superimposed on the significant maxima at 200 °C. The associated DSC signal correlates here with the detected hydrogen content of the exhaust gas. After 200 °C, the endothermic signal and the hydrogen content decrease again, finding a minimum at 300 °C. The DSC signal then decreases with increasing temperature. The second endothermic signal is revealed with a maximum at about 480 °C. Above 560 °C, hydrogen release stagnates, recognizable by a reduced mass loss, and the DSC signal reverses to an exothermic signal, resulting in a mass loss of 1.56 wt.%. The more complex desorption process can again have several causes at this point. On the one hand, a broad particle distribution could lead to different desorption temperatures, as it is known for different metal hydride systems.[93, 98-99] On the other hand, the explanation approach of the local different valence electron concentration with influence on different diffusion velocities could have led to the multiple desorption stages.[42] But experimental evidence is not possible to give at this point.

The phase stability was subsequently investigated using XRD experiments and the Pawley simulation. The results obtained are shown in Figure 29.

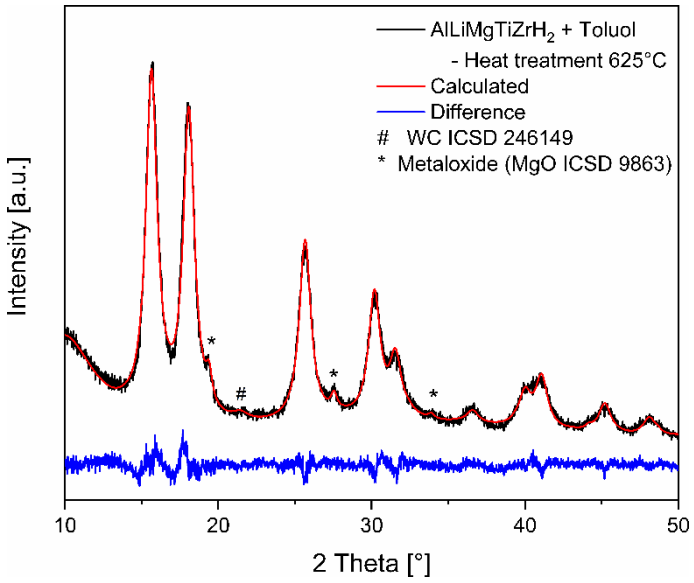

Figure 29: Powder XRD pattern of heat-treated AlLiMgTi-ZrH_2 compound (black), related Pawley simulation (red) and corresponding difference curve (blue).

Using the simulation, the lattice parameter of the *fcc* structure was determined to be 4.5280(8) Å and is, therefore, in the same order of magnitude as before the heat treatment. The only noticeable change is the increased crystalline oxide phase indicated by the stars. The reason for this may again be the sample preparation after

the measurement. The exclusion of oxygen cannot be completely guaranteed when taking samples from the TGA instrument. Apart from this, the material seems to be very stable against heat treatment and showed a high hydrogen content of 1.56 wt.%.

Additionally, Raman spectroscopy was performed on the dehydrogenated material to confirm the formation of high entropy carbide. The obtained Raman spectrum is shown in Figure 30.

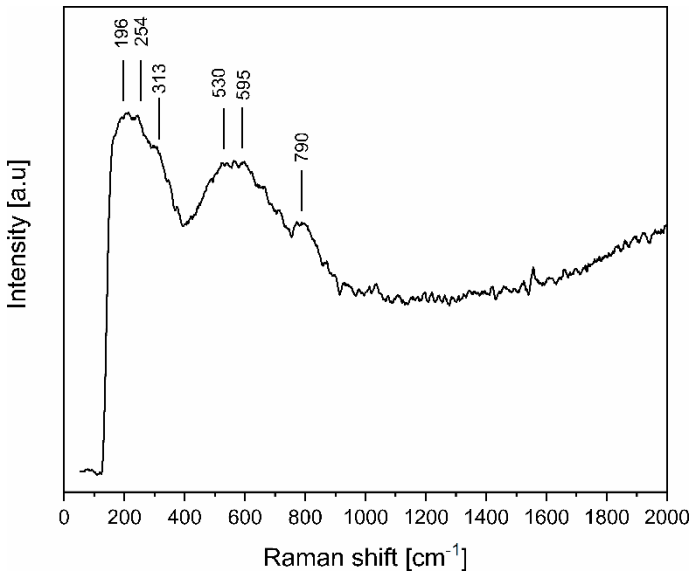

Figure 30: Raman spectrum of dehydrogenated AlLiMgTiZr-C_x and with indicated vibration modes.

As can be seen in Figure 30, the spectrum shows two broad bands (centered at ~230 and ~560 cm^{-1}) and two weaker shoulders at 313 and 790 cm^{-1}. The location of the broad bands is typical for interstitial carbides with *fcc* rocksalt crystal structure.[100] The first band in the region of 196 and 254 cm^{-1} can consequently be assigned to the low-frequency acoustic vibrational modes. The second band, around 530 and 595 cm^{-1}, corresponds to the high-frequency excitation of the optical branch. The separation between the acoustic and optical branches is well-known for monocarbides and is caused by the significant mass difference between the carbon atoms and the transition metals. The shoulder at ~313 cm^{-1} and the band at 790 cm^{-1} can then be explained by multi-phonon processes, which were also measured for $TaC_{0.99}$ at ~300 and ~800 cm^{-1}.[100] At this point, it should be mentioned that the rocksalt-like crystal structure of carbides does not usually show first-order Raman scattering, but vacancies break the local symmetry and Raman scattering can be observed. Accordingly, the measured signals reveal a non-stoichiometric interstitial carbide since no signals would otherwise be measured in the region shown at full occupancy of the sublattice. Moreover, it is known that the width of the bands strongly depends on the surface properties. In the literature, it has been shown that longitudinal and

transverse excitations on electrically polished carbide surfaces can be distinguished by measuring two Raman peaks. In contrast, a mechanically polished surface and, thus, an increased defect density on the surface resulted in a broadening of the Raman peaks.[100] The investigated sample here shows no separation of longitudinal and transverse excitation and indicates high defect density, which is typical for mechanically synthesized materials. Consequently, it can be reasonably assumed that a defect-rich, high entropic carbide has formed. At the same time, the broadening and position of the Raman peaks are still influenced by the statistically distributed alloying elements and by the particle size, which cannot be distinguished at this point.

Nevertheless, all analytical methodologies (XRD, TEM-EDX, and Raman spectroscopy) indicate that a high entropy carbide with homogeneous rocksalt-like *fcc* crystal structure has been synthesized besides the minor contaminations of tungsten carbide and metal oxide. Therefore, the unit cell could be described illustratively with the following Figure 31 and serves only as an assumption since the further investigation of the exact lithium content in the microstructure is needed to solve the crystal structure.

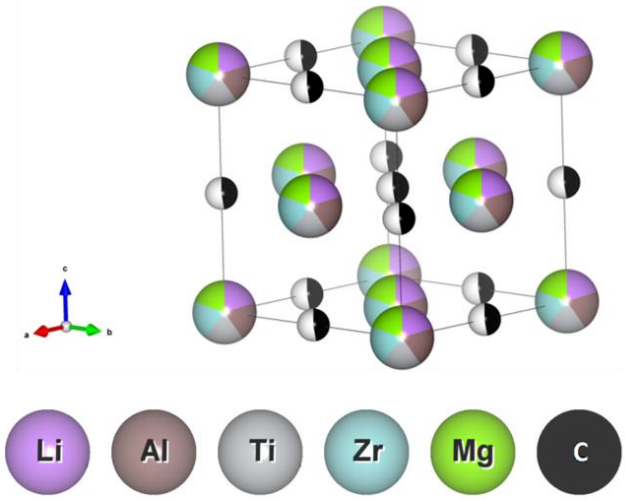

Figure 31: Proposed crystal structure with *fcc* unit cell (structure drawn using VESTA).[101]

We propose the following composition $(Al_{0.2}Li_{0.2}Mg_{0.2}Ti_{0.2}Zr_{0.2})C_{0.47}H_{0.72}$. Metal atoms randomly occupy the main lattice sites, and the sub-lattice is by either carbon or hydrogen. The carbon concentration shown was estimated from ICP-OES analysis, and hydrogen concentration was estimated from the thermal analysis. It should be noted that the real composition could differ from the theoretical composition given here due to tungsten carbide abrasion, the metal oxide phase, and slight variation in PCA amount. The exact occupation of the interstitial sites cannot be determined.

Using computational methods, a reported study of hydrogen bond strengths within monocarbides showed that the occupation of the octahedra and tetrahedra depends on several factors. On the one hand, the bond strength is influenced by the local carbon environment, corresponding to whether nearby interstitial sites are occupied by carbon. At the same time, the occupation is also influenced by the particular metal in the carbide structure itself, which has been correlated with the valence electron concentration.[96] Adapting these findings to the presented system, it quickly becomes apparent that the complexity of the random occupation of lattice sites and interstitial sites makes the exact determination of the presented high entropy carbide almost impossible. Therefore, the occupation probability of the interstitial sites is represented as 50 % by the half-filled spheres and the random occupation of the main lattice sites by the color fraction of the respective elements. Since the possible hydrogen trapping in metal carbides has already been described theoretically, and the sample presumably showed the lowest contamination according to the XRD experiments, the material was examined concerning hydrogen absorption. For this purpose, 0.550 g of the material was transferred to the Sieverts apparatus and cycled with kinetic measurements. For this purpose, the material was initially desorbed at 340 °C under a dynamic vacuum for 2 hours, followed by an absorption step. The absorption conditions consisted of a single dose of hydrogen with a final pressure of around 28 bar at 150 °C. The material was exposed to these conditions three times. Between the first two measurements, the material was desorbed at 340 °C under a dynamic vacuum for 2 hours. In order to observe the influence of the desorption kinetics, the third measurement was carried out after a desorption time of 17 hours at the same conditions. The corresponding measurement data, the hydrogen uptake, and the corresponding time are shown in Figure 32.

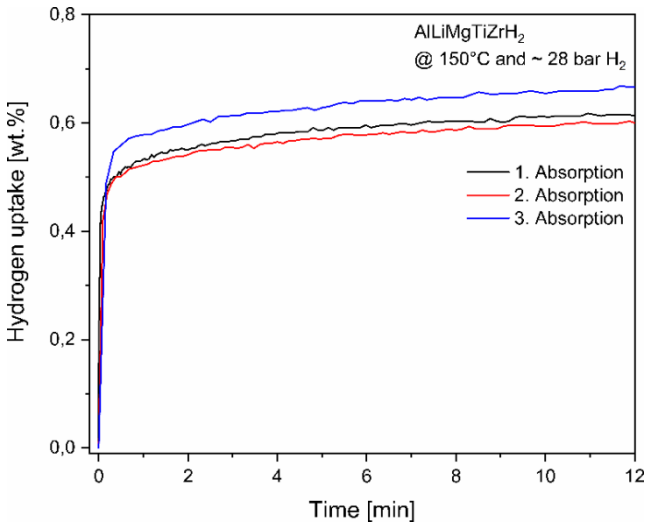

Figure 32: Kinetics of hydrogen absorption in AlLiMgTi-ZrH_2 compound measured at 150 °C and a final hydrogen pressure of ~28 bar, after dehydrogenation at 340 °C for 2 hours.

The kinetics diagram shows rapid hydrogen absorption without incubation time so that within 10 minutes almost the entire capacity was absorbed after hydrogen exposure. At the end of the measurements, the material absorbed about 0.6 wt.% in the first two cycles. In the third cycle, after the longer desorption time of 17 hours, the sample absorbs 0.66 wt.%. This could indicate that desorption is kinetically inhibited under the conditions (340 °C). The longer desorption time seems to lead to a lower hydrogen concentration in the sample, which may have led to a slightly increased hydrogen uptake in the subsequent measurement. Considering also the TGA desorption profile, which shows that temperatures above 500 °C are required for complete desorption (~1.56 wt.%), this suggests that the desorption conditions at 340 °C may not have been sufficient for complete desorption of the sample. This would be reflected in the subsequent absorption step by reduced hydrogen uptake (0.6 wt.%). This means that the remaining fixed hydrogen in the sample can account for the measured difference between TGA and PCI. In general, however, it can be concluded that the material is active towards hydrogen and that the hydrogen absorption is reversible in the first three cycles. Moreover, metal hydrides are known to suffer from degradation processes when they are cycled, so the dehydrogenated material was investigated for its phase stability by XRD experiment after three cycles. The corresponding measurement data are shown in Figure 33.

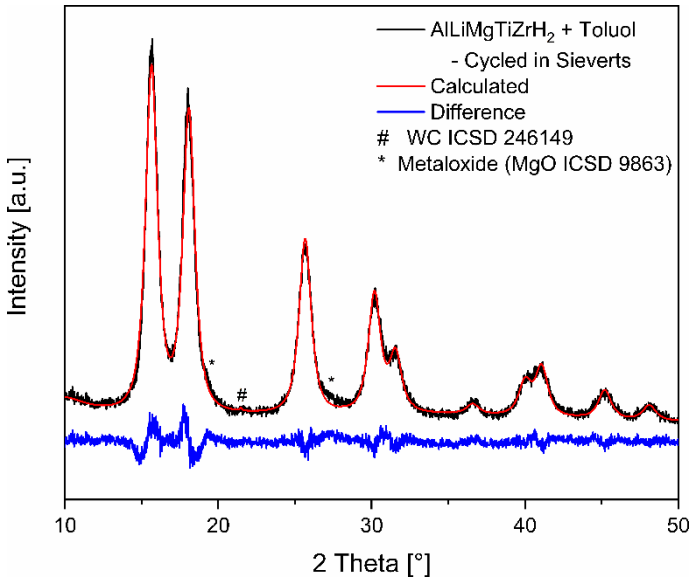

Figure 33: Powder XRD pattern of cycled AlLiMgTi-ZrH_2 compound (black), related Pawley simulation (red) and corresponding difference curve (blue).

The XRD data generally show that the material has good phase stability. Using the Pawley method, the lattice parameter is determined to be 4.5286(6) Å and agrees very well with the initial lattice parameter (4.5281(6) Å). This suggests that no phase

segregation or segregation of individual elements has occurred over three reversible cycles.

5.3. Conclusion

This chapter discusses the synthesis approaches regarding a new high entropy alloy composed of AlLiMgTiZr. It was shown that PCAs are necessary for the processability of the material composition. Otherwise, the materials have an increased cold welding effect during ball milling and thus cannot be processed in powder form. Furthermore, the influence of different PCAs (ethanol, toluene and n-hexane) during synthesis was investigated. Based on these experiments, it was found that a new compound with an *fcc* ($Fm\bar{3}m$) structure similar to a carbide structure could be synthesized. The performed tracking experiments revealed the transformation of the materials. Zirconium hydride was identified as the intermediate phase in all samples and when the milling speed was reduced. With further processing, the intermediate zirconium hydride disappeared, and the new *fcc* phase formed more strongly. This mechanism was also reported in the literature that zirconium carbide could be synthesized via the decomposition of solvents during ball milling with zirconium hydride as an intermediate phase.[85] The combination of the findings from Raman spectroscopy, XRD, and EDX analysis and the reported findings lead to the assumption that a high entropy carbide has been synthesized. The grinding speed reduction indicated that the conversion is only slowed down or that no alloying process occurs, as it was found at 400 rpm. The comparison of the lattice parameters ($a_{Ethanol}$ = 4.5145(6) Å, $a_{Toluene}$ = 4.5189(4) Å, $a_{ZrH_2,Toluene}$ = 4.5281(6) Å) suggests that in all cases, an high entropy carbide with a similar rocksalt-like crystal structure has been synthesized, and the products are isotypic. The minor variations of the lattice parameter can be attributed to different carbon concentrations within the structure, as it is also known for mono carbides, that the lattice parameters vary with the carbon content.[102-104]

The subsequent thermal analyses allowed conclusions to be drawn about the composition by comparing the theoretical proportion of hydrogen within the PCAs with the measured mass loss correlated with the hydrogen signal. The higher mass loss of the ethanol synthesized sample also corresponded to the PCA's increased hydrogen-to-carbon ratio. The literature also described a similar observation, that the hydrogen-to-carbon ratio of different PCAs was found in a titanium carbohydride phase of mechanically alloyed samples.[86] In this work, titanium was milled with n-heptane or toluene, and it was found that the incorporated carbon-to-hydrogen ratio

corresponded to the ratio of the PCAs used.[86] These observations could also be necessary for the experiment carried out with zirconium hydride. Titanium hydride was not identified during the tracking experiments but could also be responsible for the decomposition of the PCAs. Therefore, an experiment with hydrogenated titanium and zirconium would be of interest in the future to suppress PCA decomposition. However, reactive grinding showed that no crystalline *bcc* phase could be synthesized under the process conditions. Instead, the results show that a high entropy carbide with a rocksalt-like structure ($Fm\bar{3}m$ symmetry) can be synthesized. This suggests that the empirically developed parameters for VEC, δ and Ω are not necessarily applicable to the material composition studied. However, this hypothesis cannot be completely ruled out because, under the experimental conditions, other factors such as hydrogen, carbon, tungsten carbide impurities, and oxygen come into play and complicate the adaption of these selection criteria.

Concerning the hydrogen storage properties, it was also possible to incorporate further hydrogen into the structure, in which ZrH_2 served as an additional H_2 source, thereby increasing the hydrogen content to 1.56 wt.%. The cycle experiments showed that 0.6 wt.% reversible could be stored over three cycles, and the connected XRD experiments indicated a high phase stability of the material. To classify the material as a possible hydrogen storage material, we would classify it as mid-range since superior systems based on TiFe or Mg exist as storage materials. The TiFe system has the advantage of storing a higher amount of hydrogen reversible already at room temperature, and MgH_2 has to be operated under higher operating temperatures, but it is superior with a theoretical storage capacity of 7.6 wt.%.[29, 36] The investigated carbide seems to have a technical relevant time range only with respect to kinetics, where it can be charged within a few minutes. The dehydrogenation temperatures of up to 550 °C are not technically significant. Another interesting property comes from the volume stability of the investigated materials. The lattice parameters in the hydrogenated (4.5281(6) Å) and dehydrogenated state (4.5286(6) Å) do not deviate from each other, whereby it is assumed that, in contrast to the metal-based storage system, no volume change takes place during cyclization. This property is advantageous for the design of storage tanks since no empty volume for the storage material must be considered.

Furthermore, it would be interesting to investigate carbon's role in carbide formation. An interesting approach would be determining the critical carbon concentration needed for the carbide phase formation. Connected to this, it would also be interesting to see how the carbide concentration affects the hydrogen uptake. In

addition, the material could also be considered a coating material since carbides generally have high strength, and the synthesized material also contains light metals, which can lead to lower density.[105-106]

In principle, the results show how a high entropy carbide can be produced based on light metals, although a spatially resolved technique such as electron energy loss spectroscopy would still be required for the precise structure solution to be able to detect lithium locally.

Chapter 6

6. High Entropy Alloys Based on TiVZrNb

This chapter presents the investigations of various high entropy alloys (HEA) based on the previously studied four-component $Ti_{0.325}V_{0.275}Nb_{0.275}Zr_{0.125}$ system.[19] The four-component system is of interest because it has shown a high hydrogen capacity at room temperature of 2.7 wt.%, corresponding to a H/M of 1.8. Furthermore, the alloy exhibited fast absorption kinetics and showed that 2.3 wt% hydrogen could be reversibly stored over 10 cycles.[19, 107] Subsequently, Montero et al. systematically investigated the influence of individual elements in multicomponent *bcc* alloys by adding different elements to the alloy to obtain $M_{0.1}Ti_{0.3}V_{0.25}Nb_{0.25}Zr_{0.1}$ (M = Ta, Mg, Al) compositions.[19-22] Since the hydrogenation properties of multicomponent alloys are poorly studied, the purpose of this chapter is to continue the systematic investigation of Montera et al.[23] Li is to be added to the alloy and the simultaneously Li and Al as alloying elements ($Ti_{0.3}V_{0.25}Nb_{0.25}Zr_{0.1}Li_{0.1}$ and $Ti_{0.3}V_{0.25}Nb_{0.25}Zr_{0.1}Al_{0.05}Li_{0.05}$) and to evaluate the influence on hydrogen storage properties systematically. Lithium was chosen at this point to investigate the effect on gravimetric storage density. It is assumed that by reducing the average molar mass of the alloy due to the incorporation of Li while keeping the H/M ratio constant, the gravimetric storage density can be increased (c.f. Equation 4.2). In addition, it was necessary to check whether the selection criteria for forming a solid solution were met with lithium in the alloys. For this purpose, the parameters such as the VEC, δ, ΔH_{mix}, and Ω for each compound are given in Table 8 below.

Table 8: Overview of the selection parameters for the respective alloy.

Composition	VEC	δ [%]	ΔH_{mix} [kJ mol^{-1}]	Ω
$Ti_{0.325}V_{0.275}Nb_{0.275}Zr_{0.125}$	4.55	6.34	-0.30	82
$Ti_{0.3}V_{0.25}Nb_{0.25}Zr_{0.1}Li_{0.1}$	4.2	6.11	13.71	1.9
$Ti_{0.3}V_{0.25}Nb_{0.25}Zr_{0.1}Al_{0.05}Li_{0.05}$	4.3	6.00	2.31	11.96
$Ti_{0.3}V_{0.25}Nb_{0.25}Zr_{0.1}Al_{0.1}$	4.4	5.87	-9.01	2.9

Except for the enthalpy of mixing of the lithium sample, which is above the limit of 5 kJ mol^{-1}, the selection criteria are met for all parameters of each compound. The two alloys ($Ti_{0.325}V_{0.275}Nb_{0.275}Zr_{0.125}$ and $Ti_{0.3}V_{0.25}Nb_{0.25}Zr_{0.1}M_{0.1}$) were synthesized for the study following the publications to obtain two reference systems. In addition, mechanical alloying and reactive milling were applied as synthesis methods to evaluate the influence on the alloys and their storage capacity. Accordingly, the chapter is divided into two subchapters assigned to the synthesis process. In order to better categorize the materials, various techniques were applied. Tracking experiments were used to evaluate the alloying process through XRD analysis. Thermal analysis was used to investigate the desorption behavior of the materials in order to obtain information on the stability of the hydrides. SEM-EDX and ICP-OES were used to evaluate the microstructure and chemical composition of the materials. Furthermore, the Sieverts method was applied to investigate the material volumetrically as a hydrogen storage material and to obtain information on the thermodynamic parameters.

6.1. Mechanical Alloyed Samples

In this chapter, the results of mechanically alloyed samples are presented. First, the synthesis of the HEAs is discussed, and then the hydrogen storage behavior is presented.

6.1.1. Synthesis of Mechanical Alloyed Samples

The synthesis was carried out with a planetary mill in an argon atmosphere to prevent oxidation. The grinding jars and the balls were made of stainless steel. A process step consisted of 15 minutes of grinding with an associated scraping of the walls to ensure sufficient mixing. Samples were then taken at specific times and analyzed using the XRD method to evaluate the alloying progress. The corresponding XRD samples are shown in Figure 34 and marked with the respective process time for the respective XRD sample.

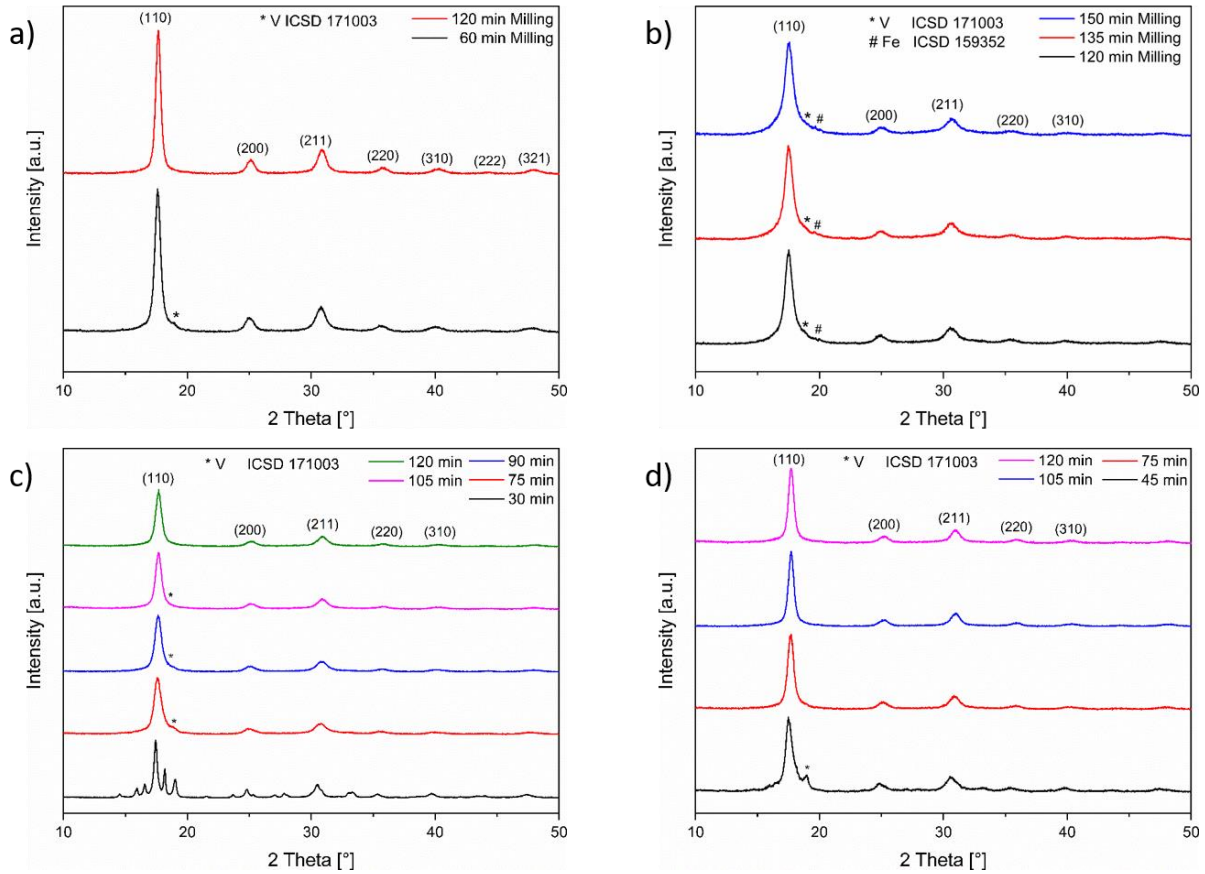

Figure 34: XRD pattern of mechanical alloyed high entropy alloys: a) $Ti_{0.325}V_{0.275}Nb_{0.275}Zr_{0.125}$, b) $Li_{0.1}Ti_{0.3}V_{0.25}Nb_{0.25}Zr_{0.1}$, c) $Al_{0.05}Li_{0.05}Ti_{0.3}V_{0.25}Nb_{0.25}Zr_{0.1}$, d) $Al_{0.1}Ti_{0.3}V_{0.25}Nb_{0.25}Zr_{0.1}$.

As the tracking experiments show, a dominant *bcc* phase (indexed space group $Im\bar{3}m$) can be identified in all four cases after 2 hours of process time. Alloy formation already takes place within the first 75 minutes, with a small amount of remaining vanadium being identified and marked by (*) in the diffraction patterns. It has to be mentioned at this point that the (110)-reflection of the pure vanadium *bcc* phase is expected to be at 19.069°, and the center of the shoulder is approximately at 18.5° - 18.8°. This slight shift of a 2 Theta value can be explained by alloy formation between vanadium and the other used elements, which occurs simultaneously with the formation of the dominant *bcc* phase. Vanadium has the smallest atomic diameter (132 pm) compared to Li (152 pm), Ti (147 pm), Nb (143 pm), and Zr (162 pm). Alloying with larger elements, i.e., forming a solid solution, then leads to an enlargement of the lattice cell.[108] The enlarged lattice cell can be recognized by shifted reflections to smaller 2 Theta values, as is also described for binary solid solutions by Vergard's law.[109-110] The element with which vanadium is alloyed cannot be identified from the diffraction patterns. However, it can be assumed that vanadium is involved to a lower extent or more slowly in the alloy formation of the dominant *bcc* phase since the position of the shoulder is very close to the reflection of the pure vanadium phase. For comparison, the (110)-reflection of the niobium *bcc* structure is expected to

be at 17.42° under the same measurement conditions (ICSD #76011). As the process continues, the intermediate phase is also depleted. The intensity of the shoulder at 18.5° - 18.8° decreases noticeably, which can be attributed to the homogenization of the dominant alloy. Interestingly, the secondary phase is transformed more slowly in the lithium samples (cf. App. 9.5. for increased time resolution). The formed shoulder, which can be attributed to the side phase, is still more pronounced after 75 minutes for the lithium-containing samples (Figure 34b and c), whereas for the other samples without lithium (Figure 34a and d), the intensity appears to be significantly lower after 60 and 75 minutes of processing. The miscibility of the individual elements could explain the delayed alloying progress by considering their binary mixing enthalpies (cf. Table 9).

Table 9 – Values of enthalpy of mixing ΔH_{mix} (kJ mol^{-1}) for atomic pairs contained in synthesized HEAs[108].

Element	Li	Al	Ti	Nb	V
Al	-4				
Ti	34	-30			
Nb	51	-18	2		
V	37	-16	-2	-1	
Zr	27	-44	0	4	-4

The enthalpies of mixing of lithium with the transition metals are all positive, which corresponds to poor or no miscibility of the elements in the binary system. Accordingly, the increased lithium content may slow the formation of the single-phase HEA. However, since mechanical alloying is also known to form metastable phases and expand the solubility ranges of the systems, mechanical alloying could be considered a successful synthesis technique of the initially difficult-to-mix elements at this point, as seen by the formed dominant *bcc* phase.[71]

Consequently, the final X-ray diffraction patterns were simulated (Pawley method) with a *bcc* phase (space group $Im\bar{3}m$) and additional consideration of the minor phase (assumed to be vanadium, $Im\bar{3}m$) as well as contamination by iron abrasion from milling equipment. The respective simulations are shown with the measured data in Figure 35.

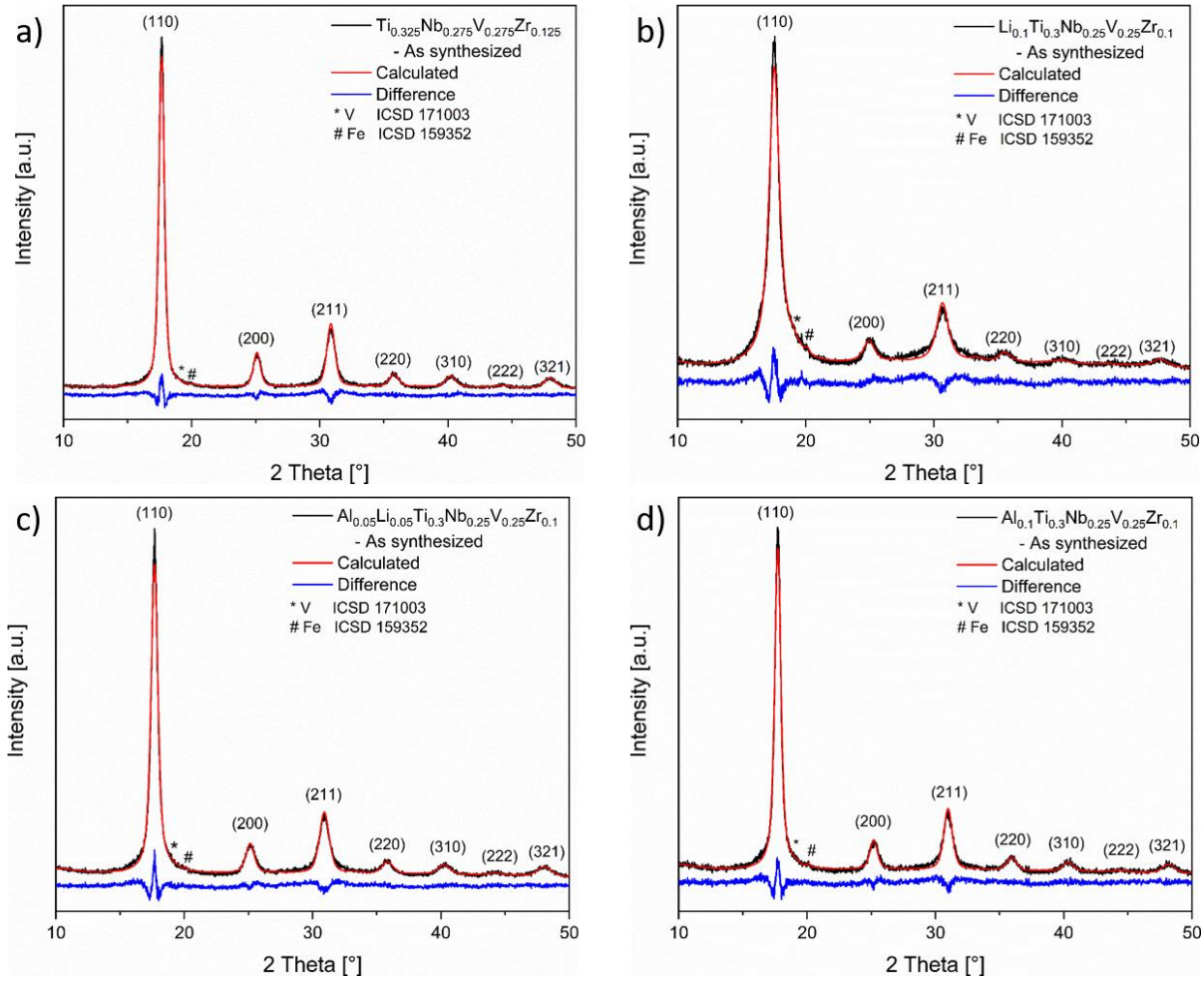

Figure 35: Powder XRD pattern of mechanically alloyed compounds (black), related Pawley simulation (red) and corresponding difference curve (blue): a) $Ti_{0.325}V_{0.275}Nb_{0.275}Zr_{0.125}$ b) $Li_{0.1}Ti_{0.3}V_{0.25}Nb_{0.25}Zr_{0.1}$ c) $Al_{0.05}Li_{0.05}Ti_{0.3}V_{0.25}Nb_{0.25}Zr_{0.1}$ d) $Al_{0.1}Ti_{0.3}V_{0.25}Nb_{0.25}Zr_{0.1}$.

First, it should be emphasized that all diffraction patterns could be simulated with the *bcc* phase. However, compared to the final diffraction patterns directly, it becomes clear that the signal widths of the samples differ. The samples synthesized with lithium (Figures 35b and c) show an increased width. In the case of the sample containing 10% lithium (b), this even leads to the result that it is not possible to distinguish between the primary phase and the two minority phases. The broadening and the presence of minority phases result in an asymmetry of the prominent reflex. Thus, making the discrimination of all phases much more difficult. The reflection broadening may be due to the extended milling time, which reduces the crystallite size reflected by the broadening in diffraction experiments.[111] However, since the reflection width of the 10% lithium-containing sample does not change significantly after 120 min of milling, it is more likely that the mechanical properties of the respective samples differ. Lithium uptake into the alloy could lead to a more brittle material, which means that the crystallites are generally expected to be smaller than in materials with higher ductility.[71-72] To examine this assumption, the morphology

of the particles was studied using SEM images, and the images obtained are shown in Figures 36 and 38.

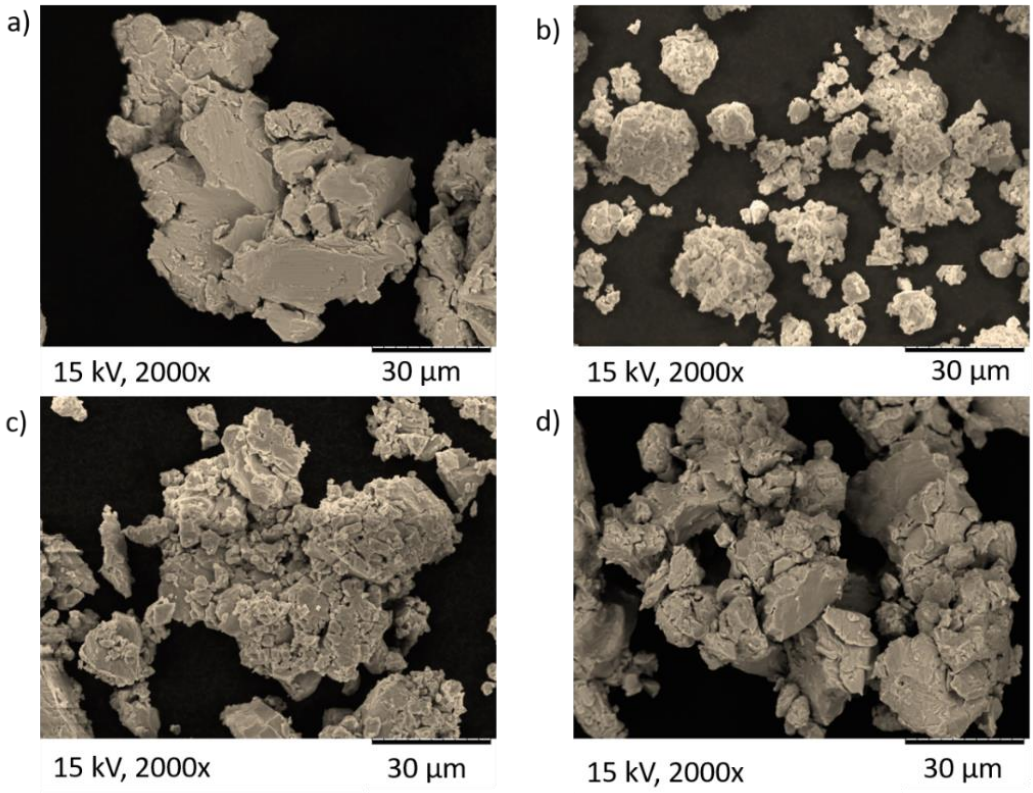

Figure 36: SEM micrographs: a) $Ti_{0.325}V_{0.275}Nb_{0.275}Zr_{0.125}$, b) $Li_{0.1}Ti_{0.3}V_{0.25}Nb_{0.25}Zr_{0.1}$, c) $Al_{0.05}Li_{0.05}Ti_{0.3}V_{0.25}Nb_{0.25}Zr_{0.1}$, d) $Al_{0.1}Ti_{0.3}V_{0.25}Nb_{0.25}Zr_{0.1}$.

All images show agglomerated particles ranging from a few to several tens of micrometers. The samples without lithium, Figures 36 a) and d), show larger coherent surface areas, suggesting a larger particle size, while the lithium-containing samples show a coarser and more open-pored surface structure. Smaller particles may account for the coarser surface area of the sample. In addition, as seen sporadically in Figure 36b), smaller particles are located adjacent to the agglomerates. Here it is assumed that lithium influences the mechanical properties via its incorporation into the solid solution and that these are more brittle than the samples without Li. Smaller crystallites would be expected for more brittle materials, which could explain the broader reflections of the XRD analysis and the sporadically visible smaller particles in the SEM images. These findings could thus provide a first indication of the successful synthesis of the solid solution with lithium.

In addition, lithium uptake into the solid solution is characterized by an increased lattice parameter, shown in Table 10. With increasing lithium content, the lattice parameter increases, which is reasonable considering the larger atomic diameter of lithium (152 pm) compared to the other alloying elements (V 132 pm, Ti 147 pm, Nb

143 pm, Zr 162 pm).[108] The lattice parameters of the two reference systems also agree well with the lattice parameters from the literature, which are also in Table 10 for comparison. Slight deviations can be attributed to the synthesis processes.

Table 10 Lattice parameters of the synthesized HEAs determined with the Pawley method and the corresponding literature values.

Composition	Lattice parameter [Å]	Reference
$Ti_{0.325}V_{0.275}Nb_{0.275}Zr_{0.125}$	3.2627(1)	Present work
	3.261(1)[a]	[19]
	3.270(1)[b]	[19]
$Li_{0.10}Ti_{0.30}V_{0.25}Nb_{0.25}Zr_{0.10}$	3.2831(4)	Present work
$Al_{0.05}Li_{0.05}Ti_{0.3}V_{0.25}Nb_{0.25}Zr_{0.1}$	3.2578(2)	Present work
$Al_{0.10}Ti_{0.30}V_{0.25}Nb_{0.25}Zr_{0.10}$	3.2507(2)	Present work
	3.247(1)[a]	[21]

a) synthesized by arc-melting and b) by mechanical alloying for 60 min.

The four-component system, $Ti_{0.325}V_{0.275}Nb_{0.275}Zr_{0.125}$, as described by Montero et al., was synthesized by arc melting, where the lattice parameter agrees very well with the lattice parameter determined in this work. However, the mechanically alloyed sample from the literature shows a higher deviation of the lattice parameter, which could be due to different process parameters.[19] In the literature, the synthesis was performed with a speed of 700 rpm, a BPR of 26 at a powder amount of 5 g, and a ball diameter of 7 mm. The higher speed compared to the present work (600 rpm) may have reduced the synthesis time to 60 min. In addition, it is expected that with a higher BPR and increased speed, more abrasion may have occurred, causing the amount of contamination to be different and thus influencing the lattice parameter. The shorter synthesis time of 60 minutes and the increased material usage (5 g) could influence the homogenization of the sample. As it is also shown in the present work that after 60 minutes, the remaining vanadium can be identified in the XRD experiments (cf. Figure 34). Accordingly, the deviation of the lattice parameter can be attributed to different synthesis conditions. The aluminum-containing sample, $Al_{0.10}Ti_{0.30}V_{0.25}Nb_{0.25}Zr_{0.10}$, also shows a deviation of the lattice parameter, which may also be process-related. The literature value was determined on a sample synthesized by arc melting, and in the present work, mechanical alloying was applied.[21] Ball milling is known to result in materials having a high defect density and increased contamination due to the abrasion of iron. Accordingly, the higher defect

concentration and the incorporation of the abrasives into the alloy may have resulted in a slight shift in the lattice parameter. The evidence of defect density is indistinguishable based on the quality of the data, with the incorporation of the abrasives confirmed by subsequent analysis using SEM-EDX.

In order to assess the alloy formation in terms of its chemical composition, SEM-EDX analysis was performed. For example, an analysis of the $Li_{0.10}Ti_{0.30}V_{0.25}Nb_{0.25}Zr_{0.10}$ sample with the respective individual mappings and the summed energy-dispersive spectrum is shown in Figure 37.

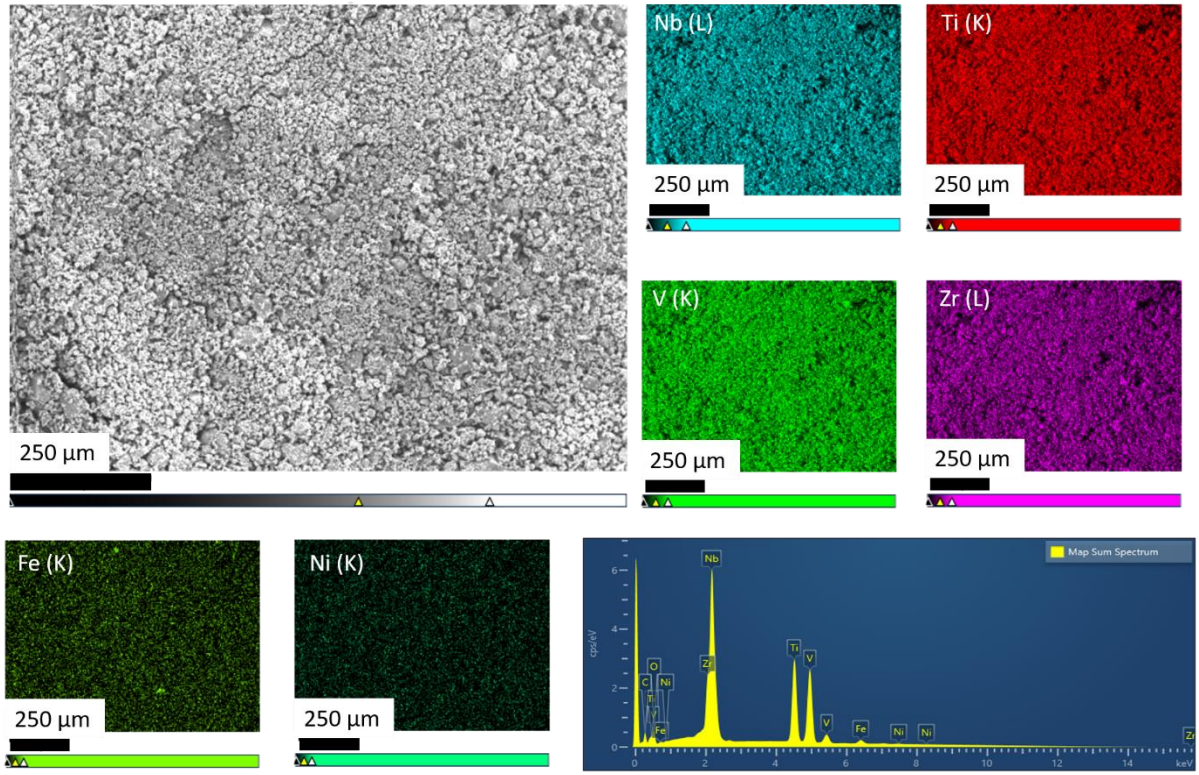

Figure 37: SEM micrograph of $Li_{0.1}Ti_{0.3}V_{0.25}Nb_{0.25}Zr_{0.1}$ sample with corresponding individual EDX mappings and energy dispersive spectrum.

The chemical analysis utilizing element distribution images shows a homogeneous element distribution over the recorded particles. The iron abrasion can be identified in isolated particles and is uniformly dispersed over the recorded particles. The identified iron leads to the assumption that iron uptake also accompanies the alloy formation into the solid solution, which could be found in all samples. In this case, the amount of iron is low relative to the metals used (< 2.3 wt.%) but cannot be prevented due to mechanical alloying as a synthesis method. The quantitative results obtained from the sum spectra and the individual images of each sample are attached to the appendix (cf. Appendix 9.6).

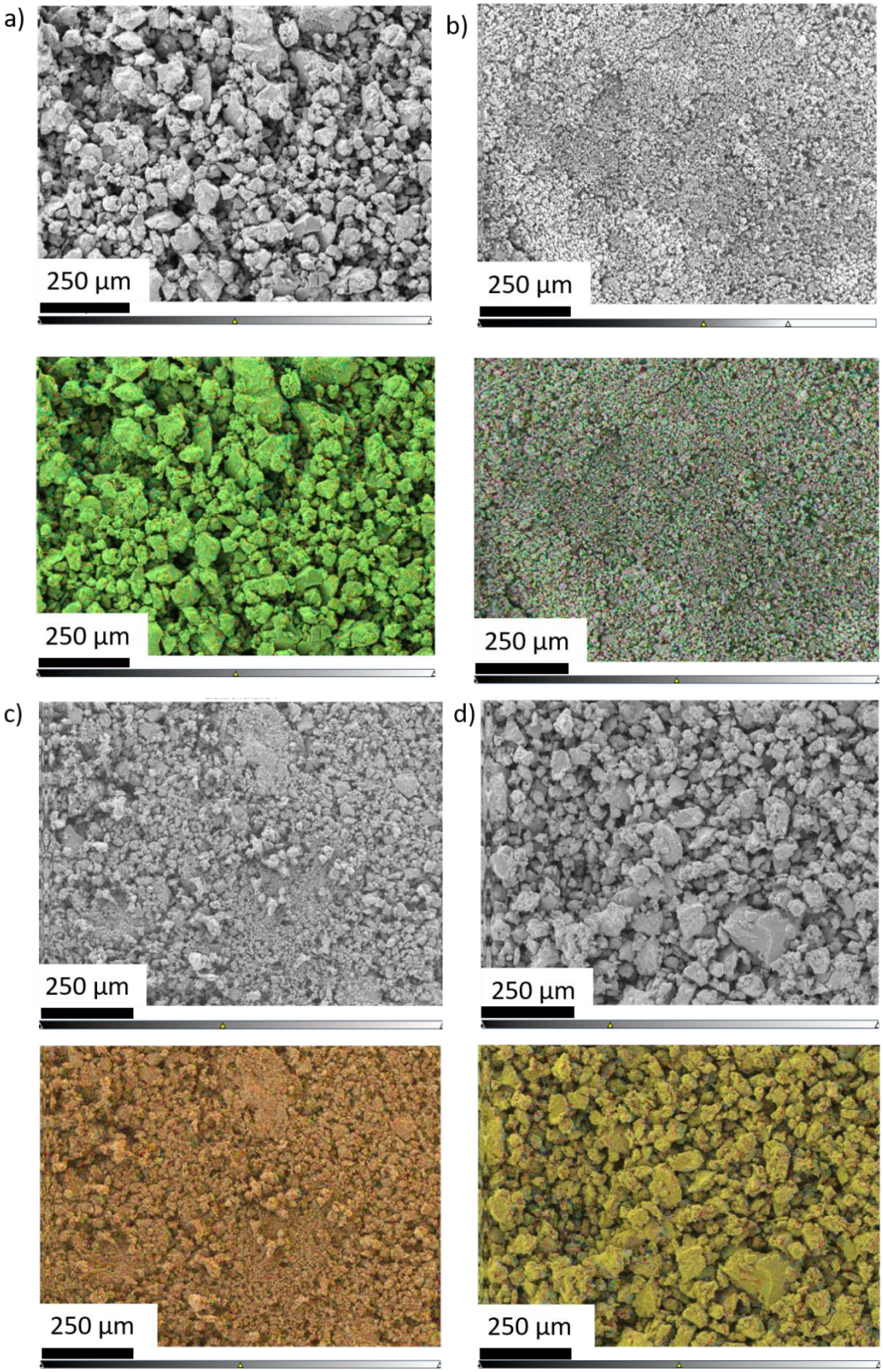

Figure 38: SEM micrographs and corresponding elemental mapping overlay without significant inhomogeneities: a) $Ti_{0.325}V_{0.275}Nb_{0.275}Zr_{0.125}$ b) $Li_{0.1}Ti_{0.3}V_{0.25}Nb_{0.25}Zr_{0.1}$ c) $Al_{0.1}Ti_{0.3}V_{0.25}Nb_{0.25}Zr_{0.1}$ d) $Al_{0.05}Li_{0.05}Ti_{0.3}V_{0.25}Nb_{0.25}Zr_{0.1}$.

From EDX analysis, it can be seen that the ratios of the elements used correspond approximately to the nominal ratios of the alloys, although the quantification of the

elements by EDX spectroscopy on particles should be considered with caution. In addition, Figure 38, with SEM micrographs and the corresponding elemental overlay, further illustrates that the detectable elements are evenly distributed without significant inhomogeneity.

Since lithium is not detectable with the EDX detector used, additional ICP-OES experiments were performed to verify the elemental composition with respect to the lithium content, and the corresponding results are shown in Table 11.

Table 11: Metal content determined by ICP-OES of alloys synthesized by mechanical alloying.

Sample	Al at.%	Li at.%	Ti at.%	V at.%	Nb at.%	Zr at.%
$Ti_{0.325}V_{0.275}Nb_{0.275}Zr_{0.125}$	-	-	33.48	27.70	26.71	12.12
$Li_{0.1}Ti_{0.3}V_{0.25}Nb_{0.25}Zr_{0.1}$	-	11.71	30.17	24.31	24.17	9.64
$Al_{0.1}Ti_{0.3}V_{0.25}Nb_{0.25}Zr_{0.1}$	9.43	-	30.42	24.74	25.14	10.27
$Al_{0.05}Li_{0.05}Ti_{0.3}V_{0.25}Nb_{0.25}Zr_{0.1}$	5.02	4.27	31.22	24.79	24.75	9.96

As the results of EDX quantification, the concentrations determined by ICP-OES show no significant deviation from the nominal concentration of the compounds. Therefore, considering the respective analytical methods, it can be assumed that a high entropy alloy with the targeted concentrations and a *bcc* phase has been successfully synthesized, which have been further investigated for their hydrogen storage properties.

6.1.2. Hydrogen Storage Properties of Mechanical Alloyed Samples

For the investigation of hydrogen storage properties, the alloys were transferred to the measuring autoclave of the Sieverts apparatus after synthesis without further treatment and initially activated according to the literature.[19-22, 107] The materials were activated at 340 °C under a dynamic vacuum for two hours, after which they were hydrogenated and dehydrogenated at different temperatures. In order to compare and evaluate the systems, the same measurement conditions were used for all materials. To investigate the hydrogenation rates at different temperatures (33, 200, and 400 °C), the materials were exposed to a hydrogen dose with an initial pressure

of 40 bar in the reservoir. After opening the valve, the final pressure was approx. 18 bar depending on the amount of hydrogen absorbed. Between each time-dependent measurement, the materials were dehydrogenated at 400 °C for at least two hours under a dynamic vacuum. Each measurement at 200 °C was performed five times. After five hydrogenations at 200 °C, the materials were then three times exposed to hydrogen at 33 °C to investigate their storage behavior under ambient conditions. The kinetics measurements were then finished with a measurement at 400 °C to check whether the material absorbed hydrogen at high temperatures. Figure 39 shows the hydrogen uptakes versus time at the respective temperatures.

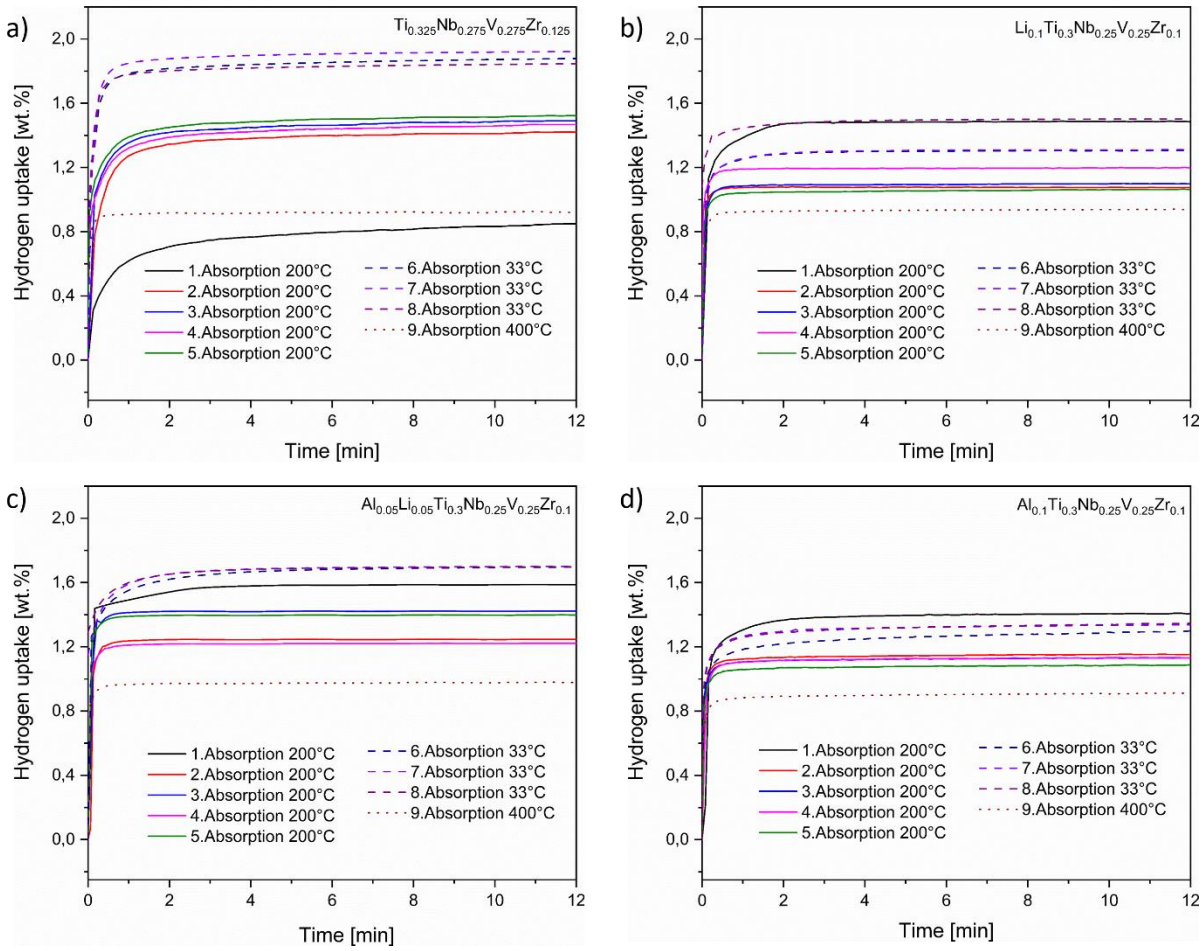

Figure 39: Hydrogen uptake versus time in mechanically alloyed samples at 33, 200, and 400 °C and a final hydrogen pressure of ~18 bar depending on hydrogen uptake and temperature: a) $Ti_{0.325}V_{0.275}Nb_{0.275}Zr_{0.125}$ b) $Li_{0.1}Ti_{0.3}V_{0.25}Nb_{0.25}Zr_{0.1}$ c) $Al_{0.1}Ti_{0.3}V_{0.25}Nb_{0.25}Zr_{0.1}$ d) $Al_{0.05}Li_{0.05}Ti_{0.3}V_{0.25}Nb_{0.25}Zr_{0.1}$.

Considering the individual samples, it is notable that the quaternary system, $Ti_{0.325}V_{0.275}Nb_{0.275}Zr_{0.125}$, initially shows a lower hydrogen uptake (~ 0.7 wt.%) during the first hydrogenation. In the second hydrogenation, however, the capacity increases to about 1.4 wt.%. This capacity increase upon second hydrogenation suggests that the quaternary compound is not yet fully activated at the first time. Activation opens accessible diffusion pathways into the material and can be achieved

by pulverization. Pulverization creates new surfaces and thus facilitates hydrogen diffusion into the materials.[45] However, the exact cause cannot be clarified at this point. The other samples, on the other hand, show an inverse trend. An increased hydrogen capacity was measured for the first hydrogenation at 200 °C than for the subsequent hydrogenations. During the first hydrogenation, the initial hydrogen capacities of the $Li_{0.1}Ti_{0.3}V_{0.25}Nb_{0.25}Zr_{0.1}$ alloy and $Al_{0.1}Ti_{0.3}V_{0.25}Nb_{0.25}Zr_{0.1}$ compound were 1.40 wt.% and 1.48 wt.%, respectively. In the subsequent second hydrogenation at 200 °C, hydrogen uptake was determined to be 1.13 wt.% and 1.2 wt.%, respectively, resulting in a loss of about 20 % for the quinary alloys in the first cycle. In contrast, the $Al_{0.05}Li_{0.05}Ti_{0.3}V_{0.25}Nb_{0.25}Zr_{0.1}$ alloy shows a loss of about 12 %, from 1.58 wt.% to 1.35 wt.% (the average of the four following cycles). A similar behavior, in terms of capacity degradation, is also described in the literature for the $Al_{0.1}Ti_{0.3}V_{0.25}Nb_{0.25}Zr_{0.1}$ compound (~11% loss) and quaternary compound (~18%), but the exact cause is not clear.[19, 21] However, it is known for other metal hydrides that several causes can be responsible for the loss. Firstly, phase segregation, also called disproportionation, in alloys can lead to loss of storage capacity, in which the storage material loses its initial crystal structure and, therefore, its previous chemical nature due to the thermodynamic favoring of the decomposition products.[28, 36, 45, 112] In addition, dislocation formation is also supposed to be responsible for reducing the storage capacity, although the complex relationship between crystalline structure and the degradation behavior is not yet fully understood.[45] Pulverization of the metals could also contribute to the reduction. Pulverization leads to the loss of crystal volume, which provides interstitial sites for hydrogen incorporation so that the increase in grain boundaries associated with pulverization can reduce the number of possible occupation sites. Consistently, the inverse trend in crystal growth towards increased capacity as a function of cyclic number has been observed.[28, 113] Furthermore, the formation of very stable hydrides can also reduce the measured storage capacity, as the hydrogen remains strongly bound during the dehydrogenation step and can, therefore, no longer be detected as a pressure drop in the subsequent hydrogenation.[112] All three mechanisms could have led to the decrease after the first hydrogenation but could not be differentiated based on the kinetic measurements since the intrinsic degradation depends on many physical and chemical properties.[45] For these two or more plateaus, volume expansion of the crystal lattice, maximum operation temperature, alloy composition, and defects in the lattice has to be considered.[28, 114]

A rapid hydrogen uptake can be observed for all samples. All samples absorb hydrogen within the first 5 minutes without additional incubation time, independent

of the temperature. Apparent differences can be observed regarding the maximum hydrogen capacity after 12 minutes. At 33 °C, the quaternary alloy with reversible hydrogen uptake of about 1.85 wt.% shows the highest uptake, followed by the $Al_{0.05}Li_{0.05}Ti_{0.3}V_{0.25}Nb_{0.25}Zr_{0.1}$ compound with a hydrogen uptake of about 1.7 wt.%. On the other hand, the lithium-containing sample shows a capacity of 1.5 wt.%, although this value was not recorded reversibly. Only during the 8th absorption was this value measured. The other two measurements (6th and 7th) were determined at 1.3 wt.% and comparable to the aluminum-containing sample. For the latter, a hydrogen uptake of 1.3 wt.% was measured. Accordingly, the quinary compounds seem to show the lowest hydrogen uptake.

Another characteristic of metal hydrides can be seen in the temperature dependence of hydrogen storage capacity. With increased temperature, the maximum storage capacity of the samples shown decreases, excluding the first hydrogenations. Accordingly, the storage capacities at 400 °C decreased to about 0.9 wt.%, with the $Al_{0.05}Li_{0.05}Ti_{0.3}V_{0.25}Nb_{0.25}Zr_{0.1}$ alloy still showing the highest capacity at 0.97 wt.% and the $Al_{0.1}Ti_{0.3}V_{0.25}Nb_{0.25}Zr_{0.1}$ compound having the lowest uptake at 0.91 wt.%. This is because the metal hydride formation is no longer favored thermodynamically and is thus temperature-dependent, which can be understood as a destabilization of the hydride phase with an increase in temperature. In the equilibrium diagram (the PCI curve), this is shown by the plateau becoming narrower as the temperature increases, and thus the maximum storage capacity is defined at a given temperature.[45] This occurs at a critical temperature when the transformation from α to β-phase continuously changes.[115] It is particularly noticeable that the temperature changes have a more negligible effect on hydrogen uptake for the five-element components, which could indicate a smaller dependence of the equilibrium pressure on temperature and was investigated with subsequent isothermal absorption measurements.

In order to better characterize the material with respect to its storage behavior, PCI curves were recorded after the time-dependent measurements. For this purpose, three isothermal hydrogen absorption measurements were performed at 400 °C, starting with a desorption isotherm followed by a cycle consisting of absorption and desorption. At this point, 400 °C was chosen to investigate the temperature dependency of the equilibrium pressure. In the literature, only one absorption isotherm at room temperature is given for the respective reference system, where the equilibrium pressure of the alloy is at the lower limit of the pressure transducers. Additionally, no information about the equilibrium pressure at higher temperatures

is given.[19, 21] It was also assumed that the kinetics at 400 °C would be sufficient to allow an acceptable time for the approximate equilibrium state to be reached since no information on the desorption kinetics was available at that time. In addition, with the increased temperature, the temperature dependence of the equilibrium pressure should be examined. The recorded PCI curves at 400 °C are shown in Figure 40, where the first desorption and the following cycle are marked as first absorption and second desorption, respectively. Furthermore, it should be mentioned at this point that not all curves could be recorded up to the same pressure since the air supply of the pneumatic valves was interrupted, and the measuring system consequently got stuck at the final or initial pressures shown.

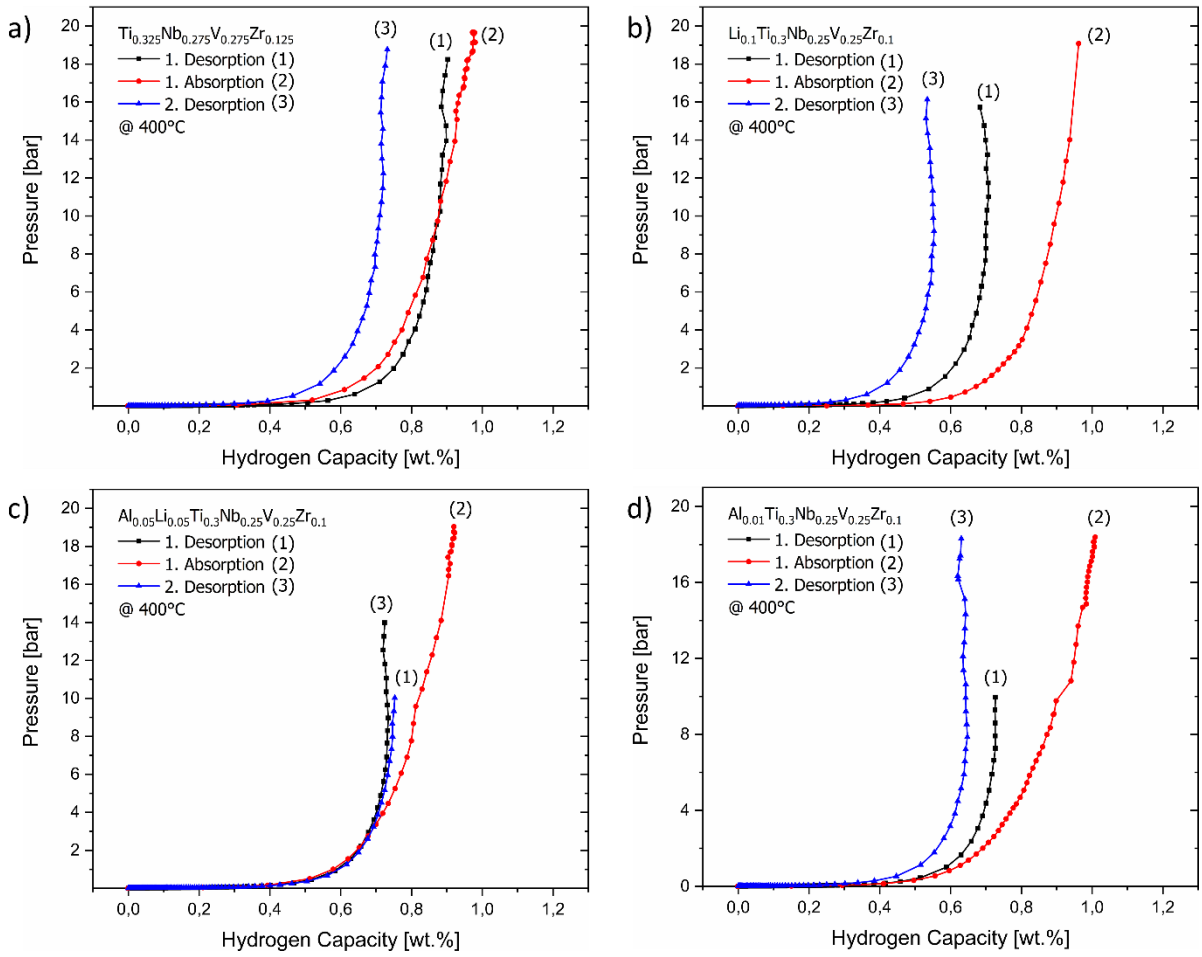

Figure 40: Absorption and desorption PCI measured at 400 °C: a) $Ti_{0.325}V_{0.275}Nb_{0.275}Zr_{0.125}$ b) $Li_{0.1}Ti_{0.3}V_{0.25}Nb_{0.25}Zr_{0.1}$ c) $Al_{0.1}Ti_{0.3}V_{0.25}Nb_{0.25}Zr_{0.1}$ d) $Al_{0.05}Li_{0.05}Ti_{0.3}V_{0.25}Nb_{0.25}Zr_{0.1}$.

The PCI curves obtained at 400 °C show a single hydrogen desorption and absorption plateau for all four alloys. One identified plateau indicates that a single-phase transformation mainly accompanies hydrogen uptake at the pressures studied. However, the equilibrium pressure at this point is still at the lower limit of the pressure transducer (10^{-3} bar) despite the temperature of 400 °C. Furthermore, the

pressure values fluctuate around -0.01 and 0.03 bar; therefore, the logarithmic plot is not reasonable and prevents the evaluation of the thermodynamic parameters using the van't Hoff plot and the evaluation of the temperature-dependent equilibrium pressure. Low equilibrium pressures indicate that in all four cases, very stable hydrides are formed based on the low-temperature dependency of the equilibrium pressure. Furthermore, it is striking that cycling at 400 °C leads to a loss of storage capacity except for the $Al_{0.05}Li_{0.05}Ti_{0.3}V_{0.25}Nb_{0.25}Zr_{0.1}$ alloy. The exact cause for this cannot be clarified, as this feature may be due to several reasons. The previously formed metal hydride may be too stable for dehydrogenation, leaving hydrogen stored in the solid phase during cycling and not further detectable as a pressure drop during re-hydrogenation. However, a comparison of the hydrogen uptake of the absorption isotherm at 400 °C and the hydrogen uptake determined as a function of time (cf. Figure 39) shows no significant difference. In both cases, the hydrogen uptake is about 0.9 wt.%, and at the same time, a reduced hydrogen release is measured for the second desorption isotherm. This speaks against a too-stable metal hydride because the second desorption isotherm should behave the same as the first one after one cycle. Accordingly, the loss due to bound hydrogen would also have been shown in advance in the first absorption isotherm in that a reduced hydrogen uptake would be measured in relation to the kinetic measurement. Furthermore, the equilibrium pressure can also play an important role. The equilibrium pressure can be far below the achievable vacuum, which cannot be reached by the used apparatus, whereby then a thermodynamic cause comes into consideration. The applied vacuum is insufficient to initiate dehydrogenation, or the kinetics are too slow at the pressure difference between equilibrium pressure and working pressure, which means that the given time for reaching the equilibrium state at each measurement point has not been sufficiently long. However, this could not be arranged due to time management. Otherwise, the measurements would require an unreasonable amount of time. In the end, the pressure sensors themselves could be a problem since they are not designed to determine such low pressures, which means that a high measurement variance is expected since the pressure for the hydrogen determination is directly included in the calculation. Considered together, the results of the desorption curves should be viewed with caution for the reasons stated above.

In order to address the issue of the different reasons for the loss of capacity, isothermal absorption measurements were subsequently performed at 33 °C, followed by thermal analyses and X-ray diffraction experiments. The corresponding PCI isotherms are shown in Figure 41.

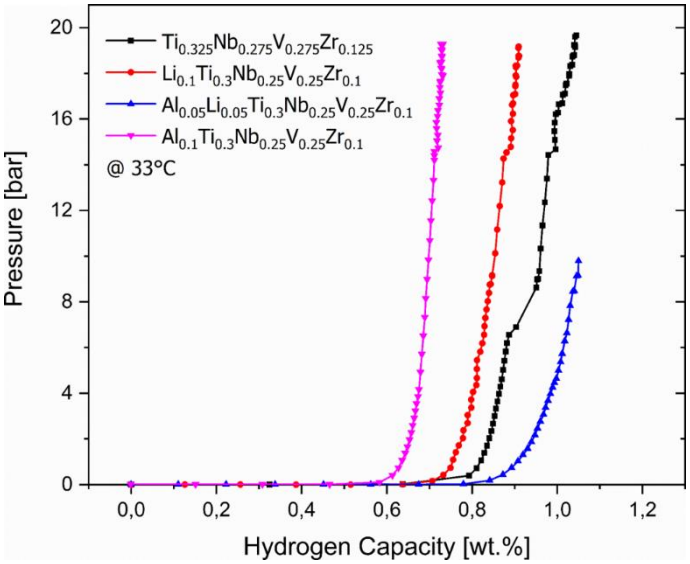

Figure 41: Absorption PCI measured at 33 °C for mechanically alloyed samples.

The isotherms recorded at 33 °C also show a single plateau at low equilibrium pressures in a range or below 10^{-2} bar. Except for the slight change in the quaternary sample characterized by a jump in the capacity from 6.8 to 8.6 bar, no unusual features of the isotherms can be observed. The maximum hydrogen capacity decreased for the samples relative to the initial capacity. Since for the $Al_{0.05}Li_{0.05}Ti_{0.3}V_{0.25}Nb_{0.25}Zr_{0.1}$ sample, the air pressure for the pneumatic valves failed, the recordings are compared at 10 bar. At 10 bar hydrogen pressure, the senary compound shows the highest uptake at 1.05 wt.% (H/M = 0.64) after 10 cycles. The quaternary alloy is close behind with 0.96 wt.% (H/M = 0.64), while uptake of 0.85 wt.% (H/M = 0.51) and 0.69 wt.% (H/M = 0.43) is measured for $Li_{0.1}Ti_{0.3}V_{0.25}Nb_{0.25}Zr_{0.1}$ and $Al_{0.1}Ti_{0.3}V_{0.25}Nb_{0.25}Zr_{0.1}$ alloy, respectively. Given the highest capacity at 10 bar, The PCI measurements give a first impression that the introduction of Al and Li has a beneficial influence on the gravimetric storage capacity. However, the H/M ratio suggests no significant difference in atomic occupation between the four-component and senar alloys. Consequently, it can be assumed that the gravimetric capacity is increased by decreasing the average molar mass of the alloy due to the introduction of lighter elements. However, it is not yet clear which cause, whether pulverization, phase separation or a too-stable hydride phase, is responsible for the decrease in storage capacity after cycling.

In order to investigate the phase segregation and the structural information of the hydride phase, the hydrogenated alloys were subsequently investigated by X-ray diffraction experiments. The obtained measured data with Pawley simulations are shown in Figure 42. To illustrate that the crystal structure of the alloys in the hydrogenated state is more challenging to differentiate and simulate, the respective

individual phases that contribute to the calculation of the envelopes are included with the quaternary compound as an example (cf. Figure 42a).

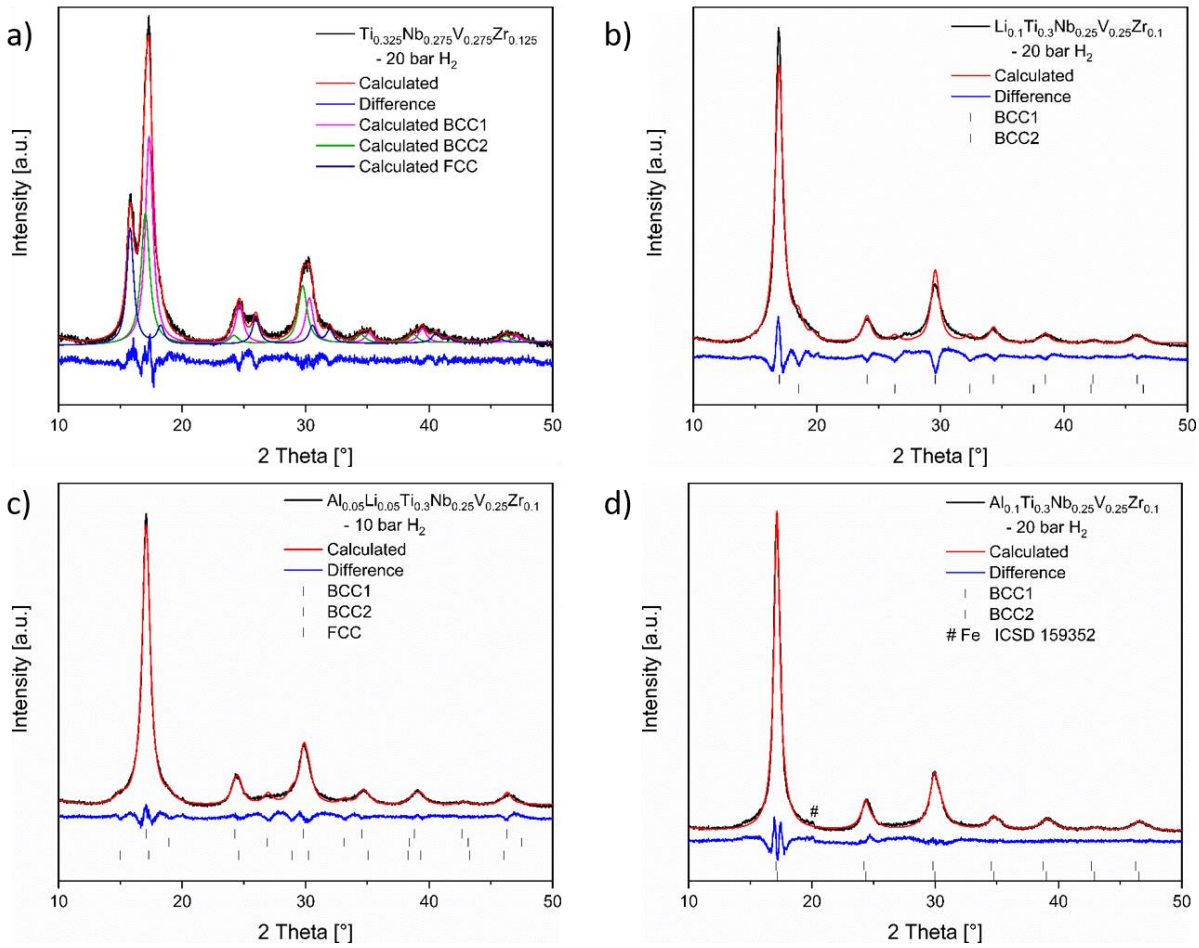

Figure 42: Powder XRD pattern of mechanically alloyed compounds (black) after hydrogen exposure during PCI measurement at 33 °C, related Pawley simulation (red) and corresponding difference curve (blue): a) $Ti_{0.325}V_{0.275}Nb_{0.275}Zr_{0.125}$ b) $Li_{0.1}Ti_{0.3}V_{0.25}Nb_{0.25}Zr_{0.1}$ c) $Al_{0.05}Li_{0.05}Ti_{0.3}V_{0.25}Nb_{0.25}Zr_{0.1}$ d) $Al_{0.1}Ti_{0.3}V_{0.25}Nb_{0.25}Zr_{0.1}$.

Simulation of the quaternary alloy required two *bcc* and one *fcc* phase to obtain a reasonable R_{wp} of 8.54. The measurement clearly shows a mixture of bcc and one fcc phase and indicates that different phases have formed in the alloy. One phase can be hydrogenated from *bcc* to *fcc* structure according to the mechanism described in the literature.[23] While for the two *bcc* phases an increased lattice parameter than the initial alloy is determined (cf. Table 9 and 11). The identified two phases, *bcc* and *fcc*, indicate incomplete hydrogenation. Another alloy composition also reported a similar behavior of reduced degree of hydrogenation. The material also consisted of a mixed phase of *bcc* and *fcc* after hydrogenation from the gas phase and indicated incomplete hydrogenation, but the authors gave no direct reason for the appearance of two phases.[58] However, it seems that two explanations can be considered. First, different particle sizes could be responsible for two identified phases, where the phase indicates a different degree of hydrogenation. A complete phase transition

from *bcc* to *fcc* corresponds to a H/M ratio of 2, whereas the expansion of the *bcc* lattice without symmetry change can be attributed to a lower degree of hydrogenation (~1 H/M). For the magnesium/magnesium hydride system, it has been reported that crystallite size (< 50 nm) can affect the enthalpy of formation. Thus, for crystallites smaller than 5 nm, an influence on the hydrogen absorption/desorption temperature was found for reversible hydrogen storage near room temperature, generally between 350 – 400 °C for bulk magnesium.[116-117] Accordingly, smaller particles of the present alloy may have enhanced hydrogen uptake and completed the mechanism from *bcc* to *fcc*. On the other hand, larger particles might be thermodynamically or kinetically hindered and only partially hydrogenated, as in the case of Mg. [116-117] The partially hydrogenated state is then reflected in an increased lattice parameter of the *bcc* phases but without phase transformation. Finally, different particle sizes may cause the two identified phases (*bcc*/*fcc*). Yet, the exact clarification requires further investigation with respect to the particle size distribution, which is generally expected to be broad in mechanically alloyed materials.[71]

On the other hand, a concentration gradient of the elements within the particles can also be responsible for the occurrence of different phases. For example, the chemical composition of the alloys determines the hydrogen storage properties and, thus, the degree of hydrogenation of the alloy. Accordingly, two phases can occur due to the different compositions, with one material composition having a higher degree of hydrogenation and undergoing the phase transformation from *bcc* to *fcc*. In comparison, the other material composition has a lower degree of hydrogenation reflected in a lattice parameter increase without symmetry change. The variant of the concentration gradient is also reasonable since dendritic structures were detected in the literature for the reference systems synthesized by arc melting, which showed apparent differences in their chemical composition.[107] Accordingly, cycling at elevated temperatures (~ 400 °C) could have driven the disproportionation of the materials studied here, resulting in different phases with different concentrations, exhibiting different hydrogenation properties.

Table 12: Overview of determined lattice parameter via Pawley simulations after hydrogenation at 33 °C.

Composition	Phase (Spacegroup)	Lattice parameter [Å]
$Ti_{0.325}V_{0.275}Nb_{0.275}Zr_{0.125}$	*bcc1* ($Im\bar{3}m$)	3.321(1)
	bcc2 ($Im\bar{3}m$)	3.381(1)
	fcc ($Fm\bar{3}m$)	4.460(1)
	fcc ($Fm\bar{3}m$)[a]	4.478(1)[a]
$Li_{0.10}Ti_{0.30}V_{0.25}Nb_{0.25}Zr_{0.10}$	*bcc1* ($Im\bar{3}m$)	3.401(1)
	bcc2 ($Im\bar{3}m$)	3.116(2)
$Al_{0.05}Li_{0.05}Ti_{0.3}V_{0.25}Nb_{0.25}Zr_{0.1}$	*bcc1* ($Im\bar{3}m$)	3.375(2)
	bcc2 ($Im\bar{3}m$)	3.049(2)
	fcc ($Fm\bar{3}m$)	4.712(3)
$Al_{0.10}Ti_{0.30}V_{0.25}Nb_{0.25}Zr_{0.10}$	*bcc1* ($Im\bar{3}m$)	3.378(3)
	bcc2 ($Im\bar{3}m$)	3.359(2)

a) Synthesized via arc melting from literature [107]

The lattice parameters determined in Table 12 also represent this for the alloys investigated. With the consideration of a second *bcc* phase, the asymmetry of the signals could be better simulated. However, this does not exclude the simultaneous presence of high stresses and strains within the crystallites and a crystal size distribution since these properties can all affect the shape of the reflections. Mechanically synthesized materials usually have many defects accompanied by high stresses and strains, which can also result in strong asymmetric to displaced reflections of the sample. However, determining the stresses and strains within the crystals requires further investigation. Nevertheless, an improved simulation could be achieved by introducing the additional *bcc* phase, which could indicate a concentration gradient within the particles. Local concentration gradients in the form of dendritic structures have been visualized for $Al_{0.10}Ti_{0.30}V_{0.25}Nb_{0.25}Zr_{0.10}$.[21] It was found that one dendritic region was zirconium rich, and the other zirconium poor. It is assumed that this difference in concentration leads to different lattice parameters since zirconium also has the largest atomic radius of the elements used. Further, it is assumed that the different concentrations led to different lattice parameters, as shown in other literature.[118-120] The observed lattice parameters of the *bcc* phases differ by 0.04 Å. However, since the deviation of the lattice parameters for the 4-component and aluminum-containing sample is also very small, it is assumed that

the effect of the local concentration deviation on the resulting lattice parameters is also small. To complicate the situation, these local concentration differences may also be of different orders of magnitude, leading to the enhanced asymmetry of the reflections. However, this needs to be further investigated using high-resolution imaging techniques, which is currently not possible due to the pyrophoric nature of the hydride particles and the unavailability of inert sample transfer equipment. These effects - local composition, stress and strain, crystallite size, and defect concentration - affect the resulting diffractogram but cannot be differentiated without complementary analytical techniques. Nevertheless, these results indicate the loss of storage capacity over the cycle number, in which the alloys could lose their chemical composition over the cycles, and consequently, the capacity is decreased.

After the volumetric measurements in the Sieverts apparatus, the materials were subjected to thermal analysis in the hydrogenated state to investigate the dehydrogenation properties of the hydride phase. In addition, the gravimetric method was used to check whether the previous volumetric measurements had been influenced by residual hydrogen. Accordingly, the previously hydrogenated samples were transferred to aluminum crucibles under an inert gas atmosphere and heated at a heating rate of 5 K min^{-1} up to 625 °C, and the exhaust gas stream was measured with a mass spectrometer for the detection of hydrogen. The measurement data obtained, mass in percentage, heat flow, and the correlated hydrogen signal are shown in Figure 43. Table 13 contains an overview of the significant parameters of the dehydrogenation properties, onset temperature, peak temperature, and the volumetric and gravimetric capacities for comparison of the two measurement methods. In brackets are the H/M ratios calculated with Equation 4.1.

Table 13: Volumetric and gravimetric analysis results and associated hydrogen storage performance.

Composition	H_2 uptake PCI[a] [wt.%] (H/M)	H_2 release TGA [wt.%] (H/M)	Onset temperature [°C]	Main peak temperature [°C]
$Ti_{0.325}V_{0.275}Nb_{0.275}Zr_{0.125}$	0.96 (0.64)	1.26 (0.84)	~ 226	288
$Li_{0.10}Ti_{0.30}V_{0.25}Nb_{0.25}Zr_{0.10}$	0.85 (0.51)	0.95 (0.57)	~ 120[b] ~230	305
$Al_{0.05}Li_{0.05}Ti_{0.3}V_{0.25}Nb_{0.25}Zr_{0.1}$	1.05 (0.64)	1.24 (0.77)	~ 230	285
$Al_{0.10}Ti_{0.30}V_{0.25}Nb_{0.25}Zr_{0.10}$	0.69 (0.43)	0.96 (0.6)	~ 230	318

a) Hydrogen uptake determined from the volumetric method at 10 bars after ten cycles b) First onset with lowered weight loss

When heating the samples to 625 °C, a multistage endothermic desorption process can be seen for all samples. Except for the 10% lithium-containing sample, all samples showed no mass loss up to the onset temperature at about 230 °C and a constant heating and hydrogen signal. After the maxima, a relatively steady hydrogen release is detected for all samples. Several reasons can be given for the more complex desorption characteristics. First, as described by Ek. et al., the desorption process depends on the local environment of the hydrogen atoms within the alloys, resulting in different activation energies depending on the locations of the atoms within the crystal, which can be reflected in the multiple steps.[62] Furthermore, the desorption temperature is dependent on the particle size, so the broad distribution of particles generated by ball milling directly influences the desorption profile.[36, 116] Finally, the change in microstructure due to disproportionation cannot be neglected since the elements' concentration gradients can influence the desorption properties.

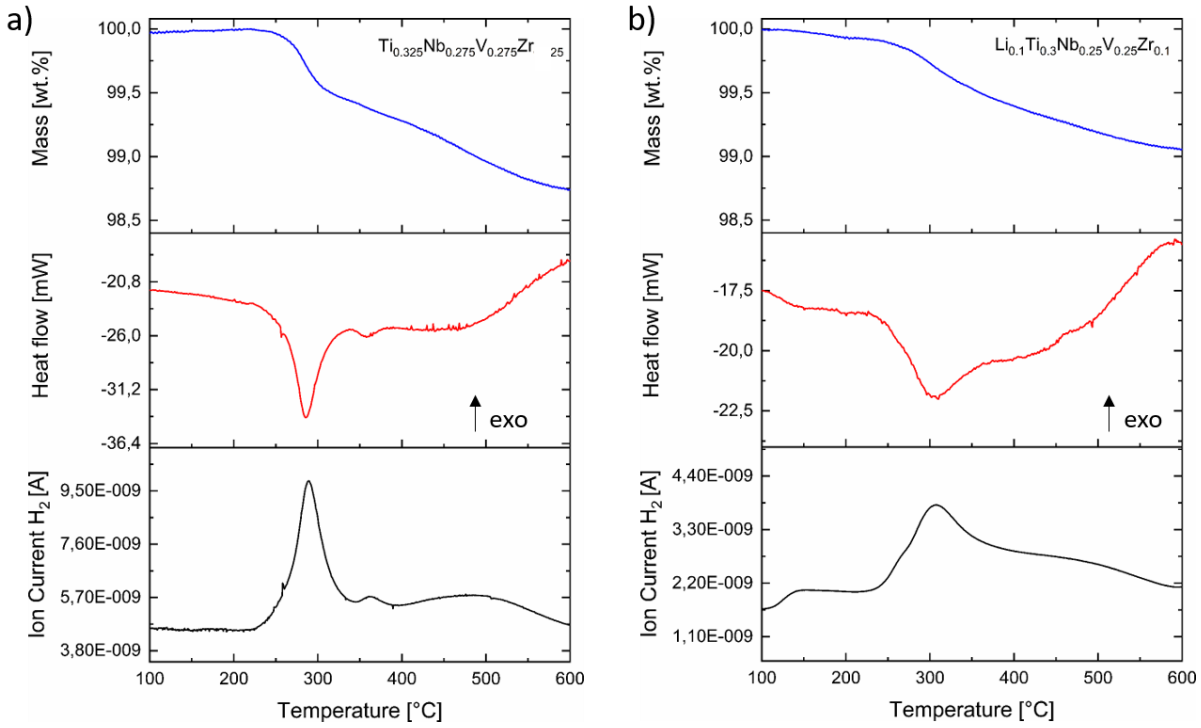

Figure 43: Thermal analysis of as hydrogenated alloys after 10 cycles; TGA weight loss profile (top), DSC heat flow (middle) and MS ion current of H_2 (bottom): a) $Ti_{0.325}V_{0.275}Nb_{0.275}Zr_{0.125}$ b) $Li_{0.1}Ti_{0.3}V_{0.25}Nb_{0.25}Zr_{0.1}$ c) $Al_{0.05}Li_{0.05}Ti_{0.3}V_{0.25}Nb_{0.25}Zr_{0.1}$ d) $Al_{0.1}Ti_{0.3}V_{0.25}Nb_{0.25}Zr_{0.1}$.

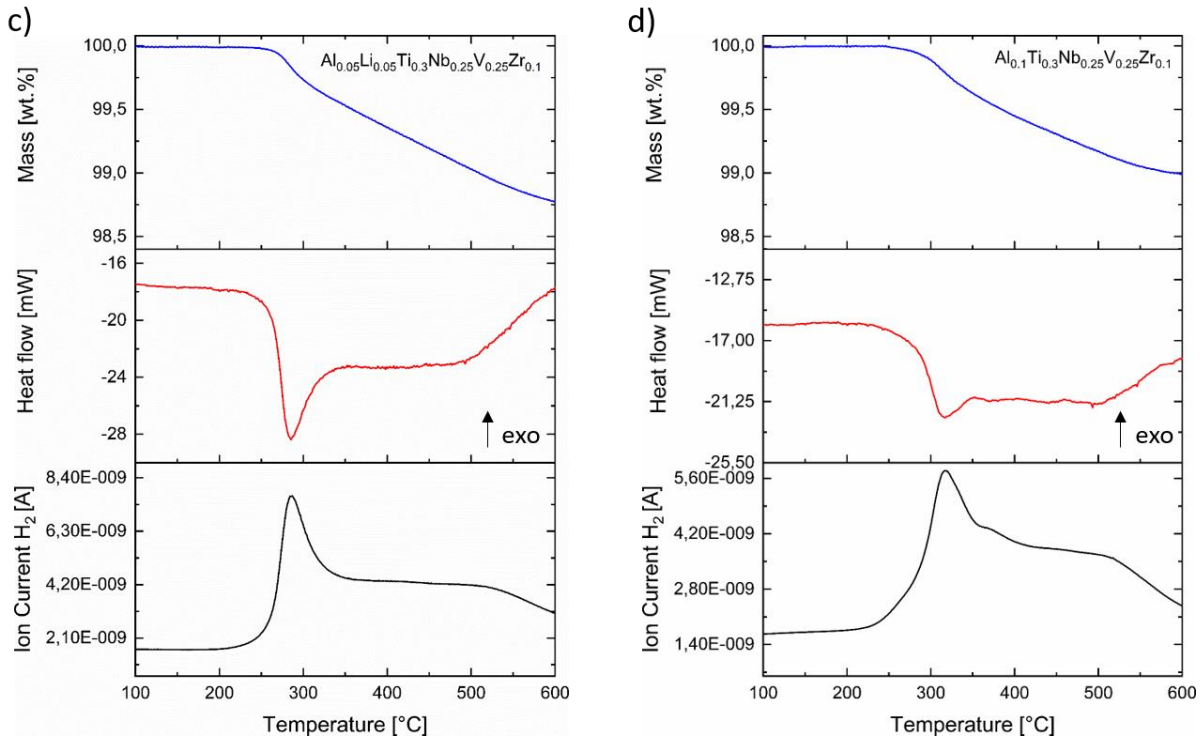

Figure 43: Thermal analysis of as hydrogenated alloys after 10 cycles; TGA weight loss profile (top), DSC heat flow (middle) and MS ion current of H_2 (bottom): a) $Ti_{0.325}V_{0.275}Nb_{0.275}Zr_{0.125}$ b) $Li_{0.1}Ti_{0.3}V_{0.25}Nb_{0.25}Zr_{0.1}$ c) $Al_{0.05}Li_{0.05}Ti_{0.3}V_{0.25}Nb_{0.25}Zr_{0.1}$ d) $Al_{0.1}Ti_{0.3}V_{0.25}Nb_{0.25}Zr_{0.1}$.

In addition, the thermal analysis results reveal that the volumetrically determined hydrogen uptakes differ from the gravimetric capacities. When heating the samples to 625 °C (limited by the melting point of the aluminum crucibles), it can be seen that all samples above 400 °C continue to release hydrogen. The continuous H_2 release above 400 °C suggests that 400 °C during dehydrogenation in the Sieverts apparatus was insufficient to fully dehydrogenate the samples, thus slightly affecting the volumetric measurements. Nevertheless, the maxima of hydrogen release are below 400 °C so the samples can be cycled under these conditions. The comparison of the gravimetric storage capacity to the storage capacities determined at the beginning of the time-dependent measurements indicates that in all four cases, the hydrogen uptake is degraded over the number of cycles (cf. Figure 39), possibly caused by the disproportionation of the samples as described above.

In order to obtain crystallographic information on the alloys in the dehydrogenated state after a total of 11 cycles (10.5 in Sieverts apparatus and 0.5 in TGA), the alloys were studied by X-ray diffraction experiments. The recorded diffractograms and the corresponding Pawley simulations are shown in Figure 44.

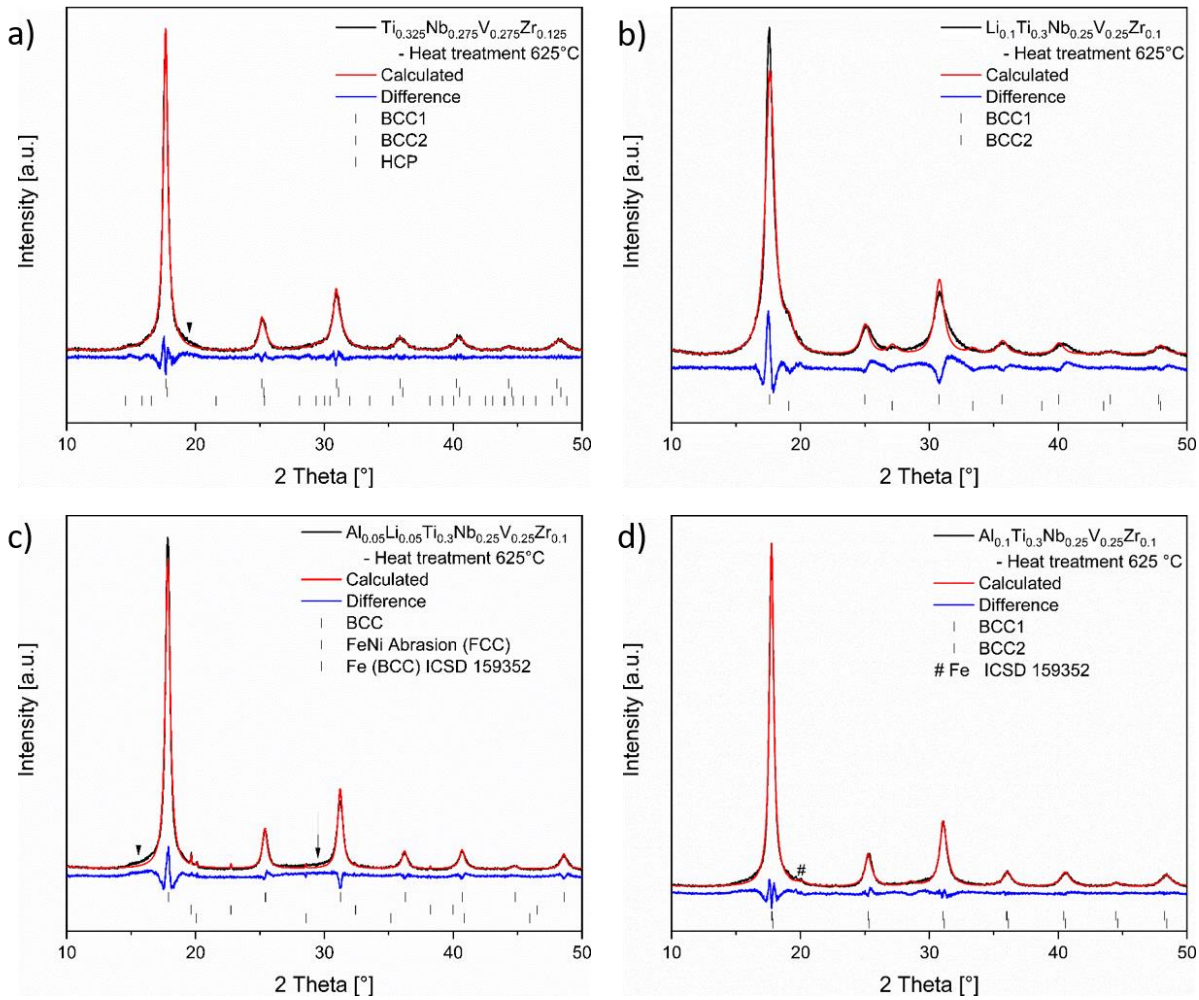

Figure 44: Powder XRD pattern of mechanically alloyed compounds (black) after 11 cycles, related Pawley simulation (red) and corresponding difference curve (blue): a) $Ti_{0.325}V_{0.275}Nb_{0.275}Zr_{0.125}$ b) $Li_{0.1}Ti_{0.3}V_{0.25}Nb_{0.25}Zr_{0.1}$ c) $Al_{0.05}Li_{0.05}Ti_{0.3}V_{0.25}Nb_{0.25}Zr_{0.1}$ d) $Al_{0.1}Ti_{0.3}V_{0.25}Nb_{0.25}Zr_{0.1}$.

After cycling, the X-ray diffraction patterns of the investigated alloys show apparent differences from the initial structure. Deviations from a single-phase bcc alloy can be identified in all four cases. The diffractograms of the alloys $Ti_{0.325}V_{0.275}Nb_{0.275}Zr_{0.125}$ and $Al_{0.10}Ti_{0.30}V_{0.25}Nb_{0.25}Zr_{0.10}$ have a slight asymmetry, which can be fitted with higher accuracy by introducing two *bcc* phases. The attempt to model the asymmetry of the sample via a size distribution function of the crystallites in the WPPM model was carried out with lower accuracy, which is reasonable due to a symmetric influence on the signal. However, it cannot be excluded that the samples are under substantial stress and strain. Stress and strain may also be responsible for the asymmetry and require further investigation. The introduction of the second *bcc* phase, for example, in the case of the aluminum-containing alloy, led to a reduction of the R_{wp} value from 11.59 to 8.07 and accordingly indicated two phases with different lattice parameters (cf. Table 14). At the same time, high-resolution imaging techniques would be

supportive of identifying the phase composition but were not possible at the present stage.

Table 14: Overview of determined lattice parameter via Pawley simulations after initial synthesis and after 11 cycles.

Composition	Initial Lattice parameter of pristine alloy [Å]	Lattice Parameters after 11 cycles [Å]
$Ti_{0.325}V_{0.275}Nb_{0.275}Zr_{0.125}$	3.2627(1)	3.2581(2) *bcc1* 3.239(2) *bcc2* a = 3.232(1) c = 5.147(1) *hcp*
$Li_{0.10}Ti_{0.30}V_{0.25}Nb_{0.25}Zr_{0.10}$	3.2831(4)	3.276(1) *bcc1* 3.024(1) *bcc2*
$Al_{0.05}Li_{0.05}Ti_{0.3}V_{0.25}Nb_{0.25}Zr_{0.1}$	3.2578(2)	3.2227(5) *bcc*
$Al_{0.10}Ti_{0.30}V_{0.25}Nb_{0.25}Zr_{0.10}$	3.2507(2)	3.245(1) *bcc1* 3.2353(7) *bcc2*

On the other hand, a dendritic microstructure has been observed for the two reference systems after the materials have been synthesized by arc-melting.[19, 21] Therefore, it is likely that over the long measurement times (3 – 4 weeks at 400 °C) during the volumetric measurements, the material has undergone phase separation. The phase separation can be observed more clearly in the sample containing 10 % lithium. The diffraction pattern shows a much more pronounced shoulder next to the primary reflection at about 19°, but the measurement data could be inadequately simulated even with two bcc phases. The right flanks at the 2nd (25°) and 3rd (31°) reflections continue to be inadequately described, which could be indicative of a third *bcc* phase but has not been investigated further since, for hydrogen storage, disproportionation is not considered to be beneficial to the lifetime as a storage material. In addition, the contribution of contamination by iron abrasion is marked in the figures. In the case of the quaternary alloy, the abrasion appears very broad, which can be caused by tiny crystallites or amorphized structures. In the case of the senary compound, on the other hand, small sharp reflections can be seen, indicating larger crystal domains consisting of the stainless steel of the grinding jar.

Furthermore, to describe the alloy of the four-component system crystallographically, an *hcp* structure was included in the simulation to describe the asymmetric background at 15° and 30° adequately. This background can also be recognized for the senary (marked with arrows) and aluminum compound, although, in the $Al_{0.10}Ti_{0.30}V_{0.25}Nb_{0.25}Zr_{0.10}$ sample, it is only slightly prominent. Considering the elements used (atomic radii: V 132 pm, Li 152 pm, Ti 147 pm, Nb 143 pm, Zr 162 pm) and the corresponding crystal structures and lattice parameters under normal conditions (V *bcc*, Li *bcc*, Ti *hcp*, Nb *bcc*, Zr *hcp*), it appears that zirconium may be responsible for the small contribution of the *hcp* phase. The lattice constant of the simulated *hcp* phase agrees very well with that of zirconium (a = 3.232 Å, b = 3.232 Å, c = 5.148 Å, ICSD 43700).[121] Consequently, the loss of zirconium from the solid solution could also be responsible for the reduced lattice constant of the dominant *bcc* phase. Finally, our notion is corroborated by literature reports. A hydrogen release-induced segregation process has also been identified for zirconium in other equimolar high entropy alloys. Above 12.5 % zirconium content within the alloys studied, phase separation into two *bcc* phases, one zirconium rich and one zirconium poor, was observed after dehydrogenation. It was found that the release of the incorporated hydrogen even induces this because no phase separation was observed in stability tests without dehydrogenation at 1200 °C for 24 hours.[64]

Accordingly, the segregation process in the alloys studied here could be similar. The cycling has driven the disproportionation of the initially disordered solid solution, resulting in two phases with a *bcc* structure and segregated zirconium. However, the disproportionation is more pronounced for the 10 % lithium-containing alloy, evident from the increased intensity and the strongly deviating lattice parameter of the second *bcc* phase, and is comparable to vanadium (ICSD 171003) when the lattice parameters are taken into account. At the same time, the broad main reflection overlaps with those of zirconium, which means that the latter cannot be identified directly.

6.2. Reactive Milled Samples

The previous chapter has shown that the mechanically alloyed materials were only partially hydrogenatable from the gas phase under the selected reaction conditions. A similar observation was also demonstrated in the work of Zepon et al. It was observed that the mechanically alloyed high entropy alloy $MgZrTiFe_{0.5}Co_{0.5}Ni_{0.5}$ was only partially hydrogenatable, characterized by a mixed phase of *bcc* and *fcc*.[58] Reactive milling, on the other hand, resulted in a complete phase change, consistent with the described mechanism of *bcc* alloys to *fcc*/*bct* metal hydride upon hydrogenation. Accordingly, this chapter aimed to investigate whether reactive milling could hydrogenate the selected alloy compositions to a higher degree. Furthermore, it should be checked whether a phase transition into the previously described *bcc* structure (cf. Chapter 6.1.1.) can be expected after dehydrogenation of the *fcc* phase. Thus, in the following, the results concerning the synthesis and the results of the hydrogen storage properties are presented.

6.2.1. Synthesis of Reactive Milled Samples

The reactive milling was carried out with a planetary ball mill under a 30 bar hydrogen atmosphere. Specially designed stainless steel high-pressure grinding jars were used for this purpose. The grinding process consisted of 30 minutes of milling at 600 rpm with a subsequent 10 minute break. In order to observe the progress of the synthesis, tracking experiments were carried out. For this purpose, the milling process was stopped after 2 hours, and a sample was taken for X-ray diffraction experiments. Further samples were then taken after a time interval of one hour, and 30 bar hydrogen was added to the autoclave after each sampling and at the beginning of the synthesis. The X-ray diffraction patterns obtained are shown in Figure 45 for the respective sample and process time.

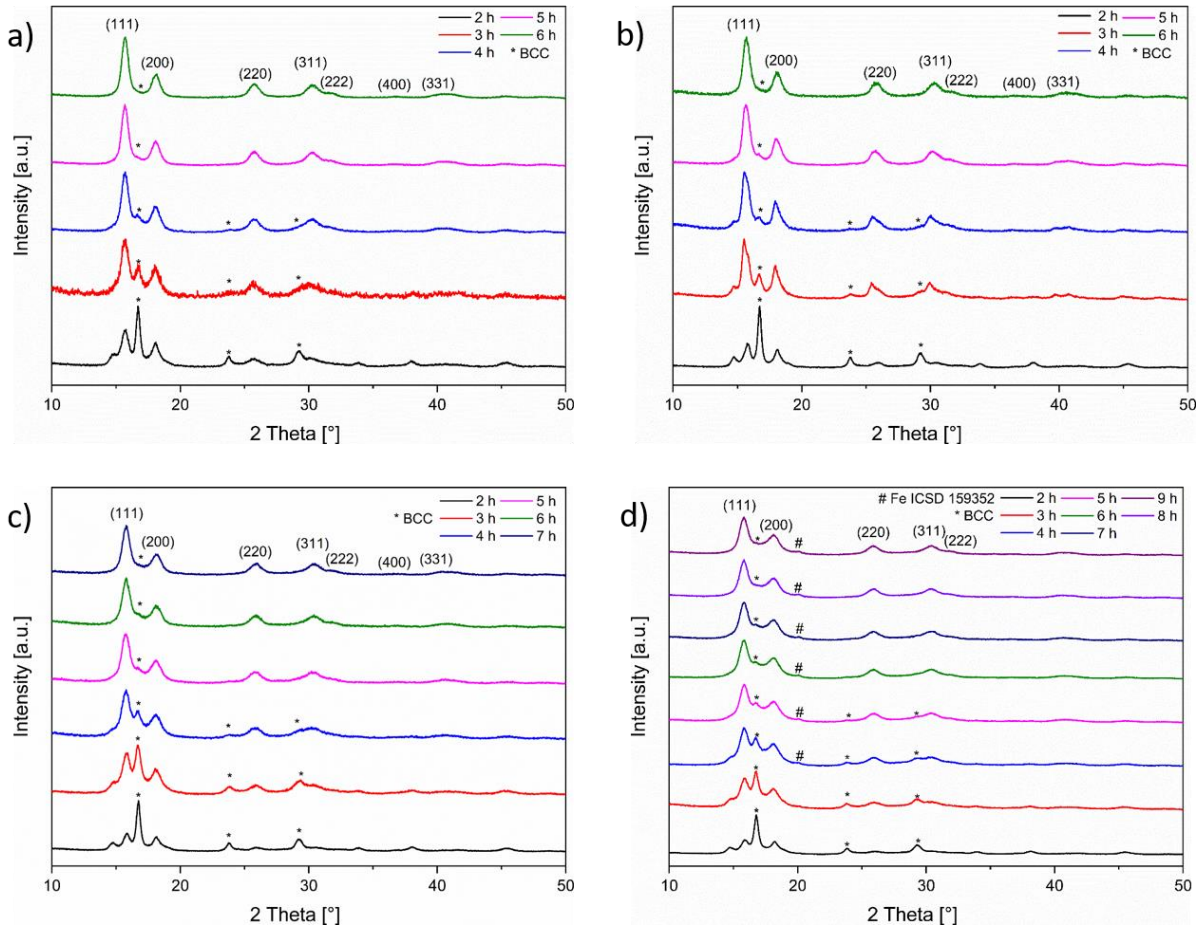

Figure 45: XRD pattern of reactive milled HEAs after different milling times: a) $Ti_{0.325}V_{0.275}Nb_{0.275}Zr_{0.125}$ b) $Li_{0.1}Ti_{0.3}V_{0.25}Nb_{0.25}Zr_{0.1}$ c) $Al_{0.05}Li_{0.05}Ti_{0.3}V_{0.25}Nb_{0.25}Zr_{0.1}$ d) $Al_{0.1}Ti_{0.3}V_{0.25}Nb_{0.25}Zr_{0.1}$.

The entire alloying process was followed for 6 – 9 h, depending on how far the formation of the expected *fcc* phase had progressed. From the diffraction patterns, different characteristics of hydride formation can be seen. First, it should be emphasized that after 2 h of process time, a relatively similar diffraction pattern can

be seen for all four samples. The first feature can be identified by the reflection at about 14.8°. This reflection can be assigned to the zirconium hydride phase (ICSD 24624), and its intensity decreases with increasing process time. After 5 h of process time, the contribution of the zirconium hydride phase is no longer observed, which can be explained by incorporating the zirconium hydride into the alloy. At the beginning after 2 hours, besides the ZrH_2 phase, the contribution of a *bcc* phase marked with the asterisk and an *fcc* phase marked by the crystal planes can be observed. Nevertheless, the intensity of the *bcc* phase decreases steadily, and in the same course, the *fcc* structure increases. According to the diffraction pattern, it can thus be assumed that a *bcc* alloy is formed within the first 2 hours. However, the positions of the primary reflections are shifted to smaller angles compared to the mechanically alloyed samples (e.g., for $Ti_{0.325}V_{0.275}Nb_{0.275}Zr_{0.125}$ from 17.66° to 16.7°). The shifting reflections indicate that the *bcc* phase has an enlarged lattice cell, which can be explained by hydrogen uptake during the first 2 hours. The identified *fcc* phase suggests that partial sample volume has been hydrogenated to the extent that phase transformation from the *bcc* to *fcc* phase has occurred. In addition, it can be noted that the zirconium hydride can be incorporated into the solid solution at a delayed rate. Consequently, it could be assumed that with advanced hydrogenation and the accompanying phase transformation into the *fcc* phase, the uptake of zirconium hydride is also favored due to the same crystal structures. Interestingly, it can also be seen from the intensities that the aluminum-containing compounds exhibit an increased ratio of maximum intensity from the *bcc* to the emerging *fcc* phase, which also persists longer over the processing time compared to the samples without aluminum. With 10 % aluminum, a higher intensity of the *bcc* phase can still be seen after 7 hours, compared to the 5 % Al-containing sample. This could be attributed to the hydrogenation properties of aluminum. Aluminum hydride has a slightly negative enthalpy of formation of -9.9 kJ mol^{-1}, resulting in a positive Gibbs free energy of 48.5 kJ mol^{-1} at room temperature, and therefore, formation is not favored under standard conditions.[122] Consequently, the results indicate that aluminum impedes hydrogen uptake during reactive milling. Accordingly, the aluminum-containing compounds also had to be milled for longer to hydrogenate the remaining parts of the *bcc* phase and observe the accompanying phase transformation. In order to identify the final lattice parameters, the final products were simulated using the Pawley method, and the data obtained are shown in Figure 46.

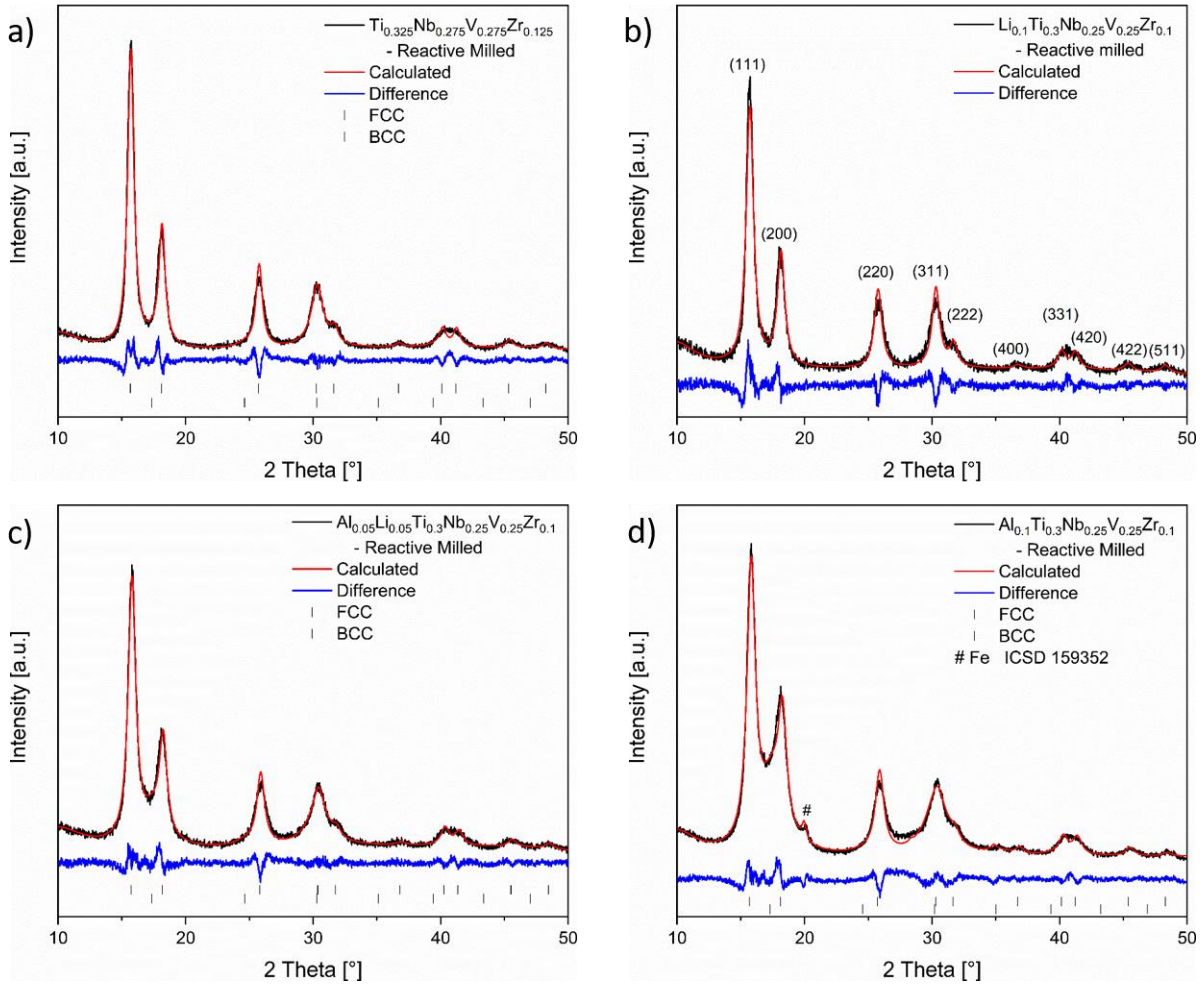

Figure 46: Powder XRD pattern of reactive milled compounds (black) after initial synthesis, related Pawley simulation (red) and corresponding difference curve (blue): a) $Ti_{0.325}V_{0.275}Nb_{0.275}Zr_{0.125}$ b) $Li_{0.1}Ti_{0.3}V_{0.25}Nb_{0.25}Zr_{0.1}$ c) $Al_{0.05}Li_{0.05}Ti_{0.3}V_{0.25}Nb_{0.25}Zr_{0.1}$ d) $Al_{0.1}Ti_{0.3}V_{0.25}Nb_{0.25}Zr_{0.1}$.

Except for the 10% lithium-containing alloy, all compounds were simulated with two phases consisting of *bcc* and *fcc*. Due to the strong signal-to-noise ratio, the lithium sample was more challenging to simulate with two phases, so it was simulated with one *fcc* phase, but the presence of a residual *bcc* cannot be excluded at this point. Nevertheless, the simulations and the measured data indicate that the products are composed of two phases since the separation of the first two reflections of the *fcc* phase is hindered in all 4 cases by an occurring background due to the residual *bcc* phase. At the same time, it is noted that the background between the first two reflections increases with aluminum concentration, indicating an increased fraction of the residual *bcc* phase. An increased *bcc* fraction indicates decreased hydrogen uptake, as less sample volume follows the phase transformation from *bcc* to *fcc*. This is consistent with the decreased hydrogen uptake due to the increased aluminum content. The lattice parameters obtained are listed in Table 15.

Table 15: Lattice parameters of reactive milled HEAs determined with the Pawley method and the corresponding literature values.

Composition	Phase (Spacegroup)	Lattice parameter [Å]	Reference
$Ti_{0.325}V_{0.275}Nb_{0.275}Zr_{0.125}$	*fcc* ($Fm\bar{3}m$)	4.508(1)	Present work
	bcc ($Im\bar{3}m$)	3.326(1)	Present work
	fcc ($Fm\bar{3}m$)	4.478(1)[a]	[109]
$Li_{0.10}Ti_{0.30}V_{0.25}Nb_{0.25}Zr_{0.10}$	*fcc* ($Fm\bar{3}m$)	4.511(1)	Present work
$Al_{0.05}Li_{0.05}Ti_{0.3}V_{0.25}Nb_{0.25}Zr_{0.1}$	*fcc* ($Fm\bar{3}m$)	4.491(1)	Present work
	bcc ($Im\bar{3}m$)	3.325(2)	Present work
$Al_{0.10}Ti_{0.30}V_{0.25}Nb_{0.25}Zr_{0.10}$	*fcc* ($Fm\bar{3}m$)	4.505(1)	Present work
	bcc ($Im\bar{3}m$)	3.334(1)	
	bct (I4/mmm)	a = 3.137(1)[a]	[109]
		c = 4.374(1)	

a) synthesized by arc-melting

From the simulations, it can be summarized that the alloys are multiphase as *bcc* and *fcc* after the entire process time, whereby the *bcc* phase can be considered as a minority due to the lower intensity. The determined lattice parameters are all in a similar order of magnitude. However, no direct statement on the successful synthesis with lithium can be made based on the lattice parameters since different hydrogen concentrations could influence all. The lattice parameter of the 4-component reference system from the literature differs slightly and can be due to the different processing using arc melting, the subsequent dendritic structure, or even the multiphase system presented in this work, but it cannot be clarified here. As a final feature, the XRD measurements as a function of process time (c.f. Figure 45) clearly show that the intensity of the *fcc* phase increases as the process progresses. An increasing *fcc* phase is associated with a higher degree of hydrogenation. Given the previously investigated solid-gas reactions on the mechanically alloyed samples (cf. Chapter 6.1.2.), where no or only partial phase transformation from *bcc* to *fcc* was observed, it can be concluded that the addition of mechanical energy favors the incorporation of hydrogen into the alloy. The favoring of hydrogen uptake by mechanical influence is also described for another system in the literature.[58] This also suggests that the hydrogen content could increase as the process progresses, but this depends on the probability of each sample volume being exposed to the mechanical impacts.

In addition, the morphology of the particles was investigated using SEM images and micrographs in Figure 47 to serve as an overview.

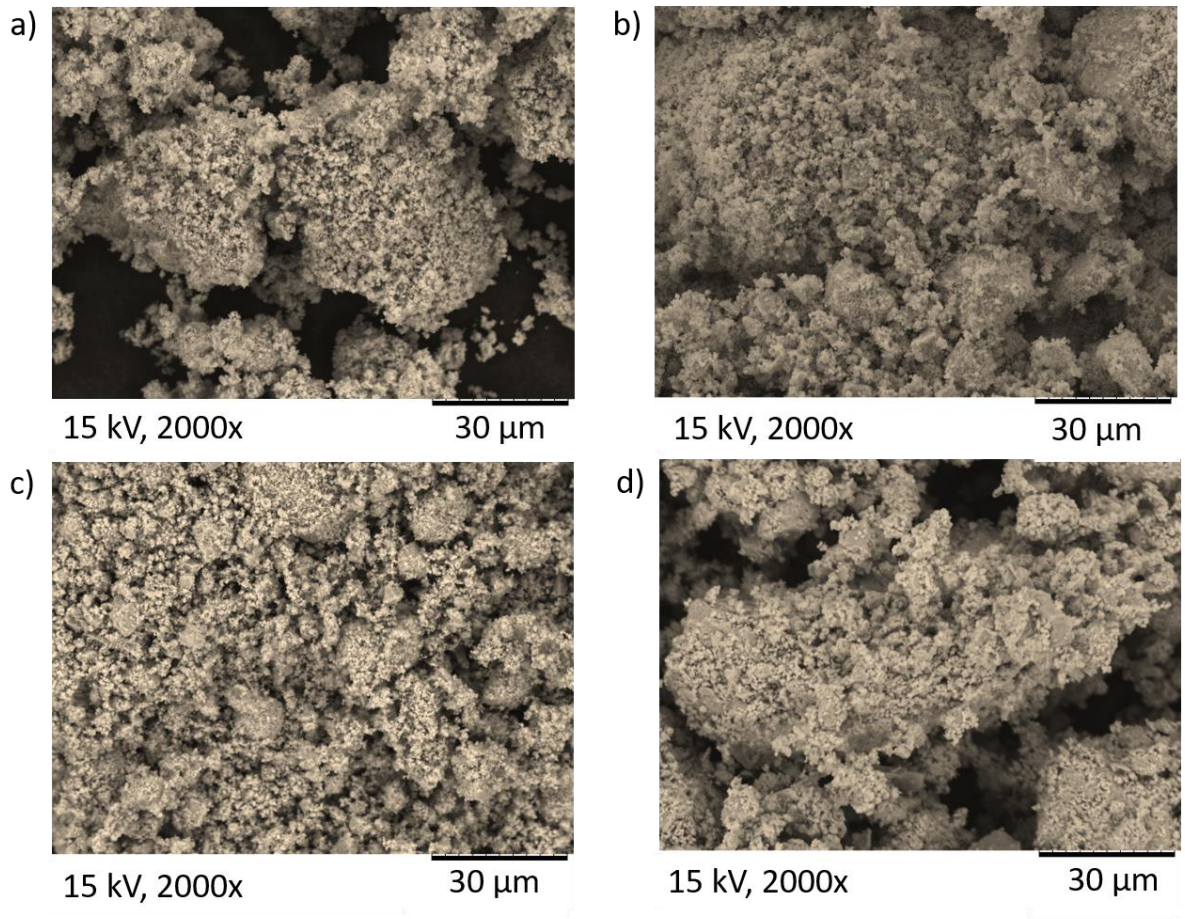

Figure 47: SEM micrographs: a) $Ti_{0.325}V_{0.275}Nb_{0.275}Zr_{0.125}$ b) $Li_{0.1}Ti_{0.3}V_{0.25}Nb_{0.25}Zr_{0.1}$ c) $Al_{0.05}Li_{0.05}Ti_{0.3}V_{0.25}Nb_{0.25}Zr_{0.1}$ d) $Al_{0.1}Ti_{0.3}V_{0.25}Nb_{0.25}Zr_{0.1}$.

All images show a particle bed ranging from several hundred nanometers to several micrometers. It is striking that the particle sizes do not show any significant differences concerning their compositions, as it occurred for the mechanically alloyed samples (cf. Figure 36). All four samples consist predominantly of agglomerates composed of relatively small particles, although larger agglomerates can be seen. The mechanical properties of the hydrides can explain the increased occurrence of small particles. As the XRD results have already indicated, hydrogenation of the metals takes place within the first 2 h of reactive milling, and it is also known that metal hydrides exhibit reduced ductility.[123] Furthermore, it is known that the milling of brittle materials leads to smaller particles.[71] Accordingly, it can be concluded that during the milling process under a hydrogen atmosphere, particle size reduction is favored, in which the metal and alloys are hydrogenated in the initial stage and consequently change their mechanical properties, which is consistent with the time-resolved tracking experiments. In addition, the shape of the particles supports the

assumption of the more brittle materials since they are not flattened, as is the case for ductile materials.[71] It is also noted that even with different process times of 6 – 9 h, the samples do not show a significant difference in the particle size, indicating that fragmentation and coalescence seem balanced.

Additionally, SEM-EDX analyses were performed on the samples to verify the chemical composition. As an example, the results of the $Li_{0.10}Ti_{0.30}V_{0.25}Zr_{0.10}Nb_{0.25}$ alloy with the respective individual mappings and the summed energy-dispersive spectrum are shown in Figure 48.

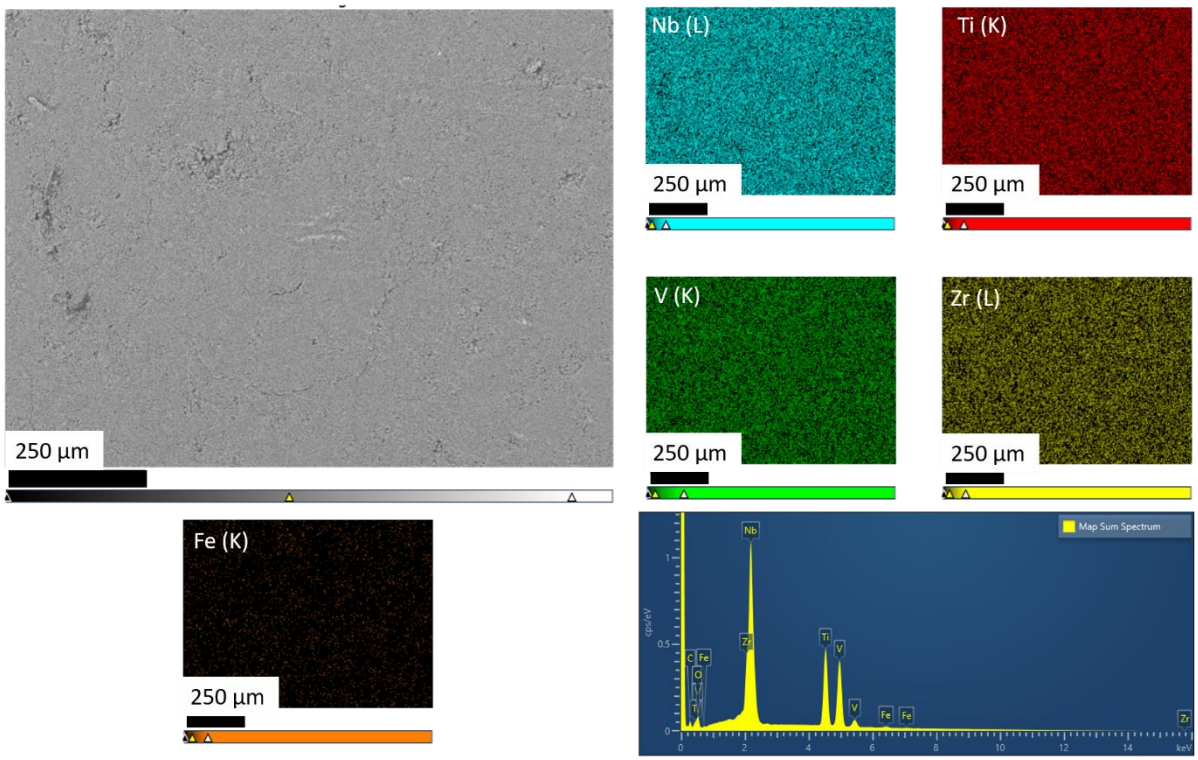

Figure 48: SEM micrograph of $Li_{0.1}Ti_{0.3}V_{0.25}Nb_{0.25}Zr_{0.1}$ sample with corresponding individual EDX mappings and energy dispersive spectrum.

As the individual element distributions show, all detectable elements are uniformly distributed over the investigated range. This supports the XRD results that a multicomponent solid solution consisting of the elements used has been synthesized. However, high-resolution imaging techniques should be used in addition to investigating the elemental distribution in more detail and simultaneously localizing the lithium in the alloys. Furthermore, no significant inhomogeneities of the elemental distributions are identified, supporting the assumption that the two identified phases in the XRD analyses must originate from different hydrogen concentrations within the alloy. The quantitative results determined from the sum spectrum as well as the individual mappings of the individual samples are attached (c.f. Appendix 9.7). From there, it can be concluded that the ratios of the individual

elements agree well with the nominal ratios used. In order to summarize these results, the overlays of the individual mappings and the corresponding micrograph are shown in Figure 49.

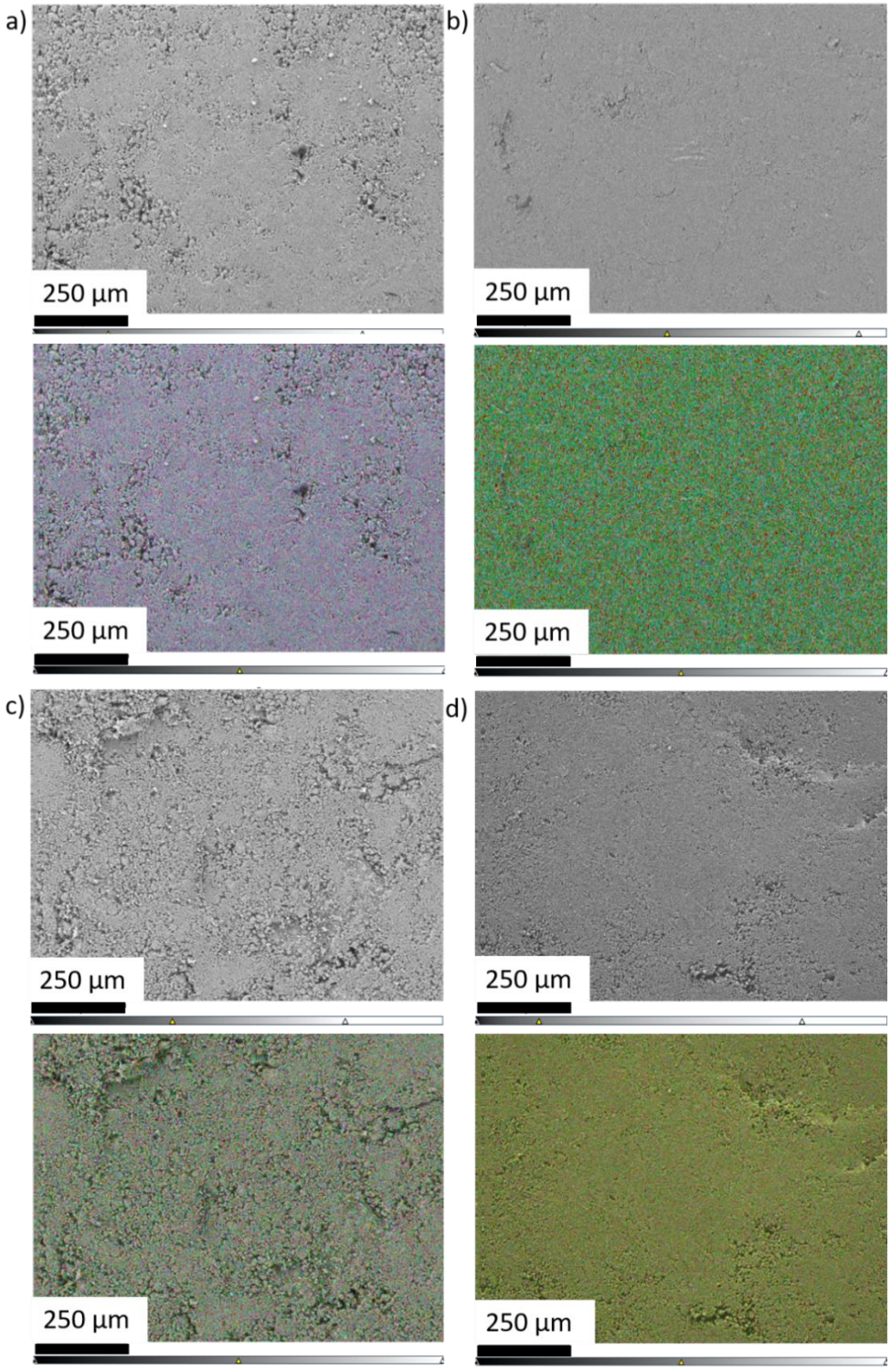

Figure 49: SEM micrographs and corresponding elemental mapping overlay: a) $Ti_{0.325}V_{0.275}Nb_{0.275}Zr_{0.125}$ b) $Li_{0.1}Ti_{0.3}V_{0.25}Nb_{0.25}Zr_{0.1}$ c) $Al_{0.1}Ti_{0.3}V_{0.25}Nb_{0.25}Zr_{0.1}$ d) $Al_{0.05}Li_{0.05}Ti_{0.3}V_{0.25}Nb_{0.25}Zr_{0.1}$.

In addition, ICP-OES experiments were performed on the samples to assess the chemical composition of lithium content. The compositions obtained are shown in Table 16.

Table 16: Metal contents determined by ICP-OES of alloys synthesized by reactive milling.

Sample	Al at.%	Li at.%	Ti at.%	V at.%	Nb at.%	Zr at.%
$Ti_{0.325}V_{0.275}Nb_{0.275}Zr_{0.125}$	-	-	33.87	27.07	25.33	13.71
$Li_{0.1}Ti_{0.3}V_{0.25}Nb_{0.25}Zr_{0.1}$	-	9.60	28.29	24.98	27.24	9.86
$Al_{0.1}Ti_{0.3}V_{0.25}Nb_{0.25}Zr_{0.1}$	9.78	-	30.79	24.73	22.89	11.79
$Al_{0.05}Li_{0.05}Ti_{0.3}V_{0.25}Nb_{0.25}Zr_{0.1}$	4.81	5.16	30.71	24.67	24.97	9.67

Like the mechanically alloyed samples, the results of the ICP-OES analysis show no significant deviations from the nominal concentrations. Therefore, in conjunction with the XRD, EDX, and ICP-OES analyses, it can be assumed that the metal hydrides have been successfully synthesized, although the XRD analyses have shown that they consist of two phases, which is possibly due to the hydrogen concentration. It should also be noted that the reactive milling process favored hydrogen uptake and led to the phase transformation from *bcc* to *fcc*, typical for *bcc* metal upon hydrogenation.

6.2.2. Hydrogen Storage Properties of Reactive Milled Samples

Since the materials were in the hydrogenated state after reactive milling, the desorption behavior was investigated with thermal analysis. For this purpose, the hydrides were transferred into aluminum crucibles under an argon atmosphere and then measured on the TGA-DSC module coupled with MS. In order to apply the Kissinger method, different heating rates (2, 5, 10, 15, and 20 K min^{-1}) were used, and the mass losses were averaged over the number of measurements. For overview purposes, Figure 50 first shows the measurement data obtained with a heating rate of 5 K min^{-1}.

As shown in Figure 50, the curves for all four samples over the temperature range from 150 °C to about 500 °C show a multistep endothermic process. The weight decrease and the heating flow correlate very well with the hydrogen signal recorded in the MS, supporting that the dehydrogenation must proceed via a multistep desorption process. Interestingly, the desorption profiles of the $Ti_{0.325}V_{0.275}Nb_{0.275}Zr_{0.}125$ and $Al_{0.05}Li_{0.05}Ti_{0.3}V_{0.25}Nb_{0.25}Zr_{0.1}$ alloys look very similar. The desorption starts at an onset temperature of 150 °C and then increases steadily to the maximum desorption peak, 250 °C and 258 °C, respectively. After the peak, the hydrogen desorption rate decreases steadily, and around 600 °C, the weight loss is no longer observed. The desorption profile of the 10% lithium-containing sample deviates slightly. The heat flow signal also initially shows an onset temperature of 150 °C and then decreases steadily to the first local minimum at about 200 °C. With further heating up to 245 °C, a sharp minimum in the heat flow signal is observed, accompanied by an increased weight loss. Subsequently, as with the other two samples, the hydrogen signal steadily decreases, and the weight loss ceases at 600 °C. In contrast to the other samples, the desorption profile of the $Al_{0.1}Ti_{0.3}V_{0.25}Nb_{0.25}Zr_{0.1}$ alloy is different in that three maxima can be identified during desorption. The onset temperature is also initially at 150 °C, but the hydrogen signal rises steeply towards the first local maximum at 190 °C. After this, both the heat flow and the hydrogen signal decrease slightly, and a second maximum of the heat flow and hydrogen signal is reached at 260 °C. Subsequently, a third maximum can be seen at about 360 °C. Interestingly, the mass loss of the aluminum-containing sample also behaves differently. None of the maxima observed correlate with a sudden mass loss as measured for the other samples. The mass loss of the aluminum sample is uniform over the entire measured temperature curve and correlates with the very broad hydrogen signal.

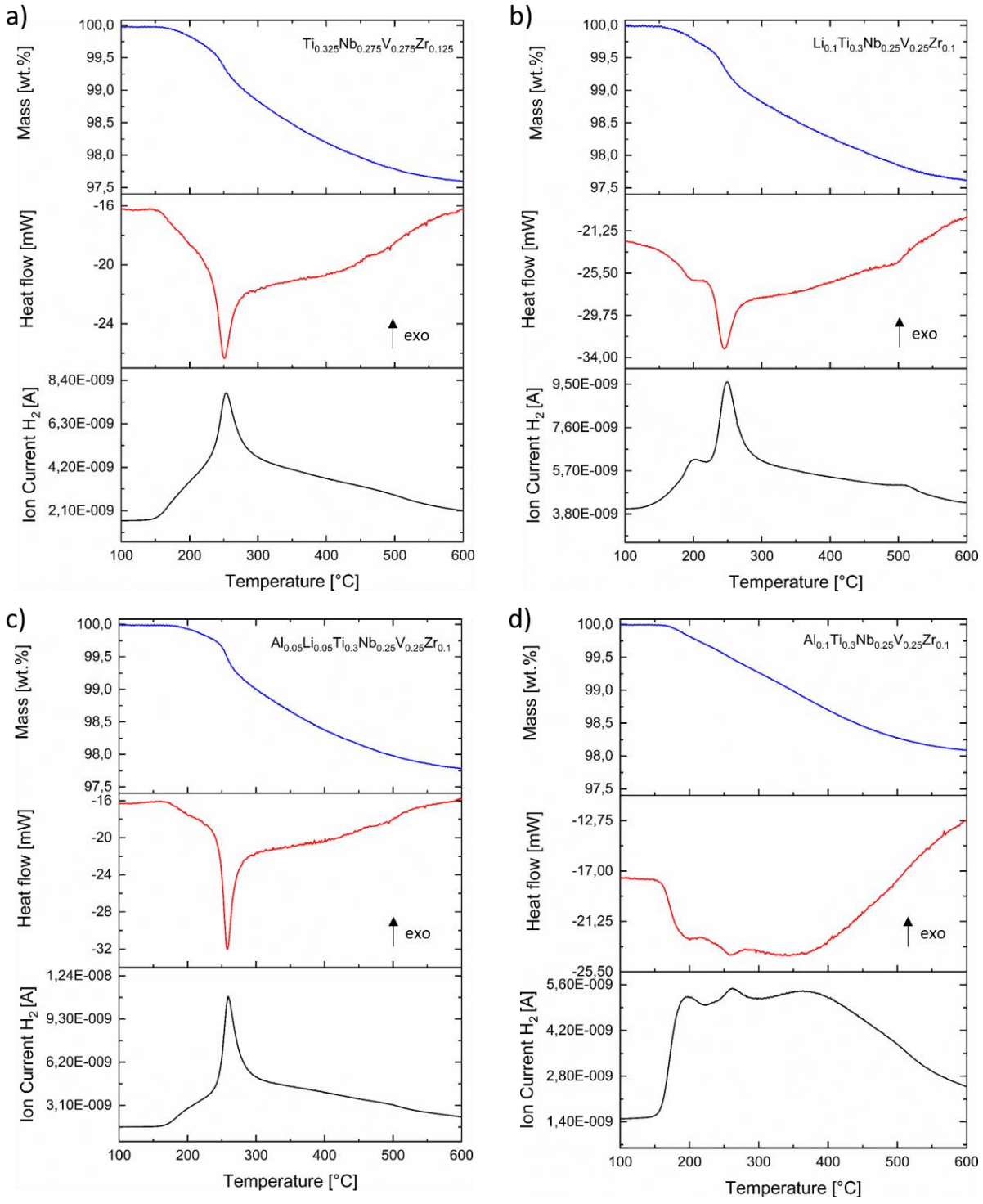

Figure 50: Thermal analysis of reactive milled alloys after synthesis; TGA weight loss profile (top), DSC heat flow (middle) and MS ion current of H_2 (bottom): a) $Ti_{0.325}V_{0.275}Nb_{0.275}Zr_{0.125}$ b) $Li_{0.1}Ti_{0.3}V_{0.25}Nb_{0.25}Zr_{0.1}$ c) $Al_{0.05}Li_{0.05}Ti_{0.3}V_{0.25}Nb_{0.25}Zr_{0.1}$ d) $Al_{0.1}Ti_{0.3}V_{0.25}Nb_{0.25}Zr_{0.1}$.

The significant parameters, such as mass loss, onset temperature, and peak temperature, are summarized in Table 17. The mass loss in wt.% represents an average of the measurements and is given with the standard deviation. The onset and peak temperatures were determined from measurements at a heating rate of 5 K min^{-1}. The H/M ratios are calculated via formula 4.1.

Table 17: Hydrogen desorption properties of reactive milled samples determined from thermal analysis.

Composition	H_2 release TGA [wt.%]	H_2 release TGA H/M	Onset temperature [°C]	Main peak temperature [°C]
$Ti_{0.325}V_{0.275}Nb_{0.275}Zr_{0.125}$	2.40 ± 0.16	1.63	~ 150	251
$Li_{0.10}Ti_{0.30}V_{0.25}Nb_{0.25}Zr_{0.10}$	2.59 ± 0.22	1.59	~ 150	245
$Al_{0.05}Li_{0.05}Ti_{0.3}V_{0.25}Nb_{0.25}Zr_{0.10}$	2.47 ± 0.14	1.54	~ 150	258
$Al_{0.10}Ti_{0.30}V_{0.25}Nb_{0.25}Zr_{0.10}$	2.00 ± 0.14	1.26	~ 150	190[a)] 260[b)]

a) 1.Maxima b) 2.Maxima

Based on the hydrogen release shown in Table 17, the first trend can be seen in which the incorporation of lithium has a positive effect on the gravimetric storage capacity. The increase in gravimetric storage capacity is explained by the lower average molecular weight of the alloy associated with the incorporation of lithium, the lightest element of the metals used. Consequently, for the $Li_{0.10}Ti_{0.30}V_{0.25}Nb_{0.25}Zr_{0.10}$ alloy, an initial superior hydrogen storage capacity of ~2.6 wt.% is determined, followed by the 6-component alloy with ~2.5 wt.%. For the $Ti_{0.325}V_{0.275}Nb_{0.275}Zr_{0.125}$ alloy, a gravimetric capacity of 2.4 wt.% has been determined. This capacity is in good agreement with the capacity of the reactive milled sample from the literature.[19] Only the 10% aluminum-containing compound deviates more strongly with a capacity of ~2.00 wt.%. In contrast, a value of 2.6 wt.% is given in the literature.[21] Nevertheless, the reference system from the literature was synthesized by arc melting and should generally have different properties. In addition, the XRD experiments show an increased residual *bcc* content in the sample investigated in the present work, which can also explain the reduced capacity since a residual *bcc* phase should reflect a reduced hydrogen concentration.

In contrast, based on the H/M ratio shown in Table 17, no trend can be observed regarding the positive contribution to the hydrogen capacity by incorporating lithium. The H/M ratio for the top three alloys is of similar magnitude. Only the alloy with aluminum is determined to be lower, with a value of 1.26. Two factors can explain this. The aluminum sample shows a significantly reduced hydrogen release temperature at 190 °C, indicating that the hydride phase is more destabilized than the other three alloys. The destabilization is possibly due to the previously mentioned influence of aluminum (cf. Chapter 6.2.1.), which could also impede the

hydrogen uptake. Furthermore, the reduced H/M ratio could also be due to the increased iron content in the $Al_{0.10}Ti_{0.30}V_{0.25}Nb_{0.25}Zr_{0.1}$ sample. The iron content due to abrasion was 3 wt.% and is increased in contrast to the other three samples (~ 0.6 wt%, c.f. Appendix 9.7). Iron also has a positive enthalpy of formation of 7.9 kJ mol^{-1} and could negatively affect hydrogen uptake in synergy with the other elements.[27] Therefore, it is expected that iron and aluminum show a destabilizing effect on the hydride phase, in which the hydrogen uptake is reduced, and the dehydrogenation temperature is lowered compared to the other samples. The slightly reduced H/M ratio (1.54) of the $Al_{0.05}Li_{0.05}Ti_{0.3}V_{0.25}Nb_{0.25}Zr_{0.1}$ compound could also be attributed to the influence of aluminum on hydrogen uptake. The latter also had to be milled for longer times under hydrogen to convert the residual *bcc* phase, which must be accompanied by an increase in the hydrogen concentration. At the same time, the EDX analysis showed lower iron contamination of 0.61 wt.% and is comparable to the samples without aluminum (c.f. Appendix 9.7). The reference system, $Ti_{0.325}V_{0.275}Nb_{0.275}$ $Zr_{0.125}$, also agrees well with the reference system from the literature, indicating that the direct influence of the minor iron impurity is negligible.[19] Therefore, the influence of the iron on the H/M can be neglected at this point. It can be assumed that aluminum destabilizes the hydride phase, which is why the storage capacity and the dehydrogenation temperature are lowered at increased aluminum concentration.

The Kissinger method was further used to determine the samples' activation energies (Ea). The required measurement curves of the heat flow at different heating rates are shown in Figure 51. The heat flow of the $Ti_{0.325}V_{0.275}Nb_{0.275}$ $Zr_{0.125}$, $Li_{0.10}Ti_{0.30}V_{0.25}Nb_{0.25}Zr_{0.10,}$ and $Al_{0.05}Li_{0.05}Ti_{0.3}V_{0.25}Nb_{0.25}Zr_{0.1}$ samples are comparable. The three samples have an on-set temperature of about 150 °C, increasing with the heating rate. On a similar order of magnitude (~ 30 – 50 °C), the endothermic peak temperature, related to the maximum desorption rate, also shifts to higher temperatures with an increased heating rate. However, the $Al_{0.10}Ti_{0.30}V_{0.25}Nb_{0.25}Zr_{0.1}$ sample shows a different behavior, where two local minima of the heat flux can be identified. The first local minimum is reached after the on-set temperature at about 150 °C and is approximately 190°C. As the temperature increases, the minimum heat flow reaches ~ 260 °C, shifting by ~ 50 °C with the varied heating rate. A linear relationship can then be established via the peak position of the endothermic maxima in relation to the heating rate using formula 4.3, and the activation energy can be determined by linear regression based on the slope.

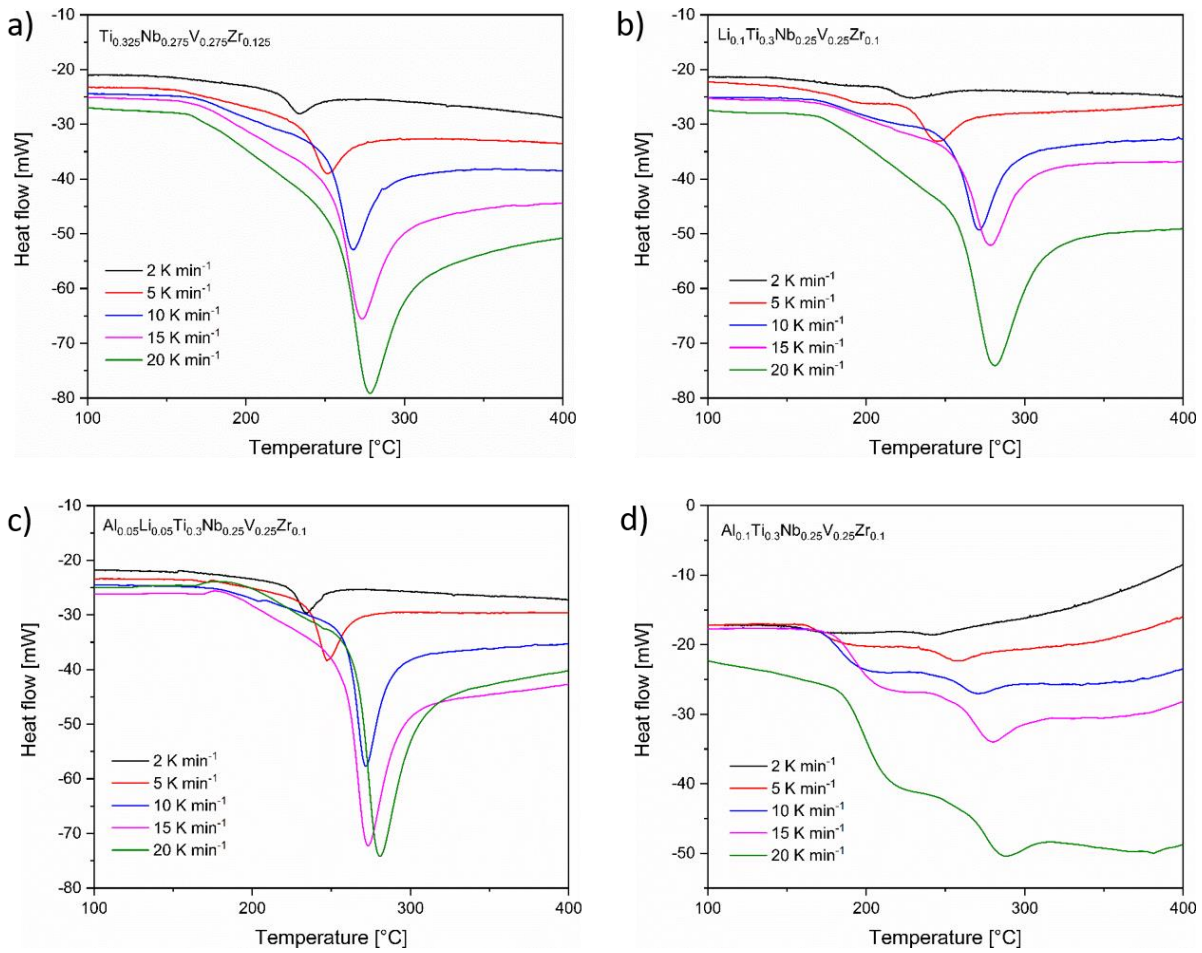

Figure 51: DSC heat flow signal recorded at varying heating rates (2, 5, 10, 15, 20 K min^{-1}): a) $Ti_{0.325}V_{0.275}Nb_{0.275}Zr_{0.125}$ b) $Li_{0.1}Ti_{0.3}V_{0.25}Nb_{0.25}Zr_{0.1}$ c) $Al_{0.05}Li_{0.05}Ti_{0.3}V_{0.25}Nb_{0.25}Zr_{0.1}$ d) $Al_{0.1}Ti_{0.3}V_{0.25}Nb_{0.25}Zr_{0.1}$.

At this point, it must be mentioned that for the alloy $Al_{0.10}Ti_{0.30}V_{0.25}Nb_{0.25}Zr_{0.10}$, the position of the total maximum (~ 260 °C) was taken into account since this point must be the maximum desorption rate. Due to the signal shape with an additional local maximum, it is assumed that the aluminum-containing sample is not comparable to the other samples. Nevertheless, according to Eq. 4.1, the following Kissinger diagrams are obtained and shown in Figure 52.

As the plots show, linear fits could be obtained in each case ($R^2 > 0.95$), and the activation energy was determined from the slope. For the reference system, an activation energy of 112 ± 4 kJ mol^{-1} is determined and deviates from the literature value. In the literature, an activation energy of 153 ± 10 kJ mol^{-1} was given for the same composition, but the difference can be attributed to the measurement methodology used.[19] The thermal analysis for the determination of E_a was done with thermal desorption spectroscopy measured on a homemade instrument, where the hydrogen partial pressure was recorded in a connected quadrupole spectrometer.[19]

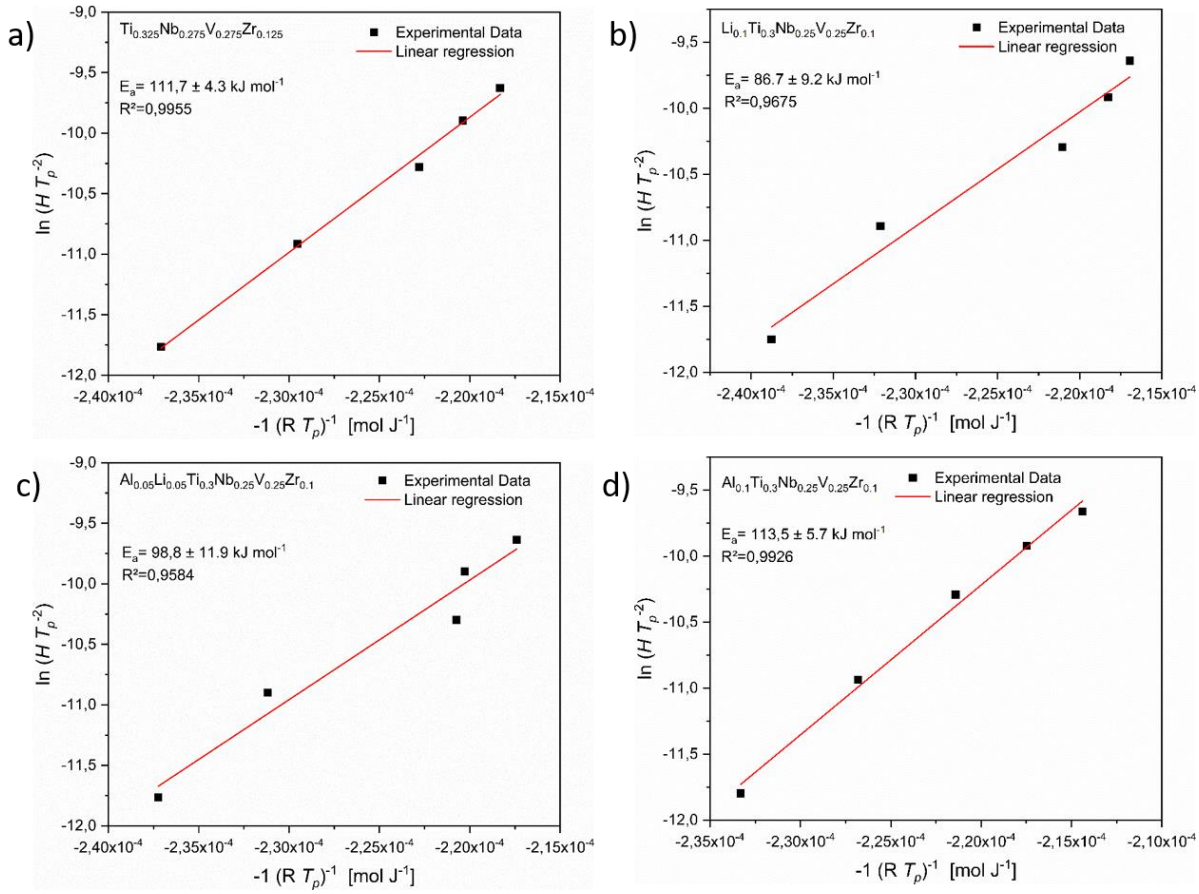

Figure 52: Kissinger plots from reactive milled samples: a) $Ti_{0.325}V_{0.275}Nb_{0.275}Zr_{0.125}$ b) $Li_{0.1}Ti_{0.3}V_{0.25}Nb_{0.25}Zr_{0.1}$ c) $Al_{0.05}Li_{0.05}Ti_{0.3}V_{0.25}Nb_{0.25}Zr_{0.1}$ d) $Al_{0.1}Ti_{0.3}V_{0.25}Nb_{0.25}Zr_{0.1}$.

In thermal desorption spectroscopy, the sample is subjected to a high vacuum at 10^{-6} mbar.[107] In contrast, during TGA-DSc measurements, the samples are measured in argon at atmospheric pressure. It is assumed that the pressure difference in the measurements led to deviating activation energies since desorption from hydrogen is pressure dependent. Therefore, independent of the literature, the results from this work can be compared. Accordingly, the activation energies of 99 ± 12 kJ mol^{-1} and 87 ± 9 kJ mol^{-1} were determined for alloy $Al_{0.05}Li_{0.05}Ti_{0.3}V_{0.25}Nb_{0.25}Zr_{0.1}$ and $Li_{0.10}Ti_{0.30}V_{0.25}Nb_{0.25}Zr_{0.10}$, respectively, indicating that the activation energy is lowered with increasing lithium concentration. The aluminum compound cannot be directly compared due to the more deviating desorption profile, but an activation energy of 114 ± 6 kJ mol^{-1} was determined for the second desorption maximum. It should also be mentioned that the desorption mechanism of hydrogen from a metal hydride is a complex process involving several phases, such as the gaseous hydrogen and two or more hydrogen-containing solid phases.[124] Considering only the phases, hydrogen desorption is influenced by interlinked processes such as the desorption of molecular hydrogen from the surface, recombination of hydrogen atoms on the metal surface, diffusion within the metal and hydride phases, and the phase transformation from

metal hydride to metal.[124] Further, the diffusion process depends on several variables, over which interstitial sites and in which phase the diffusion takes place, at which temperatures, and more.[45, 125] The complexity of the desorption process makes it clear that the activation energy represents an averaged value over all the processes mentioned, whereby the process with the highest activation energy represents the decisive variable but cannot be differentiated. Nevertheless, the results indicate that lithium leads to a reduction of E_a. Aluminum, on the other hand, contributes synergistically to destabilization, as indicated by the first local maxima at lower temperatures.

After the thermal analysis, the materials were subjected to X-ray diffraction experiments. The obtained data are from samples heated at a rate of 10 K min^{-1} up to 625 °C. The X-ray diffraction data were then simulated to determine the lattice parameters using the Pawley method, and the corresponding data are shown in Figure 53.

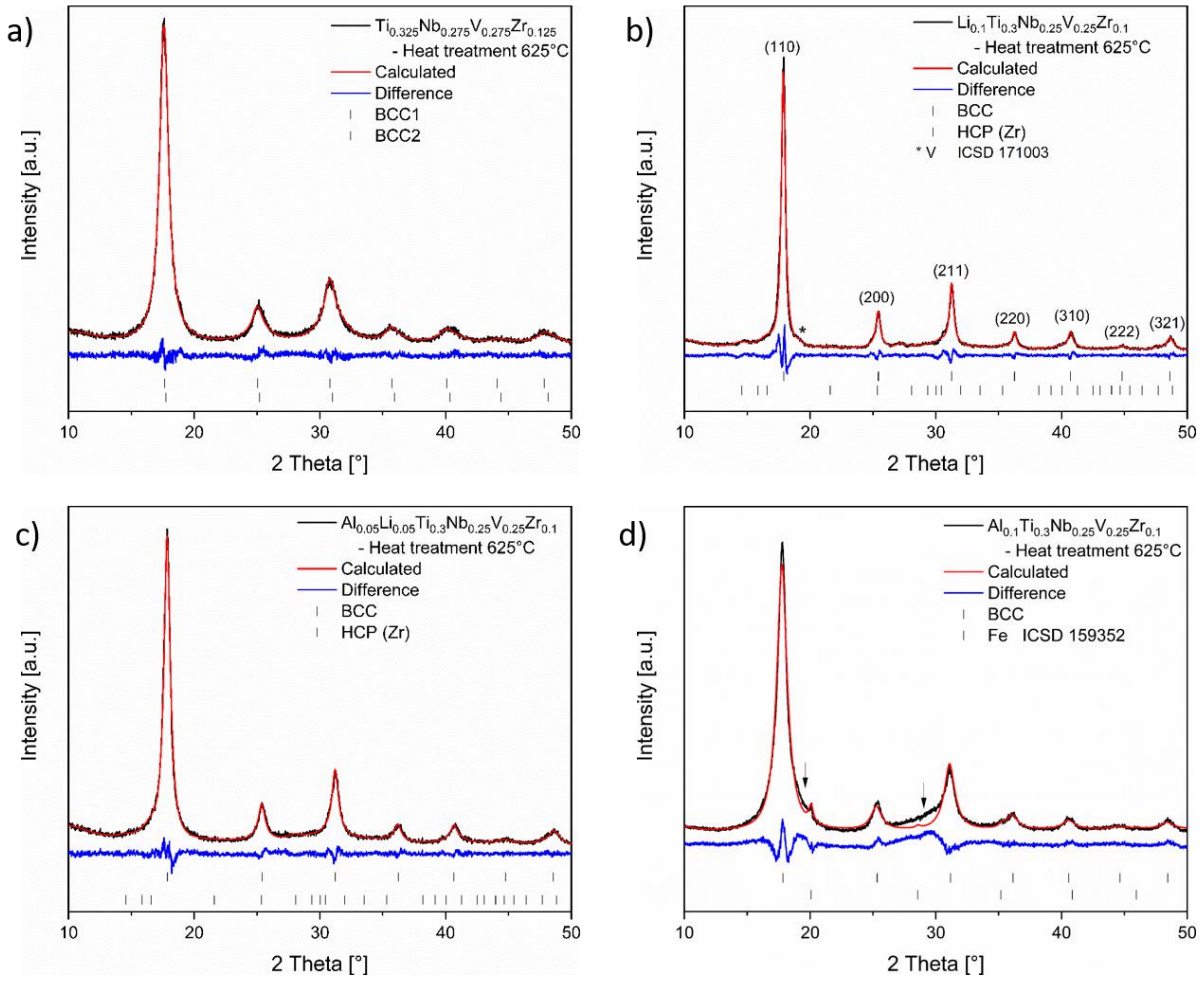

Figure 53: Powder XRD pattern of reactive milled compounds (black) after heat treatment up to 625 °C with 10 K min^{-1}, related Pawley simulation (red) and corresponding difference curve (blue): a) $Ti_{0.325}V_{0.275}Nb_{0.275}Zr_{0.125}$ b) $Li_{0.1}Ti_{0.3}V_{0.25}Nb_{0.25}Zr_{0.1}$ c) $Al_{0.05}Li_{0.05}Ti_{0.3}V_{0.25}Nb_{0.25}Zr_{0.1}$ d) $Al_{0.1}Ti_{0.3}V_{0.25}Nb_{0.25}Zr_{0.1}$.

As the diffractograms show, in all four samples, the transformation from the previously identified fcc phase to one or more bcc phases was completed after dehydrogenation. The 4-component alloy has been fitted with two *bcc* phases since the fitting of the reflections at higher 2 Theta angles with a single *bcc* phase showed a higher deviation. This indicates that the 4 component alloy also tends to disproportionate after dehydrogenation, as in the mechanically alloyed samples. The lithium alloy even shows this effect of disproportionation more strongly. Due to the asymmetric shape of the (110) reflection and the (211) reflection, zirconium with an *hcp* to lower 2 Theta angles and vanadium to larger 2 Theta angles are included. The reflections' asymmetry may indicate segregation of the Zr and V. The pattern of the $Al_{0.05}Li_{0.05}Ti_{0.3}V_{0.25}Nb_{0.25}Zr_{0.1}$ alloy, on the other hand, indicates higher stability with respect to disproportionation. The first reflection shows only a slight asymmetry towards smaller angles, which could be compensated under the introduction of the zirconium phase, but also indicates that disproportionation has taken place. These segregation phenomena can not be excluded for the $Al_{0.10}Ti_{0.30}V_{0.25}Nb_{0.25}Zr_{0.10}$ sample. The areas marked by the arrows strongly indicate unidentified phases, which may have resulted from the superposition of several segregation products. The obtained lattice parameters of the Pawley simulations are listed in Table 18 for comparison.

Table 18: Overview of the lattice parameters of the mechanically alloyed samples and the reactively milled dehydrogenated samples determined using Pawley simulations.

Composition	**Initial Lattice parameter of Pristine Alloy[a)] [Å]**	**Lattice Parameters after Cycling [Å]**
$Ti_{0.325}V_{0.275}Nb_{0.275}Zr_{0.125}$	3.2627(1)	3.2710(2) *bcc1* 3.251(1) *bcc2*
$Li_{0.10}Ti_{0.30}V_{0.25}Nb_{0.25}Zr_{0.10}$	3.2831(4)	3.2228 (1) *bcc* a = 3.232(1) c = 5.147(1) *hcp*
$Al_{0.05}Li_{0.05}Ti_{0.3}V_{0.25}Nb_{0.25}Zr_{0.1}$	3.2578(2)	3.2227(2) a = 3.232(1) c = 5.147(1) *hcp*
$Al_{0.10}Ti_{0.30}V_{0.25}Nb_{0.25}Zr_{0.10}$	3.2507(2)	3.244(1) *bcc1*

a) Mechanically alloyed samples

The segregation of the elemental zirconium from the disordered solid solution can be determined by comparing the simulated lattice parameters with those from the database. The simulated lattice parameters of the *hcp* phase agree very well with the data from the ICSD database (a = 3.232 Å, b = 3.232 Å, c = 5.148 Å, ICSD 43700). In the case of the alloys containing aluminum and/or lithium, the dehydrogenation resulted in a significant decrease in the lattice parameter when the lattice parameters of the freshly synthesized mechanically alloyed samples are considered and are well explained by the segregation of zirconium from the alloy. However, the intensities of these segregation products indicate a small amount compared to the *bcc* major phase, although the actual amount of each phase could not be refined due to the unknown composition.

6.3. Conclusion

In Chapter 6, high entropy alloys with different compositions were discussed, focusing on incorporating the light metal lithium into the alloys and evaluating its influence on the hydrogen storage properties. First, the alloys were successfully synthesized in the targeted alloy composition by mechanical alloying and reactive milling to investigate their hydrogen storage properties. Then, the X-ray diffraction experiments at different synthesis times provided insight into the alloying process and the formation of the respective crystal phase.

The time-dependent X-ray diffraction results of the mechanically alloyed samples showed that introducing 10% lithium into the reference alloy requires a longer milling time for homogenization, which can be attributed to the positive enthalpy of mixing of lithium with the four transition metals used. Nevertheless, the determination of the lattice parameters and the elemental analyses indicate the successful incorporation of lithium into the solid solution, and it was possible to synthesize all four compositions with a *bcc* phase.

Subsequently, the mechanically alloyed samples were subjected to multiple cycles of hydrogenation and dehydrogenation in the Sieverts apparatus, followed by X-ray diffraction experiments in the hydrogenated state. The results showed that the alloys with light metal addition (Al, Li, or AlLi) react upon hydrogen uptake with an increased lattice parameter, but an expected phase transformation from *bcc* to *fcc* does not occur. On the other hand, the reference system undergoes a partial phase transformation from *bcc* to *fcc*. In contrast, the investigations of the reactively milled samples showed that a phase transformation from *bcc* to *fcc* is possible in all four investigated material compositions. Furthermore, the phase transformation is

accompanied by an increased hydrogen concentration in the metal hydride, as described in the literature.[23] This suggests that the additional energy supplied during the milling process favors the hydrogen uptake. In addition, time-dependent XRD studies on the reactive milled alloys showed that hydrogen uptake decreases with increasing aluminum content, and a longer process time is required. The subsequent thermal analyses also showed that the hydrogen content of the 10% aluminum-containing sample was the lowest.

The thermal analyses showed differences in the dehydrogenation properties concerning the synthesis methodology. Reactive milling resulted in a reduced onset temperature of ~150 °C in all four cases, whereas the onset temperatures of the mechanically alloyed samples were around 220 – 230 °C. The SEM images of the reactively milled samples showed a particle network with smaller particles. It is assumed that the hydrogenated phase is more brittle in terms of mechanical properties, which should lead to smaller particles.[71] Accordingly, it was assumed that a particle size difference exists between the mechanically and reactively milled samples, which is responsible for the different dehydrogenation temperatures. However, high-resolution methods should be applied to support this assumption.

Regarding the hydrogen absorption kinetics, no significant differences were identified for all four mechanically synthesized alloys. All samples show a rapid hydrogen uptake within a few minutes. However, the dehydrogenation, as shown by the thermal analysis, proceeds up to 500 – 600 °C depending on the synthesis methodology.

The initial high storage capacities of up to 2.6 wt.% of the reactive milled samples and the low equilibrium pressure of the mechanically alloyed samples indicate the potential of the alloy composition to serve as a fast intermediate storage material and suggest that the storage capacity could be increased by introducing light metals. However, the disproportionation of the phases would cause the material to degrade too much over a technically relevant number of cycles, potentially limiting its use to a short period.

Chapter 7

7. Conclusion, Final Remarks and Outlook

Within the scope of this work, various high entropy alloys were successfully synthesized, and their use for hydrogen storage was evaluated. The main focus of the work was to synthesize new compositions based on light metals or by adding light metals to already investigated systems, to reduce the average molar masses of the alloys in order to increase the gravimetric storage capacity (c.f. Equation 4.1 and 4.2). In this respect, apart from hydrogen storage capacity, the effects of synthesis methods including mechanical alloying and reactive milling were investigated, which is strongly dependent on the metals involved and synthesis parameters used.

Chapter 5, which deals with the synthesis of a high entropy alloy with the composition AlLiMgTiZr, shows how important the process parameters are for the successful processing of such an alloy. First, the investigations showed that PCAs are necessary for processing to suppress an enhanced cold welding effect during milling. Based on the subsequent analyses via XRD, EDX, and Raman spectroscopy, it was shown that the PCAs used decompose during milling and form a high entropy carbide with a rock salt-like crystal structure as in the case of transition metal mono carbides. Moreover, the formation mechanism was demonstrated based on the tracking experiments. During the synthesis, the hydrocarbons decompose, and zirconium hydride is formed as an intermediate phase. Later in the process, the final *fcc* structure is formed and the proportion of the zirconium hydrid phase decreases. Subsequently, it was assumed that the decomposition of PCA could be suppressed via the use of ZrH_2. However, the time-dependent studies showed that even in the case of ZrH_2 as an educt, the PCA still decomposed, and the carbides were formed. Altogether, the presented experiments ended in a similar high entropy carbide structure that could be described by *fcc* symmetry. These findings led to the conclusion that, instead of the expected *bcc* alloy, mainly the rocksalt-like *fcc* high entropy carbide forms under the conditions used. Accordingly, it is assumed that the proposed empirical selection criteria VEC, δ, and Ω are not transferable to the selected equimolar composition. The further work should focuses on whether the selection criteria are transferable to high entropy carbides. Since the occupation of the sublattice, e.g., by carbon, can have a compensating influence on the atomic mismatch, which would make the application of δ negligible.

Regarding the hydrogen storage properties, it was observed that when zirconium hydride was used as an additional hydrogen source, the formed carbide exhibited a mass loss of 1.56 wt.% during the first dehydrogenation. The cycle experiments subsequently showed a reversible storage capacity of 0.6 wt.%. The time-dependent measurements indicated a fast absorption rate, with 90 % of the capacity absorbed within the first minute. In addition, a unique feature of the carbide structure is the constant lattice parameter in the hydrogenated and dehydrogenated states. In contrast to other metal hydride solid-state storage materials, it is assumed that the material does not undergo any significant volume change upon hydrogen loading or unloading. A constant volume of the storage material is advantageous for the design of storage tanks since no blank volume in the tank has to be considered for the volume change, and thus, a higher volumetric storage density can be achieved. The results show that high entropy carbides can be considered solid-state hydrogen storage materials, which to our knowledge, is the first time this has been demonstrated.

In the literature, carbides are mainly considered hydrogen-trapping materials to counteract hydrogen embrittlement in high-strength steels.[96, 126-127] To counteract hydrogen embrittlement, composite materials are produced based on metals and carbides. As hydrogen trapping material, the presented light metal high entropy carbide brings a further advantage in its average weight. The reduced weight of the carbide then becomes advantageous for the lightweight construction sector, as an additional weight due to heavy elements can be avoided. Regardless of the use as hydrogen storage or in avoiding hydrogen embrittlement, it would be interesting to know the role of carbon in the formation of the alloy or carbide and whether a minimum concentration of carbon is required to stabilize the *fcc* structure. Ultimately, the materials could also be of interest for other applications, e.g., coating materials for tools, where high wear resistance is demanded. In addition, investigating the electronic properties could be interesting, as these can be tuned via the carbon concentration, which can presumably vary via the synthesis process.

In Chapter 6, the effect of lithium and/or aluminum on a $Ti_{0.325}V_{0.275}Nb_{0.275}Zr_{0.125}$ alloy was systematically investigated. The alloys were successfully fabricated with a *bcc* structure via mechanical alloying. Based on the tracking experiments, it was found that an increased lithium content requires a longer process time, which can be attributed to the positive enthalpy of mixing of lithium with the transition metals used. Furthermore, vanadium exhibited the lowest affinity to form a solid solution. The vanadium concentration does not decrease until a *bcc* majority phase has formed. The subsequent analyses indicated that the materials had a homogeneous elemental

distribution, although investigation with high-resolution imaging techniques would be required to also identify lithium as an alloy participant in the solid solution. For this purpose, it would be interesting to perform spatially resolved electron energy loss spectroscopy, as this would allow lithium to be detected.

The connected investigations of hydrogen storage properties showed that the materials can store hydrogen with fast kinetics within a few minutes. The pressure-composition isotherms revealed a very low equilibrium pressure (< 0.01 bar) for each compound. In addition, the hydrogen absorption experiments of the mechanically alloyed samples indicated that the uptake of hydrogen (H/M < 0.64) does not occur at the expected maximum capacity, which for *bcc* alloys is typically a H/M of 2. Over the number of cycles, all samples lost capacity. The subsequent thermogravimetric analysis showed that the materials release hydrogen up to 500 °C, so the volumetric measurements were influenced by residual hydrogen. The gravimetric measurements determined a H/M ratio of up to 0.84. Furthermore, the connected X-ray diffraction experiments showed that the materials are affected by disproportionation, which can explain the loss of capacity over the cycle number.

Reactive milling proved to be beneficial for hydrogen uptake as well as for the dehydrogenation temperature. The materials had been synthesized with a majority *fcc* phase, with residual *bcc* components as a by-product. Based on the increasing intensity of the *bcc* phase with the increasing aluminum content, the influence of the non-hydride forming element could be demonstrated. Based on the required prolonged synthesis time, reduced capacity, and dehydrogenation temperature, it was assumed that aluminum destabilized the hydride phase. By introducing lithium, the intended goal of increasing the gravimetric storage capacity was achieved (2.56 ± 0.22 wt.%). In addition, the Kissinger method demonstrated that the activation energy could be lowered with increasing lithium content, but this was not significantly reflected in the dehydrogenation temperature. Furthermore, lithium proved to be phase destabilizing, which limits its applicability as an alloying element over multiple hydrogen storage cycles.

Nevertheless, because of the high number of possible combinations and concentration gradients, HEAs represent a very interesting class of materials in terms of their storage properties. Due to the diversity of composition, some storage properties could be modulated via chemical composition, as shown in this work. Technically, long-term stability and thermal properties such as hydrogenation temperature and desorption would have to be examined.

8. Bibliography

1. IPCC, 2018*: Global Warming of 1.5°C. An IPCC Special Report on the impacts of global warming of 1.5°C above pre-industrial levels and related global greenhouse gas emission pathways, in the context of strengthening the global response to the threat of climate change, sustainable development, and efforts to eradicate poverty* [Masson-Delmotte, V., P. Zhai, H.-O. Pörtner, D. Roberts, J. Skea, P.R. Shukla, A. Pirani, W. Moufouma-Okia, C. Péan, R. Pidcock, S. Connors, J.B.R. Matthews, Y. Chen, X. Zhou, M.I. Gomis, E. Lonnoy, T. Maycock, M. Tignor, and T. Waterfield (eds.)]. In Press. **2018**. https://www.ipcc.ch/sr15/ (accessed 13.03.2022)

2. Paris Agreement to the United Nations Framework Convention on Climate Change. *T.I.A.S.* **Dec. 12, 2015**, No. 16 – 1104.

3. International Energy Agency (2021), *World Energy Outlook 2021.* **2021**. Creative Commons Attribution CC BY-NC-SA 3.0 IGO https://www.iea.org/reports/world-energy-outlook-2021 (accessed 16.03.2022).

4. Kirubakaran, A.; Jain, S.; Nema, R. J. R. A review on fuel cell technologies and power electronic interface. *Renewable Sustainable Energy Rev.* **2009,** *13* (9), 2430 – 2440.

5. Luo, Y.; Wu, Y.; Li, B.; Mo, T.; Li, Y.; Feng, S.-P.; Qu, J.; Chu, P. K. Development and application of fuel cells in the automobile industry. *Journal of Energy Storage* **2021,** *42*, 103124.

6. Klell, M. Storage of Hydrogen in the Pure Form. In *Handbook of Hydrogen Storage: New Materials for Future Energy Storage*, 1st ed.; Wiley-VCH, **2010**; pp 1 – 37.

7. Schlapbach, L.; Züttel, A., Hydrogen-storage materials for mobile applications. *Nature* **2001,** *414* (6861), 353 – 358.

8. Rostrup-Nielsen, J. R. Catalytic Steam Reforming. In *Catalysis: Science and Technology,* Vol. 5, Anderson, J. R.; Boudart, M., Eds. Springer Berlin Heidelberg: Berlin, Heidelberg, **1984**; pp 1 – 117.

9. Xu, J.; Froment, G. F. Methane steam reforming, methanation and water-gas shift: I. Intrinsic kinetics. *AIChE J.* **1989,** *35* (1), 88 – 96.

10. Jones, L. W. Liquid Hydrogen as a Fuel for Future: Replacement of hydrocarbon fuel for transportation systems by liquid hydrogen is proposed and discussed. *Science* **1971,** *174* (4007), 367 – 370.

11. Mazloomi, K.; Gomes, C. Hydrogen as an energy carrier: Prospects and challenges. *Renewable and Sustainable Energy Rev.* **2012,** *16* (5), 3024 – 3033.

12. Eberle, U.; Felderhoff, M.; Schuth, F. Chemical and Physical Solutions for Hydrogen Storage. *Angew. Chem. Int. Ed.* **2009,** *48* (36), 6608 – 6630.

13. Aaldto-Saksa, P. T.; Cook, C.; Kiviaho, J.; Repo, T. Liquid organic hydrogen carriers for transportation and storing of renewable energy - Review and discussion. *J. Power Sources* **2018,** *396*, 803 – 823.

14. Jorschick, H.; Geisselbrecht, M.; Essl, M.; Preuster, P.; Bosmann, A.; Wasserscheid, P. Benzyltoluene/dibenzyltoluene-based mixtures as suitable liquid organic hydrogen carrier systems for low temperature applications. *Int. J. Hydrogen Energy* **2020,** *45* (29), 14897 – 14906.

15. Zhang, Y.; Lu, Z. P.; Ma, S. G.; Liaw, P. K.; Tang, Z.; Cheng, Y. Q.; Gao, M. C. Guidelines in predicting phase formation of high-entropy alloys. *MRS Commun.* **2014,** *4* (2), 57 – 62.

16. Zhang, Y.; Zhou, Y. J.; Lin, J. P.; Chen, G. L.; Liaw, P. K. Solid-solution phase formation rules for multi-component alloys. *Adv. Eng. Mater.* **2008,** *10* (6), 534 – 538.

17. Guo, S.; Ng, C.; Lu, J.; Liu, C. J. Effect of valence electron concentration on stability of fcc or bcc phase in high entropy alloys. *Journal of Applied Physics* **2011,** *109* (10), 103505.

18. Guo, S. Phase selection rules for cast high entropy alloys: an overview. *Mater. Sci. Technol.* **2015,** *31* (10), 1223 – 1230.

19. Montero, J.; Zlotea, C.; Ek, G.; Crivello, J.-C.; Laversenne, L.; Sahlberg, M. TiVZrNb multi-principal-element alloy: synthesis optimization, structural, and hydrogen sorption properties. *Molecules* **2019,** *24* (15), 2799.

20. Montero, J.; Ek, G.; Laversenne, L.; Nassif, V.; Zepon, G.; Sahlberg, M.; Zlotea, C. Hydrogen storage properties of the refractory Ti-V-Zr-Nb-Ta multi-principal element alloy. *J. Alloys Compd.* **2020,** *835*, 155376.

21. Montero, J.; Ek, G.; Laversenne, L.; Nassif, V.; Sahlberg, M.; Zlotea, C. How 10 at% Al addition in the Ti-V-Zr-Nb high-entropy alloy changes hydrogen sorption properties. *Molecules* **2021,** *26* (9), 2470.

22. Montero, J.; Ek, G.; Sahlberg, M.; Zlotea, C. Improving the hydrogen cycling properties by Mg addition in Ti-V-Zr-Nb refractory high entropy alloy. *Scr. Mater.* **2021,** *194*, 113699.

23. Marques, F.; Balcerzak, M.; Winkelmann, F.; Zepon, G.; Felderhoff, M. Review and outlook on high-entropy alloys for hydrogen storage. *Energy Environ. Sci.* **2021,** *14* (10), 5191 – 5227.

24. Akiba, E. Metal Hydrides. In *Hydrogen and Fuel Cells*, 1st ed.; Wiley-VCH, **2010**; pp 395 – 413.

25. Chase Jr, M. W. *NIST-JANAF thermochemical tables*. *Washington, DC: New York: American Chemical Society; American Institute of Physics for the National Institute of Standards and Technology,* **1998**.

26. Jimenez, C.; Garcia-Moreno, F.; Pfretzschner, B.; Klaus, M.; Wollgarten, M.; Zizak, I.; Schumacher, G.; Tovar, M.; Banhart, J. Decomposition of TiH_2 studied in situ by synchrotron X-ray and neutron diffraction. *Acta Mater.* **2011,** *59* (16), 6318 – 6330.

27. Tkacz, M. Thermodynamic properties of iron hydride. *J. Alloys Compd.* **2002,** *330*, 25 – 28.

28. Sakintuna, B.; Lamari-Darkrim, F.; Hirscher, M. Metal hydride materials for solid hydrogen storage: A review. *Int. J. Hydrogen Energy* **2007,** *32* (9), 1121 – 1140.

29. Dematteis, E. M.; Berti, N.; Cuevas, F.; Latroche, M.; Baricco, M. Substitutional effects in TiFe for hydrogen storage: a comprehensive review. *Mater. Adv.* **2021,** *2* (8), 2524 – 2560.

30. Mclellan, R. B.; Harkins, C. G. Hydrogen Interactions with Metals. *Mater. Sci. En.g* **1975,** *18* (1), 5 – 35.

31. Park, C. N.; Luo, S. F.; Flanagan, T. B. Analysis of sloping plateaux in alloys and intermetallic hydrides - I. Diagnostic features. *J. Alloys Compd.* **2004,** *384* (1-2), 203 – 207.

32. Sharma, V. K.; Kumar, E. A. Metal hydrides for energy applications - classification, PCI characterisation and simulation. *Int. J. Energy Res.* **2017,** *41* (7), 901 – 923.

33. Peisl, H. Lattice strains due to hydrogen in metals. In *Hydrogen in metals I*, Vol. 28 Springer, Berlin, Heidelberg, **1978**; pp 53 – 74.

34. Kumar, S.; Jain, A.; Ichikawa, T.; Kojima, Y.; Dey, G. K. Development of vanadium based hydrogen storage material: A review. *Renewable Sustainable Energy Rev.* **2017,** *72*, 791 – 800.

35. Grochala, W.; Edwards, P. P. Thermal decomposition of the non-interstitial hydrides for the storage and production of hydrogen. *Chem. Rev.* **2004,** *104* (3), 1283 – 1315.

36. Yartys, V. A. *et al.* Magnesium based materials for hydrogen based energy storage: Past, present and future. *Int. J. Hydrogen Energy* **2019,** *44* (15), 7809 – 7859.

37. Andrews, L.; Wang, X. Infrared Spectra of Indium Hydrides in Solid Hydrogen and of Solid Indane. *Angew. Chem.* **2004,** *43* (13), 1706 – 1709.

38. Jiang, W.; Wang, H.; Zhu, M. AlH_3 as a hydrogen storage material: recent advances, prospects and challenges. *Rare Met.* **2021,** *40* (12), 3337 – 3356.

39. Ding, Z.; Li, S.; Zhou, Y.; Chen, Z.; Yang, W.; Ma, W.; Shaw, L. $LiBH_4$ for hydrogen storage-new perspectives. *Nano Mater. Sci.* **2020,** *2* (2), 109 – 119.

40. Ali, N.; Ismail, M. Modification of $NaAlH_4$ properties using catalysts for solid-state hydrogen storage: A review. *Int. J. Hydrogen Energy* **2021,** *46* (1), 766 – 782.

41. Sahlberg, M.; Karlsson, D.; Zlotea, C.; Jansson, U. Superior hydrogen storage in high entropy alloys. *Sci. Rep.* **2016,** *6*(1), 1 – 6.

42. Ek, G.; Nygård, M. M.; Pavan, A. F.; Montero, J.; Henry, P. F.; Sørby, M. H.; Witman, M.; Stavila, V.; Zlotea, C.; Hauback, B. C. Elucidating the effects of the composition on hydrogen sorption in TiVZrNbHf-based high-entropy alloys. *Inorg. Chem* **2020,** *60* (2), 1124 – 1132.

43. Switendick, A. C. Band-Structure Calculations for Metal Hydrogen Systems. *Z.Phys. Chem.* **1979,** *117*, 89 – 112.

44. Westlake, D. J. Site occupancies and stoichiometries in hydrides of intermetallic compounds: geometric considerations. *J. Less-Common Met.* **1983,** *90* (2), 251 – 273.

45. Broom, D. P. *Hydrogen storage materials: The Characterisation of Their Storage Properties*. Springer London, **2011**.

46. Marmaro, R. W.; Lynch, F. E.; Chandra, D.; Lambert, S.; Sharma, A *Investigation of long term stability in metal hydrides*; **1991,** No. NASA-CR-185667. (accessed 26.07.2022)

47. Yeh, J. W.; Chen, S. K.; Lin, S. J.; Gan, J. Y.; Chin, T. S.; Shun, T. T.; Tsau, C. H.; Chang, S. Y. Nanostructured high-entropy alloys with multiple principal

elements: Novel alloy design concepts and outcomes. *Adv. Eng. Mater.* **2004,** *6* (5), 299 – 303.

48. Cantor, B.; Chang, I.; Knight, P.; Vincent, A. J. Microstructural development in equiatomic multicomponent alloys. *Mater. Sci. Eng.* **2004,** *375*, 213 – 218.

49. Zhang, Y.; Zuo, T. T.; Tang, Z.; Gao, M. C.; Dahmen, K. A.; Liaw, P. K.; Lu, Z. P. Microstructures and properties of high-entropy alloys. *Prog. Mater. Sci.* **2014,** *61*, 1 – 93.

50. Ye, Y.; Wang, Q.; Lu, J.; Liu, C.; Yang, Y. High-entropy alloy: challenges and prospects. *Mater. Today* **2016,** *19* (6), 349 – 362.

51. Amiri, A.; Shahbazian-Yassar, R. Recent progress of high-entropy materials for energy storage and conversion. *J. Mater. Chem. A* **2021,** *9* (2), 782 – 823.

52. Vaidya, M.; Muralikrishna, G. M.; Murty, B. S. High-entropy alloys by mechanical alloying: A review. *J. Mater. Res.* **2019,** *34* (5), 664 – 686.

53. Miracle, D. B.; Senkov, O. N. A critical review of high entropy alloys and related concepts. *Acta Mater.* **2017,** *122*, 448 – 511.

54. Yang, X.; Zhang, Y. Prediction of high-entropy stabilized solid-solution in multi-component alloys. *Mater. Chem. Phys.* **2012,** *132* (2-3), 233 – 238.

55. Yang, F.; Wang, J.; Zhang, Y.; Wu, Z.; Zhang, Z.; Zhao, F.; Huot, J.; Novaković, J. G.; Novaković, N. Recent progress on the development of high entropy alloys (HEAs) for solid hydrogen storage: A review. *Int. J. Hydrogen Energy* **2022,** *47* (21), 11236 – 11249.

56. Shahi, R. R.; Gupta, A. K.; Kumari, P. Perspectives of high entropy alloys as hydrogen storage materials. *Int. J. Hydrogen Energy* **2022,** DOI: 10.1016/j.ijhydene.2022.02.113.

57. Marques, F.; Pinto, H. C.; Figueroa, S. J. A.; Winkelmann, F.; Felderhoff, M.; Botta, W. J.; Zepon, G. Mg-containing multi-principal element alloys for hydrogen storage: A study of the $MgTiNbCr_{0.5}Mn_{0.5}Ni_{0.5}$ and $Mg_{0.68}TiNbNi_{0.55}$ compositions. *Int. J. Hydrogen Energy* **2020,** *45* (38), 19539 – 19552.

58. Zepon, G.; Leiva, D. R.; Strozi, R. B.; Bedoch, A.; Figueroa, S. J. A.; Ishikawa, T. T.; Botta, W. J. Hydrogen-induced phase transition of $MgZrTiFe_{0.5}Co_{0.5}Ni_{0.5}$ high entropy alloy. *Int. J. Hydrogen Energy* **2018,** *43* (3), 1702 – 1708.

59. Cardoso, K. R.; Roche, V.; Jorge, A. M.; Antiqueira, F. J.; Zepon, G.; Champion, Y. Hydrogen storage in MgAlTiFeNi high entropy alloy. *J. Alloy Compd.* **2021,** *858*, 158357.

60. Hu, J. T.; Shen, H. H.; Jiang, M.; Gong, H. F.; Xiao, H. Y.; Liu, Z. J.; Sun, G. A.; Zu, X. A DFT Study of Hydrogen Storage in High-Entropy Alloy TiZrHfScMo. *Nanomaterials* **2019,** *9* (3), 461.

61. Dewangan, S. K.; Sharma, V. K.; Sahu, P.; Kumar, V. Synthesis and characterization of hydrogenated novel AlCrFeMnNiW high entropy alloy. *Int. J. Hydrogen Energy* **2020,** *45* (34), 16984 – 16991.

62. Ek, G. *Hunting Hydrogen: Structure-property relations in High Entropy Alloy-based metal hydrides.* Ph.D. Dissertation, Acta Universitatis Upsaliensis, Uppsala, Sweden, **2021**.

63. Karlsson, D.; Ek, G.; Cedervall, J.; Zlotea, C.; Moller, K. T.; Hansen, T. C.; Bednarcik, J.; Paskevicius, M.; Sorby, M. H.; Jensen, T. R.; Jansson, U.; Sahlberg, M. Structure and Hydrogenation Properties of a HfNbTiVZr High-Entropy Alloy. *Inorg. Chem.* **2018,** *57* (4), 2103 – 2110.

64. Nygård, M. M.; Ek, G.; Karlsson, D.; Sahlberg, M.; Sørby, M. H.; Hauback, B. C. Hydrogen storage in high-entropy alloys with varying degree of local lattice strain. *Int. J. Hydrogen Energy* **2019,** *44* (55), 29140 – 29149.

65. Nygård, M. M.; Ek, G.; Karlsson, D.; Sørby, M. H.; Sahlberg, M.; Hauback, B. C. Counting electrons-a new approach to tailor the hydrogen sorption properties of high-entropy alloys. *Atca Mater.* **2019,** *175*, 121 – 129.

66. Nygård, M. M.; Sławiński, W. A.; Ek, G.; Sørby, M. H.; Sahlberg, M.; Keen, D. A.; Hauback, B. C. Local order in high-entropy alloys and associated deuterides–a total scattering and Reverse Monte Carlo study. *Atca Mater.* **2020,** *199*, 504 – 513.

67. Silva, B. H.; Zlotea, C.; Champion, Y.; Botta, W. J.; Zepon, G. Compounds, Design of TiVNb-(Cr, Ni or Co) multicomponent alloys with the same valence electron concentration for hydrogen storage. *J. Alloys Compd.* **2021,** *865*, 158767.

68. Sun, W. H.; Huang, X. J.; Luo, A. A. Phase formations in low density high entropy alloys. *Calphad* **2017,** *56*, 19 – 28.

69. Lide, D. R., *CRC handbook of chemistry and physics*. Vol. 85; CRC press, **2004**.

70. Alcock, C.; Itkin, V.; Horrigan, M. K. Vapour pressure equations for the metallic elements: 298–2500K. *Can. Metall. Q.* **1984,** *23* (3), 309 – 313.

71. Suryanarayana, C. Mechanical alloying and milling. *Prog. Mater. Sci.* **2001,** *46* (1-2), 1 – 184.

72. Suryanarayana, C. Mechanical alloying: a novel technique to synthesize advanced materials. *Research* **2019,** *2019*, 4219812.

73. Benjamin, J. S.; Volin, T. The mechanism of mechanical alloying. *Metall. Trans.* **1974,** *5* (8), 1929 – 1934.

74. Fogagnolo, J. B.; Velasco, F.; Robert, M. H.; Torralba, J. M. Effect of mechanical alloying on the morphology, microstructure and properties of aluminium matrix composite powders. *Mat. Sci. Eng. A* **2003,** *342* (1-2), 131 – 143.

75. Pawley, G. S. Unit-cell refinement from powder diffraction scans. *J. Appl. Crystallogr.* **1981,** *14* (6), 357 – 361.

76. Coelho, A. A. TOPAS and TOPAS-Academic: an optimization program integrating computer algebra and crystallographic objects written in C++. *J. Appl. Crystallogr.* **2018,** *51* (1), 210 – 218.

77. Scardi, P.; Leoni, M. Diffraction line profiles from polydisperse crystalline systems. *Acta Crystallogr., Sect. A: Found. Crystallogr.* **2001,** *57* (5), 604 – 613.

78. Scardi, P.; Leoni, M. Line profile analysis: pattern modelling versus profile fitting. *J. Appl. Crystallogr.* **2006,** *39* (1), 24 – 31.

79. Scardi, P.; Ortolani, M.; Leoni, M. WPPM: microstructural analysis beyond the Rietveld method. *Mater. Sci. Forum* **2010,** *651*, 155 – 171.

80. Scardi, P.; Azanza Ricardo, C. L.; Perez-Demydenko, C.; Coelho, A. A. Whole powder pattern modelling macros for TOPAS. *J. Appl. Crystallogr.* **2018,** *51* (6), 1752 – 1765.

81. Scardi, P. Practice, Microstructural properties: lattice defects and domain size effects. *Powder Diffraction: Theory and Practice* **2008**, 376 – 413.

82. Blach, T.; Gray, E. M. Compounds, Sieverts apparatus and methodology for accurate determination of hydrogen uptake by light-atom hosts. *J. Alloys Compd.* **2007,** *446*, 692 – 697.

83. Kissinger, H. E. Reaction kinetics in differential thermal analysis. *Anal. Chem.* **1957,** *29* (11), 1702-1706.

84. Youssef, K. M.; Zaddach, A. J.; Niu, C.; Irving, D. L.; Koch, C. C. A novel low-density, high-hardness, high-entropy alloy with close-packed single-phase nanocrystalline structures. *Mater. Res. Lett.* **2015,** *3* (2), 95 – 99.

85. Xiang, J.; Liu, S.; Hu, W.; Zhang, Y.; Chen, C.; Wang, P.; He, J.; Yu, D.; Xu, B.; Lu, Y. Mechanochemically activated synthesis of zirconium carbide nanoparticles at room temperature: A simple route to prepare nanoparticles of transition metal carbides. *J. Eur. Ceram. Soc.* **2011,** *31* (8), 1491 – 1496.

86. Dorofeev, G.; Lubnin, A.; Lad'yanov, V.; Mukhgalin, V.; Puskkarev, B. Metallography, Structural and phase transformations during ball milling of titanium in medium of liquid hydrocarbons. *Phys. Met. Metallogr.* **2014,** *115* (2), 157 – 168.

87. Prince, E. *International Tables for Crystallography, Volume C: Mathematical, physical and chemical tables*. Springer Dordrecht, **2004**.

88. Newbury, D. E.; Ritchie, N. W. Performing elemental microanalysis with high accuracy and high precision by scanning electron microscopy/silicon drift detector energy-dispersive X-ray spectrometry (SEM/SDD-EDS). *J. Mater. Sci.* **2015,** *50* (2), 493 – 518.

89. Schüth, F.; Bogdanović, B.; Felderhoff, M. Light metal hydrides and complex hydrides for hydrogen storage. *ChemComm* **2004,** (20), 2249 – 2258.

90. Wang, H.; Lin, H.; Cai, W.; Ouyang, L.; Zhu, M. Tuning kinetics and thermodynamics of hydrogen storage in light metal element based systems–a review of recent progress. *J. Alloys Compd.* **2016,** *658*, 280 – 300.

91. Ma, L.-P.; Kang, X.-D.; Dai, H.-B.; Liang, Y.; Fang, Z.-Z.; Wang, P.-J.; Wang, P.; Cheng, H.-M. Superior catalytic effect of TiF_3 over $TiCl_3$ in improving the hydrogen sorption kinetics of MgH_2: Catalytic role of fluorine anion. *Acta Mater.* **2009,** *57* (7), 2250 – 2258.

92. Malka, I.; Czujko, T.; Bystrzycki, J. Catalytic effect of halide additives ball milled with magnesium hydride. *Int. J. Hydrogen Energy* **2010,** *35* (4), 1706 – 1712.

93. Liu, Y.; Zhong, K.; Luo, K.; Gao, M.; Pan, H.; Wang, Q. Size-dependent kinetic enhancement in hydrogen absorption and desorption of the Li− Mg− N− H system. *J. Am. Chem. Soc.* **2009,** *131* (5), 1862 – 1870.

94. Norberg, N. S.; Arthur, T. S.; Fredrick, S. J.; Prieto, A. L. Size-dependent hydrogen storage properties of Mg nanocrystals prepared from solution. *J. Am. Chem. Soc.* **2011,** *133* (28), 10679 – 10681.

95. Rusman, N. A. A.; Dahari, M. A review on the current progress of metal hydrides material for solid-state hydrogen storage applications. *Int. J. Hydrogen Energy* **2016,** *41* (28), 12108 – 12126.

96. Salehin, R.; Thompson, G. B.; Weinberger, C. R. Hydrogen trapping and storage in the group IVB-VIB transition metal carbides. *Mater. Des.* **2022,** *214*, 110399.

97. Andreasen, A.; Vegge, T.; Pedersen, A. S. Compensation effect in the hydrogenation/dehydrogenation kinetics of metal hydrides. *J. Phys. Chem. B* **2005,** *109* (8), 3340 – 3344.

98. Au, Y. S.; Obbink, M. K.; Srinivasan, S.; Magusin, P. C.; De Jong, K. P.; De Jongh, P. E. The Size Dependence of Hydrogen Mobility and Sorption Kinetics for Carbon-Supported MgH_2 Particles. *Adv. Funct. Mater.* **2014,** *24* (23), 3604 – 3611.

99. Varin, R.; Czujko, T.; Wronski, Z. Particle size, grain size and γ-MgH_2 effects on the desorption properties of nanocrystalline commercial magnesium hydride processed by controlled mechanical milling. *Nanotechnology* **2006,** *17* (15), 3856.

100. Wipf, H.; Klein, M. V.; Williams, W. S., Vacancy-Induced and Two-Phonon Raman Scattering in ZrC_x, NbC_x, HfC_x, and TaC_x. *Phys. Status Solidi B* **1981,** *108* (2), 489 – 500.

101. Momma, K.; Izumi, F. VESTA 3 for three-dimensional visualization of crystal, volumetric and morphology data. *J. Appl. Crystallogr.***2011,** *44* (6), 1272 – 1276.

102. Storms, E.; Krikorian, N. The variation of lattice parameter with carbon content of niobium carbide. *J. Phys. Chem.* **1959,** *63* (10), 1747 – 1749.

103. Holt, J.; Munir, Z. Combustion synthesis of titanium carbide: theory and experiment. *J. Mater. Sci.* **1986,** *21* (1), 251 – 259.

104. Hugosson, H. W.; Korzhavyi, P.; Jansson, U.; Johansson, B.; Eriksson, O. Phase stabilities and structural relaxations in substoichiometric TiC 1− x. *Phys. Rev. B* **2001,** *63* (16), 165116.

105. Castle, E.; Csanádi, T.; Grasso, S.; Dusza, J.; Reece, M. Processing and properties of high-entropy ultra-high temperature carbides. *Sci. Rep.* **2018,** *8* (1), 1 – 12.

106. Sarker, P.; Harrington, T.; Toher, C.; Oses, C.; Samiee, M.; Maria, J.-P.; Brenner, D. W.; Vecchio, K. S.; Curtarolo, S. High-entropy high-hardness metal carbides discovered by entropy descriptors. *Nat. Commun.* **2018,** *9* (1), 1 – 10.

107. Montero Banuelos, J. *Refractory high entropy alloys for hydrogen storage.* Ph.D. thesis, Université Paris-Est, Paris, France, **2020**.

108. Takeuchi, A.; Inoue, A. Classification of bulk metallic glasses by atomic size difference, heat of mixing and period of constituent elements and its application to characterization of the main alloying element. *Mater. Trans.* **2005,** *46* (12), 2817 – 2829.

109. Vegard, L. Die Konstitution der Mischkristalle und die Raumfüllung der Atome. *Zeitschrift für Physik* **1921,** *5* (1), 17 – 26.

110. Denton, A. R.; Ashcroft, N. W. Vegard's law. *Phys. Rev. A* **1991,** *43* (6), 3161.

111. Ungar, T. Microstructural parameters from X-ray diffraction peak broadening. *Scr. Mater.* **2004,** *51* (8), 777-781.

112. Nayebossadri, S.; Book, D. Compositional effects on the hydrogen cycling stability of multicomponent Ti-Mn based alloys. *Int. J. Hydrogen Energy* **2019,** *44* (21), 10722 – 10731.

113. Dehouche, Z.; Klassen, T.; Oelerich, W.; Goyette, J.; Bose, T.; Schulz, R. J. J. o. A.; Compounds, Cycling and thermal stability of nanostructured MgH_2–Cr_2O_3 composite for hydrogen storage. *J. Alloys Compd.* **2002,** *347* (1-2), 319-323.

114. Chandra, D., Intermetallics for hydrogen storage. In *Solid-state hydrogen storage*, Woodhead Publishing, Elsevier, **2008;** pp 315 – 356.

115. Sandrock, G., Hydrogen-Metal Systems. In *Hydrogen Energy System: Production and Utilization of Hydrogen and Future Aspects*, Yürüm, Y., Ed. Springer Netherlands: Dordrecht, **1995**; pp 135 – 166.

116. Crivello, J. C.; Dam, B.; Denys, R. V.; Dornheim, M.; Grant, D. M.; Huot, J.; Jensen, T. R.; de Jongh, P.; Latroche, M.; Milanese, C.; Milčius, D.; Walker, G. S.; Webb, C. J.; Zlotea, C.; Yartys, V. A. Review of magnesium hydride-based materials: development and optimisation. *Appl. Phys. A* **2016,** *122* (2), 97.

117. Cheng, F.; Tao, Z.; Liang, J.; Chen, J., Efficient hydrogen storage with the combination of lightweight Mg/MgH2 and nanostructures. *Chemical Communications* **2012,** *48* (59), 7334 – 7343.

118. Gorr, B.; Azim, M.; Christ, H.-J.; Chen, H.; Szabo, D. V.; Kauffmann, A.; Heilmaier, M. Microstructure evolution in a new refractory high-entropy alloy W-Mo-Cr-Ti-Al. *Metall. Mater. Trans. A* **2016,** *47*, 961 – 970.

119. Gorr, B.; Azim, M.; Christ, H.-J.; Mueller, T.; Schliephake, D.; Heilmaier, M. Phase equilibria, microstructure, and high temperature oxidation resistance of novel refractory high-entropy alloys. *J. Alloys Compd.* **2015,** *624*, 270 – 278.

120. Alonso, J. C.; Alonso, O. C. Unit Cell Volume, and Lattice Parameter of Cubic High Entropy Alloys. *arXiv:2104.14541 [cond-mat.mtrl-sci], arXiv.org, e-Print Arch., Condens. Matter* **2021**.

121. Lichter, B. Precision lattice parameter determination of zirconium-oxygen solid solution. *Trans. Met. Soc. AIME* **1960,** *218*.

122. Graetz, J.; Reilly, J. J. Thermodynamics of the α, β and γ polymorphs of AlH_3. *J. Alloys Compd.* **2006,** *424* (1-2), 262 – 265.

123. Birnbaum, H. Mechanical properties of metal hydrides. *J. Less-Common Met.* **1984,** *104* (1), 31 – 41.

124. Gabis, I.; Voit, A.; Evard, E.; Zaika, Y. V.; Chernov, I. A.; Yartys, V. Kinetics of hydrogen desorption from the powders of metal hydrides. *J. Alloys Compd.* **2005,** *404*, 312 – 316.

125. Ramasubramaniam, A.; Itakura, M.; Ortiz, M.; Carter, E. Effect of atomic scale plasticity on hydrogen diffusion in iron: Quantum mechanically informed and on-the-fly kinetic Monte Carlo simulations. *J. Mater. Res.* **2008,** *23* (10), 2757 – 2773.

126. Chen, Y.-S.; Lu, H.; Liang, J.; Rosenthal, A.; Liu, H.; Sneddon, G.; McCarroll, I.; Zhao, Z.; Li, W.; Guo, A.; Cairney J. Observation of hydrogen trapping at dislocations, grain boundaries, and precipitates. *Science* **2020,** *367* (6474), 171 – 175.

127. Takahashi, J.; Kawakami, K.; Tarui, T. Direct observation of hydrogen-trapping sites in vanadium carbide precipitation steel by atom probe tomography. *Scr. Mater.* **2012,** *67* (2), 213 – 216.

9. Appendix

9.1. Calculations of the selection paramters of AlLiMgTiZr

Table 19: Values of enthalpy of mixing ΔH_{mix} (kJ mol^{-1}) for atomic pairs contained in synthesized HEAs[108]

Element	Al	Li	Mg	Ti
Li	-4			
Mg	-2	0		
Ti	-30	34	16	
Zr	-44	27	6	0

Table 20: Atomic radii, valence electrons, melting point and concentration of the respective element.[69, 108]

Element	Atomic radius [pm]	Valence electrons [#]	Melting point [K]	Concentration
Al	143	3	933	0.2
Li	152	1	454	0.2
Mg	160	2	922	0.2
Ti	147	4	1943	0.2
Zr	162	4	2130	0.2

$$\delta = \sqrt{\sum_{i=1}^{n} c_i \left(1 - \frac{r_i}{\bar{r}}\right)^2} = \ldots = 0.0478 = 4.78\,[\%]$$

$$VEC = \sum_{i=1}^{n} c_i (VEC_i) = \ldots = 2.8\,[\text{a.u.}]$$

$$\Delta H_{mix} = \sum_{i=1, i \neq j}^{n} 4 \Delta H_{ij}^{mix} c_i c_j = \ldots = 0.48\,[kj\ mol^{-1}]$$

$$T_m = \sum_{i=1}^{n} c_i (T_m)_i = \ldots = 1276.4\,[\text{K}]$$

$$\Omega = \frac{T_m \Delta S_{mix}}{|\Delta H_{mix}|} = \frac{1276.4 \cdot 0.013381}{0.48}\,[a.u.]$$

9.2. Wavelength for ICP-OES Experiments

Aluminum:	167.078 nm	394.401 nm	396.152 nm
Lithium:	670.780 nm		
Niob:	269.706 nm	295.088 nm	
Titanium:	334.941 nm	336.121 nm	
Vanadium:	209.244 nm	311.071 nm	
Zirkonium:	339.198 nm	343.823 nm	

9.3. XRD-Pattern of cryomilled sample

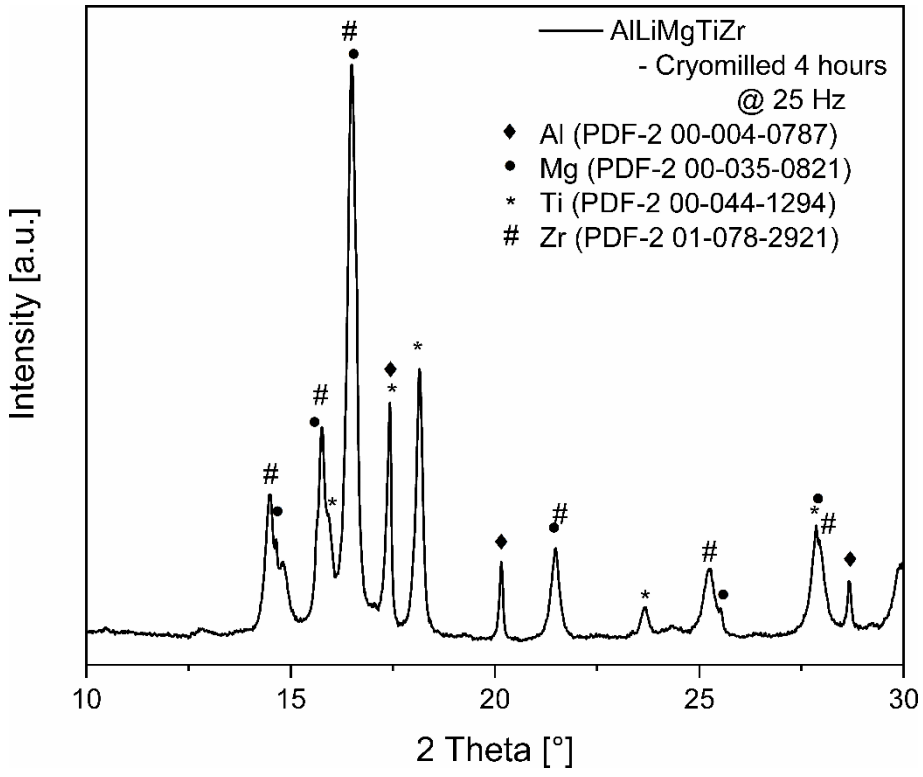

9.4. Theoretical uptake of PCAs

Hydrogen mass content within PCA:

$$wt._{H,Toluene}\ [\%]\ = \frac{M_H}{M_H + M_C} \cdot 100\ [\%] = \frac{8\ \cdot\ 1.00784}{92.14} \cdot 100\ [\%] = 8.75\ [\%]$$

$$wt._{H,Ethanol}\ [\%]\ = \frac{6\ \cdot\ 1.00784}{46.07} \cdot 100\ [\%] = 13.13\ [\%]$$

Mass of PCA assuming 8 wt.% during the synthesis:

$$m_{PCA} = 0.08 \cdot 2\ [g]\ = 0.16\ [g]$$

Hydrogen mass based on the PCA quantity used

$$m_{H,Toluene}\ =\ 0.16\ [g] \cdot 0.0875 = 0.014\ [g]$$

$$m_{H,Ethanol}\ =\ 0.16\ [g] \cdot 0.1313 = 0.021\ [g]$$

Theoretical uptake of synthesized material assuming complete uptake:

$$wt._{H,Toluene}\ [\%]\ =\ \frac{m_H}{m_H + m_{Alloy}} 100\ [\%] = \frac{0.014}{0.014 + 2} \cdot 100\ [\%] = 0.7\ [\%]$$

$$wt._{H,Ethanol}\ [\%]\ =\ \frac{m_H}{m_H + m_{Alloy}} 100\ [\%] = \frac{0.021}{0.021 + 2} \cdot 100\ [\%] = 1.04\ [\%]$$

9.5. Tracking Experiment for $Ti_{0.3}V_{0.25}Nb_{0.25}Zr_{0.1}Li_{0.1}$ compound

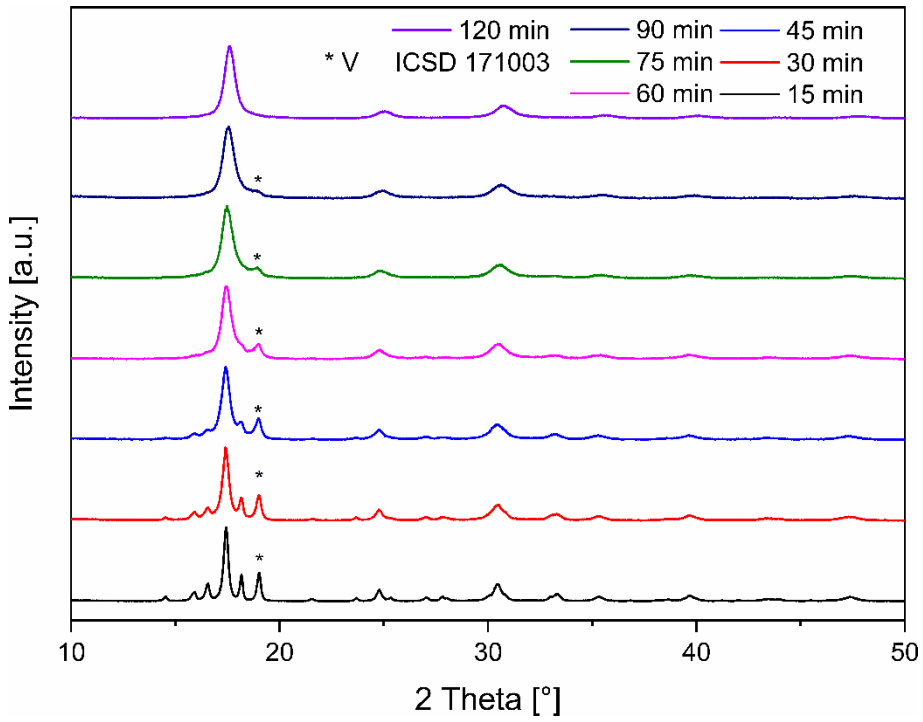

9.6. SEM-EDX Mappings of Mechanical Alloyed Samples

$Ti_{0.325}V_{0.275}Nb_{0.275}Zr_{0.125}$

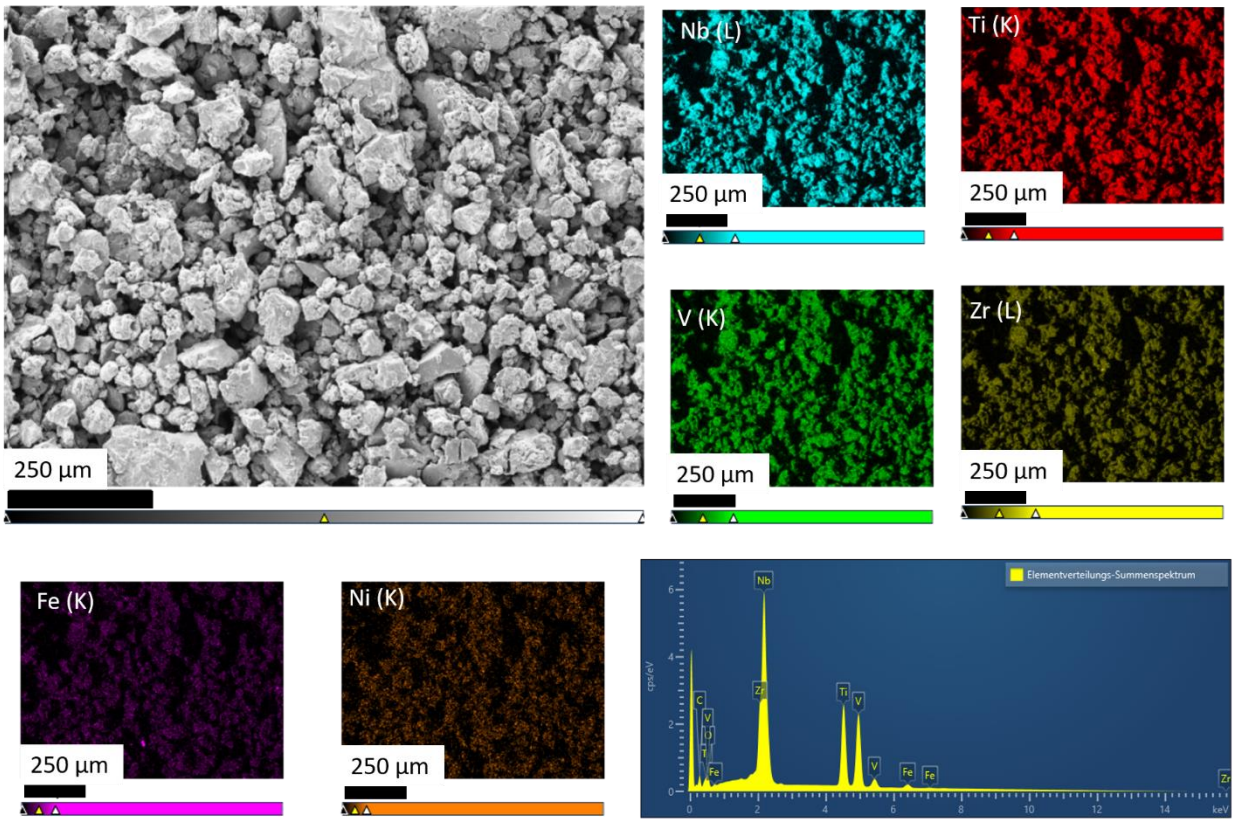

Element	Wt.%	At.%	Relative At.%
Ti (K)	21.96	25.18	33.01
V (K)	20.36	21.95	28.77
Nb (L)	34.00	20.10	26.35
Zr (L)	15.03	9.05	11.86
Fe (K)	2.15	2.12	-
Ni (K)	0.27	0.25	-
O (K)	6.22	21.35	-

$Li_{0.10}Ti_{0.30}V_{0.25}Nb_{0.25}Zr_{0.10}$

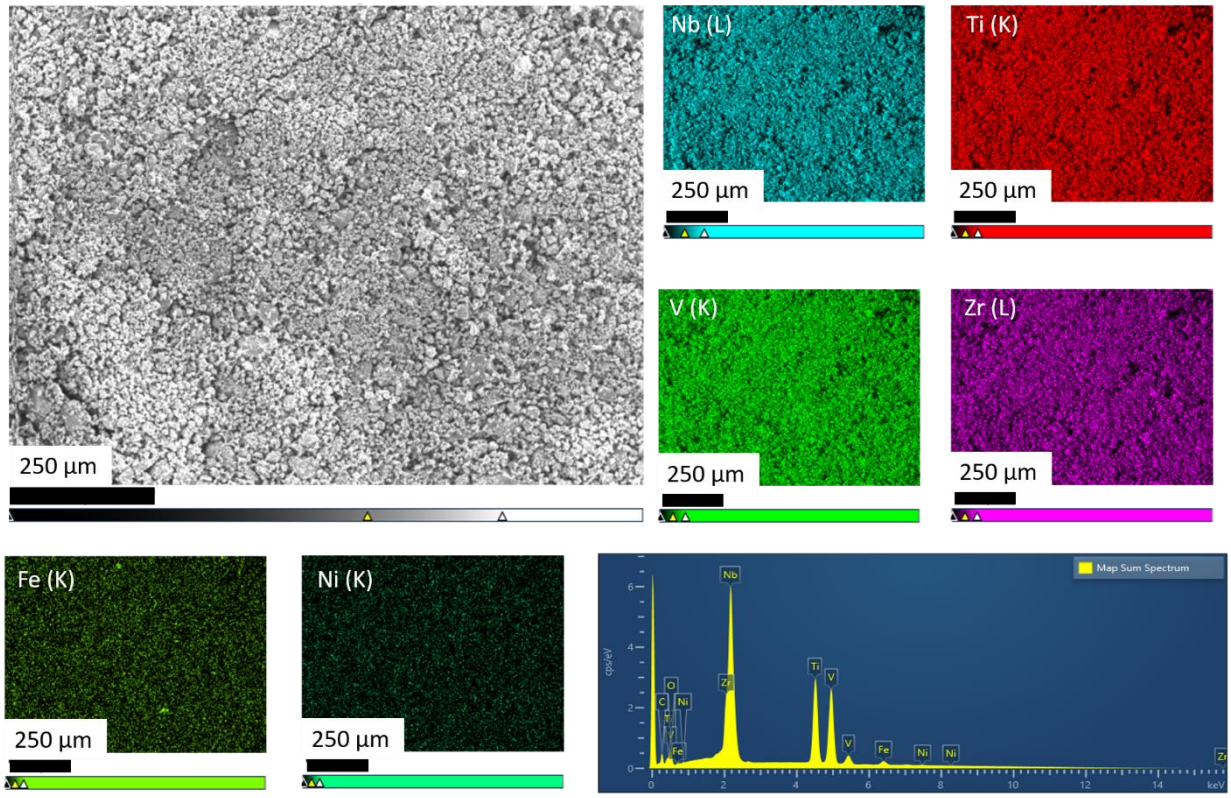

Element	Wt.%	At.%	Relative At.%
Ti (K)	22.73	23.64	34.78
V (K)	20.97	20.51	30.17
Nb (L)	31.87	17.09	25.14
Zr (L)	12.32	6.73	9.90
Fe (K)	2.15	1.92	-
Ni (K)	0.38	0.32	-
O (K)	9.57	29.81	-

$Al_{0.05}Li_{0.05}Ti_{0.3}V_{0.25}Nb_{0.25}Zr_{0.1}$

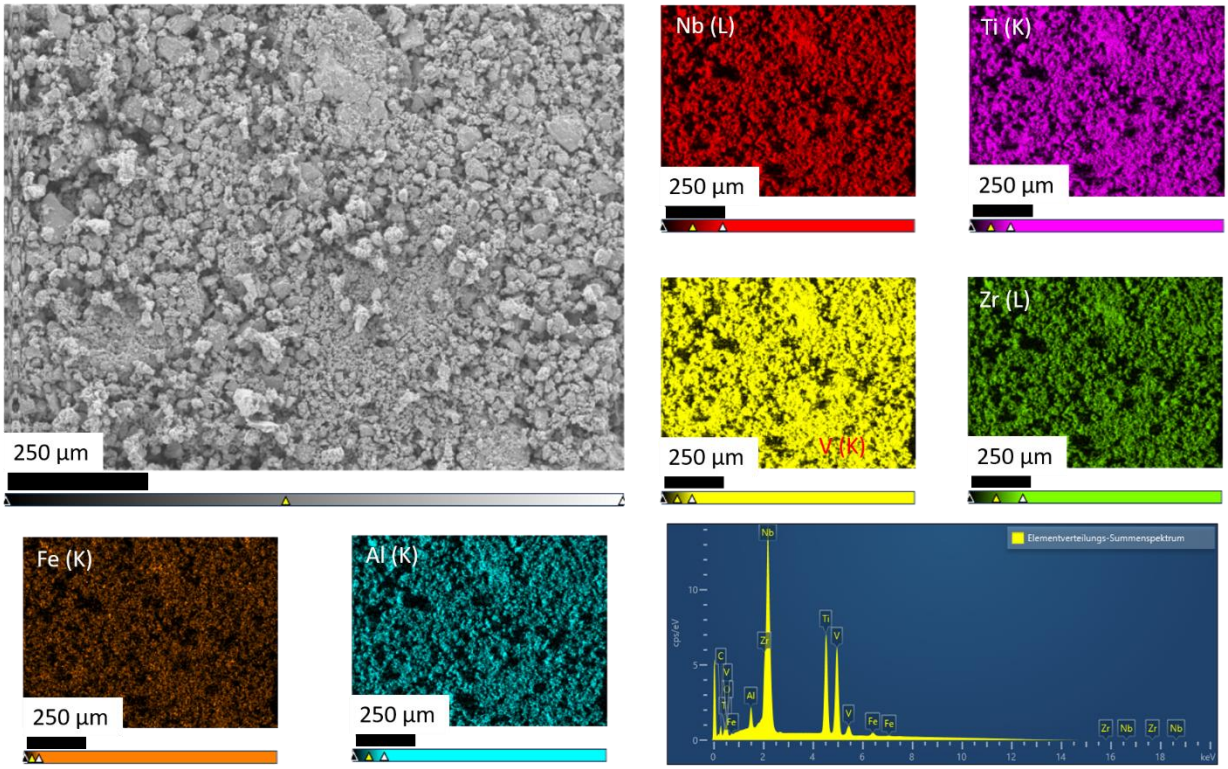

Element	Wt.%	At.%	Relative At.%
Al (K)	1.67	3.36	4.21
Ti (K)	23.61	26.77	33.47
V (K)	21.30	22.72	28.40
Nb (L)	33.20	19.41	24.27
Zr (L)	12.96	7.72	9.65
Fe (K)	1.68	1.63	-
Ni (K)	0.22	0.20	-
O (K)	5.36	18.19	-

$Al_{0.10}Ti_{0.30}V_{0.25}Nb_{0.25}Zr_{0.10}$

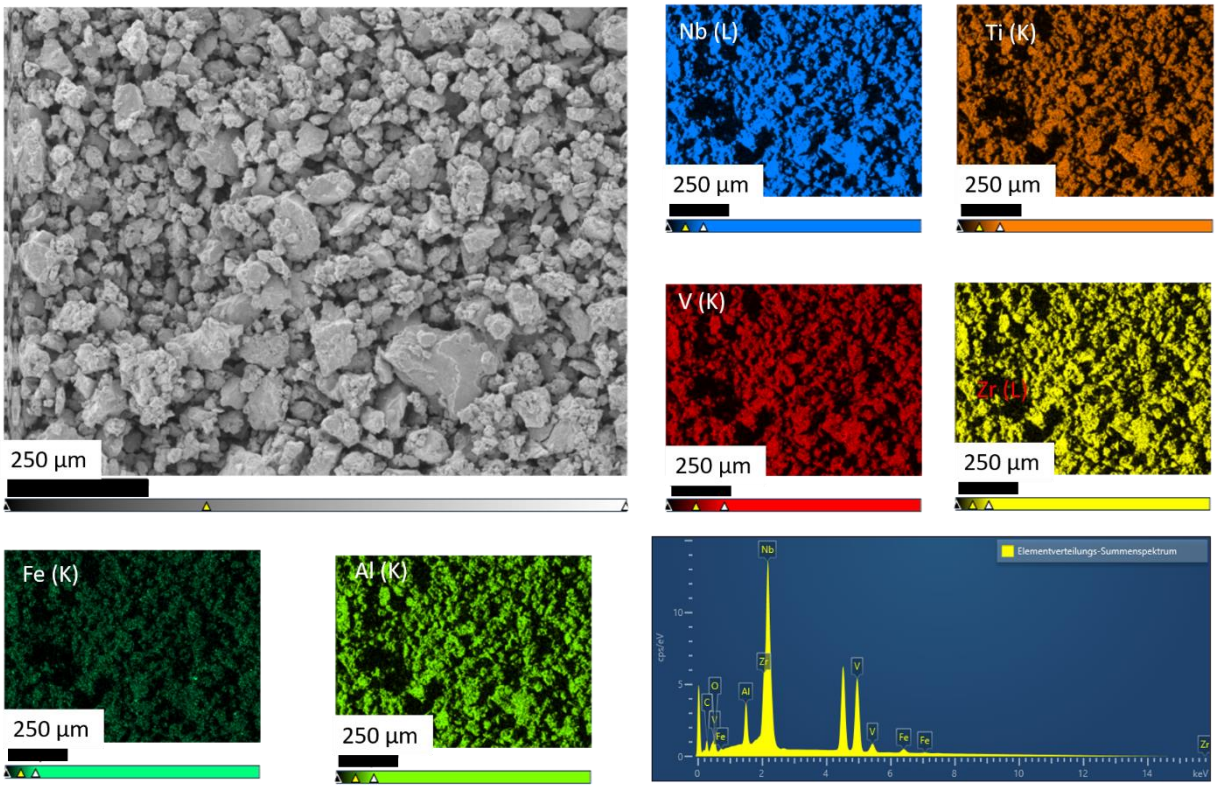

Element	Wt.%	At.%	Relative At.%
Al (K)	3.56	6.98	8.91
Ti (K)	21.96	24.26	30.97
V (K)	19.68	20.45	26.10
Nb (L)	32.94	18.76	23.95
Zr (L)	13.60	7.89	10.07
Fe (K)	2.15	2.03	-
Ni (K)	0.25	0.22	-
O (K)	5.86	19.40	-

9.7. SEM-EDX Mappings of Reactive Milled Samples

$Ti_{0.325}V_{0.275}Nb_{0.275}Zr_{0.125}$

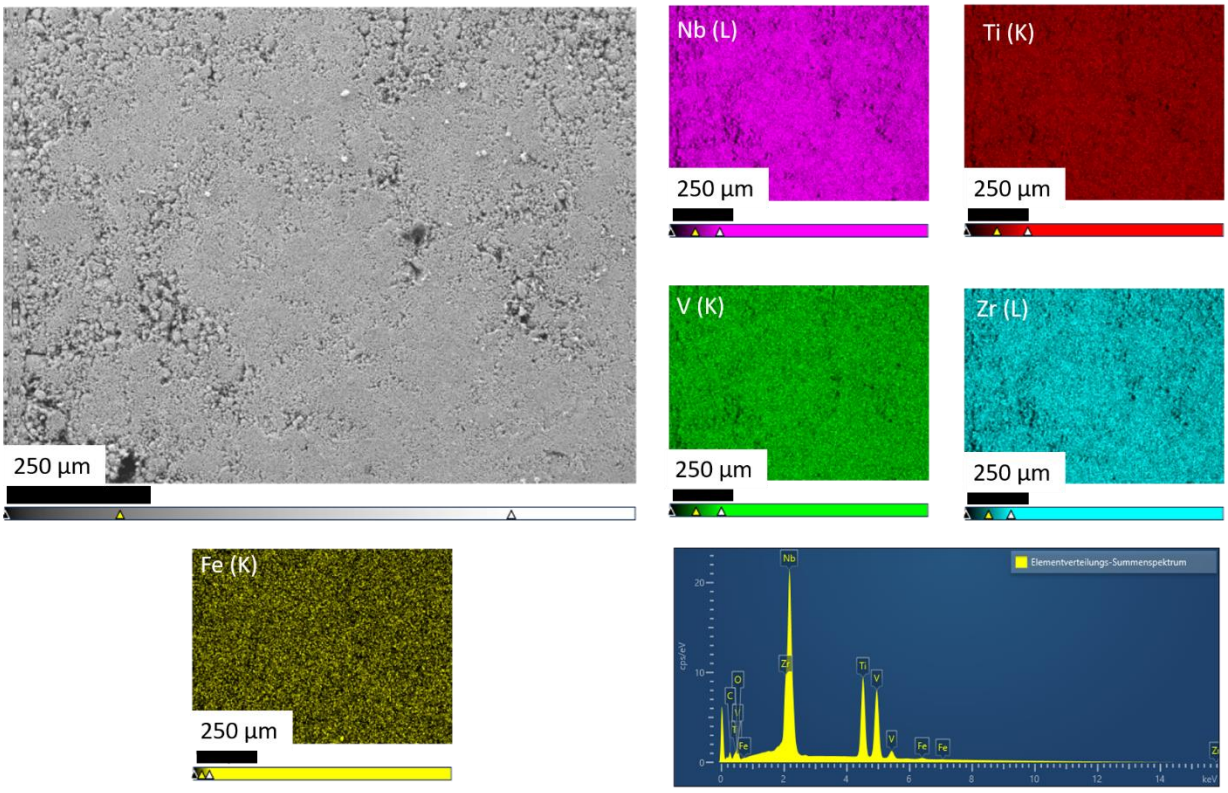

Element	Wt.%	At.%	Relative At.%
Ti (K)	22.79	25.98	33.75
V (K)	20.00	21.44	27.85
Nb (L)	34.58	20.33	26.41
Zr (L)	15.41	9.23	11.99
Fe (K)	0.68	0.67	-
O (K)	6.55	22.35	-

$Li_{0.10}Ti_{0.30}V_{0.25}Nb_{0.25}Zr_{0.10}$

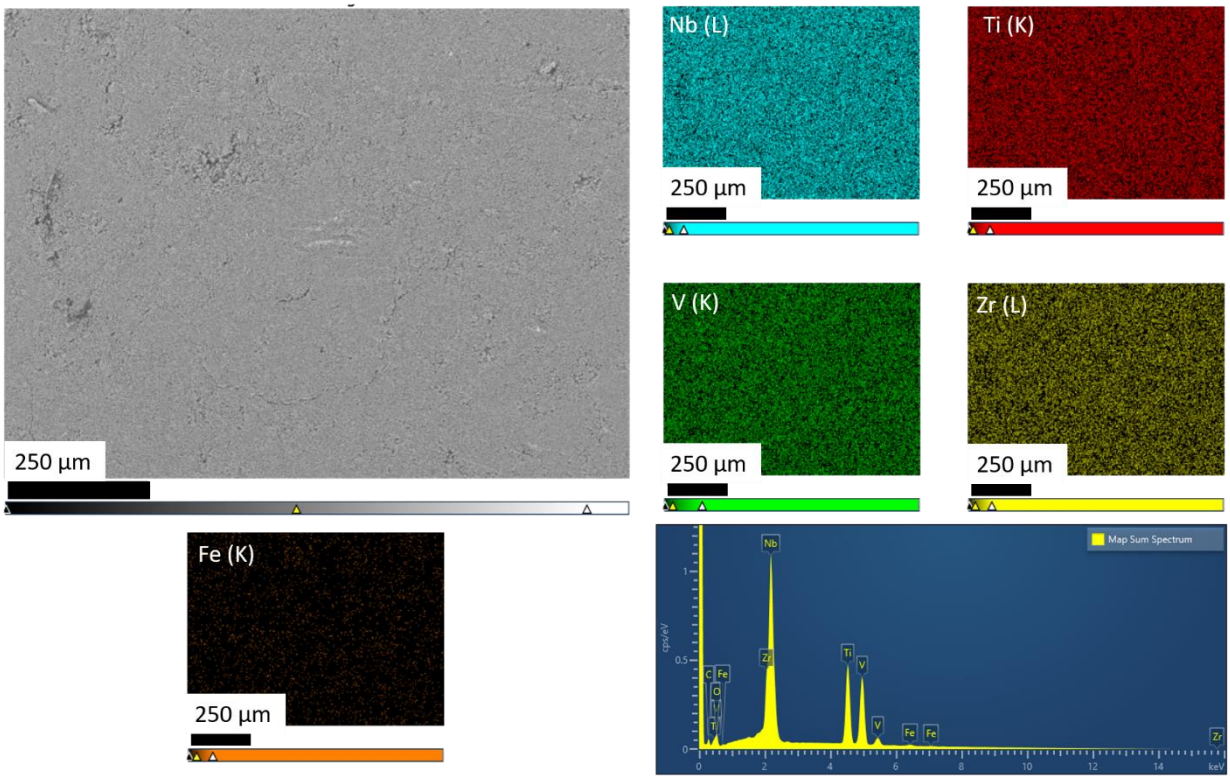

Element	Wt.%	At.%	Relative At.%
Ti (K)	22.77	25.86	33.78
V (K)	19.98	21.34	27.87
Nb (L)	35.89	21.01	27.44
Zr (L)	14.01	8.35	10.90
Fe (K)	0.64	0.62	-
O (K)	6.71	22.81	-

$Al_{0.05}Li_{0.05}Ti_{0.3}V_{0.25}Nb_{0.25}Zr_{0.1}$

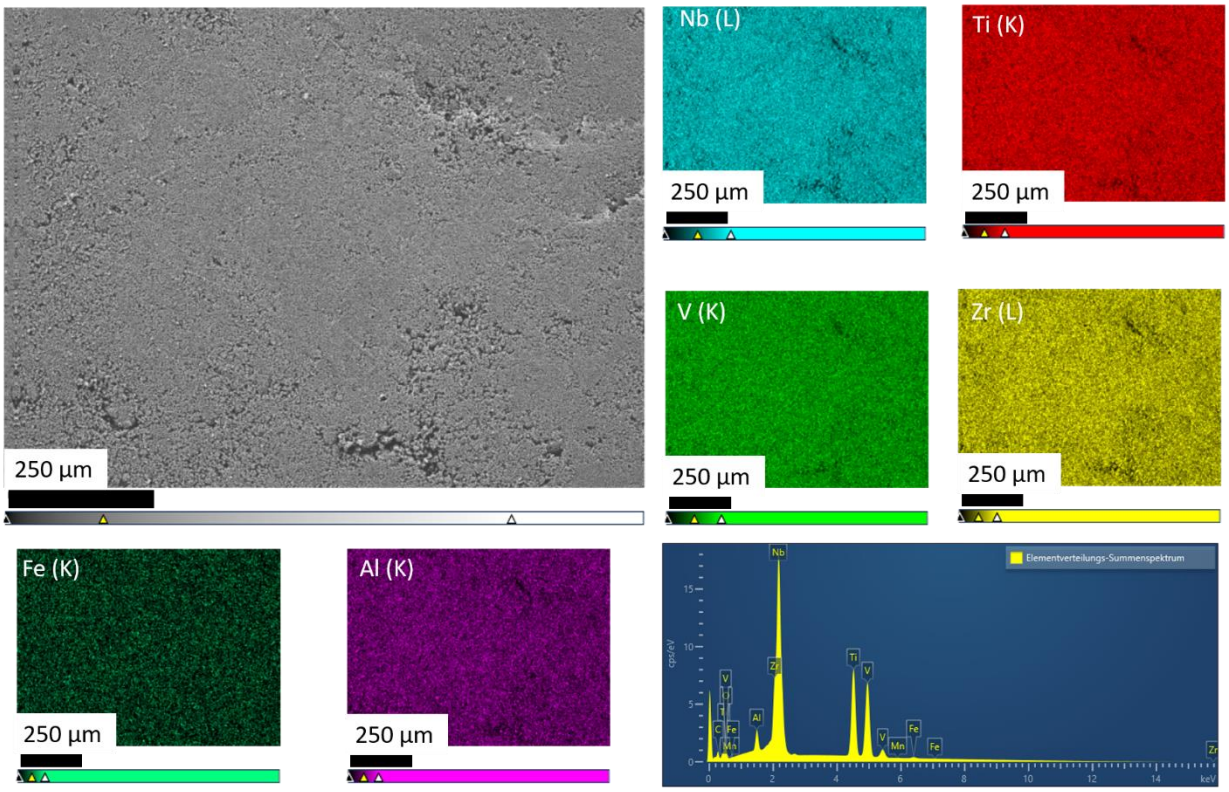

Element	Wt.%	At.%	Relative At.%
Al (K)	1.80	3.64	4.54
Ti (K)	22.92	26.13	32.59
V (K)	20.10	21.54	26.87
Nb (L)	35.27	20.72	25.84
Zr (L)	13.60	8.14	10.15
Fe (K)	0.61	0.59	-
Mn (K)	0.10	0.10	-
O (K)	5.61	19.14	-

$Al_{0.10}Ti_{0.30}V_{0.25}Nb_{0.25}Zr_{0.10}$

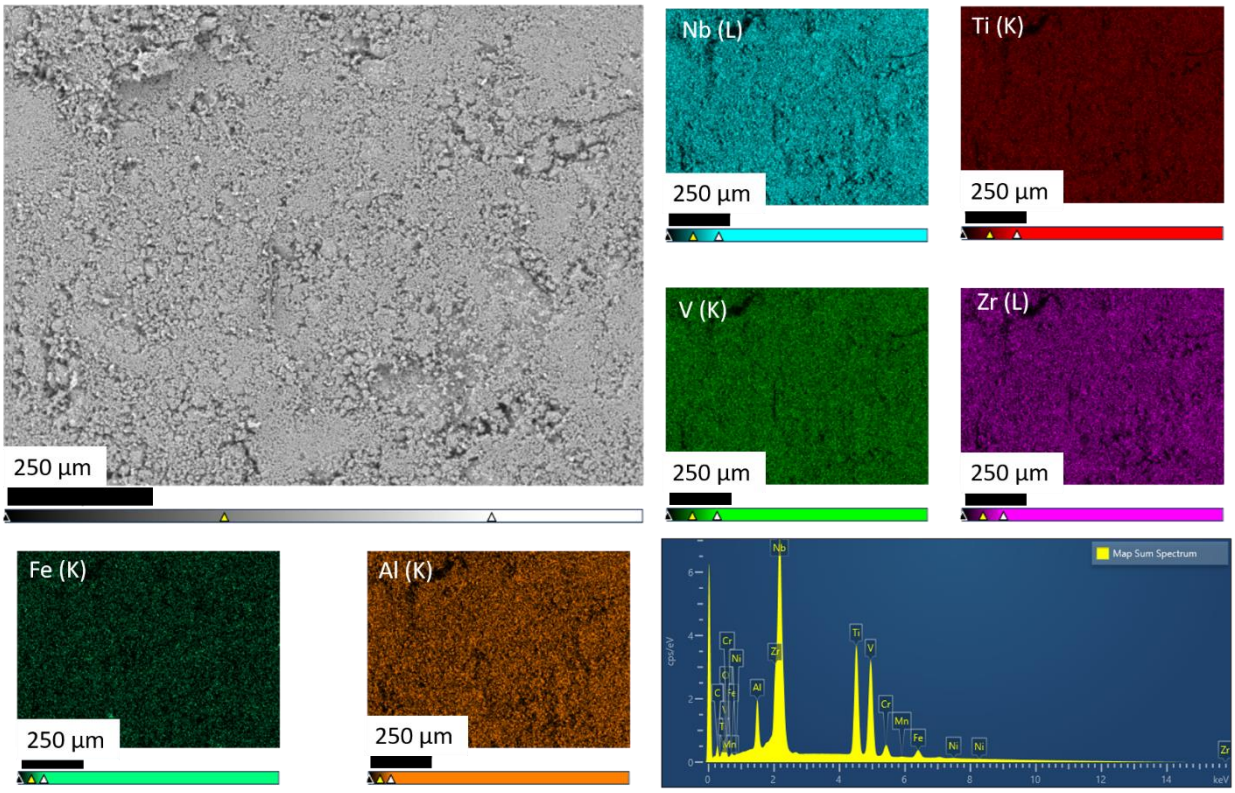

Element	Wt.%	At.%	Relative At.%
Al (K)	3.33	6.60	8.41
Ti (K)	22.31	24.87	31.72
V (K)	20.07	21.04	26.84
Nb (L)	32.37	18.60	23.72
Zr (L)	12.44	7.28	9.28
Fe (K)	3.41	3.26	-
Mn (K)	0.18	0.18	-
Cr (K)	0.38	0.39	-
Ni (K)	0.24	0.21	-
O (K)	5.61	19.14	-

DOI: 10.17185/duepublico/78721
URN: urn:nbn:de:hbz:465-20230706-140812-1